Predictive Numerical Model of the Behavior of Polymer Skin-Foam-Skin Multilayers : Influence of the Strain Rate. Comparison Tests / Simulations

Prasad Baliram Mahajan

THÈSE

Pour l'obtention du Grade de
DOCTEUR DE L'ÉCOLE NATIONALE SUPÉRIEURE DE MÉCANIQUE ET D'AÉROTECHNIQUE
(Diplôme National – Arrêté du 25 mai 2016)

École Doctorale :
Sciences et Ingénierie en Matériaux, Mécanique, Énergétique

Secteur de Recherche : Mécanique des solides, des matériaux, des structures et des surfaces

Présentée par :

Prasad Baliram MAHAJAN

****

Modèle numérique prédictif du comportement des multicouches peau-mousse-peau de polymère. Influence de la vitesse de déformation - comparaison essais / simulations

-

Predictive numerical model of the behavior of polymer skin-foam-skin multilayers. Influence of the strain rate - comparison tests / simulations

****

Directeur de thèse : GRANDIDIER Jean-Claude
Co-encadrement de la thèse: LAINÉ Eric

****

Soutenue le 27/06/2022

devant la Commission d'Examen

****

JURY

FURGIUELE Franco, Professeur, University of Calabria, Arcavacata di Rende (Italie), Rapporteur
GORNET Laurent, Maître de Conférences HDR, École Centrale de Nantes, Nantes, Rapporteur
ESPINOSA Christine, Professeur, ISAE-SUPAERO, Toulouse, Examinatrice
CHAGNON Gregory, Professeur, Université Grenoble Alpes, Grenoble, Examinateur
WENCHAO Yu, Ingénieur de Recherche, TotalEnergies, Bruxelles, Examinateur
GIGLIOTTI Marco, Professeur, Université de Poitiers, Examinateur
GRANDIDIER Jean-Claude, Professeur, ISAE-ENSMA, Poitiers, Examinateur
LAINÉ Eric, Ingénieur de Recherche, ISAE-ENSMA, Poitiers, Examinateur

ACKNOWLEDGEMENTS

First and foremost, I would like to express my sincere gratitude to Prof. Jean-Claude GRANDIDIER and Dr. Eric LAINE for giving me this PhD opportunity with Institute Pprime/ISAE-ENSMA and his immense support, encouragement, patience and motivation throughout my thesis.

Friends, too many to name here,made this journey a blast.. I would like to express my gratitude to all my friends.

I am eternally indebted to my parents and my sister who have been a pillar of support throughmy years in the wilderness.Their love and encouragement made me the person that I am.

Abstract

Sandwich materials (skin-core-skin) have a high bending and shear stiffness and are able to absorb energy under the impact, these characteristics are interesting for automotive parts. New processes are now proposed to manufacture mono polymer sandwiches (skin and core of the same material) by using foaming agents. These structures are easily recyclable, but the generated foam presents an inhomogeneous microstructure, with highly variable thicknesses and mesostructure depending on the process (rotational molding, injection molding). The question that arises then concerns the behavior of these structures: is it possible to identify the behavior of the foam with tests performed on several sandwiches with unique mesostructures? To answer this question, it is necessary to use specific protocols in order to identify the constitutive model of the skins and the foam, which is the object of this work.

The first step is to develop a viscoelastic-viscoplastic model for the sandwich skin, taking into account the effect of hydrostatic pressure. Only tensile specimens manufactured according to the same process as the sandwich are used to identify it. The DAKOTA software is used to identify the model parameters based on these tensile tests at different constant true strain rates. The predictive quality of the constitutive model is evaluated by comparing it to 3-point and 4-point bending tests on a single layer (skin) and tests on a complex structure. The main result is that it is possible to predict the multi-axial behavior of the skins with tensile tests, but is this sufficient to predict the behavior of the foam?

To answer this question, a virtual approach is chosen. As the foam generated in these sandwiches has porosity levels below 40%, it is assumed that the polymer constituting the foam had the same behavior as the bulk material. Under this condition, knowing the mesostructure, the response of the foam is predicted. As the foam is inhomogeneous, tomographies on samples are performed to characterize the whole foam layer: the porosity fields, the distribution of the pore radius, and the distances between the pores. To perform this step, a numerical tool is developed under Matlab®. A histogram of three quantities is drawn to define the size of several Representative Volume Elements (RVEs) of the foam variability. These RVEs are numerically stressed in tension to generate a response base of these mesostructures. For each RVE, the parameters of the equivalent homogeneous constitutive model are identified using DAKOTA. Relationships between the porosity and the viscoelastic-viscoplastic constitutive model parameters of the bulk could then be developed.

The last step consisted in validating the model using 3-point bending and compression tests performed on different sandwiches. Specific metrology allowed to record the global and mesoscopic response. These responses are compared with numerical simulations that integrate the porosity distribution of the tested sample. This is introduced at each Gauss point of each finite element of the model. The comparison allowed to evaluate the quality of the porosity-

dependent constitutive model and to show that 3-point bending led to a much better correlation than compression due to the limitation of the tests to identify the influence of hydrostatic pressure. Substantial work remains to be done.

In this work, Abaqus® v2017, DAKOTA v6.10.0 are the softwares used, and FORTRAN, Python and Matlab® are the programming languages used.

Keywords: Deformations (Mechanics), Polymer, Flexure, Porosity, Sandwich construction-mechanical properties, Microstructure, Simulation methods, Tomography

RÉSUMÉ

Les matériaux sandwichs (peau-âme-peau) présentent une forte rigidité en flexion et cisaillement et sont capables d'absorber de l'énergie sous impact, ces caractéristiques sont intéressantes pour les pièces automobiles. De nouveaux procédés sont aujourd'hui proposés pour réaliser des sandwichs mono polymère (peau et âme d'une même matière) en utilisant des agents moussants. Ces structures sont facilement recyclables, mais la mousse générée présente une microstructure inhomogène, avec des épaisseurs et une mésostructure fortement variables et dépendantes du procédé (rotomoulage, moulage par injection). La question qui se pose alors porte sur le comportement de ces structures : est-il possible d'identifier le comportement de la mousse avec des tests réalisés sur plusieurs sandwichs possédant des mésostructures uniques ? Pour y répondre il est nécessaire d'employer des protocoles spécifiques afin d'identifier les lois de comportement des peaux et de la mousse, c'est l'objet de ce travail.

La première étape a consisté à développer pour la peau du sandwich, un modèle viscoélastique-viscoplastique prenant en compte l'effet de la pression hydrostatique. Uniquement des éprouvettes de traction fabriquées selon le même processus que le sandwich, ont été utilisées pour l'identifier. Le logiciel DAKOTA a permis d'identifier les paramètres du modèle sur la base de ces essais de traction à différentes vitesses de déformation vraie constante. La qualité de prédiction du modèle de comportement a été évalué en le comparant à des essais de flexion trois points et quatre points sur un monocouche (peau) et des essais sur une structure complexe. Le résultat majeur est qu'il est possible de prédire le comportement multixial des peaux avec des essais de traction, mais cela suffit-il pour prédire le comportement de la mousse ?

Pour y répondre une démarche virtuelle a été choisie. La mousse générée dans ces sandwichs a des niveaux de porosité inférieur à 40%, ainsi il a été supposé que le polymère constituant la mousse avait le même comportement que le matériau massif. Sous cette condition, connaissant la mésostructure, la réponse de la mousse a été prédite. Comme la mousse est inhomogène, des tomographies sur des échantillons ont été réalisées pour caractériser dans toute la couche de mousse : les champs de porosité, la distribution du rayon des pores et les distances entre les pores. Pour réaliser cette étape, un outil numérique a été développé sous Matlab®. Un histogramme des trois quantités a été tracé pour définir la dimension de plusieurs Volume Elémentaire Représentatif (RVE) de la variabilité de la mousse. Ces RVEs ont été sollicités numériquement en traction pour générer une base de réponses de ces mésostructures. Pour chaque RVE, les paramètres du modèle de comportement homogène équivalent ont été identifiés en utilisant DAKOTA. Des relations entre la porosité et les paramètres du modèle de comportement viscoélastique-viscoplastique du modèle du matériau massif ont alors pu être élaborées.

La dernière étape a consisté à valider le modèle à l'aide de tests de flexion 3 points et de compression réalisés sur différents sandwichs. Une métrologie spécifique a permis d'enregistrer

la réponse globale et mésoscopique. Ces réponses ont été comparées avec des simulations numériques qui intègrent la distribution de porosité de l'échantillon testé. Celle-ci a été introduite à chaque point de Gauss de chaque élément fini du modèle. La comparaison a permis d'évaluer la qualité de la loi de comportement dépendante de la porosité et de montrer que la flexion 3 points conduisaient à une bien meilleure corrélation que la compression du fait de la limitation des essais d'identification de l'influence de la pression hydrostatique. Un travail substantiel reste à conduire.

Dans ce travail, Abaqus® v2017, DAKOTA v6.10.0 sont les logiciels utilisés et FORTRAN, Python et Matlab® sont les langages de programmation.

Mots-clés : Déformations (mécanique), Polymère, Flexion (mécanique), Porosité, Matériaux sandwich-propriétés mécaniques, Microstructure, Méthodes de simulations, Tomographie

Content

LIST OF FIGURES

LIST OF TABLES

Chapter 1 **General introduction and problem presentation**

In the transportation sector, energy has become a key point in developing and optimizing new structures. If the use of new sources and storage means (battery and electric motor) of energy is the subject of much scientific work, innovation, and large-scale industrial deployments then increasing the efficiency of these systems is another objective of engineers. Among other possible improvements, mass reduction is a concern.

Composite and polymer materials are the answer to this desire to reduce weight. They are perfectly integrated into the design process. The choice of these materials depends on the specifications and limitations of the material. In addition, the different polymer grades have different material properties that determine the areas of use.

For classical composites, the choice of matrix and reinforcement are selected, and optimized according to the thermo-mechanical constraints, the conditions of use, and the manufacturing process. This selection process integrates a very large number of parameters and this approach is more and more applied in design offices.

Today the use of composite materials is vast in many industrial sectors: aviation, automotive, marine, energy, construction, bio-medical, and sporting industries. The use of composites is increasing day by day. Significantly lightweight is the prime reason behind it; components are lighter than aluminum and represent 25% of the weight of steel. Their durability is significant too. In addition to that, they have excellent chemical resistance; usually, that could damage conventional metals in acidic environments.

The composite material constitutes two or more constituents with different chemical and physical properties when combined, producing a material with tailored characteristics. The primary constituents in a composite material are the matrix and reinforcement. Composite materials have unique characteristics that come from the properties of different materials. According to use or need, it can be produced with different physical properties like high strength, lightweight, corrosion resistance, durability, design flexibility, thermal and electrical insulation, etc.

By extending this material and optimizing it to 'semi-structured' like a sandwich is the solution that can also be used. Moreover, by combining various architectures, specific stiffness can become very interesting. In this respect, additive manufacturing opens more than interesting perspectives by studying mesostructure and optimizing by adapted topological algorithms [1], [2].

The possibilities are numerous, but an additional constraint has appeared today: recycling. The structures and the materials constituting them must be either treated to be destroyed

without damage to the environment, or recycled for reuse at the same level of performance or in parts of lesser capacity.

This new philosophy strongly limits the design cycle with the need to reconsider the materials and their nature. However, the process and life cycle must not be neglected in this approach. The design of new structures requires us to take a step back and open up new development avenues.

First, it is essential to underline that one of the difficulties encountered in recycling composite materials is their heterogeneity. One of the techniques to recycle the composite is consists of separating the phases [3]. If this recycling method is applicable then the energy required is high, and the processes are complex to implement and deploy on an industrial scale. For sandwiches, the problem is just as identical or even more complex because more than two materials have to be separated and then treated or eliminated.

This problem can also appear for polymer structures if several families of materials are assembled to make structures. This situation is not rare where different materials are used to form a structure. This step requires mixing materials, and consequently, it makes their recycling more complex.

Is it possible to create single-material composites? The idea is to create stiff fibers by stretching a polymer. The alignment of the macromolecular chains then helps to improve stiffness and resistance properties much higher than the polymer in massive form. If these fibers are embedded in a polymer matrix of the same nature, it is possible to generate Self-Reinforced Polymer (named in the following, SRP). A second CIFRE *TotalEnergies* thesis in parallel to this one, had an objective to study their thermo-mechanical behavior [4]. This work confirms the potential of such a composite material with Ultra High Molecular Weight Polyethylene (UHWMPE) fibers and polyethylene matrix. Furthermore, it has been shown that specific properties of epoxy glasses can be targeted, which opens up a vast application potential.

One of the outstanding results is the recycling capacity of these materials is that materials can be reused by simple grinding without separation with improved properties in the end. This last remark is important because it opens many perspectives on using this family of materials with a life cycle quite relevant. The idea of this thesis is to extend this idea of mono-material to the concept of sandwich. This concept is operational with the fabrication of foamed sandwich structures.

Rotational molding is an interesting manufacturing technique because it allows the production of complex-shaped parts in a single operation. Although the possibilities are great, the polymeric materials manufactured by this process do not reach the same level of properties as those obtained by injection. However, it is possible to create multi-layers by successively filling

the mold with different materials and adapting the temperature of the mold. Polymers have developed granules that can generate foams by releasing gas. In *TotalEnergies* patents [5] the concept called Skin-Foam-Skin (named in the following, SFS) has been proposed, and allows to elaborate single material sandwich structures. It has been demonstrated that the structures of small cars can be easily manufactured.

This idea has been deployed in the context of injection molding; it is possible in the industry to manufacture these sandwiches with fast process times. It is in accordance with the large number of the part required in the automotive industry, for example.

By combining SRP and the SFS concept, it is easy to imagine all the potential of these semi-structures in terms of specific properties and ease of recycling. As a single material makes up the sandwich as explained above, a grinding can simply be deployed for reuse.

In this very particular context, the use of such a solution in structures of the transport sector will require a perfect knowledge of their thermo-mechanical behavior. More precisely, it is aimed, for example, at the manufacturing of an engine hood. If this part does not support high loads it is not a problem. On the other hand, the impact behavior under low energy must be controlled for the safety of pedestrians during possible road accidents. The flexibility and ductility must allow to absorb the shocks and thus limit the physical damage.

The behavior and its sensitivity to a speed of semi-crystalline polymers have been studied extensively, still, the transition of this knowledge in the context of the structure is never simple. Many constitutive models have been developed with standardized tests on specimens with their own manufacturing processes. However, the spherulitic mesostructure depends strongly on the conditions of the manufacturing process. Consequently, the behavior of structure may not always correspond to the behavior of the specimens (single layer or skin) created for the characterization. Moreover, many constitutive models in the literature have not been tested to predict the behavior of complex structures. This is an essential point in an industrial context and passing this step is not an easy exercise. But it is so common in the literature not to validate the model on a structure.

This difficulty highlighted above is made even more acute for SFS-type sandwiches. Many questions arise:

- The microstructure of the skins is strongly dependent on all process parameters and steps. Differences in microstructure may appear due to the processing parameters of rotational molding and injection molding. The temperature and pressure variations are distinct between the two processes, and in the case of rotational molding, the upper and lower skin temperatures may be distinct.

- The foam generated by the injection molding process does not have a very high pore content, which has the disadvantage of limiting the effectiveness of the specific properties, while the mechanical properties are of a high level. In the case of very high pore content of foams where the walls between the bubbles are much stretched but here the distance between the edges of the pores is such that the material can more or less retain its spherulitic mesostructure. Obviously, the morphology in these areas of the material is an interesting open question but will not be addressed here due to the lack of adequate experimental means.

- Even if the porosity is low still there are gradients of porosity that appear in the sandwich. In other words, a variable field of mesostructure (porosity rate, pore size, the distance between pores, etc.) is present but is not perfectly known, and its distribution is not known. This is an obstacle to consider the use of this type of architecture in an industrial part. This architecture is directly linked to the parameters of the processes used.

- Study of the behavior of these SFS sandwiches is a scientific challenge. Two types of work can be considered. Establishing a fine relation of the behavior with the fine description of the microstructure. Which contains gradients that will require the implementation of homogenization techniques in a viscoplastic context. The question of representative volume elements (named in the following, RVE) is widely debated in the literature, and in our case, it is a real open question because the distribution of porosities interacts with the gradient of the layer. In other words, the statistical variation of the distribution of pore-defining parameters is of the same order of magnitude as the thickness of the foam layer. At an intermediate scale and closer to the interest of engineering offices, understanding this property gradient at the scale of a structure is an interesting scientific and technical issue.

The objective of the thesis is to develop a model of the behavior of a sandwich used for an engine hood application. The mechanical behavior, and the sensitivity of the speed to the behavior of SFS are at the heart of the study. With respect to the work done in the literature, the important point is, the will to create at best numerical models which can be used for the calculation of complex structures, which obviously requires a comparison between simulations and experiments on structures.

Industrial point of view it is important to develop a protocol to characterize the SFS structure. At the end of the thesis, it is necessary to consider the application of this study with respect to work in the design offices in the industry. This is an essential point to keep in mind throughout the reading of the document, especially with regard to certain choices.

The methodology followed in this thesis is expressed through the different chapters of this document.

The second chapter presents the bibliography; the objective is to detail some works on the same subject and to list the tools necessary for the fulfillment of this work. First, the capabilities of sandwiches and the classically used architectures are presented. Comparing parameters of a sandwich is proposed. A chapter details the behavior of polymers and their sensitivity to speed. It is far from being all-inclusive but provides some essential keys for the modeling of the structure. A very short summary of homogenization techniques is presented. It allows to position the technique used in this work to model the foam behavior.

The third chapter deals with the problem of modeling the skin (first and last layer in SFS). An elasto-viscoplastic constitutive model along with its identification process has been detailed. From an industrial point of view, it is important that identified constants should be able to simulate the structures in accepted industrial standards. Tensile tests are dedicated to the identification of constants of the constitutive model. The identification process is based on the optimization tool DAKOTA, which is integrated with Abaqus® to identify the parameters of the constitutive model. Validation of models is carried out by comparing simulation and experiments in 3- point and 4- point bending (named in the following, 3PB and 4PB) tests. The capabilities of the model have been studied by simulating bottles subjected to the internal pressure are detailed. The objective of this work is to create a predictive model able to simulate the structural response. This model will be used in the constitutive model of the foam.

The fourth and fifth chapter is dedicated to the experiments on SFS samples and the modeling of foam. In a first step, the morphologies of the foam obtained by rotational molding and by injection are analyzed by tomographic image processing. A statistic is obtained, and on the basis of this knowledge, RVEs are created. Virtual tensile tests are carried out to quantify the variation of the behavior according to two parameters of the RVEs which eventually define its porosity. The identification tool used in the previous part is used to link morphological parameters of RVEs to the constants of the constitutive model. This constructed model thus can be evaluated by comparisons with tests carried out on sandwiches. Finally, the ability of the SFS sandwich model to simulate the behavior of the structures is evaluated, which allows for conducting a critical analysis of the methodology.

The document is classically concluded with a conclusion and perspective.

Chapter 2 **Bibliography review and tools**

2.1 Generalities on sandwich structures

A sandwich structure (Figure 2-1 (A)) is generally made up of three components with different but complementary properties: the skins, the core, and the adhesive. The skins are thin and have very good mechanical characteristics (high modulus, high strength). Between the two-skin layers, a core material of high thickness and low density is inserted. The insertion of core between skins increases the moment inertia of the structure, and consequently, its bending stiffness while minimizing the mass of the sandwich composite. The core of the sandwich is made with several materials: honeycomb (Figure 2-1 (B)), and balsa (Figure 2-1 (C) foam (Figure 2-1 (D)). The last component is an adhesive layer which helps the composite assembly and transmit stresses.

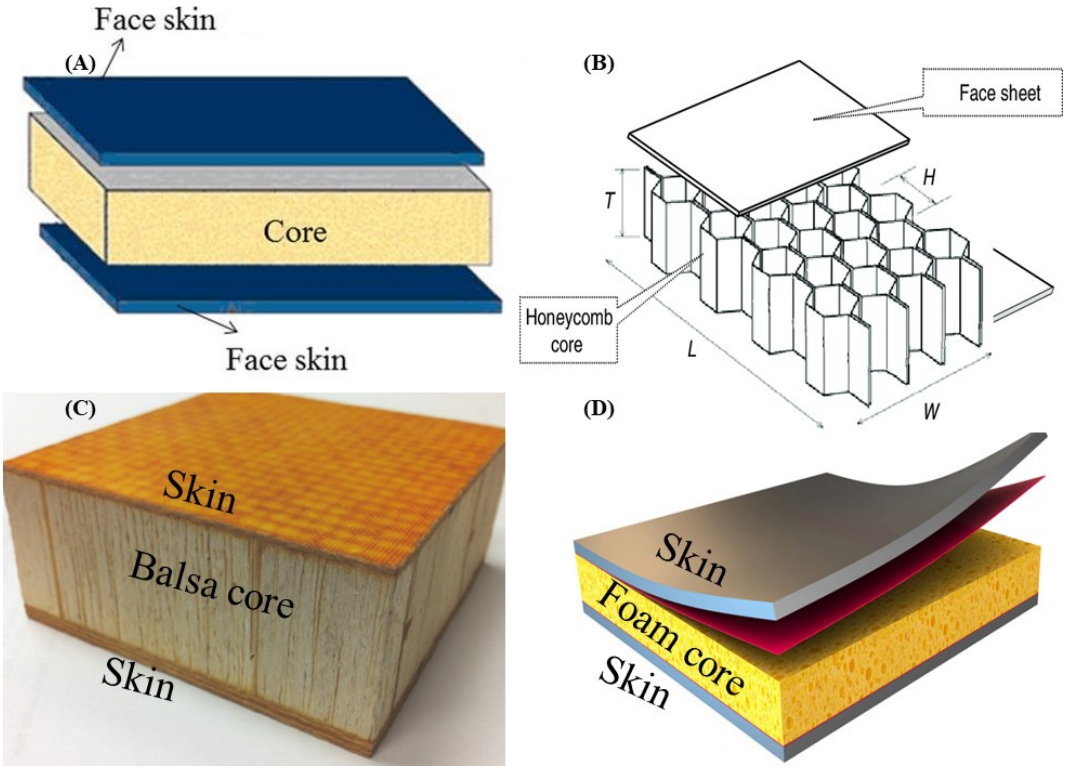

Figure 2-1 (A) Sandwich composite [6] (B) Sandwich composite with honeycomb core [7] (C) Sandwich composite with balsa core [8] (D) Sandwich composite with foam core [9]

The advantages [10]–[12] of the sandwich composite are:

a. High ratio of bending stiffness to weight as compared to monolithic construction.
b. High resistance to mechanical and sonic fatigue.
c. Good damping characteristic.

d. Improved thermal insulation.
e. No mechanical fasteners, hence, no crack initiation sites.

The disadvantages of the sandwich composite are: -

a. The complex manufacturing process (sometimes).
b. Delamination in a product.
c. Difficulties of recycling.

Remark: If the heterogeneity between the skin and the core is the very foundation of the sandwich, it is also its weak point when different materials are assembled together. There is an interface that is a source of complexity in terms of process and consequently in terms of recycling. Assembly requires particular procedures that have an impact on the life cycle, and costs because of this, choices must be made to process materials in sub-assembly because their natures can be very different. Bonding elements often come from chemistry are subject to regulations, and can be a source of environmental problems. As in honeycomb composite if there is small debonding in an adhesive layer it may cost a lot to the structural properties of the sandwich composite. During the service of honeycomb sandwich composite there is a chance of crack propagation but not in polymeric foam core.

The choice of materials in the core of the sandwich structures depends on the targeted applications and the expected performances. The pair of skins and core must also be chosen to ensure the safety of their application.

2.2 Sandwich composite with honeycomb core

Honeycomb core is widely used worldwide to manufacture sandwich composite. The design is inspired by the bees to store honey. Honeycomb composite cores are used in many applications, for example, the chassis of modern formula one car. The honeycomb is sandwiched between two carbon skins with the purpose of creating a very stiff and strong structure that offers protection to the driver in case of a severe crash.

The advantages of sandwich composite with a honeycomb core are [11]:

a. Higher tensile strength per weight ratio.
b. It can adopt large temperature variations of the environment and maintain excellent characteristics without being affected.
c. Honeycomb panel with core polyethylene is fire-resistant, so it is safe, non-toxic, and fireproof. It is also an ideal material for construction too.

The disadvantages of sandwich composite with a honeycomb core are:

a. Moisture trapped during the service process causes corrosion problems which will lead to degradation in the structural integrity of the part [10].
b. Close examination during the manufacturing process is required to make sure there is not any debonding of an adhesive layer.
c. There is a moderate chance that during service disbanding may initiate a crack in the structure.
d. Delamination in the final product leads to a reduction of the mechanical capability of the structure.
e. Performing nondestructive techniques (named in the following, NDT) on it is also a difficult task as it has the number of faces [13]–[15].
f. Recycling

2.3 Sandwich composite with foam core

Foams are another family of materials classically used for the core. They are considered for both mechanical and thermal applications. What differentiates the sub-families of foam are the densities in terms of porosity. In general, the edges and faces of a cell are formed by interconnected solid struts and thin walls to form a cellular solid. More commonly, the cell is polyhedral which packs in three-dimensional to fill the space; one calls such three-dimensional (named in the following, 3D) cellular materials like foams. If the solid of which the foam is made is contained in the cell edges only (so cells are connected through open faces), the foam is called open-celled. If the faces are solid too, so that each cell is sealed off from its neighbor, it is called a close cell. Foam are be made up of the most common, polymer (Figure 2-5) but also metal [16], [17] (Figure 2-2), ceramics, and glasses (Figure 2-3 and Figure 2-4). This study focuses on polymeric foams.

The advantages of sandwich composite with foam core are [18]:

a) Lower thermal conductivity
b) Control of the density by the process.
c) Indentation stiffness
d) Lower costs
e) Possibility to use recyclable materials
f) Damping

The disadvantages of sandwich composite with foam core are [18]:

a) The range of temperature can be limited
b) The thermochemical process to generate the foam

c) Assembly with the skin - the compatibility of link elements if skins and foam are different in physical and chemical nature
d) The similar problem at an interface in comparison to honeycomb core
e) limited sensitivity to oxidation
f) Recycling

2.3.1 Metallic foams

Metallic foam (Figure 2-2) is another recyclable material. It can be made using either liquid or solid-state processing [16]. Powdered metal and powdered titanium hydride or zirconium hydride can be mixed, compact, and then heated to the melting point of the metal to evolve hydrogen as gas and eventually form the foam. Compared to polymeric foam, metallic foams are stiffer, stronger, more energy absorbent, and resistant to fire and the weather adversities of UV light, humidity, and temperature variation. Cost, weight, and non-insulation are the major drawbacks. Metal foams are used in automotive industries as a sound damper. Also, they are used as stiffeners without increasing the mass of a structure [19]. This foam is easily recyclable, and complex mesoscopic architecture can be generated by 3D printing. High-temperature applications can be achieved.

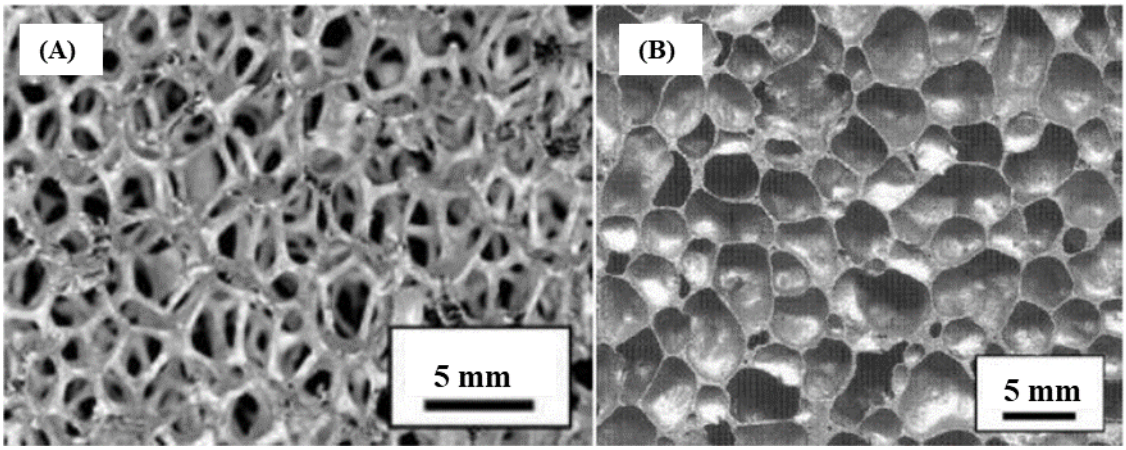

Figure 2-2 Metallic (A) Open (B) Close celled foam [20]

2.3.2 Ceramic foams

Ceramic foams (Figure 2-3) are made from ceramics. The process of manufacturing includes open-cell polymer foams internally with ceramics slurry and then in a kiln, leaving only ceramics material. Ceramics foams are used in thermal insulation, acoustic insulation, absorbing environmental pollutants, and filtration of metal alloy [21]. Specific applications used this type of foam.

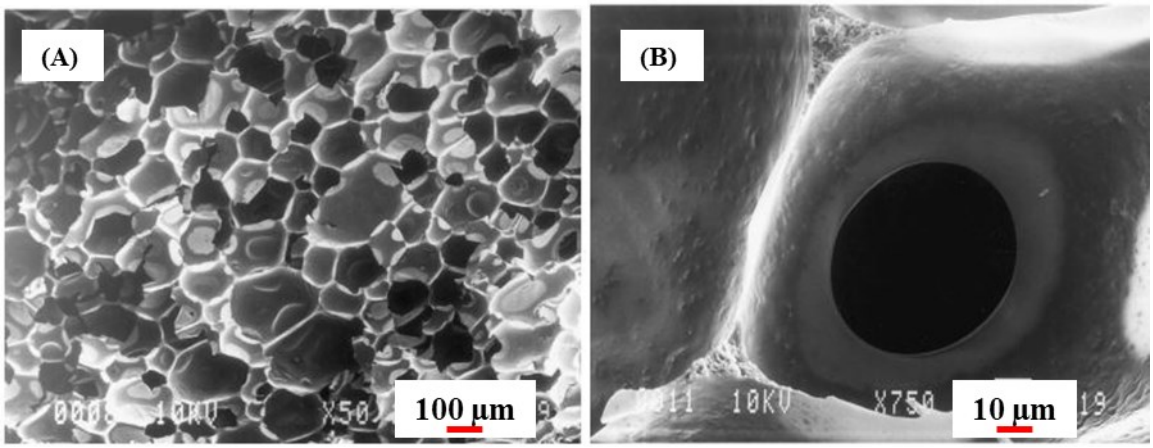

Figure 2-3 Ceramic foam (The polyurethane - 20 vol % alumina foam) Scale of (A) 100 µm (B) 10 µm [22]

2.3.3 Glass foams

Glass foam (Figure 2-4) is a porous glass foam material. It is made by mixing crushed glass and a blowing agent such as carbon or limestone. Near the melting point of the glass, the blowing agent releases a gas, producing a foaming effect in the glass. After cooling, the mixture hardens into a rigid material with gas-filled closed-cell pores comprising a significant portion of its volume. Cellular silicate glass, or foam glass, is famous for its heat-insulating properties. However, the unique nature of this material is provided by the composition of properties that none of the other known heat insulators have: complete incombustibility, high strength, and absence of corrosion and destruction over time, in addition to its low conductivity and density [23].

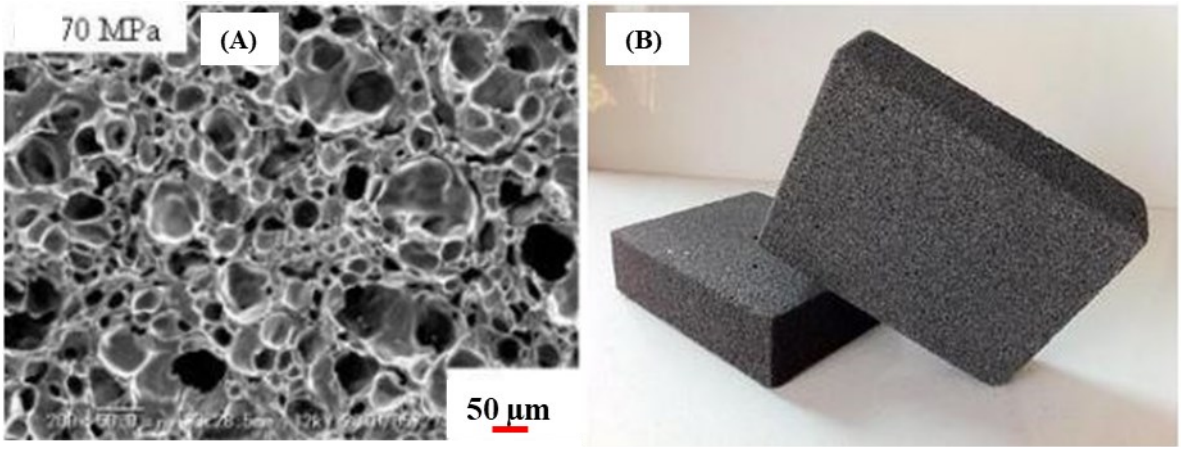

Figure 2-4 (A) Micrographs of the borosilicate glass foam [24] *(B) Glass foam*

Different materials are used to manufacture foam core: Polystyrene, Polyurethane, PVC (Polyvinyl Chloride), or PMI (Polymethacrylimide), etc. All these materials may have different properties but one property that is common for each is all are lightweight.

2.3.4 Polymeric foams

This type corresponds to our domain of interest. Polymer foams (Figure 2-5) were first made at the beginning of the twentieth century and 1930's and -40's correspond to a large expansion in the use of the foam structures. For example, polyurethane was invented by Dr. Otto Bayer [25]. The use of polymeric foam is vast and almost everywhere they could be found. The global market of polymeric foam is huge and it was worth $100 billion in 2015, use of polymeric foam is expected to increase [26]. Polymeric foam can be used in automotive, electronics, furnishing, footwear, aerospace, food, or in construction materials because of its lightweight [27]. Polymers are foams by introducing gas bubbles into the liquid monomer or hot polymer, allowing the bubble to grow, stabilize, and then solidify the whole thing by cross-linking or cooling [28].

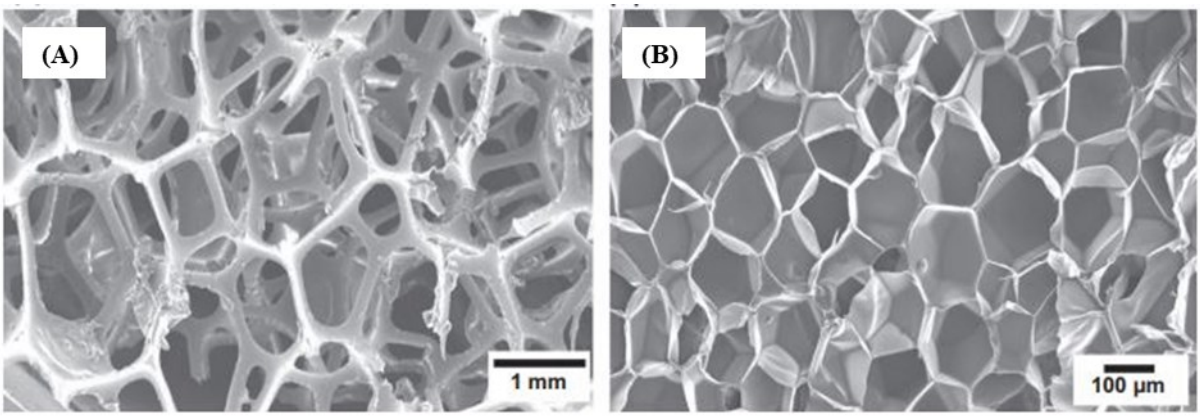

Figure 2-5 (A) Open-cell (B) Closed-cell cellular structure of polymeric foams [29]

Many levels of porosity can be generated as a function of process parameters. For most foams have a very high pore rate (porosity), and the walls between pores are thinner and highly extended. On the other hand, for lower levels, the distances between cavities can become micrometric. The material can be either a thermoset or a thermoplastic. In the first case, the cross-linking kinetics must be combined with the cavity creation phase, in the second case, the crystallization is combined with the pore inflation to ensure the stiffness of the mesostructure. The process parameters define the mesostructure in the context of classical transformation processes. As with metal foams, additive manufacturing has opened up new possibilities for innovation by being able to develop custom mesostructure.

2.3.5 Types of polymer foam

In this section, the foams are classified according to the family of polymers with respect to recycling, biodegradable, and renewable materials.

2.3.5.1 Complex biodegradable foam

Many polymers can be used for foam. One of the most used is Polyurethane. This last family corresponds a type of polymer containing chains with repeating units containing the characteristic “urea” or “urethane” [30]. Polyurethanes are polymers that are produced after the reaction of the OH group of the polyol with the NCO (isocyanate functional group) resulting in urethane linkage [31]. Polyurethanes are the most common class of polymer that keeps changing the quality of human life [25]. Polyurethanes are used in comfort materials and thermal/ sound insulation. It also can be used in the biomedical field because of its biocompatibility, bio-stability, and mechanical properties [31]. The versatility of Polyurethane is a major advantage and makes it suitable for a variety of fields. Furthermore, the material is flexible and durable, advantageous for specific industries. It is very cost-effective and fulfills the requirements of lightweight materials needed within specific areas.

One other conventional plastic is polystyrene, which is used in various industries—the characteristic of lightweight in combination with its low acquisition costs. Many industry segments benefiting from this material are the surfboard market, the food packaging, or insulation, and many structures or objects are built each year on a large volume of these materials. Unfortunately, these are not biodegradable quickly, and it is not easy to recycle [32]. Therefore, this list is not perfect, and many other families are used.

PVC has numerous advantages approving its wide usability [33], [34]. First and foremost, the material is cost-effective. Furthermore, the material has excellent durability, long-life expectancy, and good electrical and insulation properties. In addition, PVC has easy processing characteristics to achieve desired specifications. On top of that, it is resistant to many solvents, including styrene and most fuels. Moreover, the material is self-extinguishing and will not rot.

Other semi-crystalline materials such as (polyethylene, polypropylene, etc.) foamed are also used to generate foams [35], [36]. The difficulty in their use comes mainly from the ability of the material to stretch during the process of cavity growth. Some branched polymers do not always allow this or at lower porosity levels. As a result, the mechanical properties obtained can be high but with densities of a higher level than polyurethane foams, for example. One of these foams will be studied in more detail in this thesis.

2.3.5.2 Biodegradable foams

Biodegradable polymer foams are investigated because of the increasing waste and environmental problems for traditional polymer foams and the increasing price of petroleum products used in manufacturing the polymer foams [32]. Above all reasons, the researcher has proposed many biodegradable foams these last years. There is also a wide range of different candidates

of biomaterials that can be used for biodegradable foams, including ethylene vinyl alcohol, polyvinyl alcohol, polycaprolactone, polylactic acid, and starch [37].

2.3.5.3 Foam with renewable materials

In the industry, solutions are also deployed with biological materials that are renewable by nature and do not use petroleum, but this does not guarantee biodegradability and efficiency concerning the life cycle. For example, starch foam [38] was made in 1989 as biodegradable packaging and is an alternative material to the traditional polystyrene foams. Starch is derived from agricultural products such as corn, potato, and wheat. Starch granules are made up of two glucose polymers, amylose (linear) and amylopectin (branched). Starch foam can be manufactured by extrusion in which melted starch is mixed with a blowing agent [38]. Water or methanol are the two common blowing agents turned into steam when the system is heated and forms air bubbles within the starch matrix. In addition, the use of thermoplastic polymer additives can help to even out the surfaces and decrease the foam's degradability by incorporating slowly degrading or non-degradable polymers. However, obtaining high properties is often complicated and requires complex chemical transformations that are problematic for recycling.

2.4 The behavior of polymeric foam and constitutive models

In this part, the behavior of the foam is very briefly presented in its generality. Many nuances can be observed depending on the nature of the material, the parameters of the mesostructure, and the manufacturing process.

2.4.1 The behavior of foam under compression

For example, Zakaria *et al.* [39] has studied the behavior of low-density polyethylene (named in the following,LDPE) close cell foam under compression tests. The authors have performed experiments on two foams with different densities (more details about the material can be found in the article). LDPE0.5 and LDPE1 have 64.42 $kg.m^{-3}$ and 55.85 $kg.m^{-3}$ densities which have been used for the experiments. All the experiments were carried out on a universal testing machine. The samples were prepared in accordance with ASTM D575-91 [40]. Figure 2-6 shows stress vs. strain results of low-density polyethylene foam. The response is divided into 3 regions:

- The first region is called an elastic strain, foam deforms linearly elastically due to wall bending, which is 9% of the entire strain

- The second one is collapse strain; it is the plateau region which took place between 9% to 40% entire strain. During this stress plateau phase, the polyethylene foam undergoes large compressive strains and absorbs a considerable amount of specific energy.
- And the third one is called compaction strain. In the third stage, a rapid increase in compression stress because of densification occurs where the cell walls crush together.

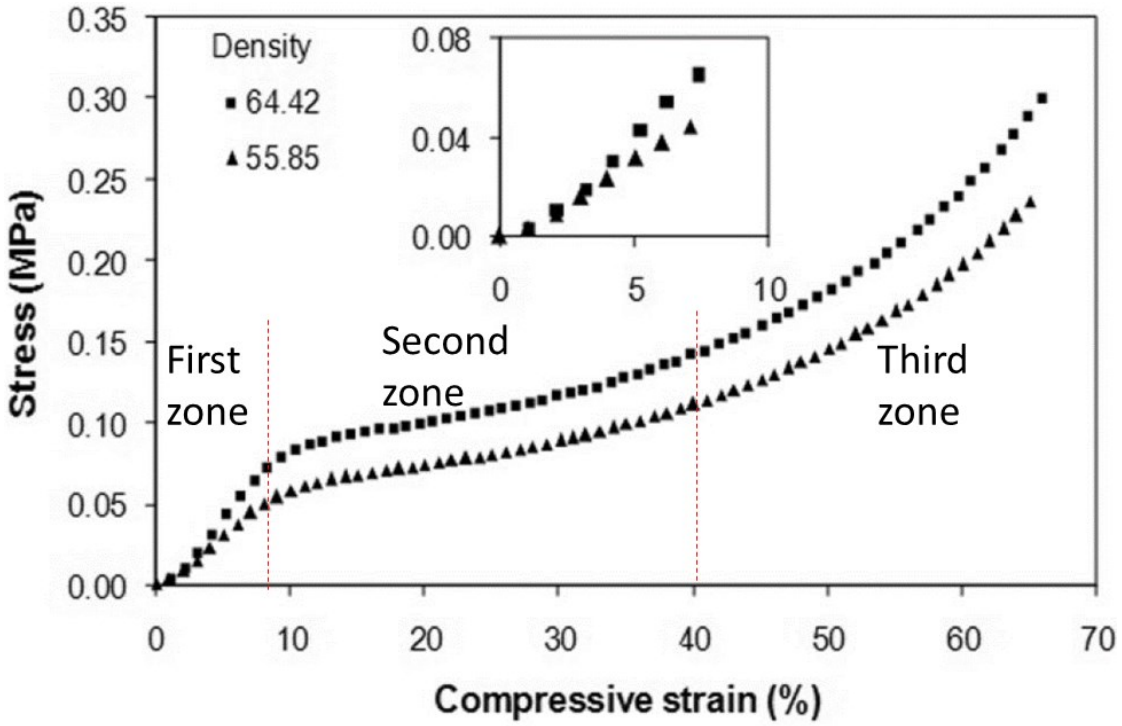

Figure 2-6 Compressive stress vs. strain curves of LDPE0.5 and LDPE1 [39]

One of the articles that most closely resembles the work conducted in this thesis is that of Saint-Michel *et al.* [34]. The study is conducted on a polyurethane foam with a very wide range of density and therefore porosity. Figure 2-7 shows stress vs. strain results with different densities of polyurethane foam. The closed-cell constitute this foam and viscoelasticity is studied and characterized by dynamical mechanical analysis. These properties are linked with relative density. The micromechanical model proposed by Gibson and Ashby [41] is compared to experiments. The phenomenological approach has given good results but the micromechanical model gives lesser good predictions.

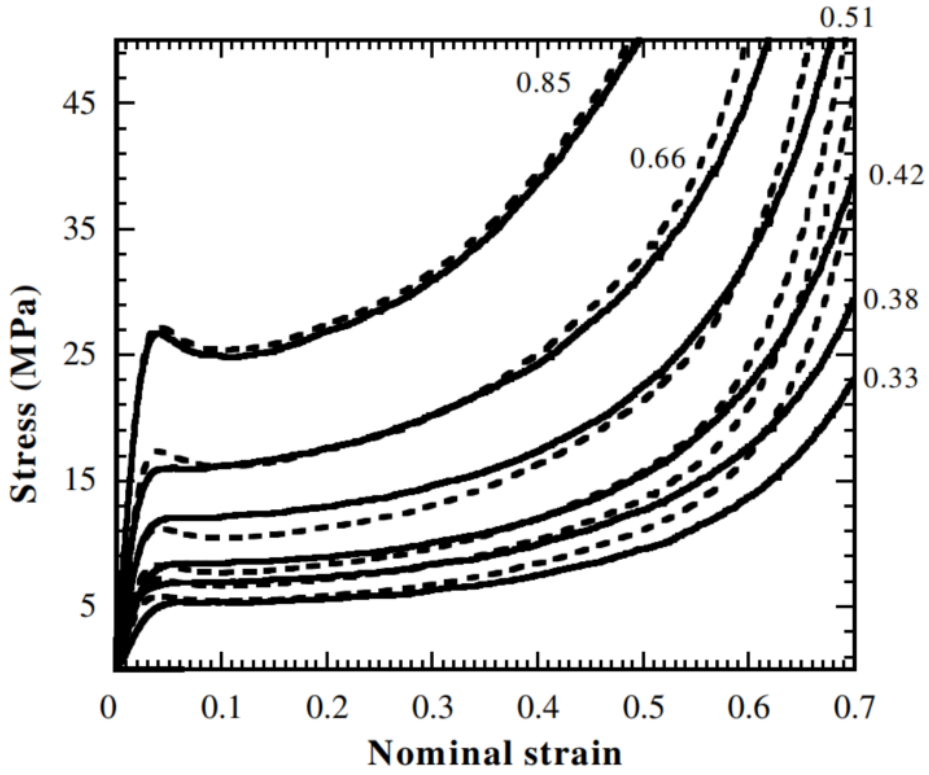

Figure 2-7 Compression tests for different relative density foams. The values on the curves represent the relative density. The dash lines represent the predicted values with the phenomenological modeling. Initial strain rate = 10^{-3} s^{-1}, $T = 30\,^{0}C$ [34]

2.4.2 The behavior of foam under uniaxial tension

Kabir *et al.* [42] performed tensile tests by prismatic bar specimens, whose gauge length was 100 mm and cross-section of 25 mm by 10 mm, width, and thickness respectively. PVC foam with two densities: 75 and 260 kg.m^{-3} (labeled as R75 and R260) and two different levels of cross-linking (labeled as H130 and HD130) with a density 130 kg.m^{-3}, have been tested under tension on the Zwick/Rowell test machine with a load cell of 2.5 kN. Cross-head speed was 0.02 mm.s^{-1}. Stress vs. strain response for different densities of PVC is represented in Figure 2-8. It can be clearly seen from these curves, that density of the foam is playing role in the response of foam both in terms of stiffness, ductility, and strength. On the other hand, cross-linking has a very small impact on the response and that can be seen with the behavior of H130 and HD130.

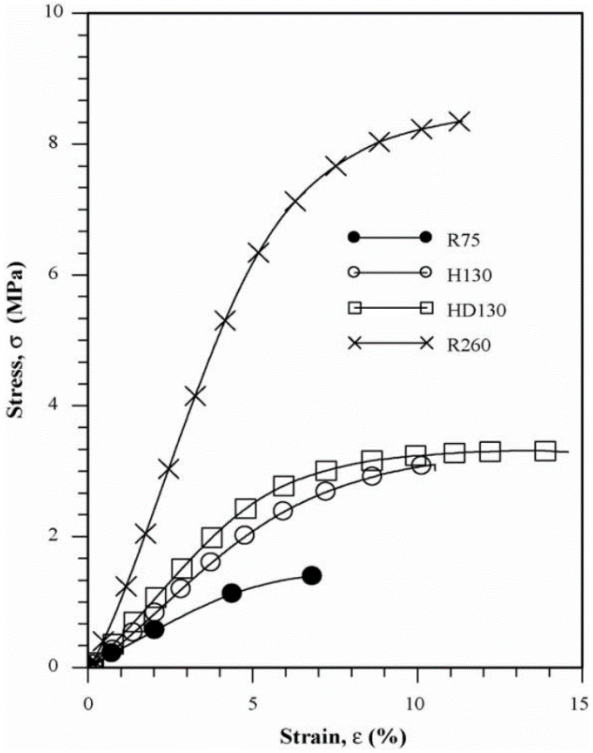

Figure 2-8 Tensile response of PVC close cell foams with different density [42]

2.4.3 Behavior of foam under shear

Zenkert and Burman [43] obtained the static shear properties from the 4PB test. Shear tests were performed by the core material manufacturer using the standard block shear test, according to ASTM-C273 [44]. The reason for using the bending test primarily, is that the block shear test and its design, often gives a non-conservative value in strain to failure for high-density foams. Three different density close cell foam of polymethacrylimide, WF51, WF110 and WF200 foam with density 52, 114, and 207 kg.m^{-3} respectively have been tested. Shear stress vs. engineering shear strain for different densities of polymethacrylimide close cell foam is shown in Figure 2-9. It is evident that the density of the foam is affecting shear the response of a material.

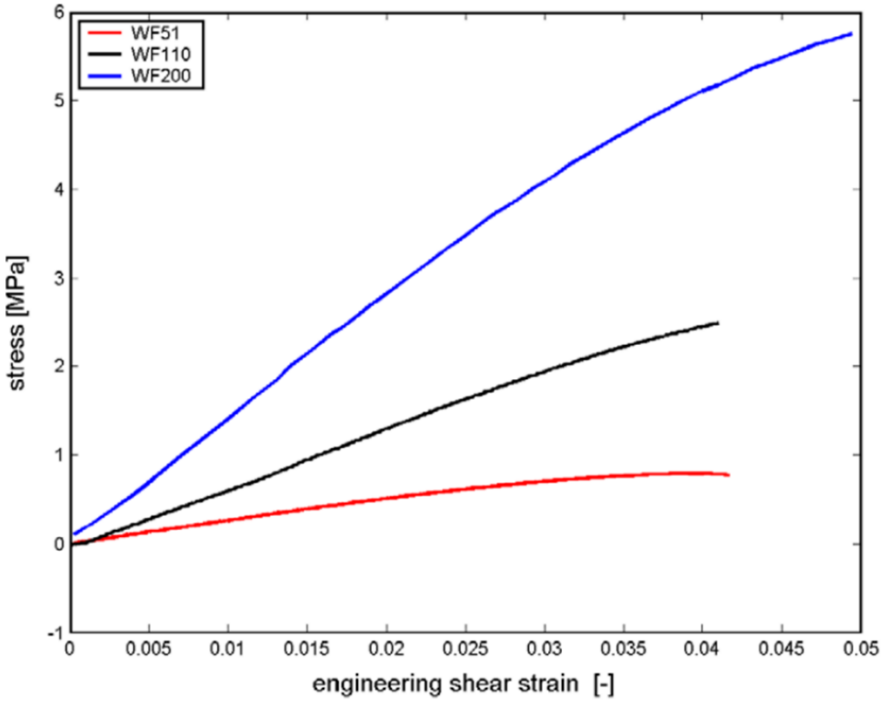

Figure 2-9 Shear response of polymeric foams [43]

2.5 Tools to build the foam behavior

Modeling the behavior of foams requires consequent theoretical and numerical developments, first of all, the problem has twofold:

a. It is often complicated to characterize the local behavior. For example, it is difficult to characterize the walls that separate the bubbles. The material is stretched and undergoes specific transformations. For low pore rates, this problem is less problematic, because the distances between cavities are of the order of the size of a spherulite. An example of it is semi-crystalline foams.

b. The other questioning is integrated into the scientific field called the micromechanics, knowing the mesostructure is it possible to predict the behavior of the foam. This problem concerns a very large number of works in the literature, below a summary of theoretical and numerical tools, is proposed.

2.5.1 Generalities on homogenization techniques

If we place ourselves in a much more general framework, now a day's, many industries are using heterogeneous materials for various applications. By mixing two base material, new material which has good properties of the base material are getting created. As a previous

remark, modeling this kind of material is a challenge. This type of material first has been modeled using a direct approach and a complete description of the mesostructure. Consequently, the entire structure has meshed, and of course, this leads to giant computation. In order to resolve the problem, many authors come up with homogenization techniques. Homogenization is a powerful tool to solve complex problem in which local analysis is limited to RVE, which help to reduce computational cost. In the industrial as well as academic sectors, to study composite responses in different loading, computational homogenization is used.

A basic framework was proposed by Adam and Doner [45]. Authors have considered composite material to consist of a rectangular array of unidirectionally oriented filament in the infinite elastic matrix, and there is perfect bonding between fiber and matrix. Following this work, Suquet [46] has proposed a finite element framework of homogenization. This type of homogenization technique is also called first-order linear homogenization. A problem in representing localized strain/stress field and boundary effects using first order-homogenization has been highlighted by Kruch and Forest [47].

First-order non-linear homogenization solves the heterogeneous non-linear structural problem on a macroscopic mesh. All the boundary conditions are defined on RVE with a lower scale. After solving this, the macro stress field is obtained by averaging. This problem can be solved in parallel, which is a major advantage. The non-linear homogenization approach is also known as “Concurrent Multiscale Methods” or “Multi-Level FEM.” Many authors in the literature have used this approach [48]–[51].

Moulinec and Suquet [52] were the first ones to propose homogenization based on fast Fourier transformation. This homogenization technique directly uses images of the microstructure, supposed to be periodically repetitive to compute overall composite properties. It also gives a local distribution of stresses and strains without requiring further geometrical interpretation by the user. The linear elastic problem is examined first. Its analysis is based on Lippmann-Schwinger's equation, which is solved iteratively by means of the Green operator of a homogeneous reference medium. Then the method is extended to non-linear problems where the local stress-strain relation is given by an incremental relation.

Another approach to homogenization is gradient and nonlocal homogenization. These methods are often used for highly heterogeneous structures, where the separation of scales cannot be considered. Forest and Sab [53] have come up with Cosserat and generalized continuum media approach in which alternative methodology consists in replacing the heterogeneous medium with a generalized continuum. Such a continuum involves additional degrees of freedom or higher-order gradients of the displacement field. Feyel [54] applied the same technique for non-linear material. The boundary conditions to be prescribed on a unit cell are derived from the

macro displacement field. The heterogeneous Cauchy medium is then replaced by a homogeneous Cosserat continuum.

Second-order computational homogenization for a non-separate problem is introduced by Kouznetsova *et al.* [55]. In this approach, the macroscopic strain gradient tensor, and its gradient are imposed on a microstructural RVE. This enables us to incorporate the microstructural size and to account for non-uniform macroscopic strain fields within the microstructural cell. Every microstructural constituent is modeled as a classical continuum and the RVE problem is formulated in terms of standard equilibrium and boundary conditions. From the solution of the microstructural boundary value problem, the macroscopic stress tensor and the higher-order stress tensor are derived based on an extension of the Hill–Mandel condition. This automatically delivers the microstructural-based constitutive response of the higher-order macro continuum. Which deals with the microstructural size in a natural way. This is an extension of the first-order (classical) homogenization method, whose scheme is depicted in Figure 2-10.

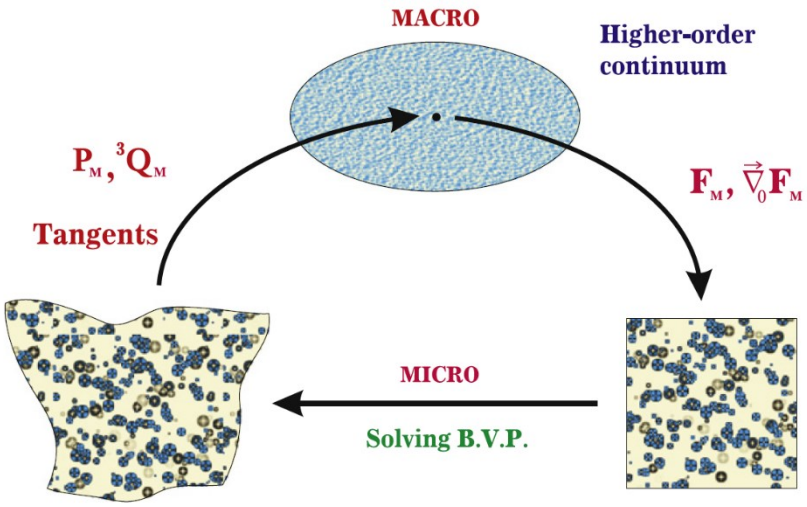

Figure 2-10 Second-order computational homogenization scheme [56]

Second-order nonlocal homogenization is another category of homogenization based on nonlocal elasticity theories. Usually, these methods use a nonlocal operator to define the behavior, which depends on a nonlocal definition of the strains. Eringer and Edelen [57] and Gao *et al.* [58] define effective stress as a spatial convolution of the strain with a nonlocal elastic operator:

$$\bar{\sigma}(x) = \int_{\widetilde{\Omega}} \mathsf{C}(x - x') : \varepsilon(x') dx' \qquad (1)$$

In Equation (1), $\mathsf{C}(x - x')$ is a nonlocal elasticity tensor, e.g. the product of the local elasticity tensor with a monotonically decreasing function such as a Gaussian or bell-shaped function defined in a domain $\widetilde{\Omega}$.

2.5.2 Application to foam case

In the literature, there are two major approaches for modeling foam, first one is macroscopic [59]–[64] and the second one is cell-level modeling. The missing link microscopic feature is a major drawback of the macroscopic approach. The cell-level modeling is connected with microstructure and the physical mechanism at this scale is an address. There are three subgroups of cell-level modeling (i) space-filling polyhedron models, (ii) tessellation-based models, (iii) image-based models

The space-filling approach is widely used in literature due to the simplicity of the generation of the space-filling polyhedron to represent cell walls in order to study the influence of morphological features on the foam response [65]–[68]. Cell geometry should be such that it minimizes the surface energy consequently which should respect the following three rules: (i) the average number of faces per cell is close to 14 (ii) the average number of edges per face is 5.1 (iii) the vertices are nearly tetrahedral, formed by four edges meeting at angles close to 109° 28' [69]. These kinds of models give some insights about microstructure but, at the same time, they simplify the real complex foam. To give an example following Images are presented. Nammi *et al.* [66] did an analysis of close-cell aluminum foam. Figure 2-11 shows the microstructure of the aluminum foam.

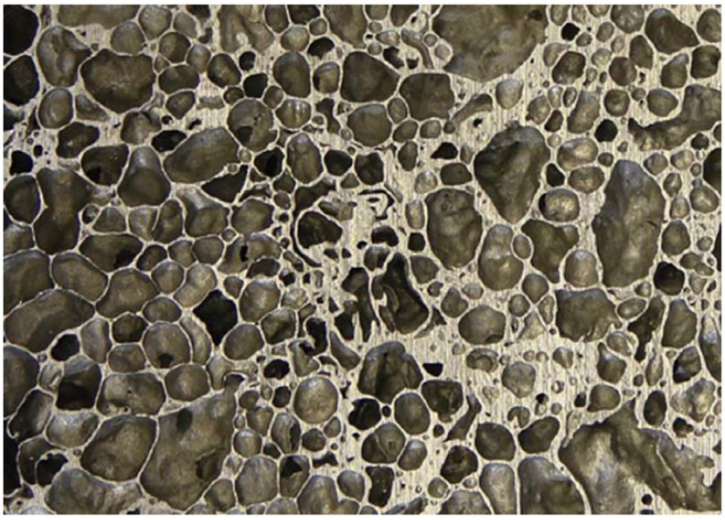

Figure 2-11 Cellular microstructure of closed-cell aluminum alloy foam (AA 6061) [66]

To model the foam, Nammi *et al.* [66] has used different types of space-filling polyhedrons shown in Figure 2-12. The authors have done a simulation to evaluate the stiffness and mechanical response of this model under large strain.

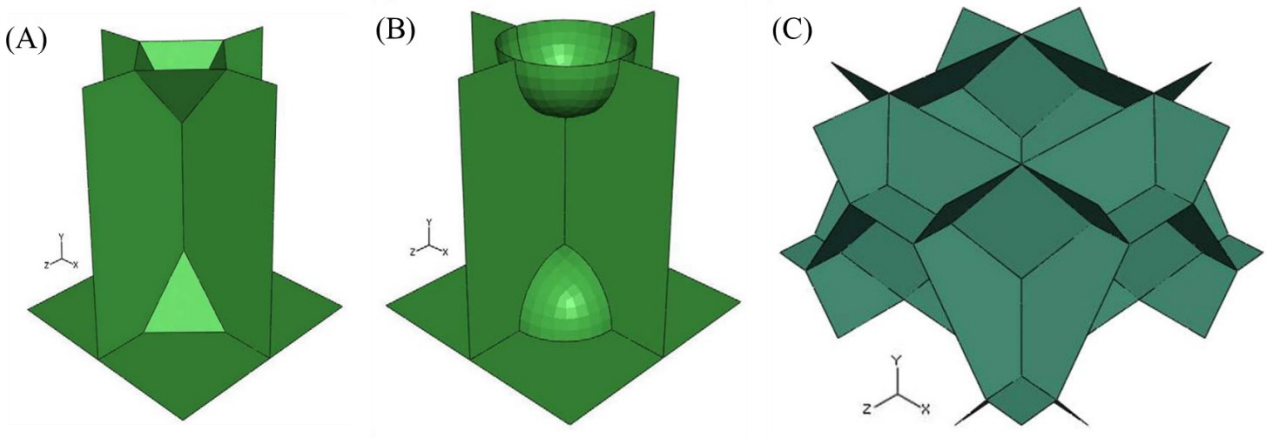

Figure 2-12 Repeating unit-cell of (A) Cruciform-pyramidal foam [70] *(B) Cubic-spherical foam (C) Tetrakaidecahedral foam* [66]

The space-filling of convex, non-overlapping polytopes that is random tessellations are used by many authors in literature to model the foam. There are two types of tessellations one is Voronoi [71]–[75] and the second one is Laguerre [76]–[78]. Basically, Laguerre is a weighted form of the Voronoi tessellation. This method is more accurate but at the same time more complex. An example of Laguerre tessellations is shown in Figure 2-13. Redenbach *et al.* [78] have studied the dependency of the elastic stiffness, i.e., Young's modulus, of isotropic closed-cell foams on the cell size variation is studied by microstructural simulation. It is clear from Figure 2-13 (A) and (B) that cell geometry is very well defined but after looking at mesh size it can be concluded that the time of simulation is high.

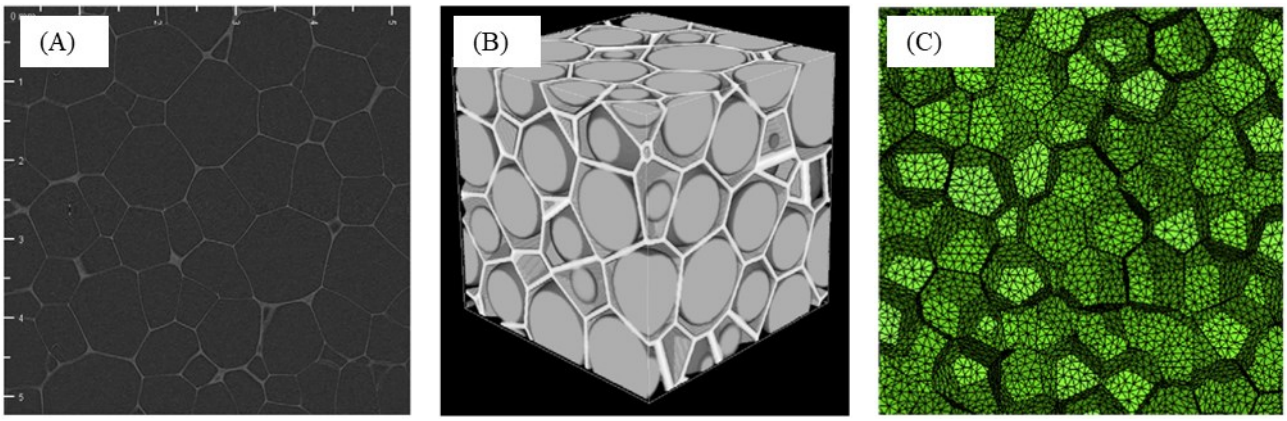

Figure 2-13 (A) Section of a tomographic image of a polymer foam [78] *(B) Visualization of a Laguerre tessellation generated by dense packing of spheres. The spheres are inscribed in their cells* [78] *(C) Finite element meshes of Laguerre tessellations of spheres with constant volume* [78]

The third method is image-based models [79]–[81] to build RVE. X-ray computer tomography obtained an accurate description of foam in this method. Instead of studying a whole full-size sample, a coupon is studied because this full randomness in the microstructure is not considered. This method is demonstrated by Caty *et al.* [80] by studying stainless steel hollow spheres that were chosen as an example of closed-cell foam with a low density. Sample of simple

parallelepipeds with dimensions of 15 x 16 x 17 mm^3 is studied. Closed-cell cellular materials can be investigated by X-ray tomography to reveal their 3D architecture (Figure 2-14 (A)). These data were used for FE meshes and calculations. For validation purposes, a sample is subjected to compression and compared with numerical simulation (Figure 2-14 (B)). Results were in good agreement with each other.

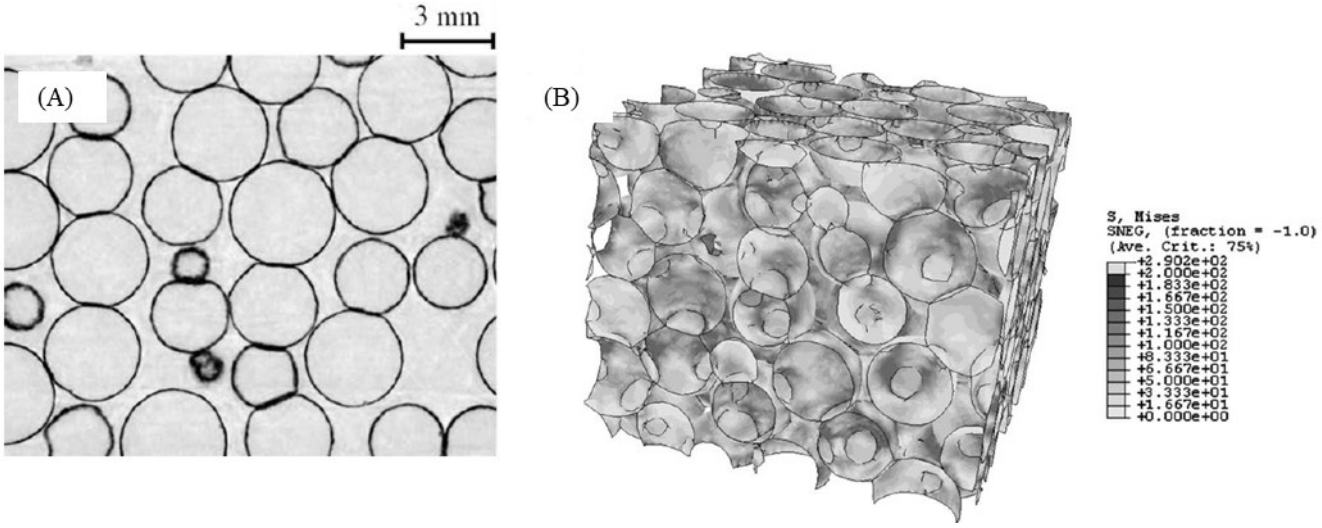

Figure 2-14 (A) Exacted slice of sample from tomography (B) Global calculation of a stainless steel metal hollow sphere structure sample. 3D visualization of the deformed contour plot of the Von Mises stress interior plane visualization [80]

The question about sizing and the definition of RVE are open-ended. In the literature, many authors tried to answer the question; here, we will discuss a few of them. First, to define the heterogeneous material statistic nature of the microstructure is used. RVE, in this case, is quite large, which includes a sampling of all microstructural heterogeneities that occur in the material [82]. Another approach is based on statistical properties. The RVE must ensure a given accuracy of the overall estimated properties obtained by spatial averaging of the stress, the strain, or the energy fields [82], [83]. In this approach, RVE size increases with the non-linearity of the considered behavior. A summary of much other work defining RVE has been presented by Gitman *et al.* [84].

- To build the RVE enough information on the microstructure is required [85]
- RVE size should be smaller than macro-structural properties but sufficiently bigger than the microstructure [86]
- the RVE must include a large number of micro-heterogeneities [87]

We are interested here, the density is low and the microstructure gradients observed in the manufactured sandwiches (Chapter 4) are of the order of magnitude of the thickness of the central layer of the sandwich. The very notion of RVE loses some of its meaning as there is a gradient. Applying one of these techniques developed in all these works will raise the question of the relevance of the model. As RVE will be developed in chapter 4, the idea will be to place

ourselves in an intermediate position. Digital virtual tensile tests with virtual measurements will be developed. These virtual tests will be carried out on digital specimens containing homogeneous descriptions. On these virtual tests, the size of a structure is limited but still has enough pore space, now the question arises that, it is possible to parameterize the macroscopic behavior with quantities defining the mesostructure by using the identification tool of Chapter 3. This approach avoids the problem of the boundary conditions and the loading to be applied on the RVE. Of course, the question of the representativeness of the behavior will always arise. This point will be taken up in Chapter 4.

However, to use these models it is necessary to have information on the behavior of the material, a point is proposed in the next chapter.

2.6 Constitutive models of polymer

In this part, a brief bibliography is proposed to present some models of polymer behavior. Application of polymers spread in many sectors such as automotive, fluid transport, aeronautics, etc., due to advantages like being more resistant to most of the chemicals than metal, lightweight as well as thermally and electrically insulating [88]. But their mechanical properties are limited, moreover, polymer exhibit complex non-linear viscoelastic behavior and viscoelasticity appears when the level of strains increases; it can be combined with the same under the form of cavities and small cracks. The coupling with the temperature plays a major role even at room temperature, and polymers can undergo relaxation and creep phenomena. As polymeric materials started replacing metals and the application range of polymers is increasing; it has been crucial to characterize and develop the constitutive model in order to understand the response of a material in a different type of loading condition and build predictive models.

Literature is very rich in different types of approaches or models to describe the behavior of polymers. Mainly literature is divided into two main domain which is physical base [89]–[95] and phenomenological modeling [96]–[103]. The physical bases modeling approach is often used for amorphous polymers, this is much more complicated for the semi-crystalline polymer. For these two families of materials, a phenomenological-based approach can be always used and the same theoretical tools can be applied.

For example, to describe the behavior of amorphous polymer, Haward and Thackray [93] propose a simple physical model based on the uniaxial test. The model consists of a Hookean spring in series with an Eyring dashpot and rubber elasticity spring in parallel. For cellulose nitrate, PVC, and cellulose acetate stress-strain curve has been compared with the predictive model with a relatively good agreement. Extension in 3D is done by Arruda and Boyce *et al.* [90], Wu and van der Giessen [95], and Anand and Gurtin [104]. They have developed the

model which is the function of strain rate, temperature, and pressure-dependent yield. Anand and Ames [105] and Ames *et al.* [106] have completed models based on Boyce *et al.* [90]. Anand and Ames [105] have taken into account the viscoelastic-plastic effects to compare the experimental response of amorphous polymeric solid. Ames *et al.* [106] have done experiments on poly(methyl methacrylate), polycarbonate, and cyclo-olefin polymer at a temperature below glass transition temperature with strain rate 10^{-4} to 10^{-1} s^{-1} and compressive true strain exceeding 100%. The authors have compared experiments and thermo-mechanical models for validation with good agreement.

Many authors in the literature are widely using physical models for modeling amorphous polymers but there are some authors who have used physical models to model semi-crystalline polymers also. The difficulty comes from the complexity of the microstructure. The amorphous phase is under stress between the lamellae and in the areas of lower density. The lamellae of the spherulite can be of complex shape evolving under the effect of time or temperature. Chains of links can connect the lamellae. This microstructure defines the mechanical behavior and is strongly transformed under the effect of large strains.

More precisely, the microstructure of semi-crystalline polymers is composed of crystalline lamellae and amorphous regions organized like a composite sandwich structure. Young's modulus and yield stress have been influenced by the degree of crystallinity. With respect to microstructure, some multi-scale constitutive models have been proposed. In these models, each macroscopic material point is assumed to be the center of a representative volume element which is an aggregate of two-phase layered composite inclusions. Each inclusion consists of a stack of parallel crystalline lamellae with the adjacent amorphous layers. The influence of the degree of crystallinity of the material has been captured in these kinds of materials [107]–[112].

In this framework, for example, an elastic-viscoplastic constitutive model for ethylene terephthalate has been developed by Ahzi *et al.* [89]. Ayoub *et al.* [92] have proposed a physical-based inelastic model to describe the behavior of polyethylene (HDPE). Authors have shown that model is able to reproduce accurately the experimental observation corresponding to monotonic loading and stress relaxation behavior in different strain levels.

As explained afore importance of crystallinity on mechanical properties of the polymer is still another type of formulation based on modern structural computation that has been developed based on thermodynamic principle by Chaboche [113]. While real material may have a physical discontinuity at the various microstructural scales, these scales are not expressed explicitly but are described globally at the level of a homogenized bulk element of the material. Khan and Khan and Yeakle [114] have proposed a viscoplastic model based on the overstress formulation. Drozdov and Christiansen [112] have developed constitutive equations derived from the viscoelastic and viscoplastic responses of semi-crystalline polymers at three-dimensional strains

with small strains. A polymer is modeled as a two-phase continuum consisting of a crystalline skeleton and an amorphous phase treated as a transient network of chains.

The importance of hydrostatic pressure has been highlighted by studies of Khan and Farrokh [115] as well as Wang and Pan [116]. Ghorbel [99] proposed a viscoplastic constitutive model by using the general principle of thermodynamics with internal variables in order to predict the viscoplastic behavior of amorphous and semi-crystalline polymers under monotonic and cyclic loading in tension and compression. During building the framework of the constitutive model hydrostatic pressure effect has been considered. Four different tests were used (uniaxial compression, tension, creep, and relaxation tests) to find the eight constants of the material.

Many models are proposed in the scientific literature, some of them are specific to particular fields of application, and others are only intended for specific families of loading (only under load, load-unload, creep, fatigue, etc.). As discussed, to characterize the behavior and identify the material parameters more or fewer experiments are necessary. At least model results should be in accordance with the experiments which are used for the identification.

However, the industry needs a constitutive model, which can predict the behavior of materials and the structures under different types of loading and with a minimum of material constants (or a minimum of experiments). If there are many material constants to be determined, then one needs to perform several types of experiments, which require a substantial investment of time and resources. So, it is crucial from the industrial point of view, to require a lesser number of material constants determined from a smaller set of (number and type) experiments.

Some phenomenological models permit to model the polymer behavior with respect to industrial requirements. Many models are studied and a few have been discussed below.

For example, under a low level of strain, Popelar *et al.* [98] have developed a non-linear viscoelastic model based on the framework proposed by Schapery [102]. To find out material constants, relaxation test experimental data performed on medium-density and high-density polyethylene are used. For validation of the model, the authors have done loading/unloading tests at different strain rates and compared them with simulation results. The model can produce good agreement during the test for a smaller strain rate ($<10^{-3}$ s^{-1}), but not for a higher strain rate ($>10^{-3}$ s^{-1}) as at a higher strain rate viscoplastic effect is not considered in the model.

Zhang and Moore [101] have developed two models for high-density polyethylene (HDPE). First, one is a non-linear viscoelastic model from the conventional mechanical analogy (a combination of spring and six-kelvin elements). Evaluation of twelve material constants was done by creep test data. The second one is a viscoplastic model using Bodner and Partom [96] viscoplastic framework by considering the inelastic strain rate in order to reproduce the highly non-linear and time-dependent response. Eight material constants were determined using the

tensile tests at different constant true strain rates. The authors have not validated the constitutive model in different loading conditions other than used for identification.

Colak and Dusunceli [100] came up with the visco-elastoplastic constitutive model of high-density polyethylene under uniaxial monotonic and cyclic loading. The model follows modified viscoplasticity theory based on overstress. There are fourteen material constants. All material constants were evaluated using uniaxial loading and unloading under compression at different strain rates and cyclic loading. For validation, the authors compared the experimental results with the results of numerical simulation, within the framework of relaxation, and creep tests.

Grandidier and Laine [117] come up with elasto-viscoplastic constitutive model based on a model proposed by Chaboche [113], that takes into account: - the effect of hydrostatic pressure - the influence of the strain rate on the modulus of elasticity, and on the coefficient of volume change. All material constants have been found only in experimental tensile tests at different constant true strains. A genetic algorithm is used to find out material constant in one dimensional (named in the following, 1D) optimization. For validation, the authors compared experimental results in the shear test with simulation results. Interestingly to note, when the authors considered tensile test data to find out material constants and simulated the shear test, the results were less promising. On the contrary, when considering both shear and tensile test experimental data to find out material constants, shear test simulation results were better than just considering tensile test data to find the material constants.

2.7 Discussion

The models proposed in the literature are very rich, and this bibliography is limited; choosing one model over another requires a step that is rarely taken. Confrontation with the responses of structures is essential to evaluate the relevance of the model in relation to others. This work is not very well done in the literature. Conducting tests on structures is complex and generates misunderstandings that often prevent authors from distinguishing the relevance of the models between them and their predictive capacity.

The model proposed by Grandidier and Laine [117] has already been tested in the context of work with the Apollor Company and the model in this phenomenological form seemed quite relevant. This may not be the best choice but it is the one we made in this work. Details of the constitutive model have been presented in chapter 3. All the material constants of the model are identified from a simple tension test following a protocol proposed by G'sell and Jonas [118].

It is important to remark this approach is very interesting for the industrial world. On the other side, the industry needs a constitutive model, which can predict the behavior of materials

and the structures under different types of loading and with a minimum of material constants (or a minimum of experiments). If there are many material constants to be determined, then one needs to perform several types of experiments, which require a substantial investment of time and resources. So, it is crucial from the industrial point of view to require a lesser number of material constants determined from a smaller set of (number and type) experiments. Above mention models require just one type of experiment to find material constants.

For the structures studied in this thesis and in a general industrial context, the question is: is it possible to predict the behavior of these particular structures from the behavior of the 'base' material while minimizing the number of characterization tests? To meet this challenge, it is necessary to develop a robust behavioral model that can consider the effect of the strain rate for the targeted applications. The transition to foam will require asking the question of the statistics of the mesostructure and how to understand the behavior by developing an effective numerical protocol. Finally, we must not forget the work to validate this chain by carrying out judicious experiments.

To try to achieve this, the flow of work is discussed below in the form of steps. Figure 2-15 shows the graphical representation of the workflow.

- First step - Find out the constitutive model of the polymeric skin.
- Second step - Validation of a constitutive model of monolayer

The numerical part of the identification of the constitutive model and its validation are presented:

- Third step - Find out the constitutive model of foam in connection with the geometrical mesoscopic properties of the foam.

Tomography of the samples has been performed and the mesoscopic geometry properties of the foam have been found. By using mesoscopic description, several RVEs are proposed to identify the influence of foam mesostructure. It is assumed that the material for the monolayer and foam is the same. Consequently, the constitutive model with the same material constant as the monolayer has been used to do the simulations of RVE under traction and this approach is evaluated. RVE is subjected to displacement rate on one face by applying symmetry conditions on other faces in Abaqus®. In this way 'numerically experimental' data is constructed and the same data has been used for the identification of new material which is representative of foam. All these steps are well explained in Chapter 5.

- Fourth step - Validate constitutive model multilayer (skin-foam-skin) constitutive model

Simulation of 3PB test and compression experimental test has been performed in Abaqus® similar to experiments for multilayer. Experimental and simulation results have been compared for the validation of the model at the end of Chapter 5.

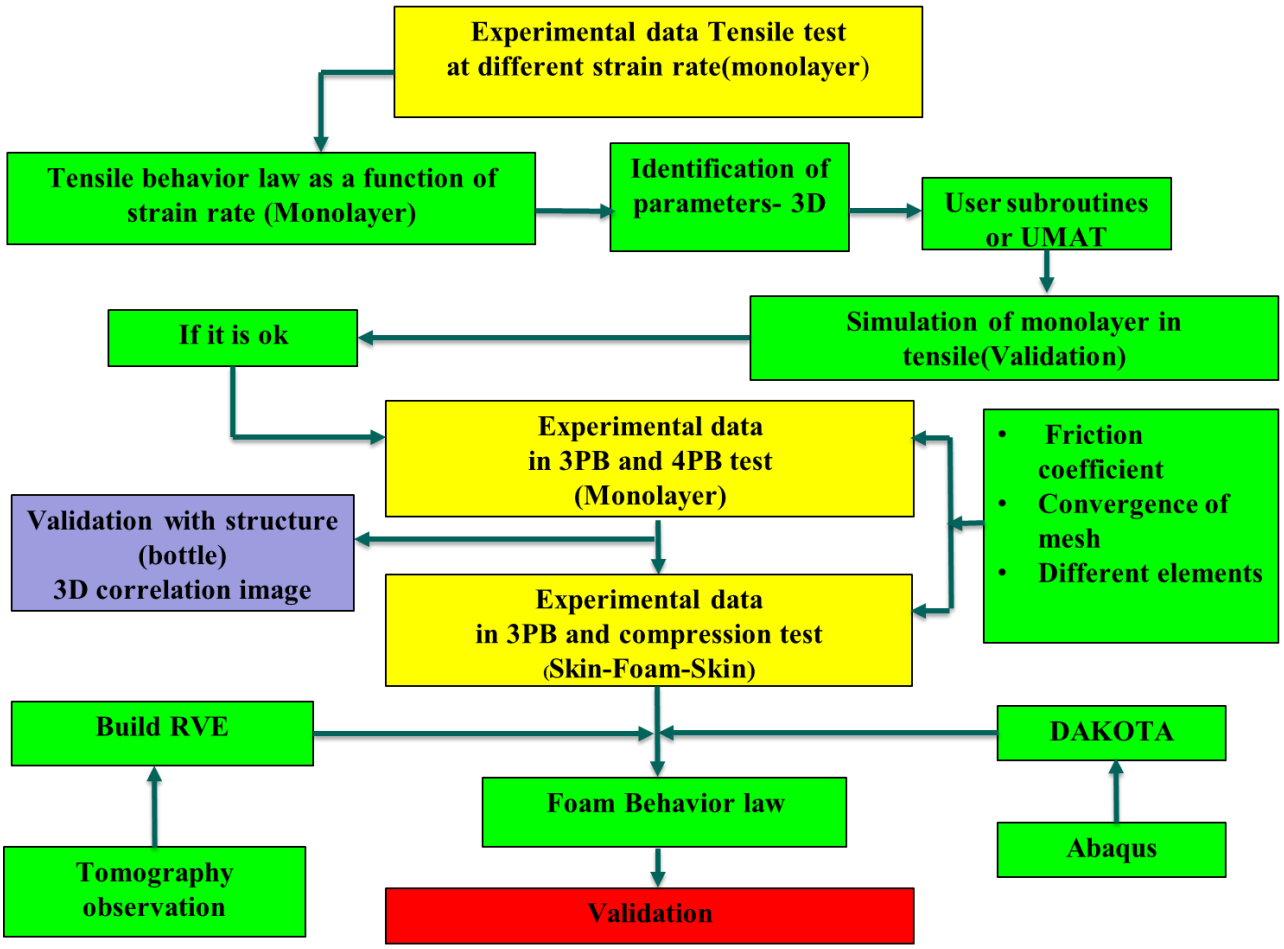

Figure 2-15 Flow of the work

Chapter 3 **Material and constitutive model of the bulk**

This chapter talks about the characterization of the bulk (skin). It involves, a tensile test with markers on it to measure local information during the test. Based on the longitudinal and transverse strains, a constitutive model is identified. The first specificity of the work lies in the identification procedure and considering the hydrostatic pressure effect. The model created is validated through a comparison of experiments and simulations. 3PB, 4PB tests, and a complex structure under internal pressure allow for testing the robustness of the model. This work is original because it has not been done frequently in laboratories. The different items presented in the chapter are as follows:

- Materials used for experiments
- Sample preparation
- Experimental procedure and results
- Constitutive model of polymer

3.1 Materials

There are two materials samples that have been tested. The first and second are polyethylene by the rotational molding process and polypropylene by an injection molding process (skin) respectively. *TotalEnergies* have supplied all samples.

3.1.1 Rotational molded sample

This material is Lumicene® mPE M4041 UV (named in the following, PE) which is a new generation metallocene medium density polyethylene (mMDPE) with hexane as comonomer supplied by *TotalEnergies*. The melt flow rate and the density of M4041 UV are 4 g/10 min. and 0.940 g.cm^{-3}, respectively, according to ISO 1133/D (190°C and 2.16 kg) and ISO 1183 standards. M4041 UV is characterized by a glass transition temperature (Tg) of -120°C. It can be processed using rotational molding and it is suitable for monolayer and multi-layer foam technology. This material fulfills harmonized requirements on plastic materials and articles intended to come into contact with food as described in the regulation (EU) 10/2011 amended up to the regulation (EU) 2015/174 and its application into national laws. It is compatible with REACH, and TSCA but incompatible with strong acids, strong bases. Detail of the material can be found in Table 3-1 which is obtained from *TotalEnergies:-*

	Method	**Unit**	**Typical Value**
Resin Properties			
Melt Flow Index 190^0 C/2.16 kg	D-1238	g/10 min	4
Density	D-792	g.cm^{-3}	0.94
Melting point	D-3417	^{0}C/F^0	126/ 259
Vicat Softening Point	D-1525	^{0}C/F^0	119/ 247
Mechanical Properties			
Tensile modulus	D-638	MPa	806.70
Tensile Strength @ Yield	D-638	MPa	20.68
Tensile Strength @ Break	D-638	MPa	11.72
Elongation @ Yield	D-638	%	8
Elongation @ Break	D-638	%	300
Flexural Modulus (1% secant)	D-790	MPa	882.52
ESCR	D-1693		
10 % Igepal		hrs	155
100 % Igepal		hrs	> 900
UV Rating			> 16

Table 3-1 Technical data sheet of Metallocene Polyethylene (mPE M4041 UV) [119]

3.1.2 Injection-molded sample

Polypropylene PPC 6742 (named in the following, PPC) is a high-impact copolymer. It allows a melt flow index of 8 g/10 min and outstanding impact/rigidity balance to optimize the injection molding of large articles (specifically crates and mechanically heavy loaded parts requiring long-term creep resistance). It is characterized by good antistatic properties and high mechanical properties, particularly at cold temperatures (impact). Detail of the material can be found in Table 3-2, which is obtained from *TotalEnergies:-*

	Method	Unit	Typical Value
Rheological Properties			
Melt Flow Index 230^{0}C/2.16 kg	ISO 1133	g/10 min	8
Mechanical Properties			
Tensile Strength at Yield	ISO-527-2	MPa	27
Elongation at Yield	ISO-527-2	%	6
Tensile modulus	ISO-527-2	MPa	1250
Flexural modulus	ISO 178	MPa	1200
IZOD Impact Strength (notched)	ISO 180	kJ.m^{-2}	
at 23^{0}C			45
at 20^{0}C			7
Thermal Properties			
Melting Point	ISO 3146	^{0}C	165
Vicat Softening Point	ISO 306	^{0}C	
50N-50^{0}C per hour			70
10N-50^{0}C per hour			140
Heat Deflection Temperature	ISO 752	^{0}C	
1.80 MPa - 120^{0}C per hour			48
0.45 MPa - 120^{0}C per hour			90
Other Physical Properties			
Density	ISO 1183	g.cm^{-3}	0.905
Bulk Density	ISO 1183	g.cm^{-3}	0.525

Table 3-2 Technical data sheet of Polypropylene – Heterophasic Copolymer (PPC) [120]

3.2 Sample preparation

3.2.1 PE Monolayer

Samples to perform the tensile and bending tests have been cut from the bottle (Figure 3-1 (A)). A 5 mm thickness bottle has used to cut the samples for the tensile tests. A representative image of the plane of cutting for the tensile test sample is shown in Figure 3-1 (B). Figure 3-1

(C) shows the real dimension of a tensile test sample. For bending tests, different thicknesses of the samples have been tested with different lengths. A representative of the cutting plane of the bending samples from a bottle is shown in Figure 3-1 (D). The nominal width and length of the bending samples are 25 mm and 90 to 220 mm, respectively

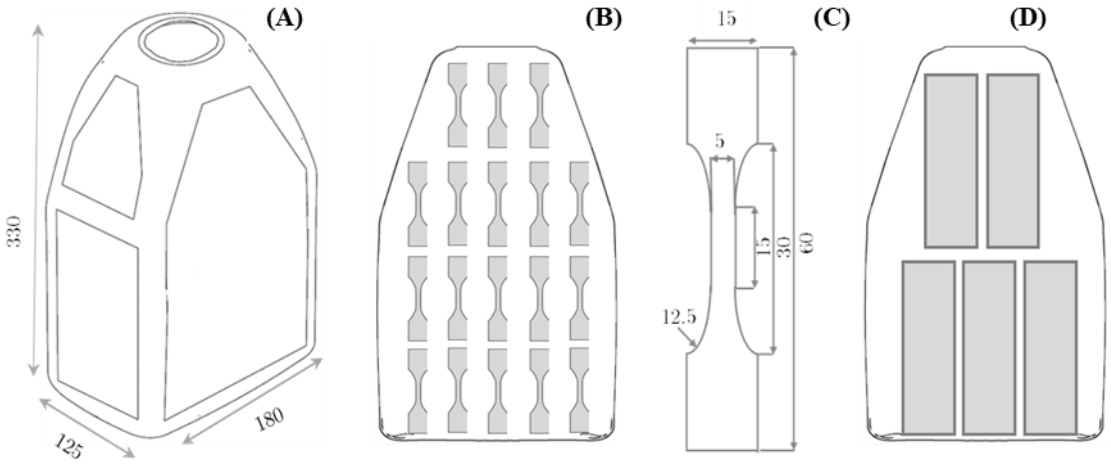

Figure 3-1 (A) Isometric view of a bottle (B) Tensile test samples representative cutting plan (C) Real dimension of the tensile test sample (D) Bending test samples representative cutting plan (all dimensions are in mm)

Charly Robot 2U has been used here because of its ease of use, its amazingly fine machining results, and its large machining surface. Another reason to use is that, Charly 4U/2U 3-axis CNC milling machines set the standard in their field with the ability to machine metals such as aluminum and brass, for a reduced budget. The specifications mentioned in Table 3-3 have been used while cutting samples by Charly robot.

Machine	CHARLY ROBOT 2U
Cam Software	GO2CAM
Setup	On vacume table
Tool	Carbide milling tool (1 tooth) Diameter : 3 mm Non-stick coating
Process	Conventional milling with 3 in feeds
Cutting Speed	84 $m.min^{-1}$
Spindle Speed	9000 RPM
Feed Rate	750 $mm.min^{-1}$
Feed Per Tooth	0.02 $mm.teeth^{-1}$
In feed Depth	1 mm x 3
Processing + Treatment	Blower on milling tool Lowest time delay during tool's descent

Table 3-3 Charly robot specification used for cutting

3.2.2 PPC Monolayer

TotalEnergies have provided plates of dimensions 60 x 60 mm (Figure 3-2 (A)). The dumbbell shape samples have been cut from the eight plates using Charly Robot 2U. The detail of dimension and plan is represented in Figure 3-2. In order to locate the longitudinal strain, the dimensions of the ASTM D638M specimens have been modified. The dimensions of a dumbbell shape sample (Figure 3-2 (B)) are 60 x 15 x 3 mm (length, width, and thickness). The dimensions of the gripping area of a sample are 15 x 15 x 3 mm. The gauge length is 10 mm, and the nominal cross-section size of a rectangle gauge length area is 5 x 3 mm^2. Figure 3-2 (C) shows the bending sample and its dimensions.

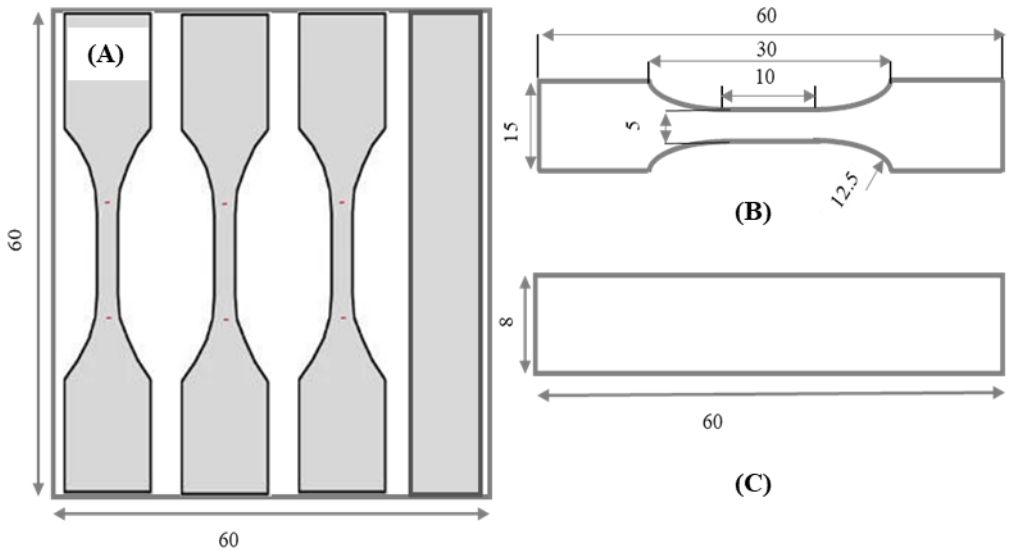

Figure 3-2 (A) Plan of cutting with detail dimension (B) Dog bone sample for tensile test (C) Rectangle sample for bending (all dimensions are in mm)

The specifications mentioned in Table 3-4 have been used while cutting samples by the Charly robot. Once samples have been cut, the spatters are removed using polish paper. Samples have been painted black and kept for drying for approximately 10 to 20 minutes. Once the paint is dry white color markers are made on it, as shown in Figure 3-3 (A). The purpose of the sample painting, is to have contrast as the camera will follow these markers during the test. The diameter of white markers is approximately 0.2 mm. At the ends of samples, there is no black paint, to avoid slipping at the jaws of the machine. The longitudinal distance between makers is 8 mm, whereas the transverse is 3 mm for a tensile test sample (Figure 3-3 (A)). For the bending sample distance between markers for 3PB is 11.25, whereas for 4PB is 7.5 mm (Figure 3-3 (B)).

Machine	CHARLY ROBOT 2U
Cam Software	GO2CAM
Setup	On vacume table
Tool	Carbide milling tool (1 tooth)
	Diameter : 3 mm
	Non-stick coating
Process	Conventional milling with 3 in feeds
Cutting Speed	108 $m.min^{-1}$
Spindle Speed	11500 RPM
Feed Rate	700 $mm.min^{-1}$
Feed Per Tooth	0.02 $mm.teeth^{-1}$
In feed Depth	1 mm x 3
Processing + Treatment	Blower on the milling tool
	Lowest time delay during tool's descent

Table 3-4 The specifications of the Charly robot used during the cutting of the specimens

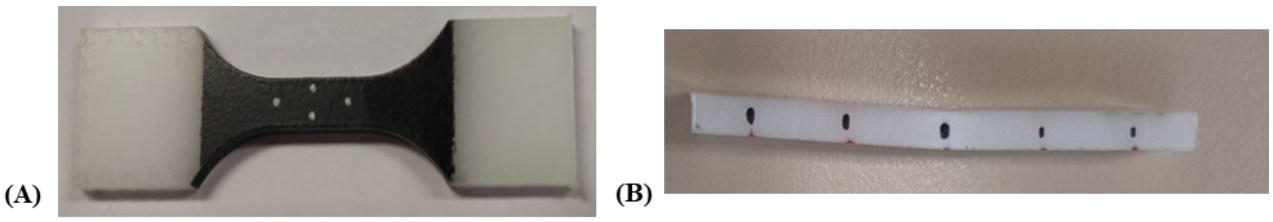

Figure 3-3 (A) Real image of a color sample with black and with white markers on it (B) Real bending sample with markers

3.3 The experimental test procedure for monolayer

Tensile test data obtained from the below tests have been used to identify the constitutive model. Bending data is used for the validation of the constitutive model.

3.3.1 Experimental procedure of tensile test PE

In the literature, conventional tensile tests are extensively discussed. Cross and Haward [121] considered curve load vs. extension, Oberst and Retting [122], Andrews and Ward [123], Pezzin *et al.* [124] used nominal stress and strain to describe the physical behavior of a material. Unfortunately, nominal stress and strain are not sufficient to describe the material's physical properties (magnitude of yield drop, rate of strain hardening) due to consideration of the initial area of cross-section and length of the specimen to calculate nominal stress and strain, respectively [118]. Meinel and Peterlin [125] applied constant nominal strain using crosshead speed, which does not keep a constant strain rate locally, limiting the determination of a material's

constitutive relation. To overcome these issues, G'sell and Jonas [118] put forward the experimental procedure and setup to obtain a locally constant strain rate, and the same has been used in this thesis.

Instron testing machine 1195 with a 500 N load cell is used to perform the experiments. All experiments are performed at a temperature of 23 °C. To calculate true strain, the position of four markers on a sample is tracked by Videotraction® software (by ProViSys Engineering, France). A detailed explanation of the method and process to calculate strain can be found in the article by G'sell and Jonas [118]. CCD camera with a resolution 800 x 600 pixels and frame rates 1.875-15 fps is used in real-time to track the position of the markers. The true longitudinal and transverse strains are calculated by the following Equation (2) and (3) :

$$\varepsilon_l = \ln\left(\frac{l}{l_0}\right) = \ln\left(1 + \frac{\Delta l}{l_0}\right) \tag{2}$$

$$\varepsilon_t = \ln\left(\frac{W}{W_0}\right) = \ln\left(1 + \frac{\Delta W}{W_0}\right) \tag{3}$$

where l, l_0 and W, W_0 is the current and initial distance between longitudinal and transverse markers, ΔL and ΔW are the increments of these values.

By assuming isotropy of transverse strains, the longitudinal Cauchy stress (or true stress σ_v) is calculated with the following Equation (4) [126]:

$$\sigma_v = \frac{F}{S} = \frac{F}{S_0}\frac{1}{\exp(2\varepsilon_t)} \tag{4}$$

where S_0 is the initial cross-section area, S is the actual cross-section area and F is the current axial load.

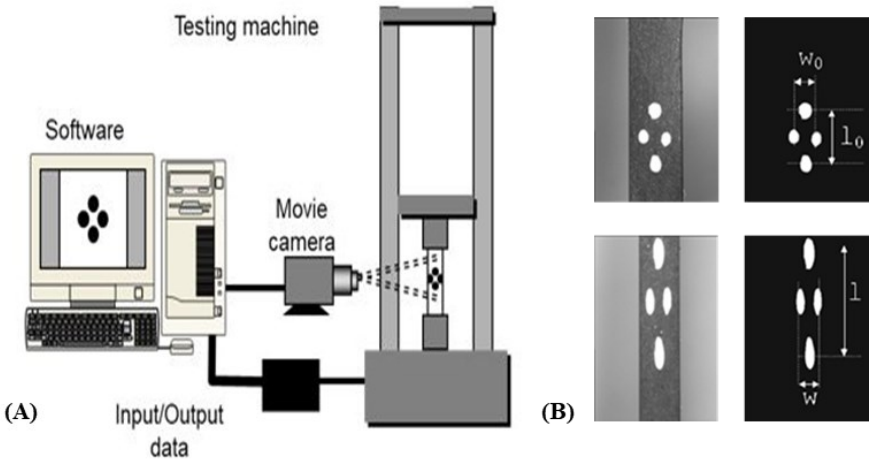

Figure 3-4 (A) Experimental setup of tensile test (B) Markers position before and after the strain

The schematic system represented in Figure 3-4 (A) has been used to apply the constant local true strain rate. Local constant true strain rate is entered in the computer on which tensile test needed to be performed. The camera has connected to a computer, which recorded the position of the markers. The displacement rate is applied on a machine to have the desired constant true strain rate locally. Figure 3-4 (B) shows the position of markers before and after the strain. Tensile tests with six different strain rates, 10^{-2}, 5.10^{-3}, 10^{-3}, 5.10^{-4}, 10^{-4}, and 5.10^{-5} s^{-1} are performed.

3.3.2 Experimental procedure of tensile test on PPC

A precisely similar procedure has been used to do the constant true strain rate tensile test of PPC as PE (as explained in 3.3.1). Instead of six tensile tests at a constant true strain rate, five are used to perform the tensile test. Parameters of experimental setup do not allow to perform the tensile test at a constant true strain rate 10^{-2} s^{-1}. Basically, it is due to instability in Proportional Integral Derivative (PID) controller. To regulate constant true strain rate, a PID controller is used which automatically optimizes and accurate the control system. Compared with PE sample thickness of PPC samples is less, which leads to instability of PID controller at high true strain rate like 10^{-2} s^{-1}.

3.3.3 Experimental procedure of 3PB and 4PB tests of PE sample

3PB and 4PB tests are performed on the different specimens with several thicknesses. These tests permit the evaluation of the structure's response under a different type of loading. In 3PB (Figure 3-5 (A)), the top and bottom of the sample are in compression and tension, respectively. Simultaneously shear is also in effect. In the 4PB test (Figure 3-5 (B)), pure bending accurse between two load supports. Maximum bending stress occurs at the loading anvil in 3PB test, whereas, in the 4PB test, it is distributed over the section of a beam between the loading point [127], [128].

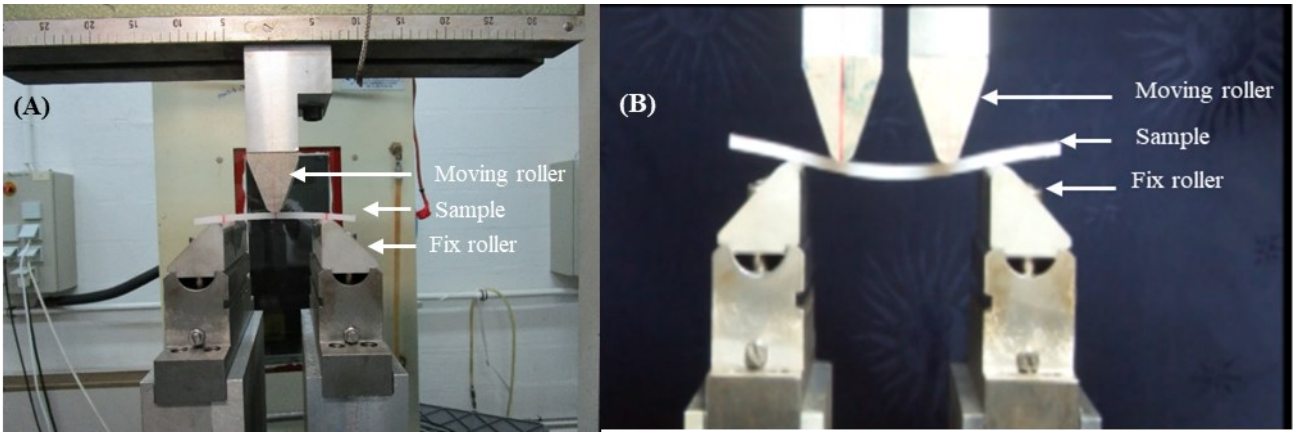

Figure 3-5. Experimental setup of (A) 3PB and (B) 4PB test

Instron 4505 machine is used to perform the tests. Oil as a lubricant is applied at the point of contact of the moving roller and sample. During 3PB and 4PB, PE samples with 2, 4, 6, and 8 mm nominal thicknesses are used to see the effect of the manufacturing process (rotational molding) on response and evaluate the numerical response with the constitutive model. The experiments conducted in bending are based respectively on the standards NF EN ISO 178 [129] and D790 [130] for 3PB test and D6272 for 4PB test. Table 3-5 and Table 3-6 show the different characteristics of the tests for the 3PB and 4PB tests, respectively, such as the distance between the fixed rollers and between the moving rollers (for the 4PB) as a function of the nominal thickness of the specimens. In addition, the actual thicknesses and widths of the specimens in the 3PB and 4PB tests are provided in these tables. The average width of the sample is measured at three locations, 1A-1B, 2A-2B, and 3A-3B, as shown in Figure 3-6. Widths at different locations are mentioned in Table 3-5 (3PB tests) and Table 3-6 (4PB tests). The thickness of the samples is measured at six locations (1A, 2A, 3A, 1B, 2B, 3B) shown in Figure 3-6. The average of values at each location thickness is mentioned as real thickness in Table 3-5 and Table 3-6 for 3PB and 4PB respectively. In these two tables, the thicknesses and widths are given as follows, Equation (5) and Equation (6) respectively:

$$\text{Average (2A, 2B)}^{\text{Average (1A,1B)}-\text{Average (2A,2B)}}_{\text{Average (3A,3B)}-\text{Average (2A,2B)}} \tag{5}$$

$$\text{Distance (2A, 2B)}^{\text{Distance (1A,1B)}-\text{Distance (2A,2B)}}_{\text{Distance (3A,3B)}-\text{Distance (2A,2B)}} \tag{6}$$

The length of the samples is between 90 and 220 mm, depending on the configuration (distance between the fixed supports).

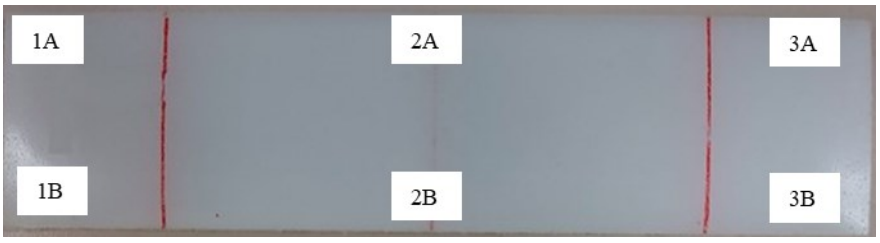

Figure 3-6. Location of thickness and width measurement points on 3PB and 4PB test samples.

Thickness (mm) Nominal	Thickness (mm) Real at 2A and 2B	Width (mm) Real at 2A and 2B	Distance between fixed rollers (mm)	Displacement rate applied on moving roller ($mm.s^{-1}$)
2	$2.05^{+0.01}_{+0.12}$	$24.97^{+0.03}_{+0.03}$	30	$1.33\ 10^{-2}$
4	$3.72^{+0.01}_{+0.08}$	$25.64^{-0.34}_{+0.02}$	60	$2.66\ 10^{-2}$
6	$6.20^{-0.07}_{+0.09}$	$24.71^{+0.08}_{+0.02}$	90	$3.99\ 10^{-2}$
8	$8.12^{-0.01}_{-0.01}$	$25.15^{+0.01}_{+0.05}$	120	$5.33\ 10^{-2}$

Table 3-5 3PB test details of PE

Thickness (mm) Nominal	Thickness (mm) Real at 2A and 2B	Width (mm) Real at 2A and 2B	Distance between fixed rollers (mm)	Distance between moving rollers (mm)	Displacement rate applied on moving rollers ($mm.s^{-1}$)
2	$2.15^{-0.13}_{+0.03}$	$25.03^{-0.01}_{+0.02}$	60	30	$1.33\ 10^{-2}$
4	$4.11^{-0.04}_{-0.13}$	$25.00^{+0.01}_{+0.00}$	80	40	$5.33\ 10^{-2}$
6	$5.83^{+0.15}_{-0.08}$	$24.89^{-0.13}_{+0.00}$	120	60	$3.99\ 10^{-2}$
8	$8.16^{-0.32}_{-0.10}$	$25.08^{-0.07}_{-0.15}$	160	80	$1.06\ 10^{-1}$

Table 3-6 4PB test details of PE

3.3.4 Experimental procedure of 3PB and 4PB tests of PPC sample

Instron 1195 machine with a load cell of 2 kN is used to perform the tests. First experiments are done on monolayer PE samples in which local (mesoscopic) strain hasn't been tracked, but an improvement, the local strain has been tracked while performing tests with all the PPC samples. While performing the real-time test position of the markers has been tracked using idpix 1.7 software (developed by Pprime). As shown in Figure 3-7 (A), LED light and camera are used for tracking real-time position. Figure 3-7 (B) shows an image from a camera that is subjected to image processing with idpix 1.7 software (Pprime software) to calculate the real-time strain or position of markers.

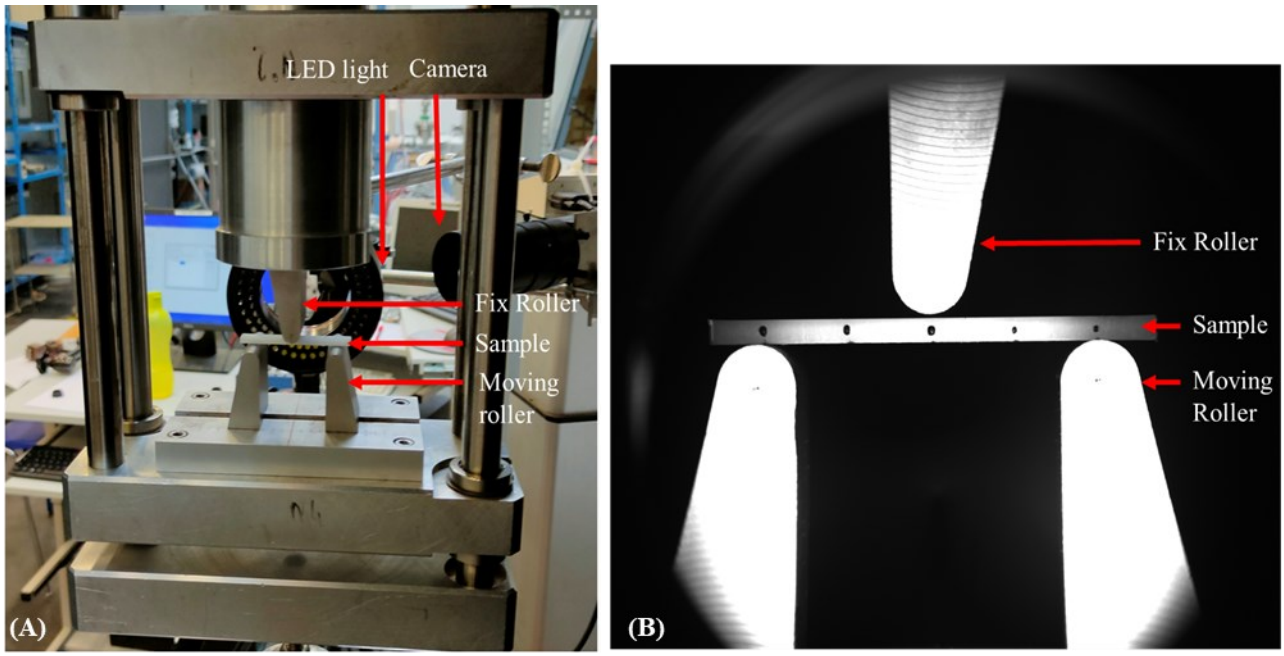

Figure 3-7 (A) Experimental setup of 3PB test (B) Image from camera used to track the markers

PPC sample's width and thickness for 3PB and 4PB tests are mentioned in Table 3-7. Unlike PE (rotational molded) samples, the thickness of the injection-molded samples is relatively homogeneous; that is why all the dimensions are measured at the center of the sample. No norm has been followed while performing experiments, as this data is used to validate the constitutive model.

Type of test		Distance between		Width (mm)	Thickness (mm)	Displacement rate ($mm.s^{-1}$)
		Fix roller (mm)	Moving roller (mm)			
3PB	Test-1	45	-	7.92	2.96	$1.866\ 10^{-2}$
	Test-2	45	-	7.84	2.98	$1.866\ 10^{-2}$
	Test-1	45	-	7.85	3.01	$3.99\ 10^{-2}$
	Test-2	45	-	7.93	2.99	$3.99\ 10^{-2}$
4PB	Test-1	45	10	7.98	2.99	$1.866\ 10^{-2}$
	Test-1	45	10	7.99	2.95	$3.99\ 10^{-2}$
	Test-2	45	10	7.82	2.99	$3.99\ 10^{-2}$

Table 3-7 Details of the PPC 3PB and 4PB tests

3.3.5 PE Bottle tested under internal water pressure

Tests under internal pressure on a bottle are performed with a setup capable of applying different load types on a sample such as tensile-compressive, torsion, and internal pressure (pressurized water is used to apply the pressure). Test bench Endomat has dimensions equal to 700 x 700 x 1800 mm and a volume of 882 L is shown in Figure 3-8 (A). The maximum

capacity of a machine is 1200 bar in internal pressure. In this study, the internal pressure is imposed with the different load and unloading paths, and the pressure rate is equal to 5 bar.min^{-1}. For tracking the position of the markers (Figure 3-8 (B)) in the space [131]–[133] an optical device (Figure 3-8 (C)) is used. Two camera permits to localize the vector of displacement for each marker. More detail is presented in an article by Lainé *et al.* [131].

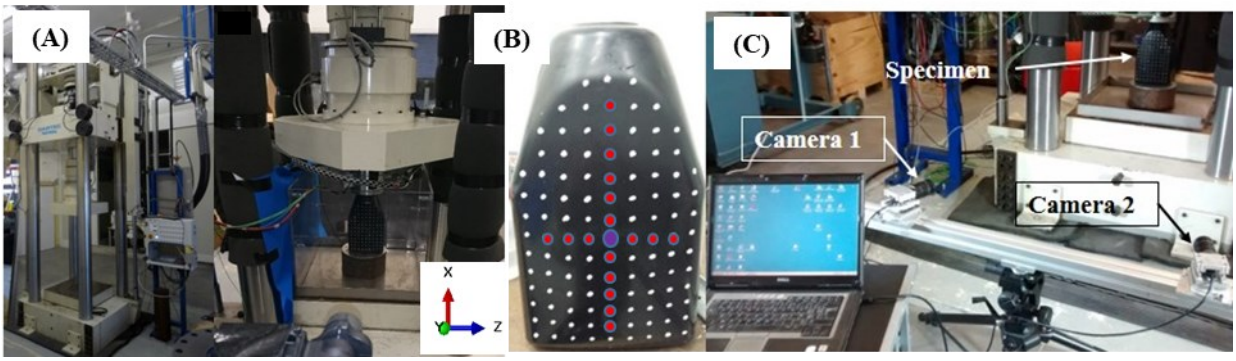

Figure 3-8 (A) Endomat test machine (B) Sample with markers in white, red and violet color (C) Optical device

3.4 Experimental results of monolayer

3.4.1 Tensile test results of PE

Different color curves shown in Figure 3-9, represent the true stress vs. longitudinal as well as transverse strain at the different constant true strain rates. Yield stress has been considered as 1.5 MPa after that plastic part starts, it is evident that the material follows viscoelastic behavior, as the slop at the initial points of the curves is different for each strain rate. It can be noted that the slope of initial points of curves increases as imposed strain rate increases which results in an increase in effective elastic Young's modulus. When longitudinal plastic strain vs. stress is observed then well-separated curves at different imposed strain rates give us concrete proof of viscoplasticity. Due to confidentiality values on the X and Y-axis are not presented. This data will be used for the identification of the constitutive model of PE.

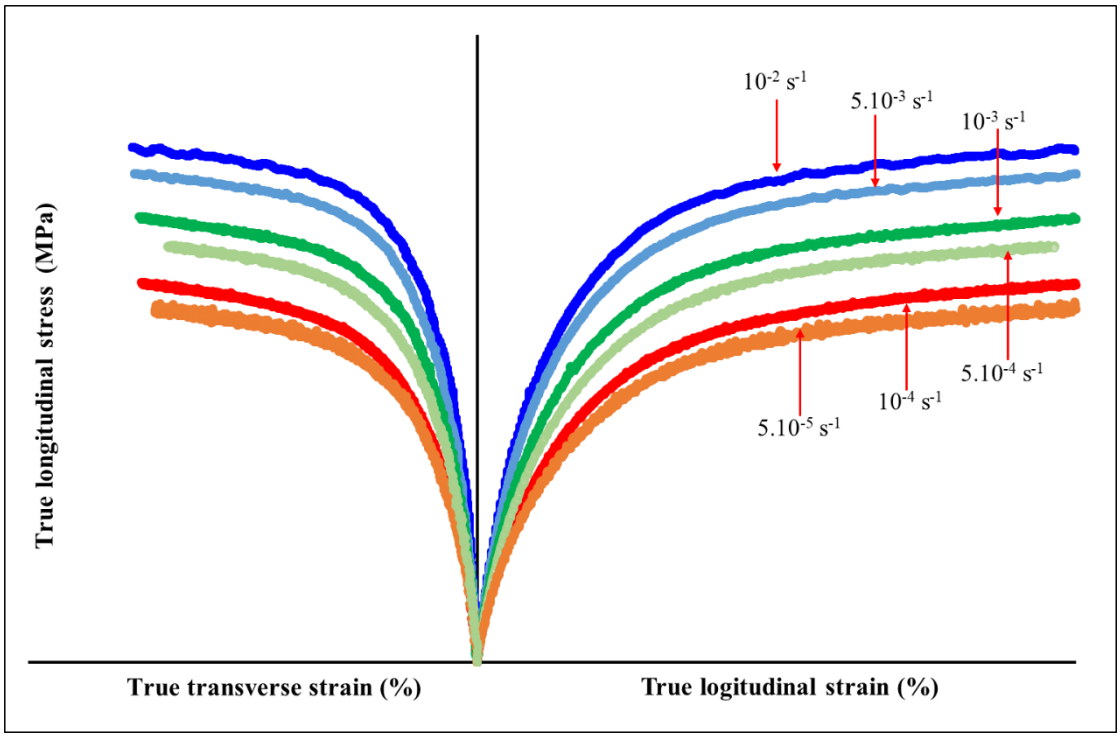

Figure 3-9 Tensile test results of PE samples at different constant strain rates

3.4.2 Bending test results of PE

Figure 3-10 (A) and Figure 3-10 (B) show the 3PB and 4PB test results, respectively. In order to normalize the results and to allow comparison between the different tests at a given thickness, the force per unit area of the cross-section measured in the middle of the PE sample and the displacement imposed on the moving roller (for both 3PB and 4PB tests) are represented. Indeed, this (force per unit area) specific representation allows for comparing all the tests (two to three per thickness) and gives the means to eliminate the effect of the area of cross-section. All curves (dotted line as well as a solid line) of the same color signify the results of the samples with the same nominal thickness. Solid curves correspond to the sample whose dimensions are used for simulations. It is essential to mention that more than two samples for each thickness have been tested and do not have the same geometrical dimension. The ratio of the distance between fix and moving roller with thickness is different for 2 mm when compared with 4, 6, and 8 mm thickness samples in 4PB experiments. While performing experiments, for the practical purpose, it is not possible to have 20 and 10 ratios of the distance between fixed and moving rollers with thickness, respectively, instead, 30 and 10 as the ratio have been used. That might be one of the reasons why we do not have the same order of curve as 3PB test in 4PB tests. The ratio of displacement rate applied to thickness for 4 and 8 mm nominal thickness sample is 1.33 10^{-2} s^{-1}, whereas for other samples of 3PB and 4PB tests is 6.65 10^{-2} s^{-1}. Because of technical reasons ratio of displacement rate applied to thickness for 4 and 8 mm

sample is different from other samples. Due to confidentiality, values on Y-axis are not presented. Details of the sample dimension are mentioned in Table 3-5 and Table 3-6. Variability is low when experiments are repeated with the same nominal thickness. This data will be used to validate the constitutive model of PE.

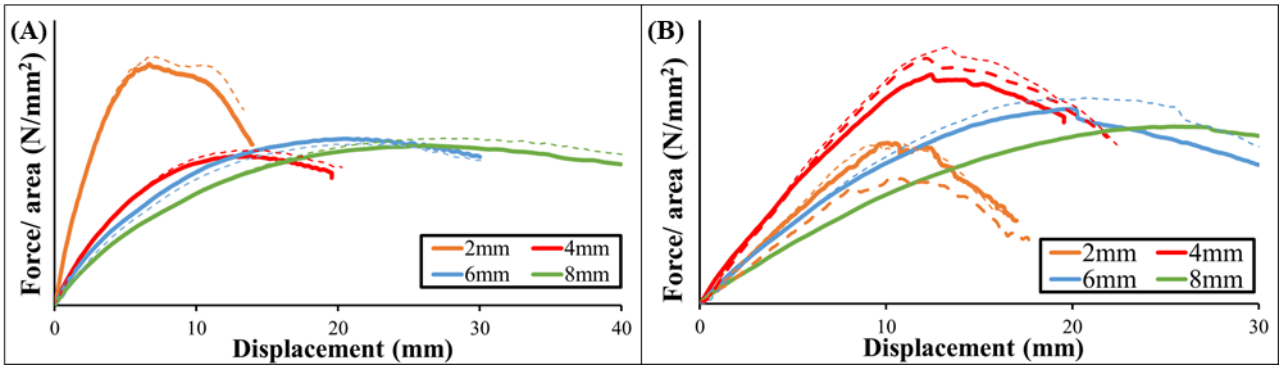

Figure 3-10 (A) 3PB and (B) 4PB test results

3.4.3 Results of PE Bottle tested under internal water pressure

Figure 3-11 (A) and (B) show a variation of load vs. internal pressure for the bottle in the loading and loading-unloading scenario respectively. When internal pressure has been applied to the bottle, the bottom surface of a bottle creates a reaction which is represented as load. Light blue and green dots curves in Figure 3-11 (A) and (B) represent measured load and displacement in the Y-direction of maximum strain point (shown in Figure 3-8 (B) with purple dot), respectively, with respect to internal pressure. Figure 3-11 (A) corresponds to a monotonic test and Figure 3-11 (B) load-unload test.

During the monotonic loading experiments, the movement of the markers is tracked. Experimental displacement in the Y-direction (Maximum swelling) of markers (Red color points in Figure 3-8 (B)) present at the vertical and horizontal direction of bottle results are represented in Figure 3-11 (C) and (D) respectively. Orange, red, and blue color dots represent the displacement of markers when internal pressure is 2, 5, and 10 bar respectively. This data will be used to see the capabilities of the PE constitutive model.

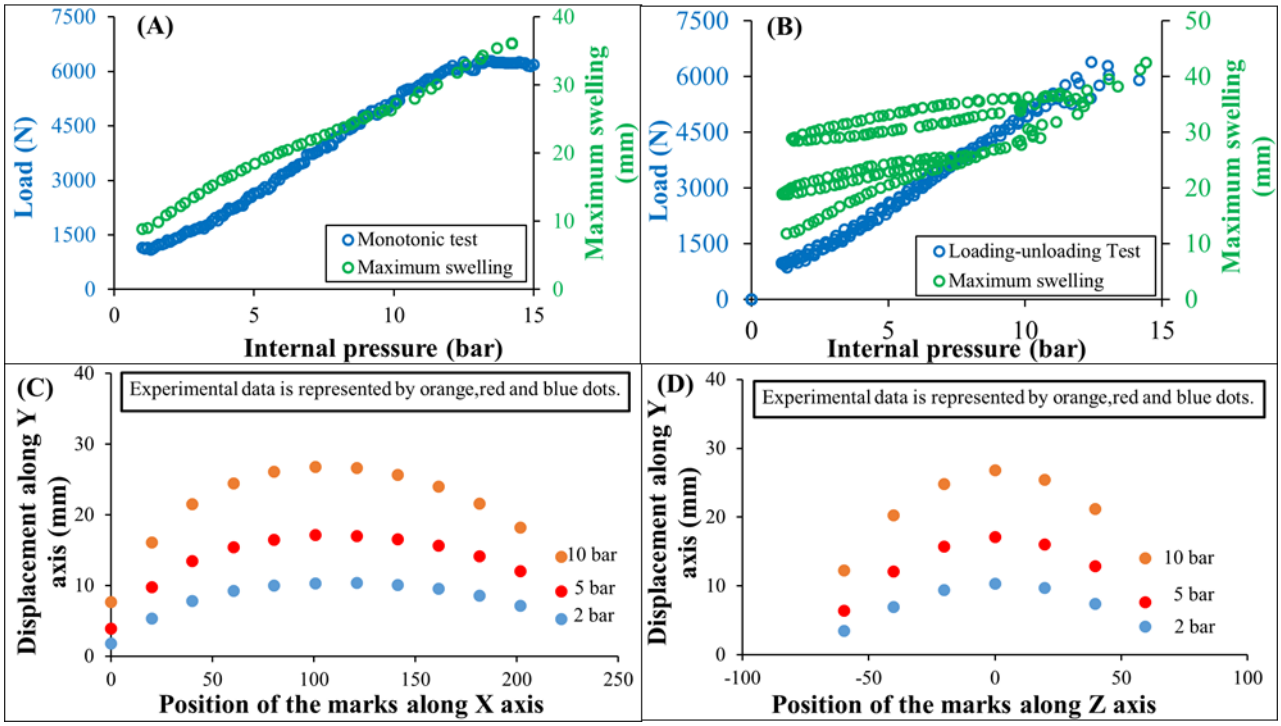

Figure 3-11 (A) Monotonic pressure application experimental test (B) Loading un-loading pressure application experimental test, displacement along Y-axis of markers (C) Along X-axis (vertical direction of a bottle) (D) Along Z-axis (horizontal direction of a bottle) at a different internal pressure

3.4.4 Tensile test results of PPC

Figure 3-12, shows the stress vs. strain graph more precisely transverse and longitudinal percentage strain vs. true longitudinal stress at different strain rates for the PPC samples. The different colors show the different strain rates applied while performing experiments. At the beginning of the curves, different strain rate curves have different slopes as it is not as prominent as the PE sample but still gives proof of viscoelasticity. Well, separated curves at different strain rates give an indication of viscoplasticity. As explained above (heading 3.3.2), the tensile test at strain rate 10^{-2} s^{-1} is not possible due to technical problems; the same can be seen in curve 5.10^{-3} s^{-1} with many undulations (instability). Instead of using this raw experimental data for identification, smoothening has been performed on curves and the same data has been used for the identification of constants of the constitutive model.

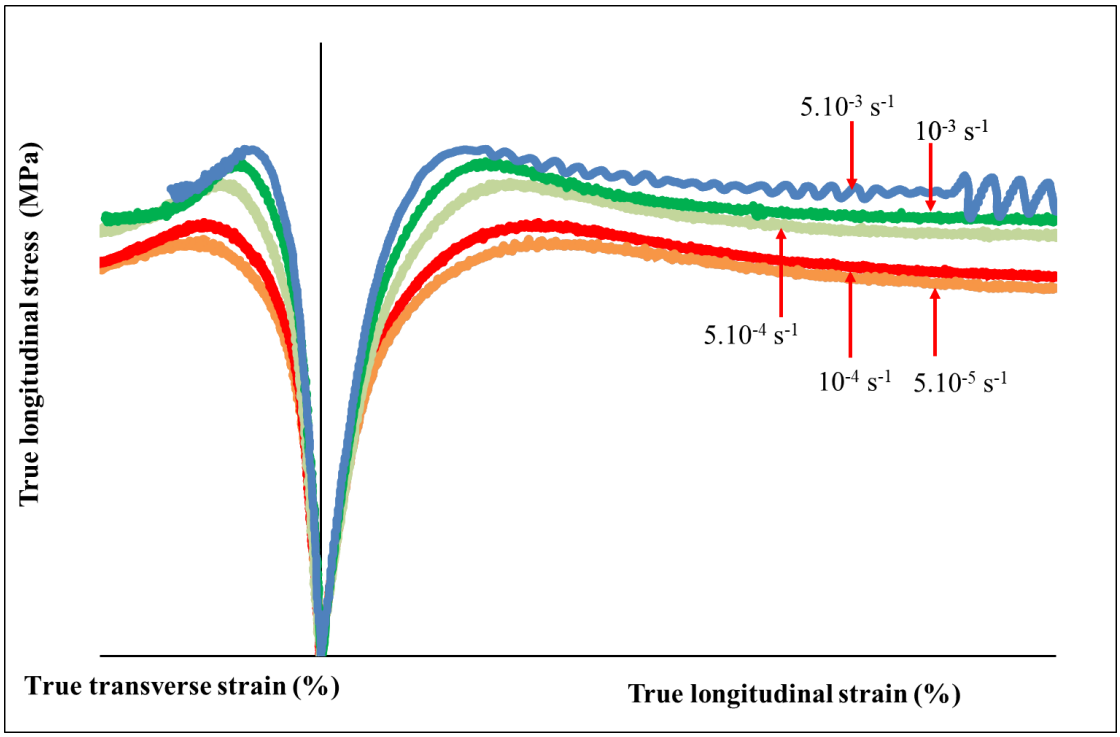

Figure 3-12 Results of tensile tests on PPC at different constant strain rates

3.4.5 Results of the PPC bending tests

Force per unit area vs. displacement imposed during bending is represented in Figure 3-13. On the Y-axis (range is the same for all the graphs), force per unit area (cross-section area is calculated at the center of the sample) is plotted instead of force alone to eliminate the effect of the cross-sectional area on the results. Figure 3-13 (A) and (B) show 3PB test results at displacement rate 3.99 10^{-2} mm.s^{-1} and 1.99 10^{-2} mm.s^{-1} respectively. Figure 3-13 (C) and (D) represent 4PB results displacement rate at 3.99 10^{-2} mm.s^{-1} and 1.99 10^{-2} mm.s^{-1} respectively. Normally 2 samples for each displacement rate are tested to quantify the variability of experiments and the same two curves can be seen in each Figure 3-13 except Figure 3-13 (D) as data of the second test has been lost. The detailed dimensions of the samples are mentioned in Table 3-7. These data will be used later for the validation of the PPC constitutive model.

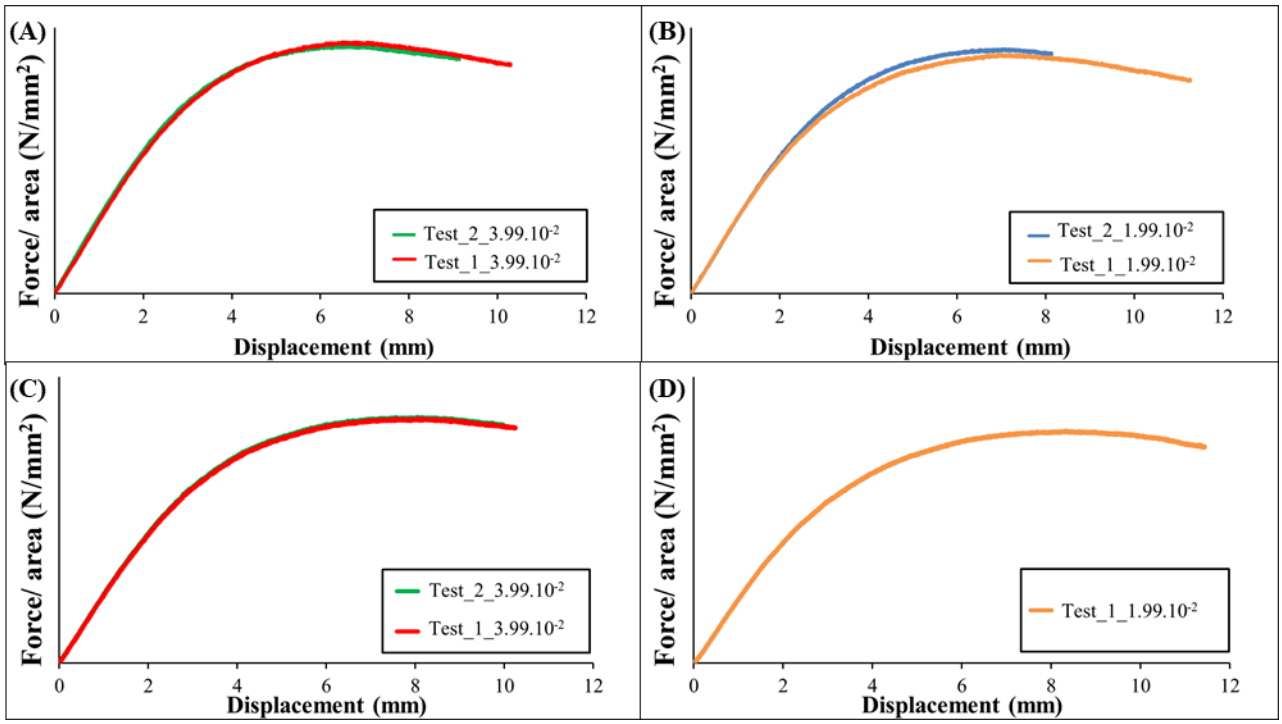

Figure 3-13 3PB test results at applied displacement rate (A) 3.99 10^{-2} mm.s^{-1} and (B) 1.99 10^{-2} mm.s^{-1}, and 4PB test results at applied displacement rate (C) 3.99 10^{-2} mm.s^{-1} and (D) 1.99 10^{-2} mm.s^{-1}

3.4.6 Discussion

A substantial experimental database has been established. It is important to note that all experiments are at increasing load except for one bottle test. The tensile curves show the viscoelastic behavior encountered in this family of materials. The transverse tensile responses are relatively well understood, a pivotal point in the identification phase.

The structural tests cover many situations because 3PB and 4PB tests generate compressive loads with more or less shear. On the other hand, the bottle is in biaxial tension when pressurized. The variability in the tests is quite low, and, on the bottle, a wide range of displacement could be captured.

3.5 Constitutive model

It is important to note that this part is taken from the article that is submitted for publication to the International Journal of Mechanical Sciences. Grandidier and Lainé [117] developed a constitutive model based on the idea of a superposition of two forms (linear and non-linear) of the kinematic hardening mechanism adopted by Chaboche [134] and taken up by Chambaudet [135] for the thermodynamic formulation of thermoplastic and thermosetting polymers. The basis of the model assumes that the total strain rate is decomposed into viscoelastic and viscoplastic parts:

$$\dot{\varepsilon}^{vel} + \dot{\varepsilon}^{vpl} = \dot{\varepsilon} \quad (7)$$

where $\dot{\varepsilon}^{vel}$ is the viscoelastic strain rate, $\dot{\varepsilon}^{vpl}$ is the viscoplastic strain rate and $\dot{\varepsilon}$ is the total strain rate.

A tensile test has been performed as explained in heading 3.3.1. During the test, true longitudinal and transverse strains have been recorded along with the force. In a range of small strains, the behavior is viscoelastic. To easily take into account this effect, a dependence of Young's modulus on the strain rate is proposed. More precisely, this modulus is a function of the total equivalent strain rate. It is identified by imposing an elastic threshold equal to 1.5 MPa irrespective of strain rate in order to capture the non-linearity at the beginning of the stress-strain curve. Figure 3-14 shows longitudinal stress vs. strain for strain rate is equal to 5.10^{-5} s^{-1}. From Figure 3-14 it is clear by a red solid line that if more longitudinal stress is used for the calculation of Young's modulus, then nonlinearities, in the beginning, are not taken into account. As stress value decreases for calculation of young's modulus then non-linearity, in the beginning, is taken care, same has been shown by a green solid line in Figure 3-14.

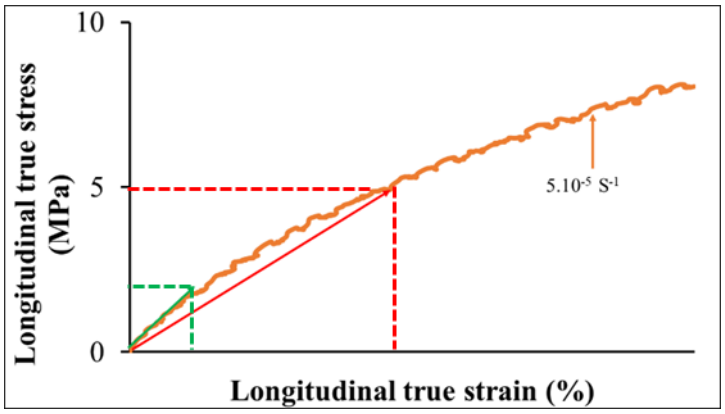

Figure 3-14 Explanation of elastic threshold is equal to 1.5

From experimental data, Young's modulus is calculated and plotted on the graph vs. the total equivalent strain rate. Asymptotic Equation (8) defined by the authors, is used to fit the curve:

$$E = E_1 + E_2 * \left(1 + \tanh\left(E_3 * \log\left(\dot{\varepsilon}_{eq}\right) + E_4\right)\right) \quad (8)$$

where E_1,E_2,E_3, and E_4 are the material constants, $\dot{\varepsilon}_{eq}$ is the total equivalent strain rate defined as: $\left(\frac{2}{3}\,\dot{\varepsilon} : \dot{\varepsilon}\right)^{1/2}$. The expression has two asymptotes, at very high strain rates and low rates at the relaxed modulus.

Stress-strain relation in elastic part is given by Equation (9)

$$\bar{\bar{\sigma}} = \lambda\, tr\, \bar{\bar{\varepsilon}}^{el}\, I + 2\,\mu\, \bar{\bar{\varepsilon}}^{el} \quad (9)$$

where λ and μ are the lame constant, I is an identity matrix.

$$\bar{\bar{\sigma}} = \frac{E\nu}{(1+\nu)(1-2\nu)}\, tr\, \bar{\bar{\varepsilon}}^{el}\, I + \frac{E}{(1+\nu)}\, \bar{\bar{\varepsilon}}^{el} \tag{10}$$

where ν is the Poison's ratio.

Viscoplastic strain rate is defined by Drucker postulated associated flow [136],

$$\dot{\bar{\varepsilon}}^{pl} = \dot{P}\, \bar{\bar{n}} \tag{11}$$

where $\dot{P}$ is the tensor modulus of cumulated viscoplastic strain rate $= \left(\frac{2}{3}\, \dot{\varepsilon}^{vpl} : \dot{\varepsilon}^{vpl}\right)^{1/2}$, n is normal to the load surface defined after. In the literature, more sophisticated models adapted to polymers are proposed. Here, it is chosen to keep the initial proposal relatively simple. The flow rule is as follows [117]:

$$\dot{P} = \left(\frac{(1-a)\, J_2\left(\bar{\bar{\sigma}} - \bar{\bar{X}}\right) - R + a\, tr(\bar{\bar{\sigma}})}{K}\right)^N \tag{12}$$

where R, N, K, and a are respectively elastic threshold, strain sensibility factor, coefficient of viscosity, and hydrostatic pressure coefficient. Hydrostatic pressure coefficient variation with total equivalent strain rate is defined by Equation (14). The expression of the tensor of the external normal to the load surface takes then the following form [117]:

$$\bar{\bar{n}} = (1-a)\frac{3}{2}\left(\frac{\bar{\bar{\sigma}}' - \bar{\bar{X}}'}{J_2\left(\bar{\bar{\sigma}} - \bar{\bar{X}}\right)}\right) + a\bar{\bar{I}} \tag{13}$$

Where $\bar{\bar{\sigma}}' = \bar{\bar{\sigma}} - \frac{1}{3}\, tr(\bar{\bar{\sigma}})$ and $\bar{\bar{I}}$ = Identity matrix.

A simplified version is used in the following; the kinematic hardening is not considered because the identification is based only on monotonic traction tests. Therefore, it is not possible to evaluate the kinematic hardening, but it turns out that isotropic strain-hardening is sufficient.

The hydrostatic pressure coefficient is proposed as a function of the total equivalent strain rate to consider the effect of viscoplasticity on bulk behavior. But it depends upon each material. The following form is proposed for PE

$$a = A_1 * \left(1 - exp\left(-A_2 \dot{\varepsilon}_{eq}{}^{A_3}\right)\right) + A_4. \tag{14}$$

Following Equation (15) is proposed for the PPC

$$\begin{aligned} a = &\left(A_1 + A_2 * \left(1 + \tanh\left(A_3 * \log\left(\dot{\varepsilon}_{eq}\right) + A_4\right)\right)\right) * \left(1 - \exp\left(-\left(A_5 + A_6 *\right.\right.\right. \\ &\left.\left.\left.\left(1 + \tanh\left(A_7 * \log\left(\dot{\varepsilon}_{eq}\right) + A_8\right)\right)\right) * 3P\right)\right) + \left(A_9 + A_{10} * \left(1 + \tanh\left(A_{11} *\right.\right.\right. \\ &\left.\left.\left.\log\left(\dot{\varepsilon}_{eq}\right) + A_{12}\right)\right)\right) * 3P + \left(A_{13} + A_{14} * \left(1 + \tanh\left(A_{15} * \log\left(\dot{\varepsilon}_{eq}\right)\right)\right)\right). \end{aligned} \tag{15}$$

These two models have been developed following the analysis of the volume strains as a function of the hydrostatic pressure for different strain rates. The observations are in agreement with the literature [137], [138].

3.6 Implementation of constitutive model in Abaqus UMAT

The above constitutive model presented in heading 3.5 is implemented in Fortran as UMAT in Abaqus®. UMAT is an extension that is capable of doing the following things:

User subroutine UMAT [139]:

- Can be used to define the mechanical constitutive behavior of a material;
- Will be called at all material calculation points of elements for which the material definition includes a
- Can be used with any procedure that includes mechanical behavior;
- Can use solution-dependent state variables;
- Must update the stresses and solution-dependent state variables to their values at the end of the increment for which it is called; $\frac{\partial \Delta\sigma}{\partial \Delta\varepsilon}$, must provide the material Jacobian matrix, for the mechanical constitutive model.
- Can be used in conjunction with user subroutine USDFLD to redefine any field variables before they are passed in the code.

To solve the differential equation of viscoplastic flow, Runge-Kutta 4^{th} order method is used.

The identification of the parameters has been made in the literature using a 1D procedure associated with a genetic algorithm. This solution is not accurate, and considering the sensitivity on Young's modulus and the hydrostatic pressure increases the number of parameters. A more sophisticated technique must be deployed. The validated identification protocol consists of three steps:

- Identification of the modulus sensitivity to strain rate via the tangent modulus of responses
- Identification of the sensitivity of the hydrostatic pressure to the strain rate via the volume strain
- Identification of the viscoplastic parameters

These different steps are detailed in the following paragraphs.

3.7 Procedure for identification of the modulus and hydrostatic pressure coefficient of PE

The slopes of each curve have been measured at the point corresponding to 1.5 longitudinal stress. This point has been chosen to avoid the fluctuations in measurement at beginning of tests. A table with Young's modulus in the function of stain rate is generated. Variation in Young's modulus with respect to the total equivalent strain rate is represented in Equation (8). Material constants (E_1, E_2, E_3, and E_4) in this equation are found using the predefined function "fmincon" in MATLAB®. Root mean square error is used as the objective function, and convergence tolerance is 0.01.

In the case of a tensile test, hydrostatic pressure coefficient (a) is calculated experimentally according to the following expression:

$$\left(\frac{\varepsilon_l + 2\varepsilon_t - \frac{\sigma(1-2\nu)}{E}}{3P}\right) = a \tag{16}$$

where ε_l, ε_t are the longitudinal and transverse strains respectively. σ is the true stress calculated during tensile tests. The numerator of the equation is called volumetric viscoplastic strain.

By fitting a straight line in the curves represented in Figure 3-15 (A) value of the hydrostatic pressure coefficient is calculated which is nothing but the slope of the fitted line. It is clearly visible that for each strain rate will be having one value, which is independent of plastic strain. Experimental a is calculated by using Equation (16) and asymptotic Equation (14) is used to fit the experimental data. It can be observed in Figure 3-15 (B) that variation of true transverse strain with respect to 3 times plastic strain ($3P$) is linear and slop is constant for all the strain rates.

All the parameters in Equation (14) are found using optimization with the help "fmincon" in Matlab®. Root mean square error is used as an objective function and convergence tolerance is taken as 0.01.

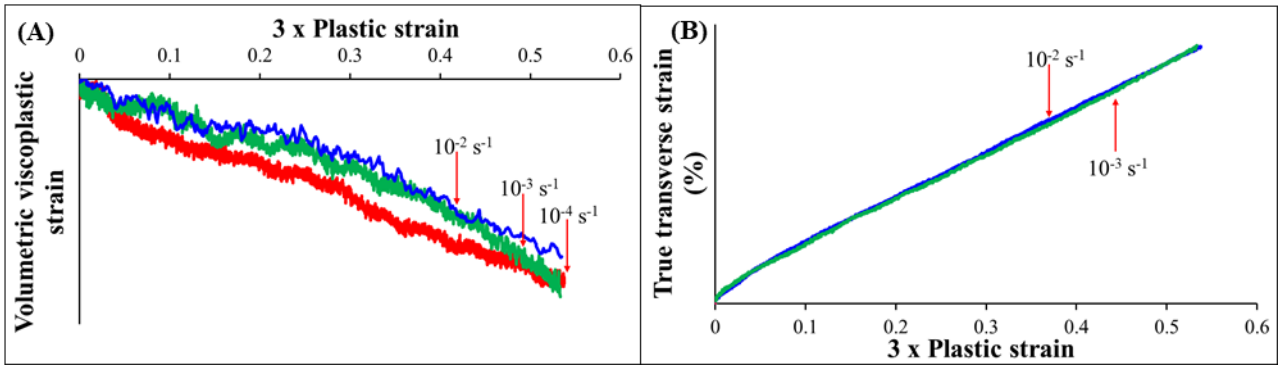

Figure 3-15 Experimental data for calculation of hydrostatic pressure coefficient for PE, (A) Volumetric viscoplastic strain, and (B) True transverse strain vs. 3P (3 x Plastic strain)

3.8 Procedure for the identification of the modulus and hydrostatic pressure coefficient of PPC

In the same way as PE, Young's modulus has been calculated experimentally for the PPC. For identification excel solver is used to fit experimental values with the curve generated by Equation (8).

Variation of hydrostatic pressure coefficient for PPC is different than that of PE. Figure 3-16 (A) shows a variation of volumetric viscoplastic strain vs. *3P* (corresponding in volume). Figure 3-16 (B) shows a variation of transverse strain vs. *3P* of experiments with different strain rates. The straight line cannot be fitted with the curves presented in Figure 3-16 (A). This implies hydrostatic pressure coefficient is varying with respect to plastic strain and it does not have only one value like PE for one strain rate. Equation (15) is constructed to fit the slope of the curves presented in Figure 3-16 (A). From Equation (16) it is clear that the value of transverse strain is also affecting the value of hydrostatic pressure coefficient. After doing more investigation it is observed that the transverse strain is not varying linearly with $3P$, it can be seen in Figure 3-16 (B). Because of this reason, identification of the parameters has been done with 3D optimization tool. From Equation (15) influential parameters are identified which are A_1, A_5, and, A_9.

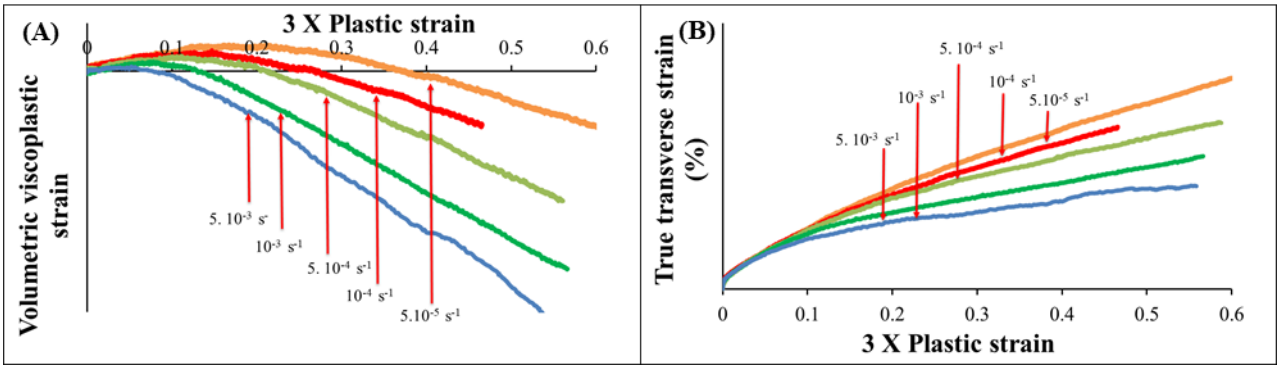

Figure 3-16 (A) Experimental calculation of hydrostatic pressure coefficient for PPC (B) True transverse strain vs. 3P for PPC

3.9 Procedure for the identification of isotropic hardening parameters using a 3D identification tool

The isotropic hardening curve is represented by the Equation (17)

$$R_F = R + Q_1(1 - e^{-B_1 P}) + Q_2 (1 - e^{-B_2 P}) \quad (17)$$

Constants *Q1, Q2, B1, B2, K, N* from Equation (17) and Equation (12) should be found using 1D optimization. Multiple tests comparing numerical simulation results and experimental curves concluded that: 1D optimization is not sufficient to identify the parameters of the 3D constitutive model. Therefore, the 3D optimization tool and protocol are discussed as follows.

3.9.1 Dakota

- In order to do optimization, software called DAKOTA [140] is used. The Dakota project delivers both state-of-the-art research and robust, usable software for optimization. Broadly, the Dakota software's advanced parametric analyses enable design exploration, model calibration, risk analysis, and quantification of margins and uncertainty with computational models. In addition, the Dakota toolkit provides a flexible, extensible interface between such simulation codes and its iterative systems analysis methods, which include: optimization with gradient and non-gradient-based methods;
- Uncertainty quantification with sampling, reliability, stochastic expansion, and epistemic methods;
- Parameter estimation using nonlinear least squares (deterministic) or Bayesian inference (stochastic); and
- Sensitivity/variance analysis with design of experiments and parameter study methods.

These capabilities may be used on their own or as components within advanced strategies such as hybrid optimization, surrogate-based optimization, mixed integer nonlinear programming, or optimization under uncertainty [140].

DAKOTA version 6.10 and Abaqus® 2017 with Python 3.7.3 are used for this part.

The detailed workflow of DAKOTA during the optimization loop can be observed in Figure 3-18. A standard input file (.in) must be provided to DAKOTA, which contains the type of optimization methods (Ex: gradient-free/Genetic algorithm or gradient-based/Least-square method), parameters initial values, bounds, interface with simulation codes, and the number of objective functions (calibration terms) to minimized should be defined inside this. An example of an input file for the "non-linear least square (nl2sol)" method is shown below:

```
************************DAKOTA Input File*****************************

environment,
        tabular_graphics_data

method,
        nl2sol
        max_iterations = 100
        absolute_conv_tol = 1e-1
        convergence_tolerance = 1e-1
        #function_precision = 1e-5
        output quiet

variables,
        continuous_design = 6
        cdv_initial_point =  9.8061 4.867  78.42  16.16  18.95  4.28
        cdv_lower_bounds  =  0  -300  0  0  10  0
        cdv_upper_bounds  =  300  300  100  100  100  10
        cdv_descriptor    =  'Q1'  'Q2'  'B1'  'B2'  'COEFK'  'COEFN'

interface,
        fork,
        parameters_file = 'params.in'
        results_file    = 'results.out'
        analysis_driver = 'abaqus.sh'
        file_save
        work_directory named 'work'
        dir_save
        dir_tag
        copy_files 'Template/*'

responses,
        calibration_terms = 99
        numerical_gradients
        interval_type central
        method_source dakota
        fd_gradient_step_size = 0.001
        no_hessians
```

3.9.2 Modeling of the tensile test sample in Abaqus®

Modeling of the tensile test has been done in Abaqus®. Just 1/8th part of the gauge length is considered in order to reduce the time of the simulation. Partition is done according to real markers' position during the tensile test experiments. The geometric properties of the tensile test sample have been shown in Figure 3-17 (A). X, Y, and, Z-symmetry boundary conditions are represented in Figure 3-17 (B), (C) and (D) respectively. The displacement rate corresponding to experiments is applied in order to impose a constant true strain rate on the top face of the sample as shown in Figure 3-17 (E). Non-linear displacement rates have been imposed to get linear constant true longitudinal strain same with respect to experiments. During simulation, the C3D20 element is used for meshing purposes. Six different models with corresponding displacement rates have been created in Abaqus®.

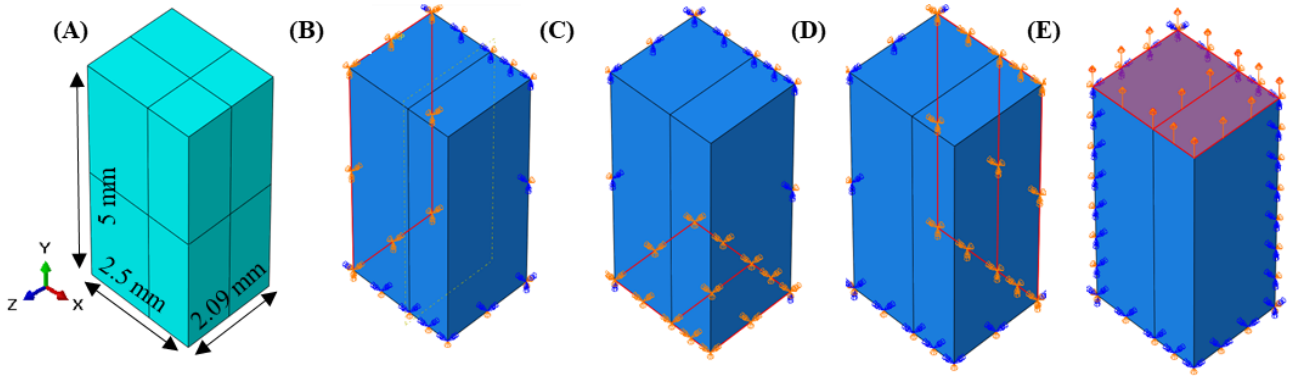

Figure 3-17 (A) Geometrical dimension of the tensile test sample, Boundaries conditions applied during simulation of tensile test (B) X-symmetry (C) Y-symmetry (D) Z-symmetry (E) Imposed displacement

3.9.3 Identification loop for PE

After completion of modeling, the author has obtained 6 input files from Abaqus® which contain 6 constants Q_1,B_1, Q_2, B_2 from Equation (17) and K, N from Equation (12) for which optimized values are to be found. Initial values have been taken from 1D dimensional optimization. DAKOTA fork is connected with a python script ("dako_to_aba.py") to Abaqus®. This file interacts with DAKOTA and contains calling the functions which are defined in another script called "identAba.py". Initially, DAKOTA starts by giving initial values of 6 constants to the python script "dako_to_aba.py". According to the definition of functions in python script "identAba.py" Abaqus® job gets launched. Using Abaqus® solver and according to the constitutive model definition in UMAT, the job gets completed. Once .odb files are generated then true stress vs. strain data is extracted from it, using the function defined in python script "identAba.py". After calculating relative error by comparing experimental and simulation values of true stress vs. strain, the objective function is created that goes back to DAKOTA to minimize it. DAKOTA selects new guess points based on the objective function

and the loop goes on, if the objective function reaches 0.01 tolerance it stops. The same has been represented in Figure 3-18 (A) and (B).

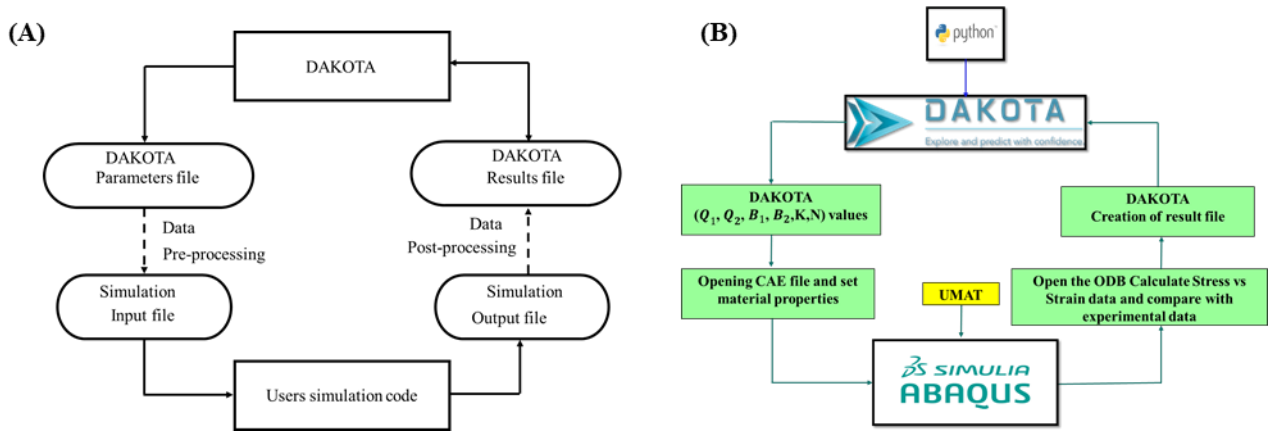

Figure 3-18 (A) "Black-box" interface between Dakota and a user-supplied simulation code [140] *(B) Integration of DAKOTA with Abaqus®*

3.9.4 Identification loop for PPC

The identification loop of PPC is similar to PE. Different points are only discussed here. Q_1,B_1, Q_2, B_2 from Equation (17), K, N from Equation (12), and A_1, A_5, and, A_9 from Equation (15) are to be identified using a 3D identification loop. For the construction of the objective function along with true longitudinal stress vs. longitudinal strain data, transverse strain experimental and simulation data are compared absolutely to construct the objective function.

3.10 Identification results of Young's modulus and hydrostatic pressure coefficient as a function of equivalent true strain rate for PE

It is important to note that this part is taken from the article that is submitted for publication to the International Journal of Mechanical Sciences. In Figure 3-19 (A) and (B), the black dots represent the experimental values, and the red curves are the fitted curve defined by Equation (8) and Equation (14), respectively. Matlab® has been used to determine the constants present in these two equations and is sufficient to optimize. It can be seen clearly that there is good agreement between experimental and optimized values. Due to confidentiality, values on the Y-axis are not presented. In addition, two experimental points are out of scope due to the difficulties of measuring true transverse strain during the experiments. They have been kept for the sake of completeness.

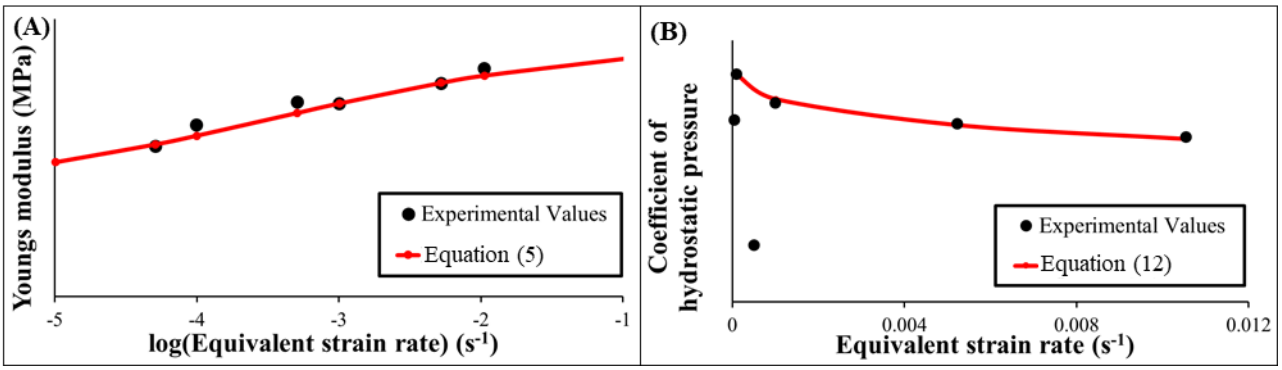

Figure 3-19 (A) Young's modulus and (B) Hydrostatic pressure coefficient vs. equivalent strain rate curve fitting

3.11 Identification results of Young's modulus as a function of equivalent true strain rate for PPC

In Figure 3-20, the black dots represent the experimental values, and the red curves are the fitted curve defined by Equation (8). It can be seen clearly that there is good agreement between experimental and optimized values. Due to confidentiality, values on the Y-axis are not presented.

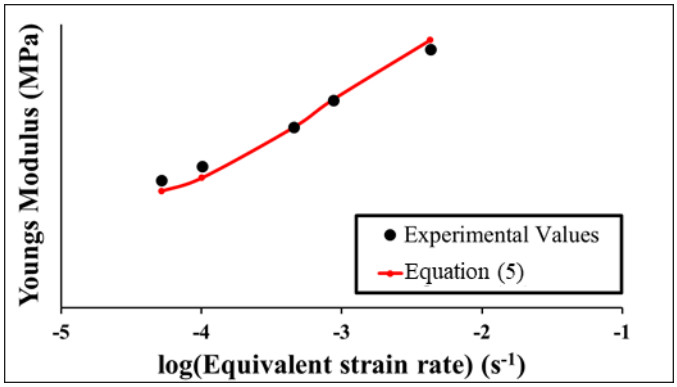

Figure 3-20 Experimental and simulated Young's modulus vs. equivalent strain rate, curve fitting

3.12 Identification of viscoplastic behavior in function of equivalent true strain rate (PE)

It is important to note that this part is taken from the article that is submitted for publication to the International Journal of Mechanical Sciences. A comparison of experimental and simulation results (after identification) of true stress vs. true longitudinal strain for different constant strain rates is represented in Figure 3-21. All the below results are obtained when the identification loop provided optimal values for the constitutive model. Experimental and simulation results are in good agreement. 99 points are selected to do optimization for each curve, average relative errors for each strain rate 10^{-2}, 5.10^{-3}, 10^{-3}, 5.10^{-4}, 10^{-5}, 5.10^{-5} (s^{-1}) are 0.97 %, -

0.024%, -2.193%, 0.049%, 1.89% and 5.57% respectively. Also, it can be observed that at 10^{-3} s^{-1} strain rate simulation result is below the experiment curve also explained by the fact that relative error ((simulation value – experimental value) / experimental value) is -2.193%, but on the other hand, at 5. 10^{-5} s^{-1} strain rate simulation result is above the experiment curve that gives evidence as to why relative error value is positive. Norton's law for describing strain rate sensitivity is relatively poor, but the comparison shows abilities that are considered are sufficient.

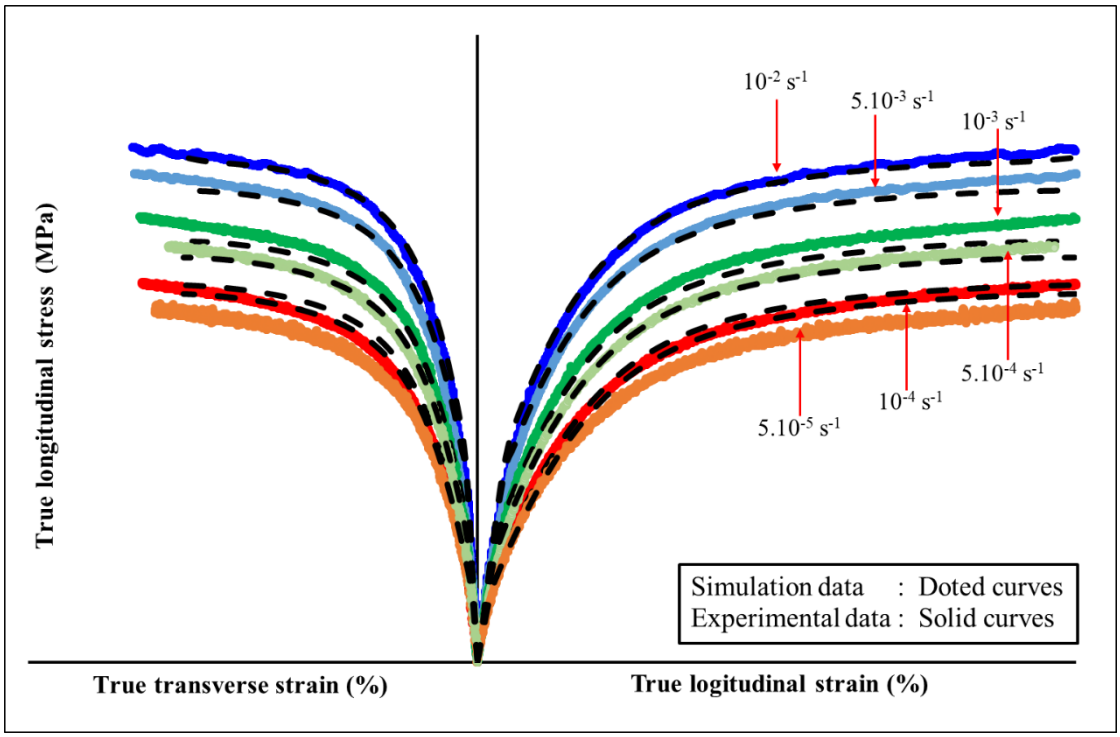

Figure 3-21 Comparison of experimental and simulated tensile test results for constant true strain rate (PE)

The relatively good correlation with true transverse strain is due to the identification protocol that considers the transverse strain at a constant longitudinal strain rate. The elastic part is taken care of by a constant Poison's ratio. On the other hand, the hydrostatic pressure coefficient performed a crucial role in the plastic part for simulation. This optimization permits matching experimental true transverse strain results, which should be accurately measured. This last point is not easy to perform.

3.13 Identification of viscoplastic behavior in function of equivalent true strain rate (PPC)

A comparison of experimental and simulation results (after identification) of true stress vs. true longitudinal strain for different constant strain rates is represented in Figure 3-22. All the below results are obtained when the identification loop provided optimal values for the constitutive model. Experimental and simulation results are in good agreement.

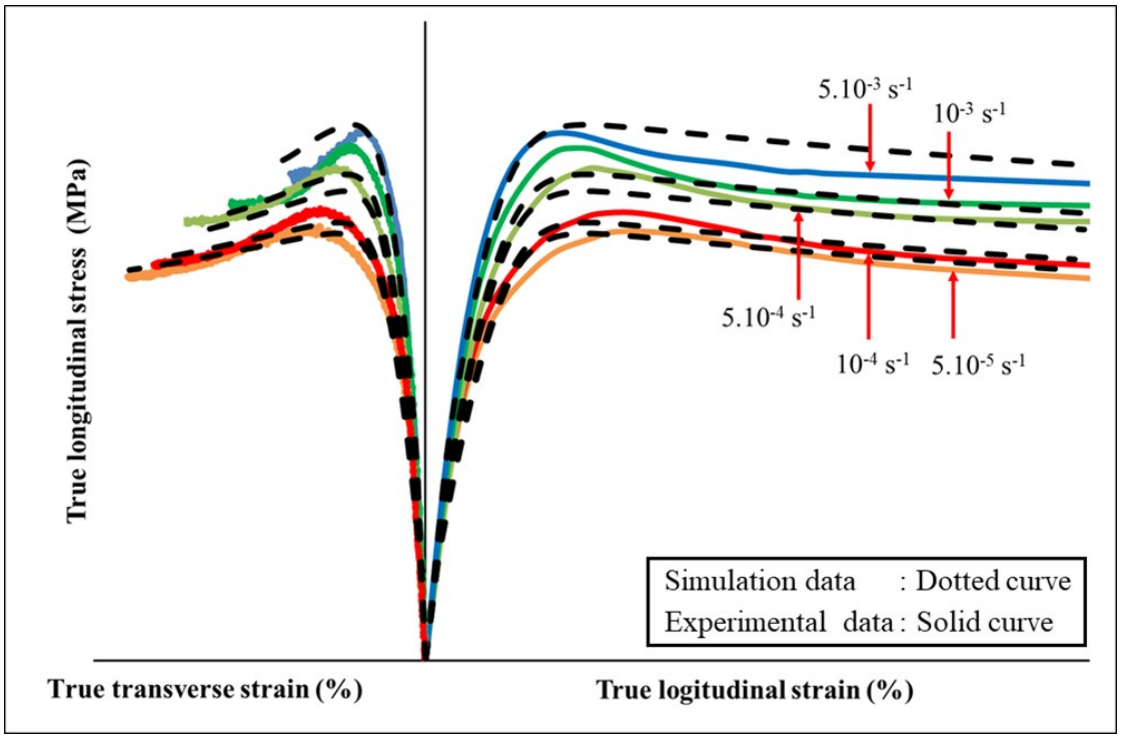

Figure 3-22 Comparison of experimental and simulated tensile test results for constant true strain rate (PPC)

3.14 Validation of a constitutive model for PE

In this part, the predictive capacity of the constitutive model is tested to identify its limitations and shortcomings in strain rate domains similar to the identification but slightly more complex strain paths.

As previously presented 3PB and 4PB tests are used to assess the difference between tension-compression and transverse shear contribution. In addition, as different thicknesses are tested, the possible effects of the process (core-skin effect - crystallization) have been evaluated on a macroscopic scale.

Then a test on a structure under internal pressure generating biaxial stresses allows for demonstrating the extended possibilities of the model. This part is the subject of an article submitted.

3.14.1 Presentation of models for the correlation with 3PB and 4PB tests at different thicknesses of samples

It is important to note that this part is taken from the article that is submitted for publication to the International Journal of Mechanical Sciences. Two symmetry assumptions are made to simulate the 3PB and 4PB tests and reduce computation time, which allowed for representing only one-quarter of the sample. As shown in Figure 3-23 (A) and (B), these two symmetries are along the X and Z-axis. For each configuration (nominal thickness), the geometry of 3PB and 4PB test specimens are defined by their measured dimensions defined in Table 3-5 and

Table 3-6, respectively. Figure 3-23 shows that the rollers on top are moving, whereas the ones at the bottom are kept fixed. The same displacement rates as the experiment mentioned in Table 3-5 and Table 3-6 are imposed on a moving roller. R3D4 elements are used for roller in order to do meshing. A higher element density is used for both parts at the point of contact between the roller and the plate. This mesh density is identical for both parts to improve contact management, especially in the initial state. Where there is no contact, a lower density of elements has been considered in the sample. C3D8 and C3D20 elements are tested for meshing. Convergence of mesh is also studied. By choosing the load as a criterion, the comparison of the results of the different numerical simulations showed no significant difference in the values. The differences are less than the measurement accuracy. In addition, the total simulation time with C3D20 elements is significantly higher. Thus, the CPU times for the simulation of a 3PB test for a 2 mm specimen and a total displacement of the movable support of 20 mm with C3D8 elements (6240 nodes) and C3D20 elements (23342 nodes) are 1.35 hours and 5 hours, respectively. It can be observed that in this case, the simulation time is almost ~3.7 times higher. Thus, obtaining almost the same results in a shorter time led to using the C3D8 element. Finally, all models include four elements in the thickness for the simulation of 3PB and 4PB tests. Table 3-8 gives the number of elements and nodes for each mesh for the finite element calculation according to the bending mode and the thickness of the specimen.

Bending	Nominal Thickness of sample (mm)	C3D8	
		Number of elements	Number of nodes
3PB	2	4700	6240
	4	7072	9315
	6	7800	10270
	8	9300	12220
4PB	2	7300	9620
	4	11800	15470
	6	12800	16770
	8	13800	18070

Table 3-8 Number of elements and nodes for each mesh

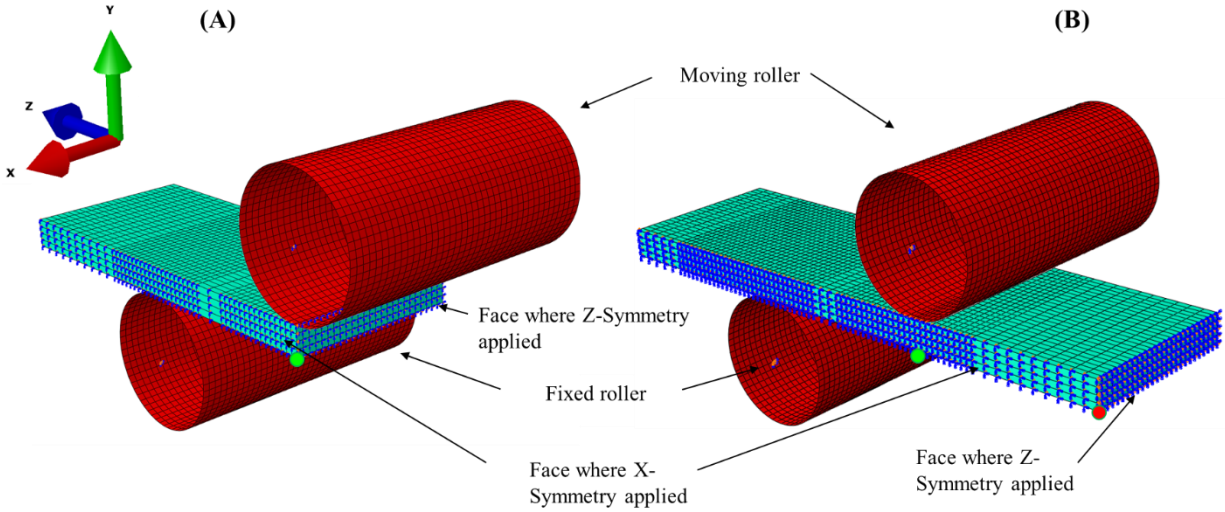

Figure 3-23 Modeling of (A) 3PB and (B) 4PB test in Abaqus® (PE)

3.14.2 Comparison of experiments with numerical simulation in bending

It is important to note that this part is taken from the article that is submitted for publication to the International Journal of Mechanical Sciences.

3.14.2.1 Different solutions with different friction coefficients

All the simulations have been performed with different friction coefficients (FC) in the range of 0.25 to 0.5. Overall, the influence of this parameter on numerical curves is relatively tiny in the 3PB tests (Figure 3-24 (A) and (B)) and more important in the 4PB tests (Figure 3-24 (C) and (D)). The friction coefficient affects the maximum force and its corresponding displacement recorded during the test. In the case of the 3PB tests, the effect is close to the variability of tests. It is not the case for the 4PB tests, where the curve's maximum increases to 30% when the coefficient changes in the investigated range.

The friction coefficient of 0.25 gives the best results for the sample's 2 and 4 mm thickness. On the other hand, the friction coefficient of 0.4 gives the best results for 6 and 8 mm samples. However, the simulation purpose is 0.3 as it gives almost good results for all thicknesses in 3PB and 4PB tests in almost ± 5% variation (Figure 3-24 in grey color) of experimental results. Furthermore, samples are extracted from the bottle, and surface roughness is not uniform on the bottle's surface, which results in a variation of friction coefficient for the best results of simulation compared with experimental results.

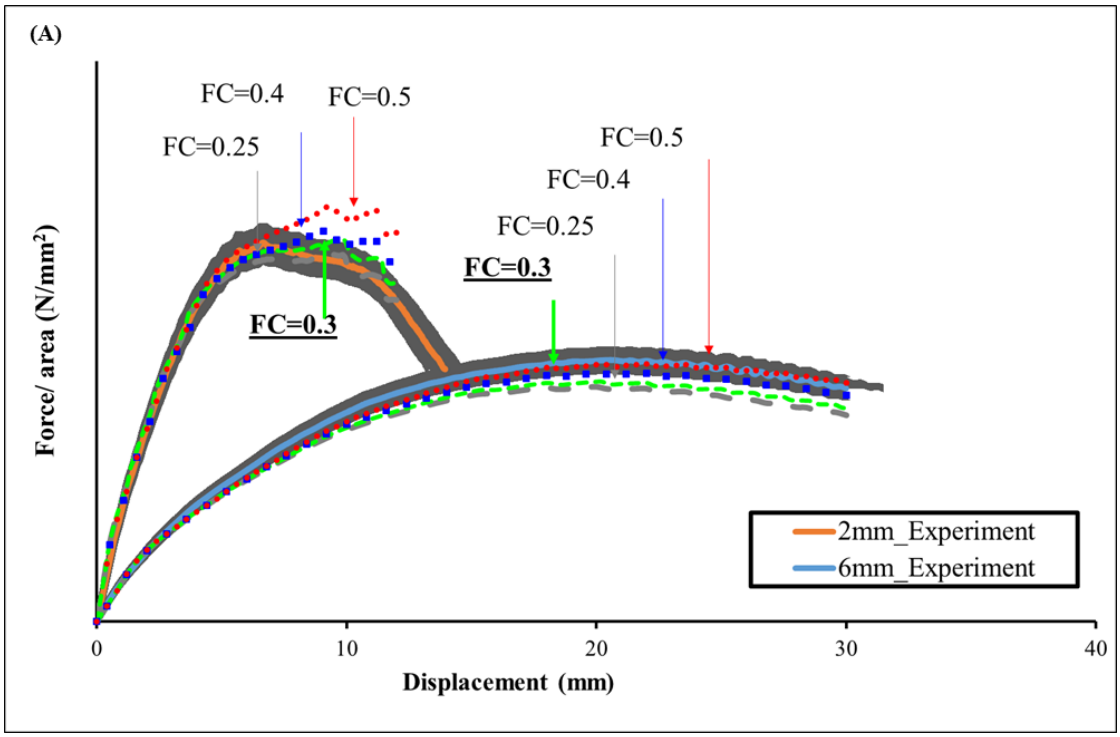
(A)
FC=0.4
FC=0.5
FC=0.25
FC=0.5
FC=0.4
FC=0.25
FC=0.3
FC=0.3
Force/ area (N/mm²)
2mm_Experiment
6mm_Experiment
0
10
20
30
40
Displacement (mm)

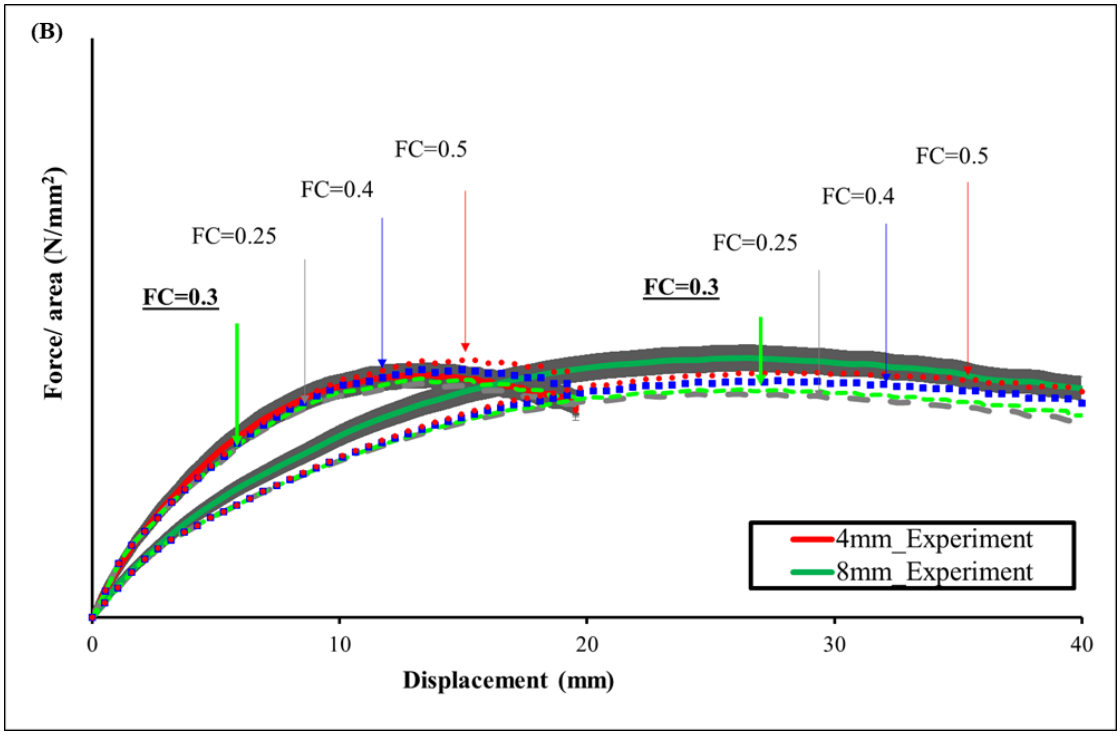
(B)
FC=0.5
FC=0.4
FC=0.5
FC=0.4
FC=0.25
FC=0.25
FC=0.3
FC=0.3
Force/ area (N/mm²)
4mm_Experiment
8mm_Experiment
0
10
20
30
40
Displacement (mm)

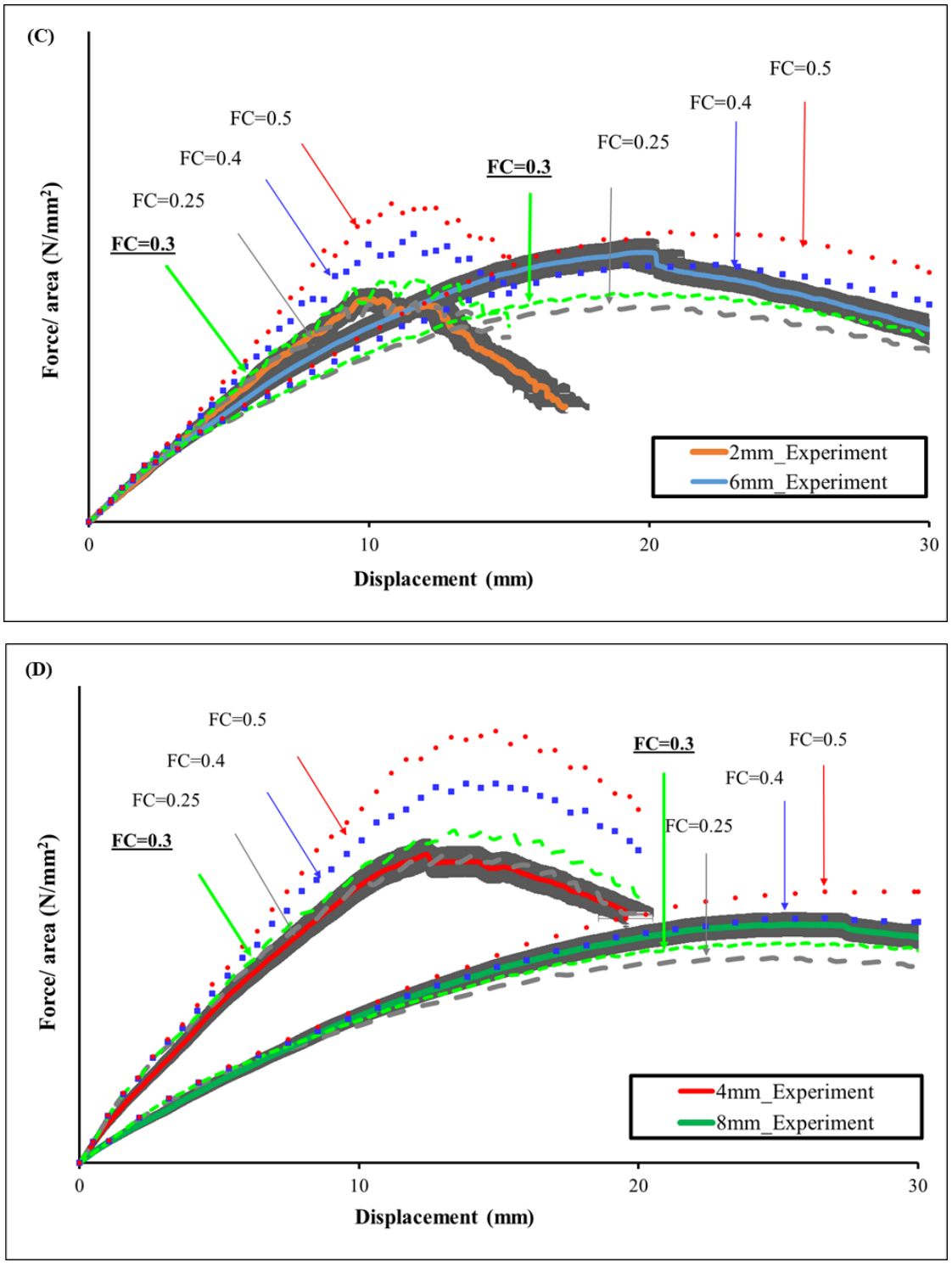

Figure 3-24 Influence of friction coefficient (FC) - Comparison of experimental and numerical the force per unit area of the cross-section measured vs. crosshead displacement in 3PB test for thicknesses of (A) 2 mm and 6 mm and (B) 4 mm and 8 mm and in 4PB test for thicknesses of (C) 2 mm and 6 mm and (D) 4 mm and 8 mm

3.14.2.2 Strain rate and strain verification

Figure 3-25 (A) and (B) show the variation of true strain rate along with Z-axis vs. imposed displacements during 3PB and 4PB tests, respectively. Different solid curves represent the

true strain of the node at the bottom of the point of contact (Green dots in Figure 3-23) for different thicknesses of samples for bending tests. Figure 3-25 (C) and (D) show equivalent strain rates vs. imposed displacements during 3PB and 4PB tests, respectively. In Figure 3-25 (D), the suffix "Sym" represents the equivalent strain rate at the point of symmetry (Red dots in Figure 3-23). The objective of showing equivalent strain rates in two different locations is to show that variation is more at the bottom of the point of contact. It can be seen clearly in Figure 3-25 (C) and (D) that the equivalent true strain rate is well within the strain rate used for the identification because no equivalent strain rate is going beyond the maximum range, which has been used for identification that is 10^{-2} s^{-1}. That might be one of the reasons why 3PB and 4PB test results are in good agreement with the experimental data.

In the standard European NF EN ISO 178 [129], the distances between rollers and rate displacement imposed are chosen to fix the center longitudinal strain rate. Unfortunately, the tests carried out do not follow this rule due to technical difficulties, and hence results differ between them. To validate the standard, simulations with corrected imposed displacement rate, consistent with the norm, 2.66 10^{-2} and 5.33 10^{-2} $mm.s^{-1}$ for 4 and 8 mm thickness samples, respectively, in 4PB test have been performed, and results are shown by dotted curves in Figure 3-25 (B) (Doted dark blue and green curves respectively). With this rule, the Z-direction strain rate has the same level for 4, 6, and 8 mm and slightly decreases but keeps at the same level. The response is very close to 3PB tests.

For the 2 mm specimen in 4PB test, the problem is different. The distance between the roller generates shear stress, the field inside the specimen is very close to 3PB test ones. This is the reason why the 2 mm response curve is below the others. Consequently, reducing the distance between the moving rollers is necessary to generate bending field stress (the distance between the fixed and moving rollers is 40 and 20 mm, respectively). In Figure 3-25 (B) the curve 2mm-modified gives the equivalent strain rate, which increases compared to other thicknesses. The norm is challenging to apply for 2 mm samples, but these simulations with this behavior confirm the role of setup.

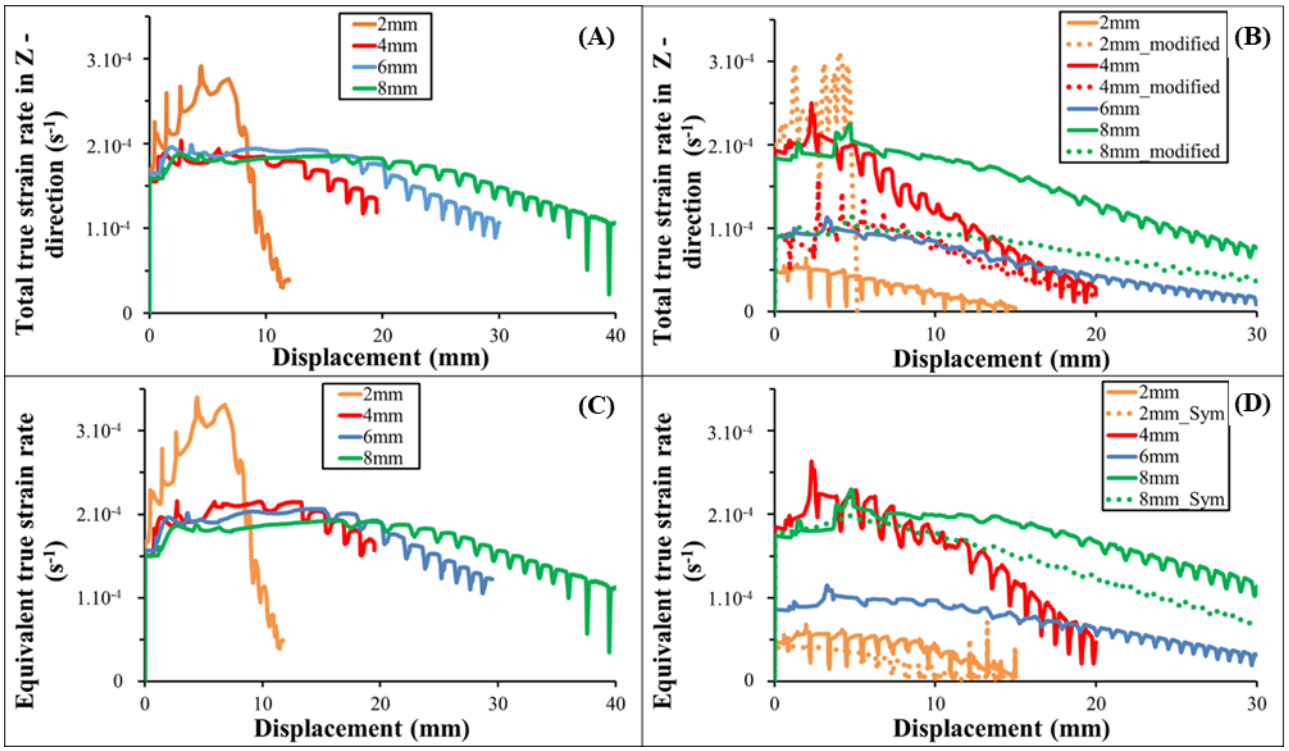

Figure 3-25 True strain rate variation in Z-direction vs. displacement (A) 3PB test of 2, 4, 6, and 8 mm sample (B) 4PB test of 2, 4, 6, and 8 mm sample - Equivalent true strain rate vs. displacement (C) 3PB test of 2, 4, 6 and 8 mm sample (D) 4PB test of 2, 4, 6 and 8 mm sample

3.14.2.3 Discussion on comparison

Colors curves are shown in Figure 3-26 (A), and Figure 3-26 (B) plotted between force per unit area of cross-section and displacement imposed on moving roll, measured during experiments on all samples with different nominal thicknesses. Two or three specimens are tested for one nominal thickness, depicted through colored lines in Figure 3-26, which permit realize the variability of experiments. Black color dotted curves represent simulation results of each nominal thickness. Figure 3-26 indicates that simulation and experimental results are very close; the difference has the same level compared to the variability of experiments. During simulation, the friction coefficient used is 0.3. As explained above, the ratio of displacement rate to thickness is different for 4 and 8 mm samples of 4PB tests compared with other examples. Same as experiments, all the parameters applied to simulation and results complement each other, which gives weight to the above constitutive model.

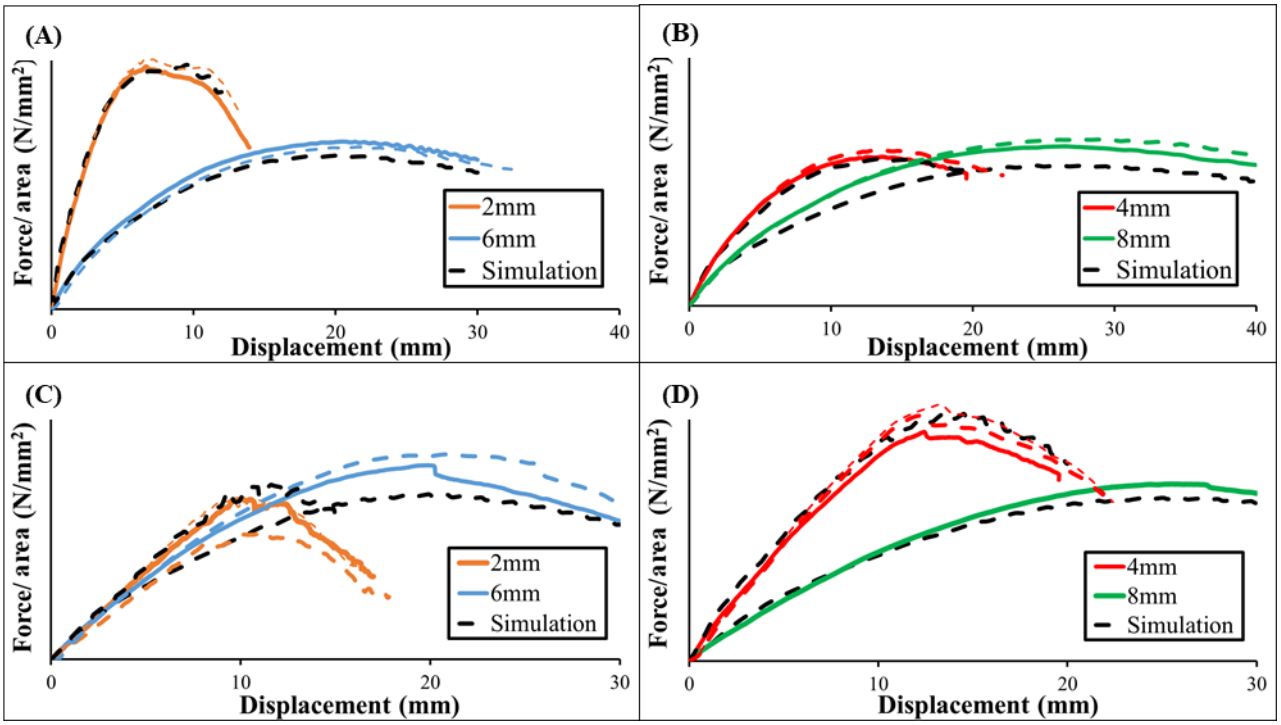

Figure 3-26 Comparison of experimental and simulation, (with coefficient friction at 0.3) the force per unit area of the cross-section measured curves vs. crosshead displacement in 3PB tests for thicknesses of (A) 2 mm and 6 mm and (B) 4 mm and 8 mm and in 4PB tests for thicknesses of (C) 2 mm and 6 mm and (D) 4 mm and 8 mm

During 3PB and 4PB tests, the model can consider the strain rate effect. It is important to note that this model is valid for strain rates between 5.10^{-5} to 10^{-2} s^{-1} as this is the range for which material constants are found. During simulation, it is observed that the strain rates are well within the range of strain rates used for experimental tensile tests, and the maximum true strain is around 20% in bending.

The compressive strain range is from 3.27% to 19.35% for the 3PB and 4PB tests. The shear strain range is 9.4% to 20.75% for the 3PB and 4PB tests. It is given evidence to conclude that this model is valid till approximately 20% of tensile, compressive, and shear strain.

It is essential to highlight the assumption made on yield stress. In order to consider the non-linearity at the beginning, a less yield stress value of 1.5 MPa, is necessary to consider here. If yield stress is chosen as 4.5 MPa, the model implies a linear behavior until 4.5 MPa, and it does not reflect the experimental observations.

These results show that the thickness does not influence the bending response, the process must generate microstructures very close to each other, or the skin effect is of second-order and is expressed at a level below the experimental variability, the model permits a predictive simulation with the condition to ameliorate the information of coefficient friction.

The tensile tests with measurement of transverse strains might be enough to identify hydrostatic pressure parameters in this range of stains and strain rate effects, which permits building an effective constitutive model.

Another interesting point is the effect of thickness, the constitutive model accounts for the bending response of all samples from 2 to 8 mm thick. This suggests that either the microstructures are very close for the different thicknesses, or the microstructure variations are of second-order on the macroscopic response. In any case, they are less than the variability of the geometry which if not defined precisely enough, discrepancies between simulations and experimental measurements appear.

3.15 Verification of capabilities of the constitutive model of PE

3.15.1 Presentation of models for the correlation with rotational molded structure (Bottle) under internal pressure

To evaluate the model's capability, the structure choice is a rotational molded bottle, and it is subjected to internal hydrostatic pressure. In order to compare experimental and numerical results, it is essential to model in the numerical tool the most realistic geometry of the bottle possible. Thus, this is obtained using tomography (Figure 3-27 (A)). In order to reduce the time of the simulation, a strong assumption is made. Two symmetries are considered, representing only a quarter of the bottle. However, measurements made in the thickness at different locations of the bottle (height) from the tomographic images show that this assumption is entirely acceptable, and the variation in the kinetic response of the bottle under pressure is second-order. For the loading in the simulation, the same pressure amplitude as in the experiments is applied as internal pressure (Figure 3-27 (B)). Partitions are created using a reference plane, and the intersection of the planes represents the position of the markers (red dots) on the tested bottle (Figure 3-27 (C)). Finally, the structure is meshed using C3D20 elements (as for bending). There are 2639 elements (Figure 3-27 (D)) and 15626 nodes, including one element in the thickness. Before, it is pointed out that linear and quadratic elements give close results; however, in the case of the bottle, strong curvatures must be geometrically represented, and for this reason, it is chosen elements with higher geometric interpolation degrees. The support on which the bottle rests is considered non-deformable, so a rigid analytical surface models it. Following the bending study, the contact between the support and the bottle is considered with a friction coefficient of 0.3.

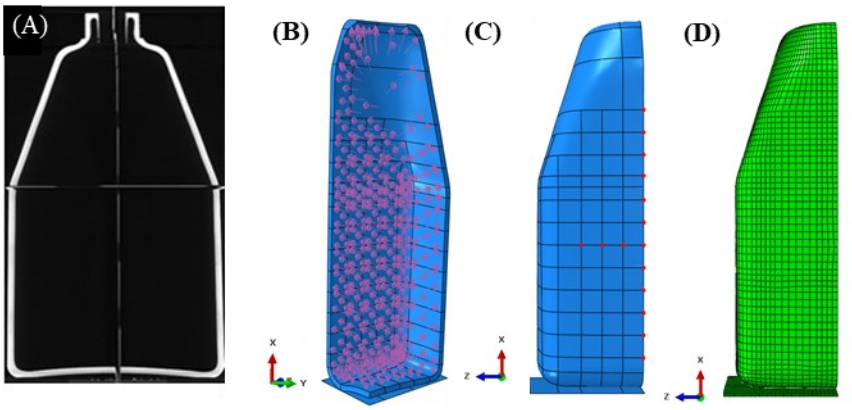

Figure 3-27 (A) Tomographic image of the bottle section (B) Application of internal pressure on a quarter of the CAD model (C) Partitions of the structure to geometrically locate the markers (D) Mesh of the bottle

It is important to note that these tests are carried out by E. Lainé and the measurements by J-C Dupré.

3.15.2 Discussion on comparison

To complete the validity of the model, it is tested on a complex structure submitted to hydrostatic pressure, which generates biaxial tension stress and double curvature bending. This constitutes a state of stress very different from that of traction.

During this pressure test, the bottle is connected to the water supply system by its closure and is in contact with a plate at its base. The distance between the plate and the nozzle is kept constant. Consequently, when internal pressure is applied to the bottle, the bottom surface of a bottle creates a reaction represented as load. The contact evolves during the test, and the simulation considers this phenomenon and calculates the reaction. Figure 3-28 (A) and (B) show the variation of load (blue curve) and maximal bottle swelling (green curve) vs. internal pressure for the bottle in the loading and loading-unloading scenario, respectively. Solid curves correspond to numerical results and circles to the experimental curve. Experimental and simulation results agree with each other hence it can be concluded that the constitutive model can represent the behavior of the bottle when internal pressure is applied. The numerical curves of the unloading do not present hysteresis because the model is identified without integrating this phenomenon (reduced viscosity and no consideration of kinematic hardening). Despite this strong assumption, the average unloading path is correctly observed in the results.

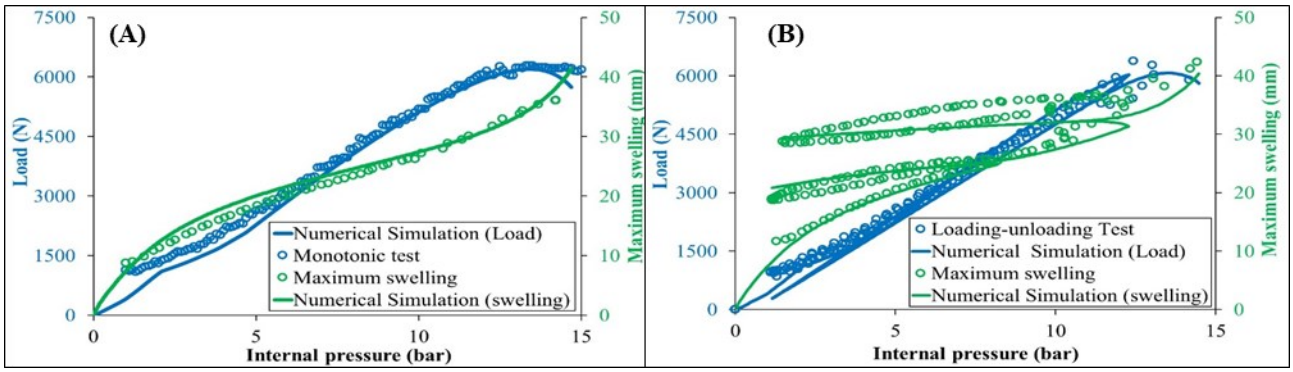

Figure 3-28 (A) Load (blue) and maximum swelling (green) vs. internal pressure curves in monotonic pressure and (B) Pressure loading-unloading tests (dotted) and corresponding simulations (continuous lines)

During the monotonic loading experiment, the displacement of the markers is tracked. In the definition of geometry, specific partitions are created to fix the position of nodes corresponding to the localization of markers. Comparison of experimental displacement in the Y-direction of markers (Red color points in Figure 3-27 (C)) present in horizontal and vertical directions of a bottle with simulation results are represented in Figure 3-29 (A) and (B) respectively. Orange, red, and blue color dots represented the displacement of markers when internal pressure is 2, 5, and 10 bar, respectively. Experimental and simulation results are almost overlapping. This gives weight to the conclusion that the constitutive model can describe the behavior of a bottle when internal pressure is applied to it.

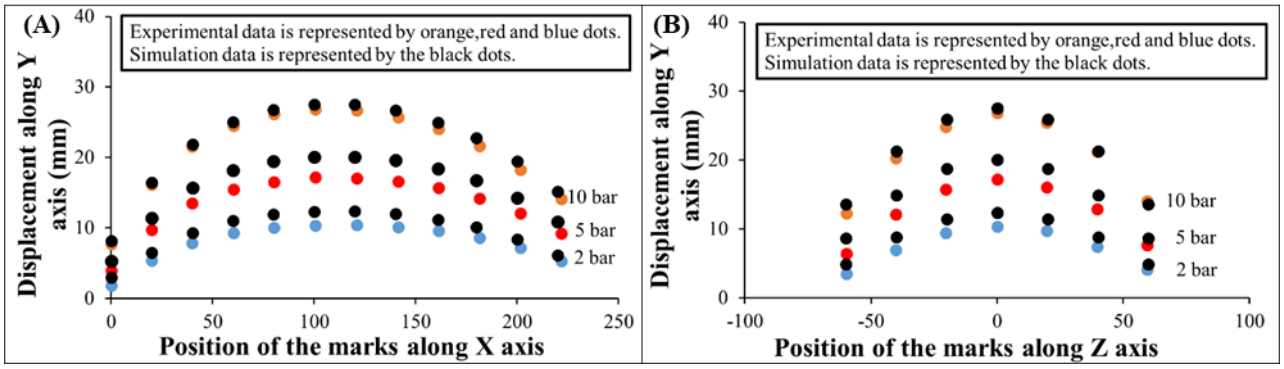

Figure 3-29 Displacement along Y-axis of markers (A) Along X-axis (vertical direction of a bottle) (B) Along Z-axis (horizontal direction of a bottle) at a different internal pressure

The stress field components in the X and Z-directions at 7.5 bar pressure (Figure 3-30 (A) and (C)) have the same level in the central part of the bottle, indicating that the structure is under biaxial stress; the stress in the Y-direction (thickness) is lower. At 7.5 bar pressure (Figure 3-30 (A) to Figure 3-30 (D)), a gradient of all stress components in the perpendicular direction of the corner is observed. For all the stress components at pressure of 15 bar (Figure 3-30 (F) to (I)), the gradient near the edge of the central part of the bottle localizes and intensifies.

At the end of the loading (Figure 3-30 (F) to (I)), the stress localization is visible in a zone close to the corner in the central part; the stress state becomes strongly tri-axial with a non-

negligible shear (Figure 3-30 (I)). The curvature of the corners generates a gradient on a quarter of the sidewall. The loading is complex and very different from the cases used for the model identification. The hydrostatic pressure coefficient follows the same trend as the stress components during the loading (Figure 3-30 (E) and (J)). At 7.5 bar, the value of the coefficient is relatively homogeneous (Figure 3-30 (E)) on the flat face of the cylinder, and at 15 bar, it localizes close to the corner (Figure 3-30 (J)).

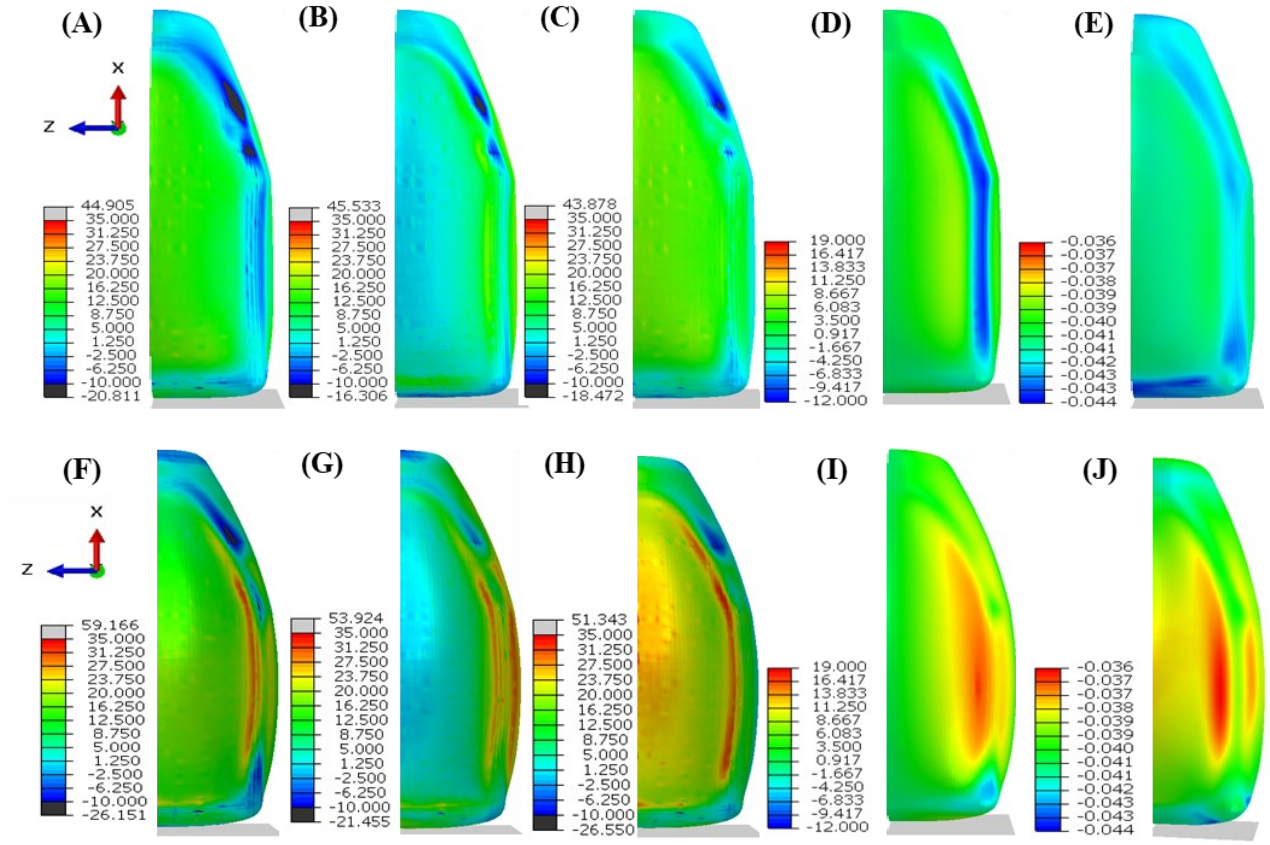

Figure 3-30 Fields of Cauchy stress (MPa) (A) Stress in X-direction (B) Stress in Y-direction (C) Stress in Z-direction (D) Shear stress in YZ plane (E) Hydrostatic pressure coefficient at middle step (pressure = 7.5 bar), Fields of Cauchy stress (MPa) (F) Stress in X-direction (G) Stress in Y-direction (H) stress in Z-direction (I) Shear stress in YZ plane (J) Hydrostatic pressure coefficient at end step (pressure = 15 bar)

Figure 3-31 shows the equivalent strain rate field during simulation inside the bottle. If the localization of the strain is found in agreement with that of the stresses, the position of maxima changes during the load. In the beginning, it is localized in the central part of the bottle (Figure 3-31 (A)); at the end, it is translated close to the corner (Figure 3-31 (B)). At these two points (the black dots represented in Figure 3-31 (A) and (B) evolution of equivalent strain vs. the internal pressure is plotted in Figure 3-31 (C). A very slight decrease can be observed after that an increase in the strain rates at the two considered points with a very strong acceleration for the point near the corner showing the localization. The rate is well within the range on the whole history of the load, which is used to find out material constant

in a tensile test. This also confirms that the selection of strain rate range for identification is sufficient.

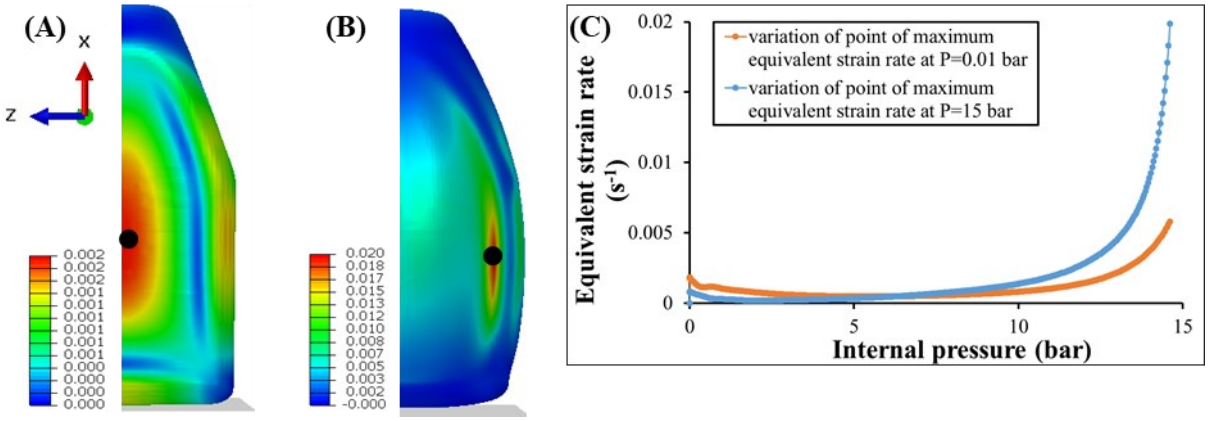

Figure 3-31 Field of equivalent strain rate (A) At 1st step of simulation (pressure =0.01 bar) (B) Last step of simulation (pressure = 15 bar). (C) Variation of point of maxima of equivalent strain rate at pressure = 0.01 bar and 15 bar

In Figure 3-32 (A), the failure mode is visualized with the help of a tomography close to one corner; a crack appears and propagates along with the bottle by following the lateral corner. When internal pressure increases after the limit point, the crack appears due to the local viscoplasticity instability generated by the reduction of a section. The shape used in the simulation considers the variability of thickness that permits localization of the strain easily. This scenario is in correspondence with the field of equivalent strain rate, plotted in regard to deformed structure in Figure 3-32 (B). The hydrostatic pressure field is negative and localized in the same area, spreading all along the corner (Figure 3-32 (C)). It is important to note that in the model, rupture criteria are not incorporated, but the model predicts the local necking, and it can be used to apply an onset criterion.

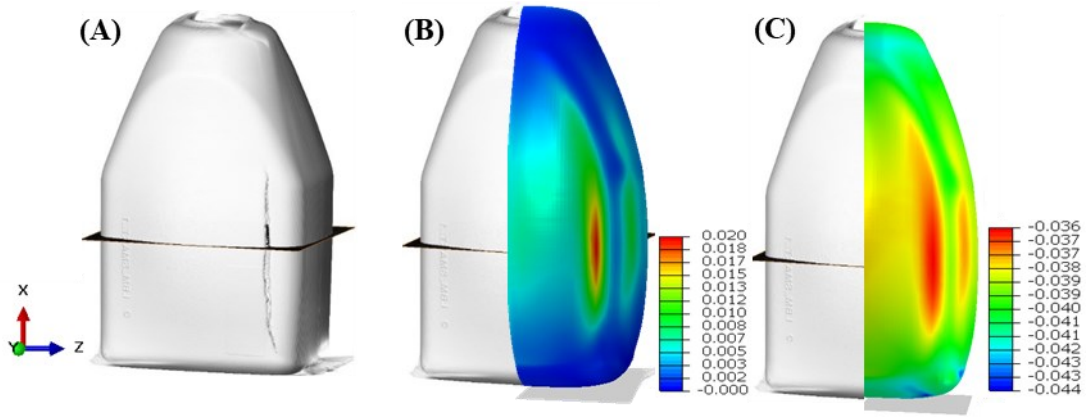

Figure 3-32 (A) Image of the bottle after rupture (reconstruction following tomography) superimposed (B) On equivalent strain rate field and (C) On hydrostatic pressure from the simulation at a pressure of 15 bar

3.16 Validation of a constitutive model for PPC

3.16.1 Presentation of models for the correlation with 3PB and 4PB tests at different thicknesses of samples

Two symmetry assumptions are made to simulate the 3PB and 4PB tests and reduce computation time, which allowed for representing only one-quarter of the sample. These two symmetries are along the X and Z-axis, as shown in Figure 3-33 (A) and (B). For each configuration (nominal thickness), the 3PB and 4PB tests specimens are defined by their actual geometrical dimensions given in Table 3-7. As shown in Figure 3-33, the rollers on top are moving, whereas the ones at the bottom are kept fixed. The same displacement rates as the experiment mentioned in Table 3-7 are imposed on a moving roller. R3D4 elements are used for roller in order to do meshing. A higher element density is used for both parts at the point of contact between the roller and the plate. This density is identical for each part to improve contact management, especially in the initial state. Where there is no contact, a lower density of elements has been considered in the sample. For the meshing sample, C3D8 elements are used, the reason behind it is well explained in heading 3.14.1.

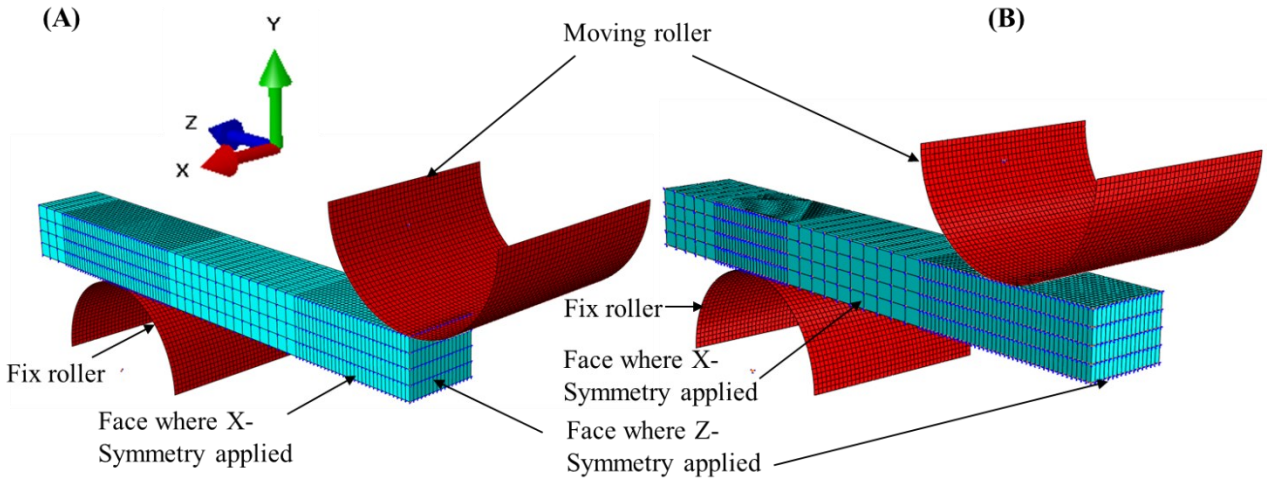

Figure 3-33 Modeling of (A) 3PB and (B) 4PB tests in ABAQUSs® PPC

3.16.2 Comparison of experiments with numerical simulation in bending

Colors curves are shown in Figure 3-34 (A) and (B) plotted between force per unit area of cross-section and displacement imposed on moving roll, measured during experiments. Black color dotted curves represent simulation results. It can be observed that simulation stopped in between.

As the simulation is stopped in between without going till the end. Faced with this situation, an extensive numerical study is carried out in order to identify the parameter that is at the origin of the problem. This point is the subject of the following paragraph.

Nevertheless, the simulated curves are in good order of magnitude.

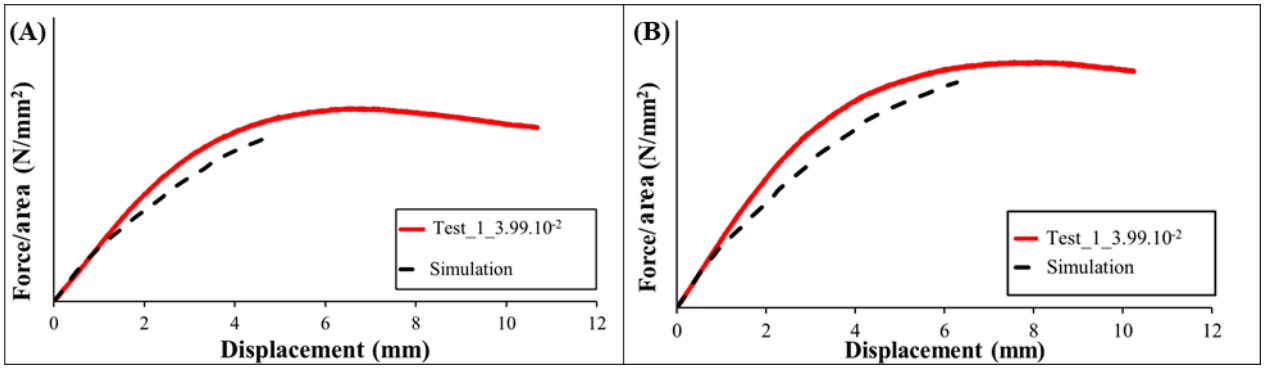

Figure 3-34 Comparison of experimental and numerical the force per unit area of the cross-section vs. cross-head displacement in (A) 3PB (B) 4PB tests

3.16.3 Analysis of simulation results

Several hypotheses have been put forward to explain the numerical problems, of which there are three:

- Due to contact in the simulation
- Due to element selection
- Due to the equation of hydrostatic pressure coefficient

One by one all the above reasons are studied. There is contact at two locations during the simulation. One is on the top of the sample and upper roller. The second is lower roller and sample. Instead of rollers, a direct displacement rate is imposed on the sample in order to eliminate the contact keeping everything the same. But again simulation stopped. That gives us concrete reason to conclude that the problem is not due to the contact.

Different elements are used for simulation by keeping other things the same. C3D8 -tetrahedron, C3D8-wedge, C3D20, C3D20R, C3D8R, C3D8I (incompatible mode to eliminate possible locking), and C3D8H (to eliminate volume locking) elements tested for simulation but the problem persisted. By using this it can be concluded that element is not a problem behind the termination of simulation in between.

The last possible solution is a complex equation of hydrostatic pressure coefficient that might be creating the problem. In order to resolve this one, the same different equation of it has been created as follows:

$$a = A_1 * 3P + A_2 \quad (18)$$

$$a = A_1 * (1 - \exp(-A_2 * 3P)) + A_3 * 3P + A_4 \quad (19)$$

$$a = ((A_1 + A_2 \left(1 + \tanh(\left(A_3 * \left(log10(\dot{\varepsilon_{eq}})\right)\right) + A_4\right) + A_5 \quad (20)$$

Simulation of a with individual equations and experimental values of a plotted vs. $3P$ for different strain rates in Figure 3-35. Dotted curves are showing the variation of a using different equation which has been created for testing. Solid curves show a variation of experimental data. Figure 3-35 (A) shows a variation of a using Equation (15) with $3P$ using. Figure 3-35 (B) shows a variation of a using Equation (18) with $3P$ using. Figure 3-35 (C) shows a variation of a using Equation (19) with $3P$ using. Figure 3-35 (D) shows a variation of a using Equation (20) with $3P$ using.

It can be observed from Figure 3-35, that the complexity of the equation has been increased gradually to locate the problem. It is important to note that these curves cross the abscissa at different values of $3P$, at this point of crossing the change contraction dilation appears.

In order to identify the numerical problem, the different evolutions studied are plotted in:

- Figure 3-35 (A): a nonlinear case with strain rate influence, the model used in simulations presented in Figure 3-34 (A) and (B),
- Figure 3-35 (B): linear case without strain rate influence high slope, this curve crosses the abscissa at low values of $3P$,
- Figure 3-35 (C): nonlinear case without strain rate influence,
- Figure 3-35 (D): a linear case with strain rate influence low slope, these curves cross the abscissa at high values of $3P$
- Figure 3-35 (E): a linear case with strain rate influence and a limit,
- Figure 3-35 (F): a bi-linear case with strain rate influence and a limit,

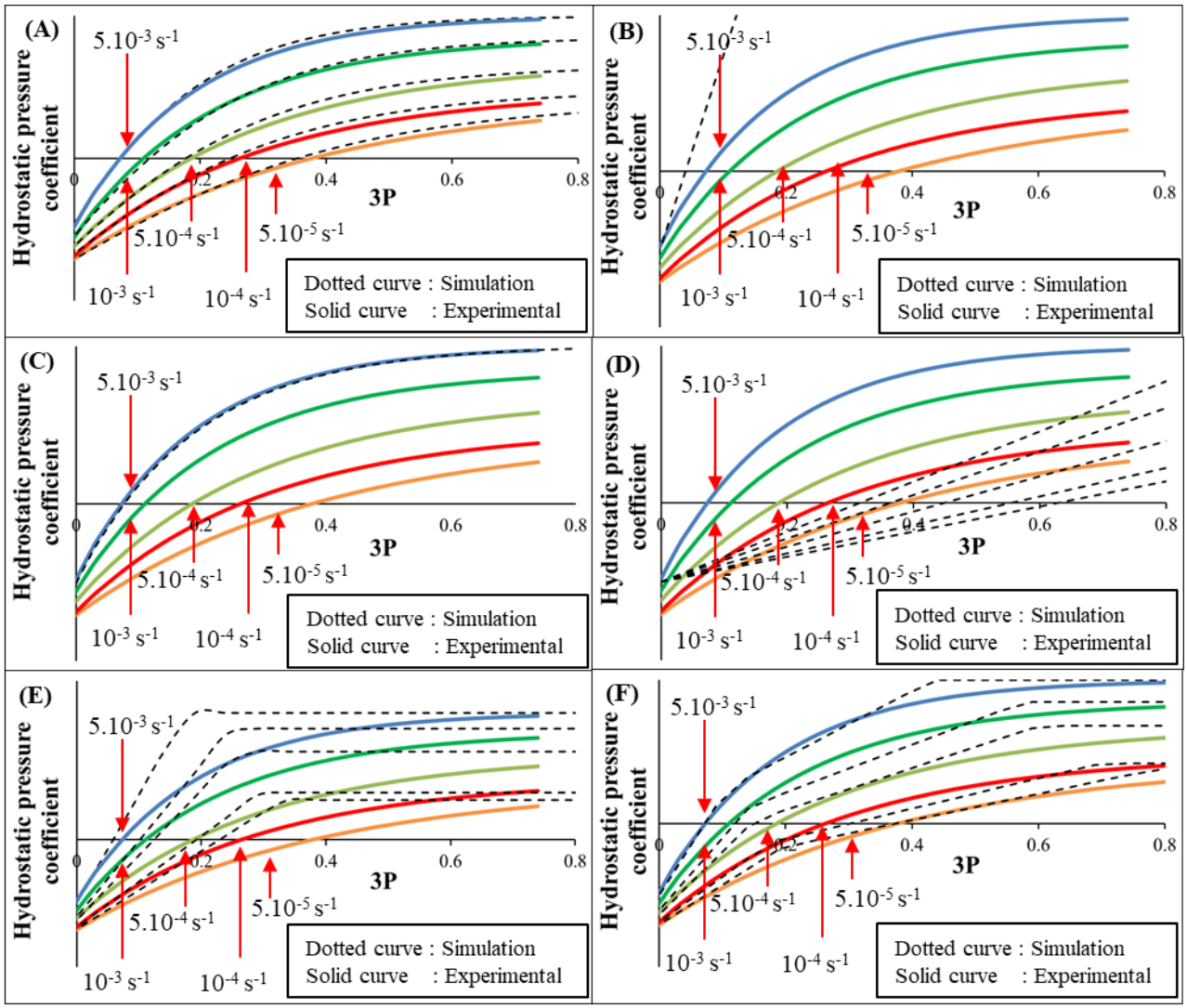

Figure 3-35 Representation of curves created by respective equations of hydrostatic pressure coefficient (A) to (F)

The different equations which are proposed for testing have been implemented in UMAT for the constitutive model. Figure 3-36 show variation in the force per unit area vs. displacement imposed during 3PB simulation. A solid curve is experimental data. Dotted lines are simulation data with an equation of curves of hydrostatic pressure coefficient represented in Figure 3-34. Figure 3 35 (A).

In a few cases, it is clear that simulation is going till the end, this result proves that problem is due to the expression of a. The challenge is to fine the hydrostatic pressure coefficient equation which is the more relevant to experimental data and permits to simulate the tests. In the same time, it is interesting to determine the parameter which generates the divergence.

Figure 3-36 (B) shows simulation results performed with hydrostatic pressure coefficient shown in Figure 3-35 (E) and (F). It is evident Figure 3-36 (B) that the simulation is not finished successfully, and the maximum point cannot be passed.

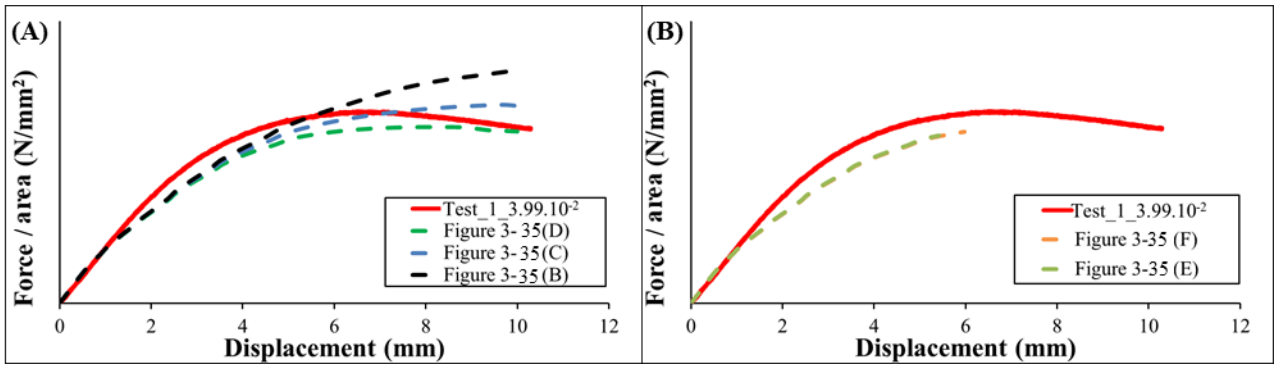

Figure 3-36 Comparison of experimental and simulation results of 3PB test which are generated by different equation of hydrostatic pressure coefficient (A) and (B) correspond to different models used

The simulations are successful with the models B, C, and D. It should be noted that the curves with models (B) and (C) are increasing and with a model (D) the drop of the force is very low and progressive until the end of the calculation.

A nonlinear model without strain rate sensitivity does not pose any difficulty. Linear models with a high slope without velocity sensitivity or a low slope with velocity sensitivity go to the end of the simulation. This last case gives the best results, which is very close to case (A) Figure 3-34 (A) and (B).

The linear models with a threshold or bilinear lead to a stop of the simulation for a displacement of around 6 mm, when the maximum force is reached.

The combination of the strong evolution of the coefficient with the effect of the strain rate is limiting to find the equilibrium after the point of maximum force.

3.17 Conclusion

The aim of the study is to find the constitutive model of a sandwich. In this work, the first brick is to propose a constitutive model of the bulk (skin) as discussed in this chapter. For this purpose, only tensile tests at different constant true strain rates are performed. The only tensile test is performed to reduce the time and effort needed to find the material constants of the constitutive model, which is very interesting from an industrial point of view. In addition, the optical measurements (longitudinal and transverse strains) during this test allow the hydrostatic pressure coefficient to be evaluated. Two materials are studied: polyethylene (PE) and polypropylene (PPC).

Then, the visco-elastoplastic constitutive model is presented. The Abaqus® extension which is UMAT is used to write a constitutive model in Fortran. To identify the material parameters of the constitutive model, Abaqus® with UMAT is integrated with the open-source optimization toolkit DAKOTA.

Once the material parameters are identified, the next step is to validate the constitutive model in 3PB and 4PB tests by comparing the experimental data with the simulation data. The first validation is performed on the bulk PE. The 3PB and 4PB tests results are in good agreement. To see the capabilities of the constitutive model for PE, a simulation of a bottle (complex structure) that is subjected to internal pressure is performed. After comparing the simulation and experimental results, it can be concluded that this model is capable of simulating a complex structure subjected to complex loading conditions. To validate the constitutive model of the PPC, the experimental and numerical simulation results are compared in 3PB. Initially, the experimental and simulation results are close but after 6 mm of displacement, the 3PB simulation stopped. A thorough study of the problem is done which led to the localization of the problem on the hydrostatic pressure coefficient.

As our industrial partner wanted us to work on the PPC, a more thorough study is done on the PPC.

Chapter 4 **Characterization of skin-foam-skin (SFS)**

This chapter discusses the characterization of the sandwich and, more specifically, the architecture of the foam present in the stack. It begins with a reminder of the two manufacturing methods (the rotational and injection molding process) developed by *TotalEnergies*, without being able to go into a detailed description because of the confidentiality that generally surrounds the processes. To understand deeply the mesostructure of the foam inside the sandwich, X-ray tomography is used. This chapter talks about how tomography of multilayer injection molded plates is performed and how results have been treated using Matlab®. It also gives insight into tools developed in Matlab® to treat raw images from tomography. Two types of data have been extracted using the tool with 2 dimensional (named in the following, 2D) and 3D RVE (probe of RVE which analyses the images). The data gathered extensively from this 3D and 2D RVE tool will be used to create RVE of foam presented in the following chapter.

As the foam present in the structure is not uniform and has gradients, it is impossible to analyze them outside their structures. Consequently, only tests on the complete structure can be conducted to characterize their behavior. The second part of this chapter explains the experiments performed on the multilayer samples of both rotational-molded and injection-molded. This data of bending and compression of the injection-molded sample will be used to validate the SFS model presented in the following chapter. Basically, data extracted from tomography will help create numerical RVE of foam, and experimental data of multilayer injection-molded sample will be used for validation of the constitutive model.

Similar to monolayers, multilayer plates with 80, 85, 90, and 95% PPC and dimensions 60 x 60 mm are provided by the *TotalEnergies*.

4.1 Multilayer concept

To create multilayer sandwiches from a single polymer material, several techniques are used by the industrial partner. The process parameters are quite different, but the foam structure is quite similar; remember that we are talking here about foam with a low porosity with the distance between pores more or less consistent.

4.1.1 Rotational molding

A patent of this process has been filed by Eric Maziers [5]. This process has been used in the past to manufacture hollow plastic articles. In this process, thermoplastic polymer grains are added to the mold. Mold is heated and, at the same time, rotated so that molted polymer deposits on the internal surface of the mold. After this, the mold is allowed to cool, which

results in the solidified plastic article (part). This process is unique and has advantages. The ease of implementation makes it a low-cost method. The big size of the parts is essential, and they are made in one step. It is possible to integrate inserts and generate complex shapes. On the other hand, this process does not apply stress and strain to the plastic. Plastic does not undergo compaction as in extrusion molding; this can limit the final mechanical properties.

The material is introduced into the mold in several successive steps to generate the sandwiches. First, after having classically created the external skin, which is deposited on the internal walls of the mold, specific granules containing foaming agents are introduced, and the temperature is regulated so that pores appear and grow. Then the inner skin is added, and during this stage, the materials of the layers, bind and crystallize together, which allows continuity of the matter.

This process is preferred to manufacture large parts like furniture, tank, drum, reservoirs, etc.

The most commonly used polymer in this process is polyethylene, but other polymers like vinyl polychlorides (PVC), polyamides, polycarbonates, and polypropylenes can also be used. All the polymers tend to shrink somewhat and deform, which results in non-uniform wall thickness. In addition, these polymers, used alone, are characterized either by slow coalescence or a raised melting point, which increases the duration of the production cycle. Polyesters, on the other hand, often lack good thermal and mechanical properties.

However, not all materials can be foamed, PE being the simplest to use.

To avoid non-uniform thickness, shrinkage, and warpage, a polymer used during this process should coalesce more rapidly. Here PE multilayer part has been manufactured by *TotalEnergies* and supplied to study during this work. Due to the single material, more attention toward the bounding layer is reduced.

4.1.2 Injection-molding

The injection molding manufacturing process involves mold with molten plastic. The mold is filled with molten plastic under pressure. The temperature of this mold is regulated by using the valve. After cooling the mold, a final part is removed from the mold using an ejection device [141].

This foaming process is also being developed for injection molding. As previously mentioned, a foaming agent is integrated into the material. This is part of the company's confidential know-how; no details can be provided on this procedure. Obviously, the control of the injection pressure and the transformation temperatures are key elements.

4.2 Mesostructure characterization

Plates are therefore developed with these foaming processes; their particularity is that we gradually transition between the skins and the foam without a specific interface. The mesostructure of the foam is not constant in the manufactured structures, and the variations of the morphology are pretty representative of those generated by these industrial processes. Indeed, the dimensions are limited, but the parameters and techniques are those deployed to produce parts.

In this section, the protocol is presented which, is used to characterize the mesostructure of the foam. This one can be applied in a generic way for this family of low porosity foam and, it is based on X-ray recordings.

4.2.1 Tomography observations

To perform tomography on the samples UltraTom is used. UltraTom (Figure 4-1) [142] is mainly used for academic research and industrial R&D application mainly because of its open and flexible system. To avoid changes concerning each test machine is installed in the large bunker. Complex experiments can be performed in-situ CT experiments as there is space all around the machine. Different materials and sample size tomography can be performed with this machine very easily. Up to 100 kg sample easily can be positioned. UltraTom is equipped with three sources that can be used for various purposes as per need. UltraTom can go up to 0.4 µm. "X-ACT" software which is integrated with UltraTom provides means to streamline acquisition and enhance the reconstruction of images.

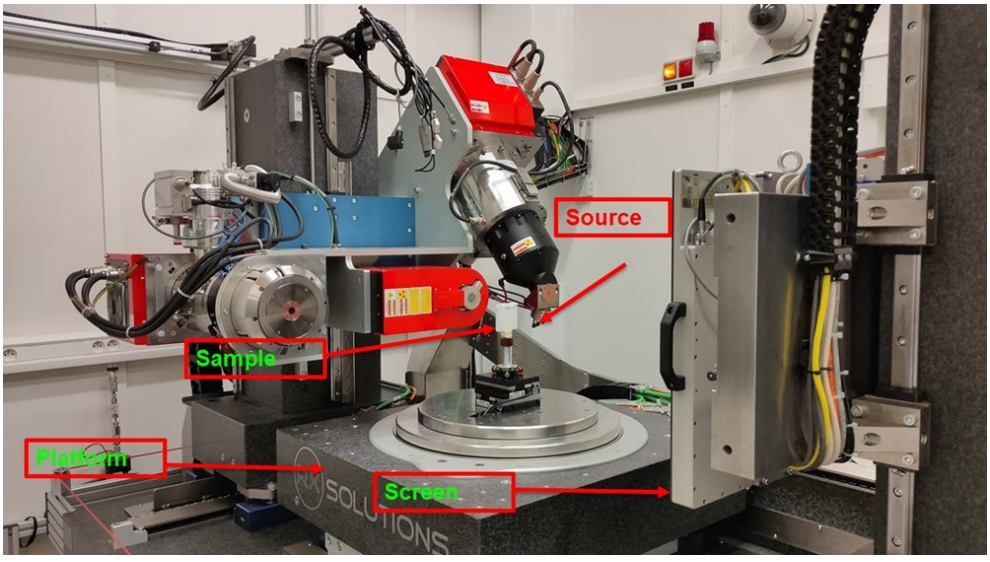

Figure 4-1 UltraTom

As presented before, the machine has three sources one is for high, low accuracy, and the other for intermediate accuracy. Here, an intermediate accuracy source has been used to scan the complete geometry of the injected plate. From the source, rays are passed through the sample and collected on a screen to form an image of a sample. The ratio between the sample size and width of the image recording panel defines the precision: 26 µm by pixel. X-ray scans from tomography are post-treated in X-act software to generate a collection of slices, as shown schematically in Figure 4-2. The accuracy is a function of the size of the specimen, the source, and the imaging panel.

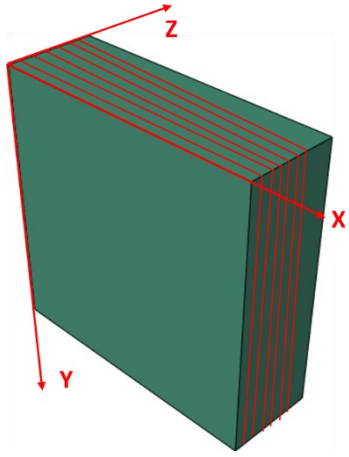

Figure 4-2 Schematic representation of tomography

4.2.2 Tools for describe the porosity

In order to treat the data obtained from tomography, Matlab® has been used. A tool has been developed which is capable of taking raw images from tomography and processing them to the final stage, the specifications of the tool are not detailed, but an overview of the same has been provided in Figure 4-3.

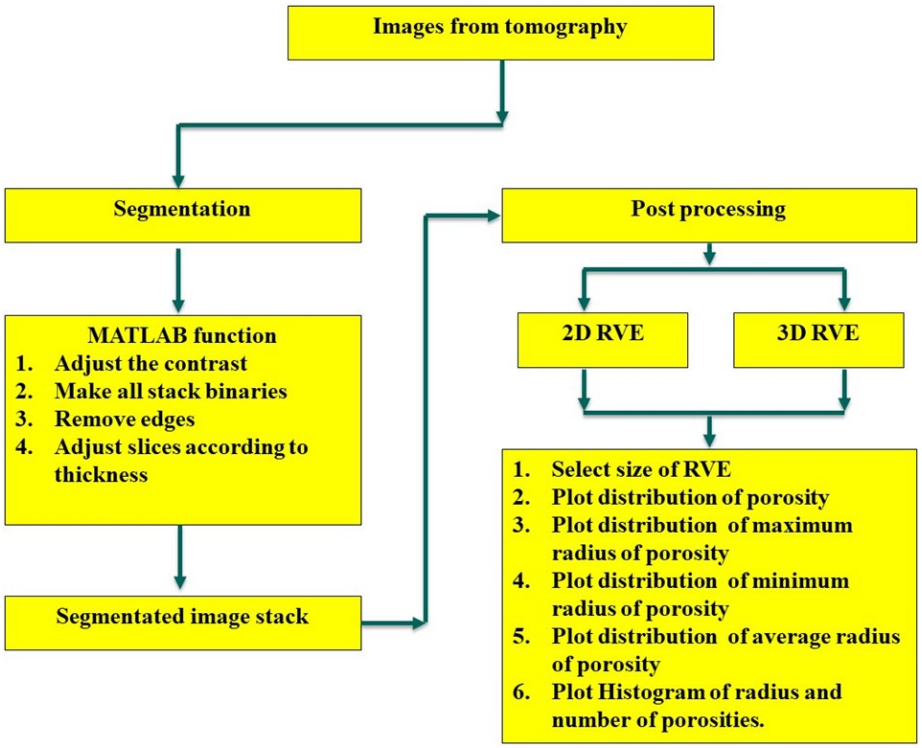

Figure 4-3 Flow diagram of segmentation and post processing in Matlab

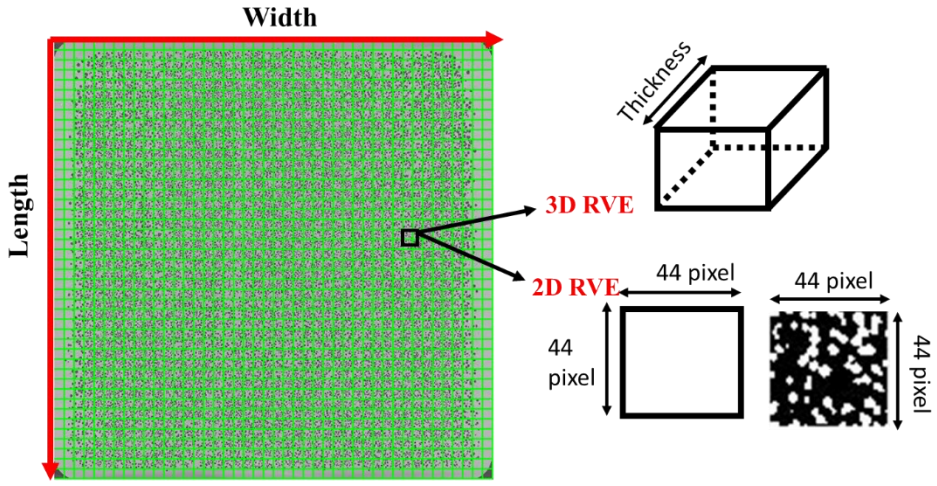

Figure 4-4 Grid formation and definition of 2-3D RVEs

Images from tomography first go in Matlab® function, where the contrast is adjusted for the best visibility of pores and then converted into binary images for post-processing. From the slices, the pores are referenced by their position and diameter.

This pores field is then analyzed based on the slices in the thickness. The tool uses a grid defining the dimensions of the zones of interest to achieve this. One image with this grid in green is shown in Figure 4-4. If the grid's each square is integrated into total thickness, it is called 3D RVE; this one is translated in X and Y-directions to generate the field in the 2D space. On the other hand, 2D RVE is a box with a part of the thickness. The porosity is

calculated by integration on this part of the thickness; then, it is translated in X and Y-directions and reproduced inside the thickness to describe the architecture variation in the 3D space. A schematic representation of 2-3D RVE, based on this grid, is shown in Figure 4-5 (A) and (B) respectively. Remark: 2D or 3D refer to the volume of integration to calculate porosity.

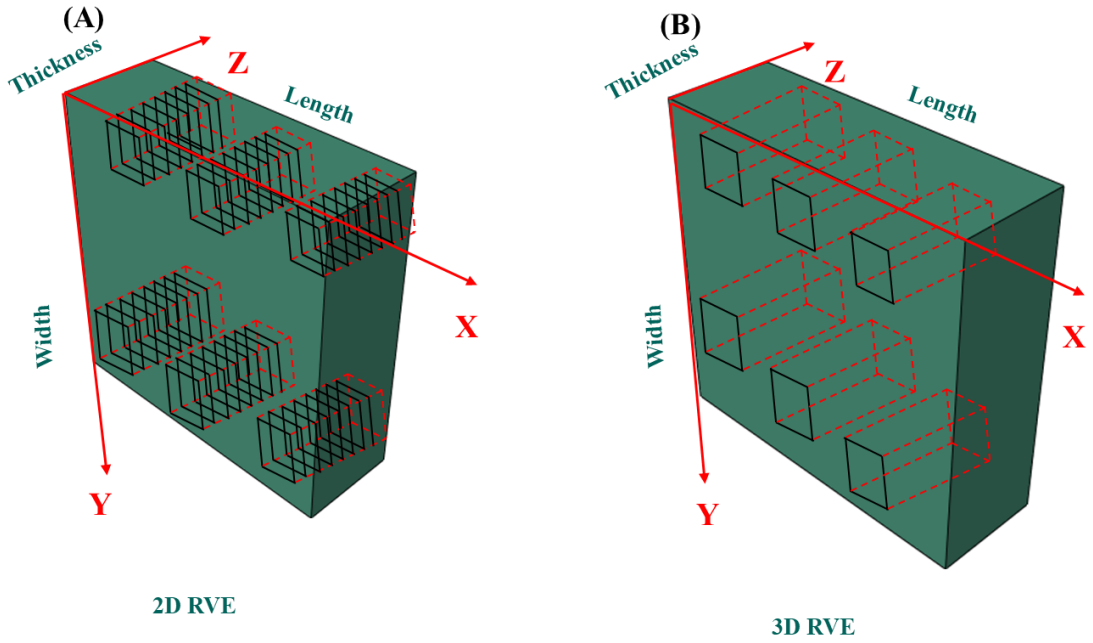

Figure 4-5 Schematic representation of (A) 2D (B) 3D RVE in a global context of sample

All identified pores by the tool are numbered and recorded in a list. Then the software provides for each grid cell the porosity, the minimum distance between pores, and the mean radius of the pores. Thus, a field for each of these properties can be created, and it is possible to generate a histogram of a minimum distance between pores, diameters of pores, and porosity of the sample. According to the selection of 2D and 3D RVE, all quantities have been calculated.

Due to the curved geometry of some samples poses analysis difficulties for the PE samples taken from the sides of a rotationally molded bottle. The numerical tool cannot be automated, and the analysis of the porosity has been realized on the whole sample but only in specific areas presented in the chapter on the analysis of the results.

Important note: There is no doubt that the fields created to correspond to the pores are identifiable with the precision of the machine. There are cavities without any ambiguity at a lower scale, but we do not have access to them with this technique. The hypothesis postulated here is that cavities at a smaller scale will have a second-order effect compared to pores of larger dimensions. Secondly, in the following chapter, it will be assumed that the behavior of the polymer in the foam is identical to that of the solid parts. However, this will depend on the microporosity and crystallinity and to study it at such a scale is a subject in itself that

would require a complete thesis. But some elements will be given to evaluate the validity of this assumption.

4.2.3 Results of PPC

Figure 4-6 (A) shows porosity distribution in different locations of the 80% PPC sample. Red arrows show the correlation between distributions of porosity of real sample and analyzed by Matlab® tool. It is clearly visible that near to edges, there is a drop of porosity and, at the edges again porosity increases (Figure 4-6 (B)) same has been captured by the Matlab® tool. In the middle section of a sample, porosity is quite uniform same has been pointed out by the tool. Figure 4-6 (C) shows the mean radius distribution inside the sample using 3D RVE (integrated into the complete thickness). Let's remember that the mean radius is calculated by taking an average of the radius of the pores inside one RVE. Red arrows show the correlation of the mean radius distribution observed by the tool in corresponding to the sample's tomography image. At the edges size of pores increases same has been captured by the Matlab® tool using 3D RVE in Figure 4-6 (C). In the middle part of the sample, porosity and the size of pores are uniformed, and the tool has reflected the same. Also, there is the gradient of the size of pores at the edges from top to bottom of a sample, the same has been well represented by the tool.

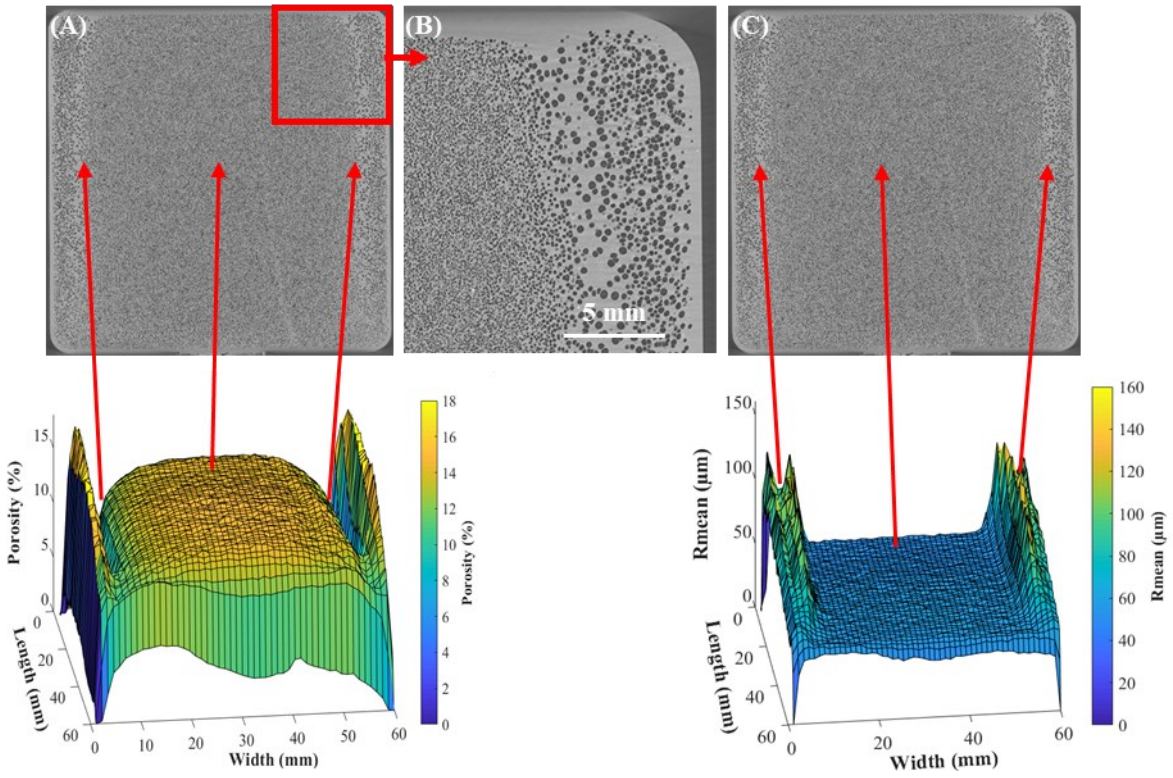

Figure 4-6 (A) Porosity and (B) Mean radius distribution of the 80% PPC sample using Matlab® 3D RVE tool

Figure 4-7 (A) and Figure 4-7 (B) show the porosity and mean radius distribution of 80% PPC quarter part sample, respectively, calculated using the 2D RVE tool (3D fields). From porosity distribution, it is evident that there is a porosity gradient in the thickness. From the middle to extremities of thickness porosity is gradually decreasing. At the corner of the width, there is porosity variation visible in the tomography image; the tool has captured the same. Mean radius distribution follows the same kind of pattern as porosity. As it is visible in the tomography image, the porosity size is relatively uniform at the center same has been captured by the tool. However, at the edge of the width, the size of porosity is increased, the same has been represented in the tool.

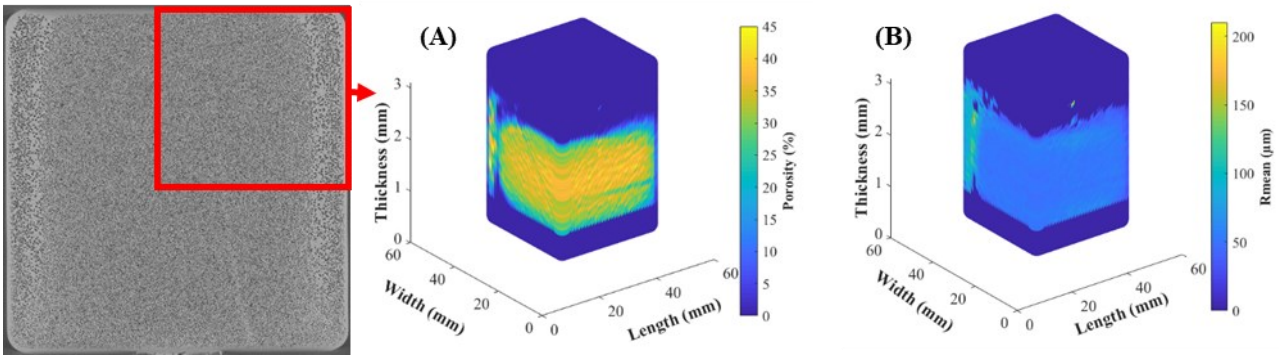

Figure 4-7 (A) Porosity (B) mean radius distribution of the 80% PPC sample using Matlab® 2D RVE tool

Tomography has been performed on the 8 samples with different % of PPC. Only two sample results are shown here. Figure 4-8, show the porosity and mean radius distribution of the 90 % PPC sample. Red arrows show the correlation of quantities calculated by the tool with real sample tomography images. Figure 4-8 (A) shows the distribution of the porosity which is similar to the horseshoe shape, the same has been captured by the tool. Figure 4-8 (B) shows zoomed view, it is clear that there is a gradient of porosity at the edges of the sample. The tool has captured this variation efficiently. Figure 4-8 (C) shows the distribution of the mean radius. There is a gradient in the size of pores from top to bottom same has been captured by the tool as well. At the border there is porosity variation as well as an increase in the mean radius.

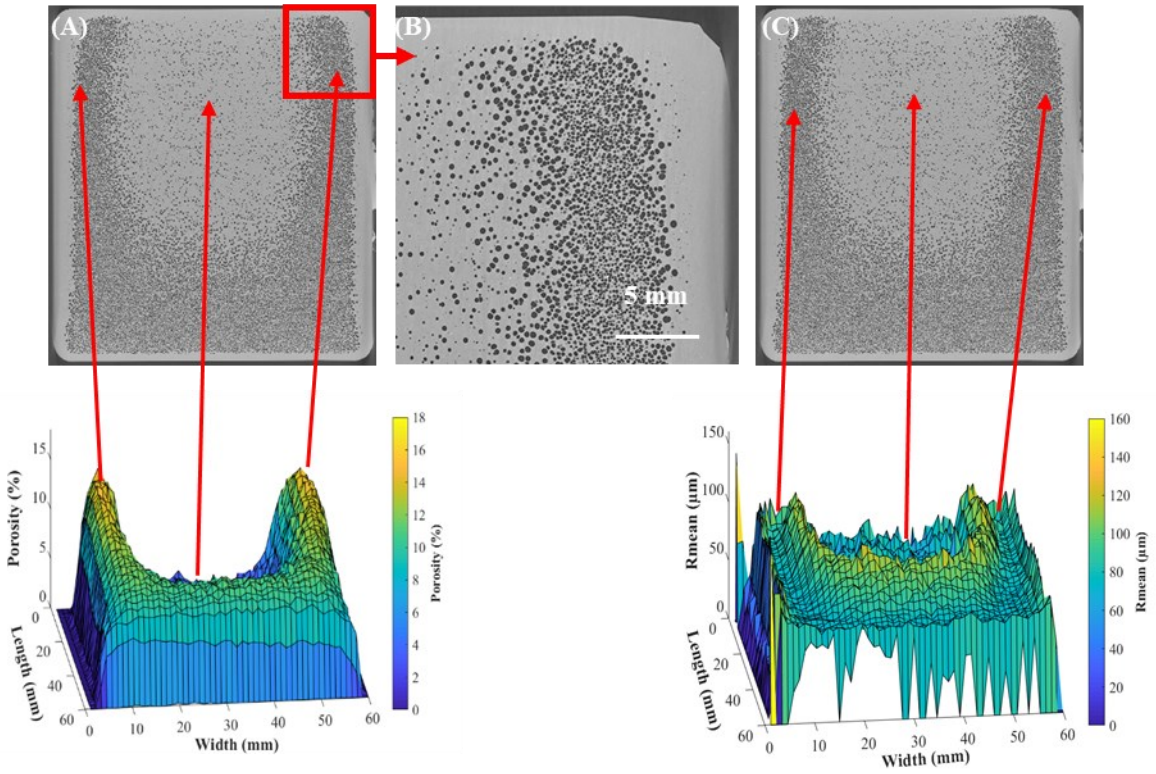

Figure 4-8 (A) Porosity (B) Mean radius distribution of the 90% PPC sample using Matlab® 3D RVE tool

Figure 4-9 (A) and Figure 4-9 (B) show the porosity and mean radius distribution of 90% PPC quarter part sample respectively using the 2D RVE tool. From porosity distribution, it is evident that there is a strong gradient of porosity in the thickness. At the corner of the width, there is porosity variation which is visible in the tomography image, the same has been captured by the tool. Mean radius distribution follows the same kind of pattern as porosity. As it is visible in the tomography image that, pores size is quite uniform at the center same has been captured by the tool. At the edge of the width size of porosity is increased same has been represented in the tool.

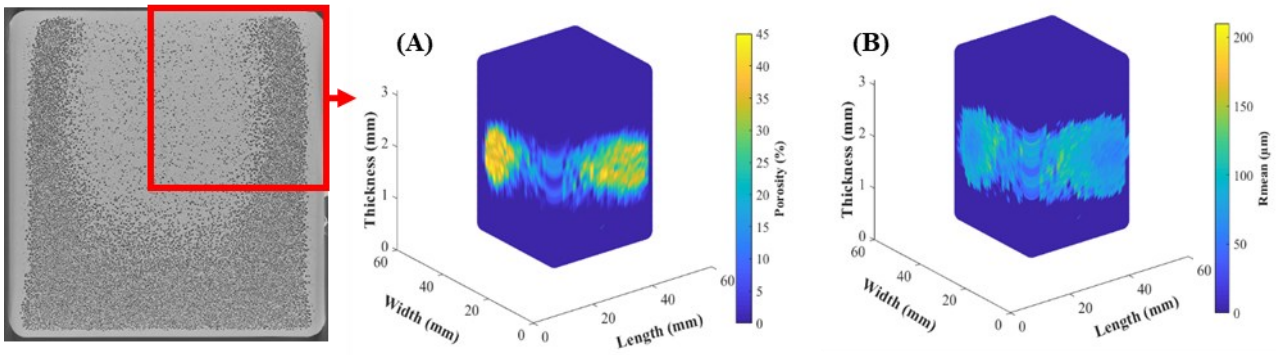

Figure 4-9 (A) Porosity (B) Mean radius distribution of the 90% PPC sample using Matlab® 2D RVE tool

4.2.4 Discussion

It is clear that the mesostructure presented has strong gradients in the plate. This variation relates to both the rate of pores and their size and the distances between the pores. The mesostructure evolves strongly at the thickness scale and the entire plate. This variation is dependent on the process parameters. This is a point that will deserve a parametric study to link these fields to the process parameters in the future. Such knowledge opens up the prospect of creating custom variable sandwiches.

The tool developed allows describing the fields of the pores visible with the tomography at the scale of the complete structure. It is a significant result of the work because it will be used to work out a constitutive model of the sandwich integrating these gradients of microstructure at the scale of the mesostructure.

4.2.5 Results of PE

Along with PPC, some work on image processing samples of PE sandwiches is also done. As explained above UltraTom is used for tomography. 26 µm pixel size is used for PE samples. As the sample's length is much higher than the PPC sample, instead of doing tomography on the whole sample, on the particular region is performed. The same is shown in Figure 4-10.

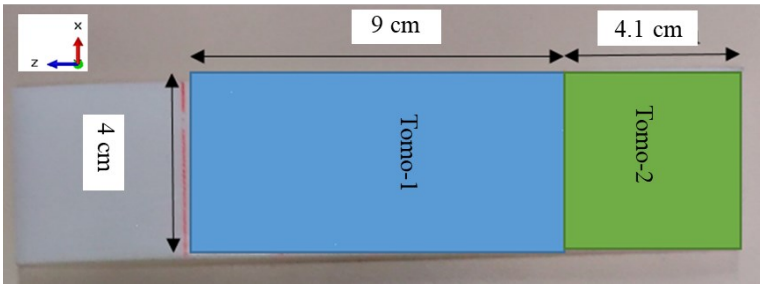

Figure 4-10 Sample with foam thickness of 6 mm with designated regions in which tomography has been performed

Figure 4-11 shows the tomography image of "Tomo-1" along the X-axis. Unlike PPC, samples of PE are highly heterogonous in the thickness of the foam, and there is a curvature in the sample. There are considerable porosities in the skin as well. It appears that the density of the foam in the center layer is lower compared to the PPC. Smaller pores are found next to larger pores, and the distribution is more random than in the PPC, where the distribution of the mesostructure is more homogeneous. The layers of solid material contain pores of visible size and in non-negligible numbers. The effect of the process is first ordered on the size distributions and on the distribution of this porosity at the sample scale. Figure 4-11 presents a slice in the sample, plane positioned in the middle of the width. It appears that the foam is homogeneous except for the corners.

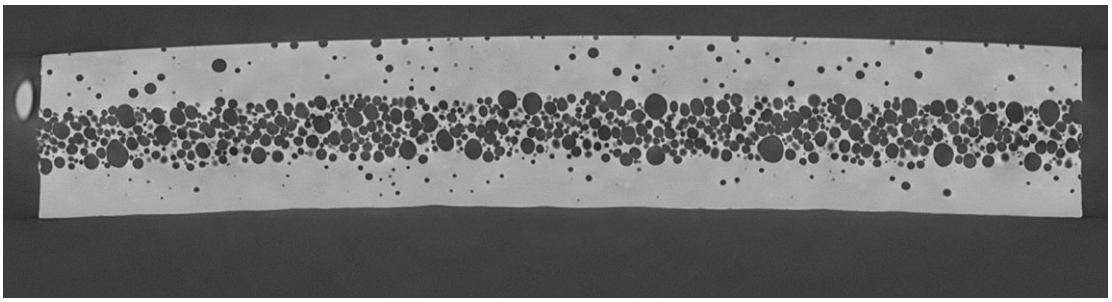

Figure 4-11 Tomographic image of "Tomo-1" along X-axis.

It is clear that the sample is bent at an initial state, but the tool developed in Matlab® is not capable of taking curvature into account for image processing. In order to resolve this problem, images along the Y-axis of "Tomo-2" (Figure 4-12) have been considered. As shown in Figure 4-12 five squares have been considered at different locations. The size of this square also varied from 2, 4, 6, and 10 mm, thickness is varying in order to keep the square in the foam only. For all the samples of the 3PB tests (samples detailed in Table 4-1), the same has been done. In these cubes, porosity is calculated in different sizes of a cube and plotted on the graph.

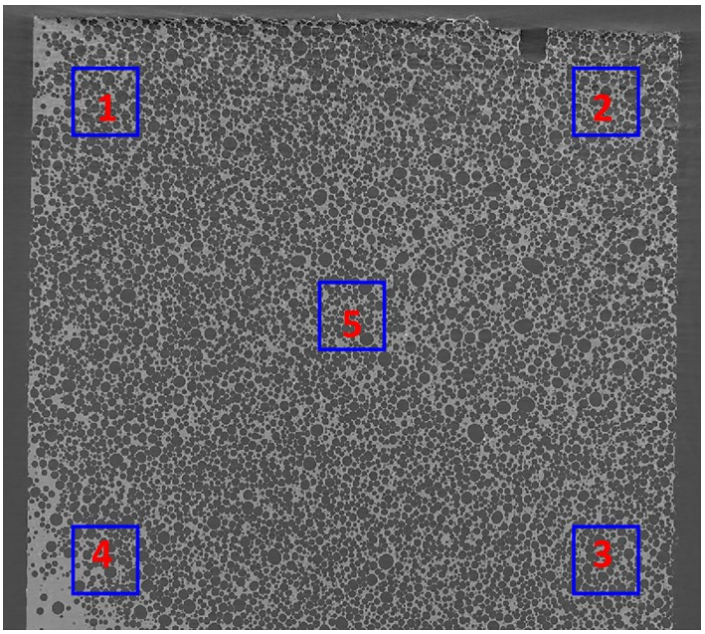

Figure 4-12 Tomography of "Tomo-2" along Y-axis

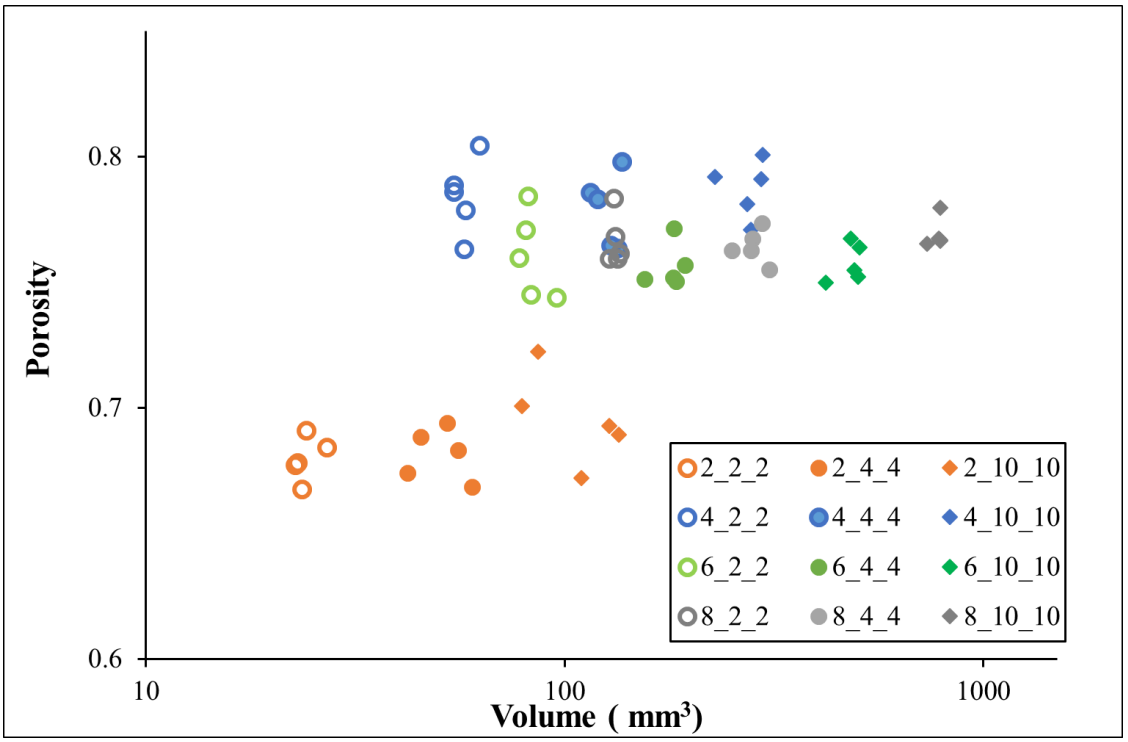

Figure 4-13 Calculation of porosity in considered cubes

Figure 4-13 shows the porosity vs. volume of the cube considered for calculating porosity. Legends are also representative of the thickness of foam and the size of the square considered. For example, 4_10_10 means a sample with 4 mm of foam thickness and 10 x 10 mm^2 of a square is considered.

When the volume used to calculate the porosity decreases, the result is still in the same order of magnitude, confirming that the porosity is relatively homogeneous in the volume of the central layer. On the other hand, with the specific conditions applied during the manufacturing of these structures. It can be observed that the thicker the foam layer is, the lesser its porosity. Therefore, this graph confirms that the porosity is much higher than the PPC in PE sandwich.

4.2.6 Discussion

The porosity in the case of rotational molding is quite different from that generated by injection. Small pores are next to larger ones, and there is no more homogeneity in the structure. In addition, the distribution field is more complex, and the pores are no longer spherical.

The porosity levels are much higher, and this structure is close to one of the classical foams of very low density with a thin wall between the cavities.

In the future, it will be interesting to link the characteristics of the foams with the process parameters to produce customized materials. For example, the temperature control on a mold with hot or cold spots can be one of the levers to modulate this microstructure.

Let us recall that our objective is to develop a prediction chain for the behavior of these mono-polymer sandwiches. The guiding principle is to use only tensile tests to predict the behavior of the structure, but this path can be followed only under the condition that the polymer is under a similar physical state (crystallization) between a solid specimen and between the pores. This assumption is not relevant in the case of rotational molded specimens. As a consequence, the experimental results will be compared only to those of the PPC.

4.2.7 Global parameters

To complete this analysis, histograms (Figure 4-14) are plotted for two plates named 80% PPC and 90% PPC. The percent corresponds to the ratio between the mass of the plate divided by the mass of an equivalent plate without pores.

The objective of these graphs is to describe the population of pores with a limited number of parameters: For the porosity analysis, the size of RVE's for both samples is the same. Histogram of porosity (using 2D RVE), diameters of pores, and minimum distance between pores (Using 3D RVE), have been performed and presented one below the other in the following table. The left column corresponds to 80% PPC and the right column 90% PPC.

It can be noted that:

- The distribution of porosity for both specimens is different. For 80% PPC more RVE contains a porosity lower than 10%. For 90% PPC, a pic is present with close to 35% of porosity.
- The first column on the histogram corresponds to pores with one pixel.
- For 80% PPC sample results maximum and minimum diameter of pores ranges from 50 to 250 µm. The minimum distance between pores is from ~5 to 90 µm.
- For 90% PPC sample results maximum and minimum diameter of pores ranges from 40 to 350 µm. The minimum distance between pores is from ~5 to 150 µm.
- As 80% PPC sample means 20% of porosity which results in a greater number of pores as compared to 90% PPC sample.
- For 90 % the diameters and minimal distance between pores is larger corresponding to 80%

For both the samples at zero minimum distance and diameter, some pores indicate the noise in the images for 3D RVE results, whereas for 2D RVE results that is porosity histogram represents RVE calculation inside the skin where there are no pores.

80% PPC	90% PPC
Porosity	
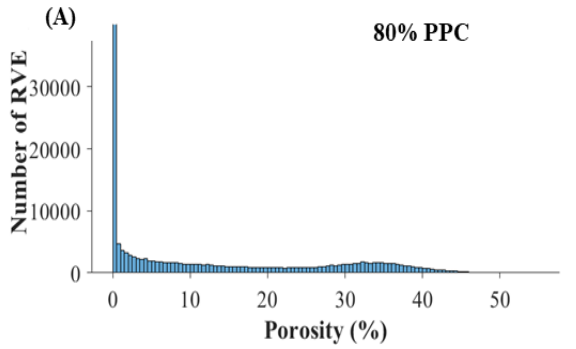	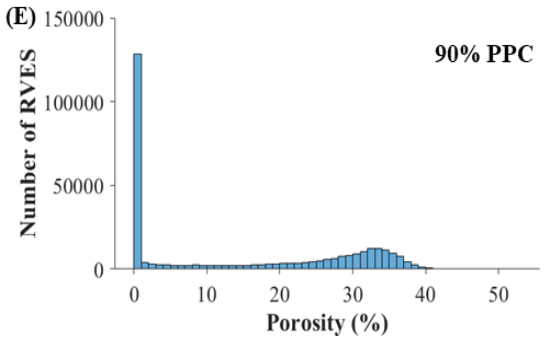
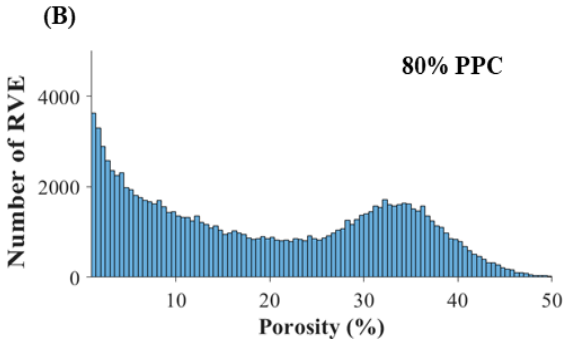	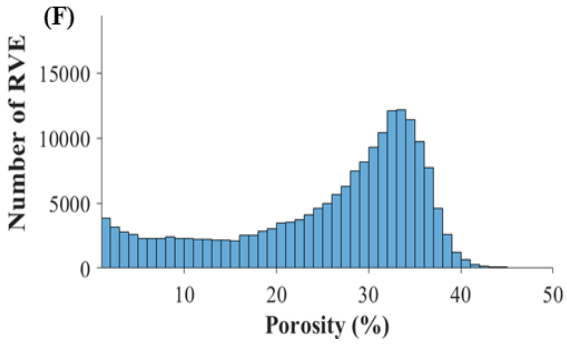
Diameter of pores	
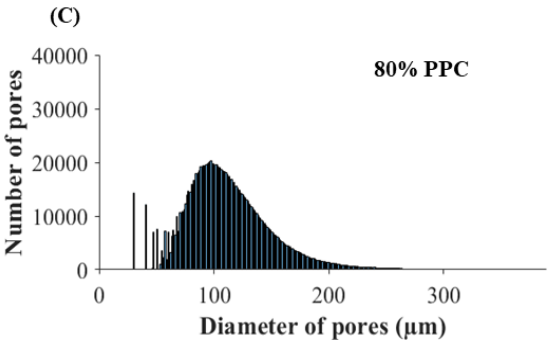	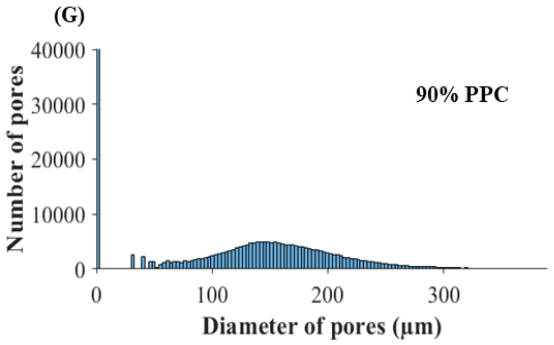
Number of pores	
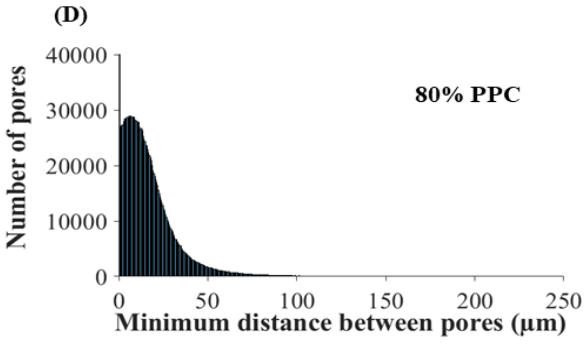	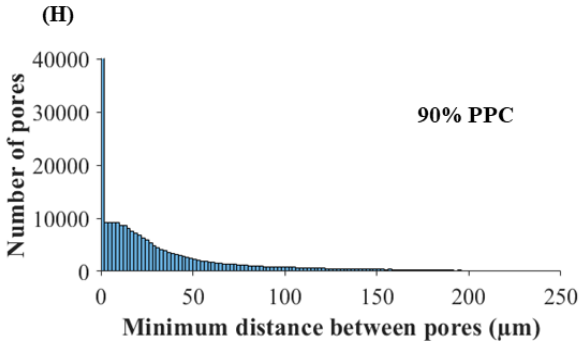

Figure 4-14 Histogram of (A) Porosity (B) Zoom view of Porosity (C) Diameters of pores (D) Minimum distance between pores of 80% PPC sample, Histogram of (E) Porosity (F) Zoom view of Porosity (G) Diameters of pores (H) Minimum distance between pores of 90% PPC sample

These results will help to build the RVE of foam that will be discussed in Chapter 5.

4.3 Mechanical characterization

In this part, tests on sandwiches are carried out. The specimens are extracted from rotational molded and injected semi-structures. It is essential to underline that these samples contain microstructure gradients. The complexity at the mesoscopic scale will be expressed in the mechanical response to understand it better; specific observations are set up. These experiments aim to have macroscopic, mesoscopic, and global scale results during experiments to compare with simulation results with respective scales.

These experimental results will be used as a basis to validate the model of the sandwich behavior.

The tests performed on the sandwich, and the associated metrology is detailed below.

4.3.1 PE Multi-layer (sandwich)

Similar to monolayer, multilayer samples are cut from the bottle. The nominal width and length of bending samples are 40 and 100 to 200 mm, respectively. All multilayer bending samples have a nominal 2 mm thickness of the skin at the top and bottom, whereas foam thickness varies from 2, 4, 6, and 8 mm. Charly robot specifications are the same as the monolayer is mentioned in Chapter 3 Table 3-3.

4.3.2 PPC Multi-layer (sandwich)

Like monolayers, multilayer plates with 80, 85, 90, and 95% PPC and dimensions 60 x 60 mm are provided by the *TotalEnergies*. As before, samples are cut from the injected plates.

Tomography of those plates is done. Plates with 80, 85, 90, and 95% PPC are shown in Figure 4-15 (A), Figure 4-15 (B), Figure 4-15 (C), and Figure 4-15 (D), respectively. According to porosity, plates are cut at a specific location, the same has been shown in Figure 4-15. Rectangular samples for the bending test, square and circular samples for the compression test are cut. A red mark on the top corner is made on plates to represent the orientation of plates during cutting. Similarly, on each sample in the top right corner red dot is made for the samples to have the same orientation during simulation and experiments. All the dimensions

mentioned in Figure 4-15 are in millimeters. The same specification mentioned in Chapter 3 Table 3-4 for the Charly robot is used while cutting the plates.

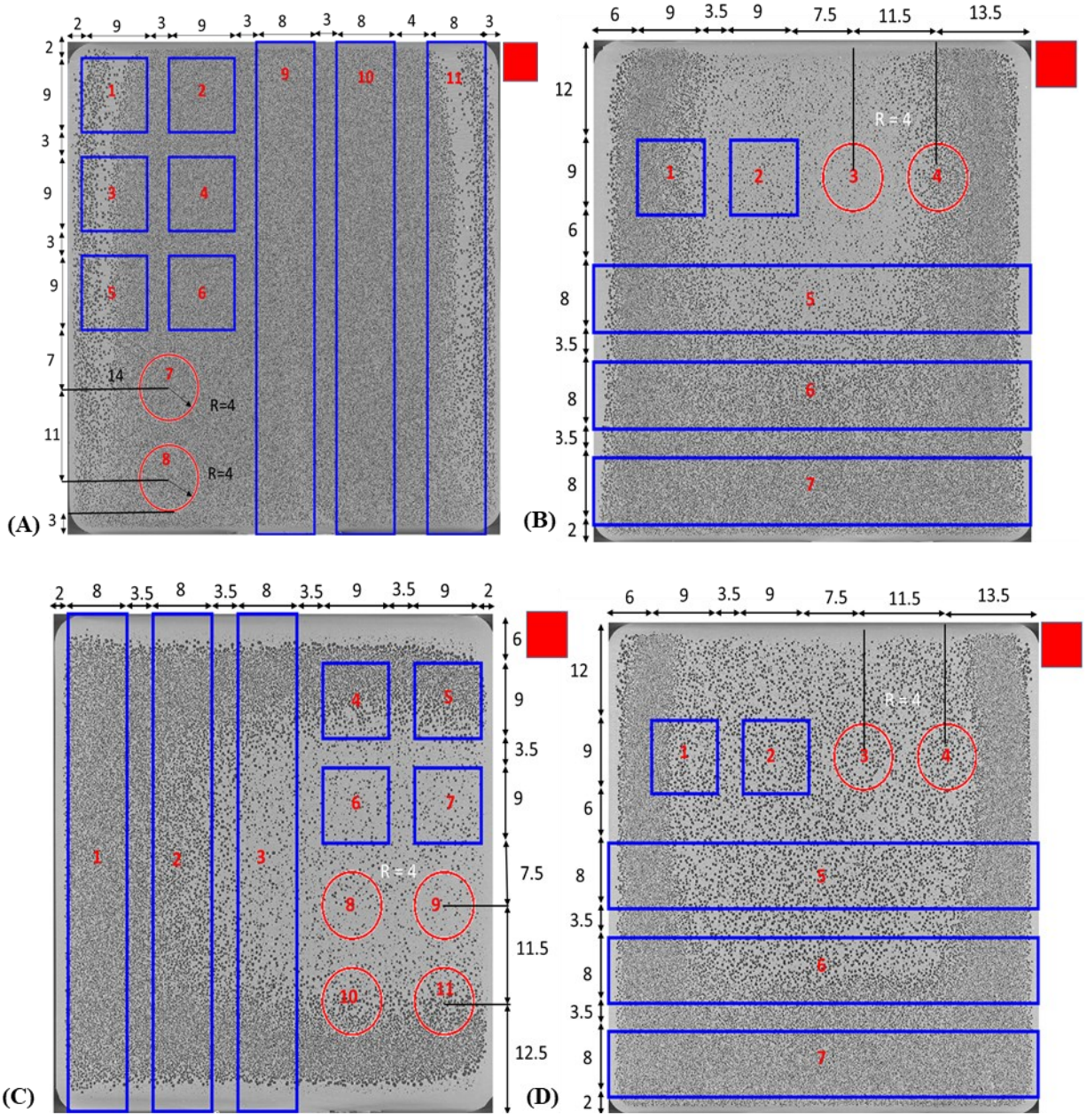

Figure 4-15 Cutting plan of plates with (A) 80% (B) 85% (C) 90% (D) 95% PPC

Once samples are cut, spatters are removed using polished paper, the same as monolayer samples. Black dots are made in the thickness of samples and along the length of samples. At each 5 mm along the length, black dots are made, and three dots at the center of each layer along the thickness are made. The diameter of the black markers is approximately 0.2 mm. Figure 4-16 shows real samples of bending and compression along with markers in the thickness. Markers are made to follow local displacement at that location, which will be used to compare experimental and simulation results locally. Two-line at the corner of Figure 4-16 (A)

and Figure 4-16 (C) show the samples' orientation, which eventually gives the porosity distribution inside the sample. Figure 4-16 (B) and (D) show the black dots are made in the thickness of samples and along the length of samples in bending and compression respectively.

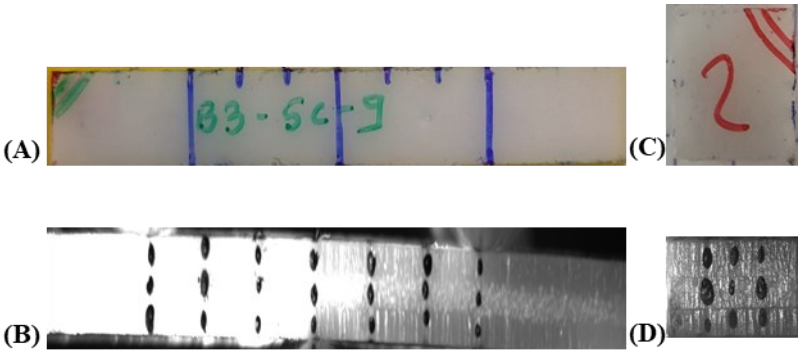

Figure 4-16 (A) Rectangular sample for bending (B) Black dots in the thickness to track local information (C) Square sample for compression (D) Black dots in the thickness to track local information

4.4 The experimental test procedure for Multilayer

4.4.1 Experimental procedure of 3PB and 4PB tests of PE sandwich sample

Instron 4505 machine with a load cell of 500 N is used for getting global scale information. Table 4-1 and Table 4-2 present the different characteristics of the tests such as the distance between the fix and moving roller, the nominal, real thickness, and width of the sample during 3PB and 4PB tests. The average width of the sample is measured at three locations, 1A-1B, 2A-2B, and 3A-3B as shown in Figure 4-17. Widths at different locations are mentioned in Table 4-1 (3PB test) and Table 4-2 (4PB test). The thickness of the samples is measured at six locations (1A, 2A, 3A, 1B, 2B, 3B) shown in Figure 4-17. The average of values at each location thickness (location as shown in Figure 4-17), is mentioned as real thickness in Table 4-1 and Table 4-2. For example, the average of thickness and width at 1A and 1B, 2A and 2B, etc. is mentioned in Table 4-1 and Table 4-2.

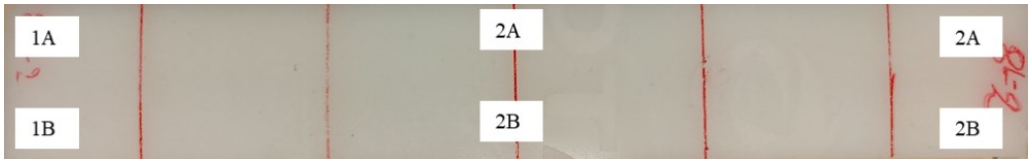

Figure 4-17 Multilayer sample for 3PB and 4PB tests where thickness and width are measured

Thickness (mm)				Width (mm)			Distance between		Displacement rate applied on moving roller (mm.s^{-1})
	Real average at			Real at					
Nominal	1A and 1B	2A and 2B	3A and 3B	1A and 1B	2A and 2B	3A and 3B	Fix roller (mm)	Moving and fix roller (mm)	
6	6.12	6.06	6.29	39.98	40.01	40	90	22.5	5 10^{-3}
8	8.46	8.66	8.66	39.97	40.03	40.1	120	30	6.7 10^{-3}
10	10.58	10.4	10.55	40.13	40.4	40.5	150	37.5	8.3 10^{-3}
12	12.77	12.7	13.03	39.98	40.07	40.1	180	45	1 10^{-2}

Table 4-1 3PB details of PE multilayer

Thickness (mm)				Width (mm)			Distance between		Displacement rate applied on moving roller (mm.s^{-1})
	Real average at			Real at					
Nominal	1A and 1B	2A and 2B	3A and 3B	1A and 1B	2A and 2B	3A and 3B	Fix roller (mm)	Moving and fix roller (mm)	
6	6.375	6.2	5.82	40.05	40.11	40	90	22.5	5 10^{-3}
8	8.18	8.29	7.97	40.07	40.08	40	120	30	6.7 10^{-3}
10	10.07	10.9	10.6	40.2	40.3	40.2	150	37.5	8.3 10^{-3}
12	11.28	12	11.7	39.9	40.0	40	180	45	1 10^{-2}

Table 4-2 4PB test details of PE multilayer

4.4.2 Experimental procedure of 3PB tests of PPC sandwich sample

Instron 1195 machine with a load cell of 2 kN is used to perform the tests. Ten samples are tested with different displacement rates imposed on the moving roller during 3PB test. The distance between the moving rollers is 30 mm, and the nominal length of all the samples is 60

mm. Detail about the samples and experimental configuration is mentioned in Table 4-3. The numbers given to the samples during the test can be seen in Figure 4-15. The thickness of the sample is measured at the center of a sample as there is not much variation of thickness along the length of the sample unlike rotational molded samples of PE.

% of PPC in the sample	Number given to sample during the test	Thickness (mm)	Displacement rate ($mm.s^{-1}$)	Note
80%	10	3	$2.5\ 10^{-3}$	
	11	3.04	$2.5\ 10^{-3}$	
	5	304	$2.5\ 10^{-2}$	Data lost
85%	6	3.08	$2.5\ 10^{-3}$	
	7	3.1	$2.5\ 10^{-2}$	
90%	1	3.12	$2.5\ 10^{-3}$	
	2	3.08	$2.5\ 10^{-3}$	
95%	5	3.24	$5\ 10^{-2}$	
	6	3.26	$1.25\ 10^{-2}$	
	7	3.28	$1.25\ 10^{-2}$	

Table 4-3 3PB test details of PPC multilayer samples

Figure 4-18 shows the experimental setup used for the 3PB test and the cameras used to record different properties at different scales. Allied Vision 9 MP (Figure 4-18 (B)) camera is used for recording macroscopic properties. QUESTAR (Figure 4-18 (D)) is long distance, compact and lightweight microscope. Therefore, a microscopic resolution could be achieved from a long distance without cluttering the work area with instrumentation. It has a focus range from 56 cm to 152 cm. At 56 cm, it has a 2.7-micron optical resolution [4]. QUESTAR is used to record the mesoscopic properties of the sample. Although QUESTAR is fixed, it does not move during the test, and while performing the 3PB test aim is to record the mesoscopic properties of the sample under the central roller. The central roller made a fix to resolve this problem, and two extreme rollers made moving. Both cameras record the images with an asked interval of the time, those images are processed to have experimental results compared with simulation results. Also, it is essential to remark from Figure 4-18 (E) that the orientation of a sample is also noted during the test to define the orientation.

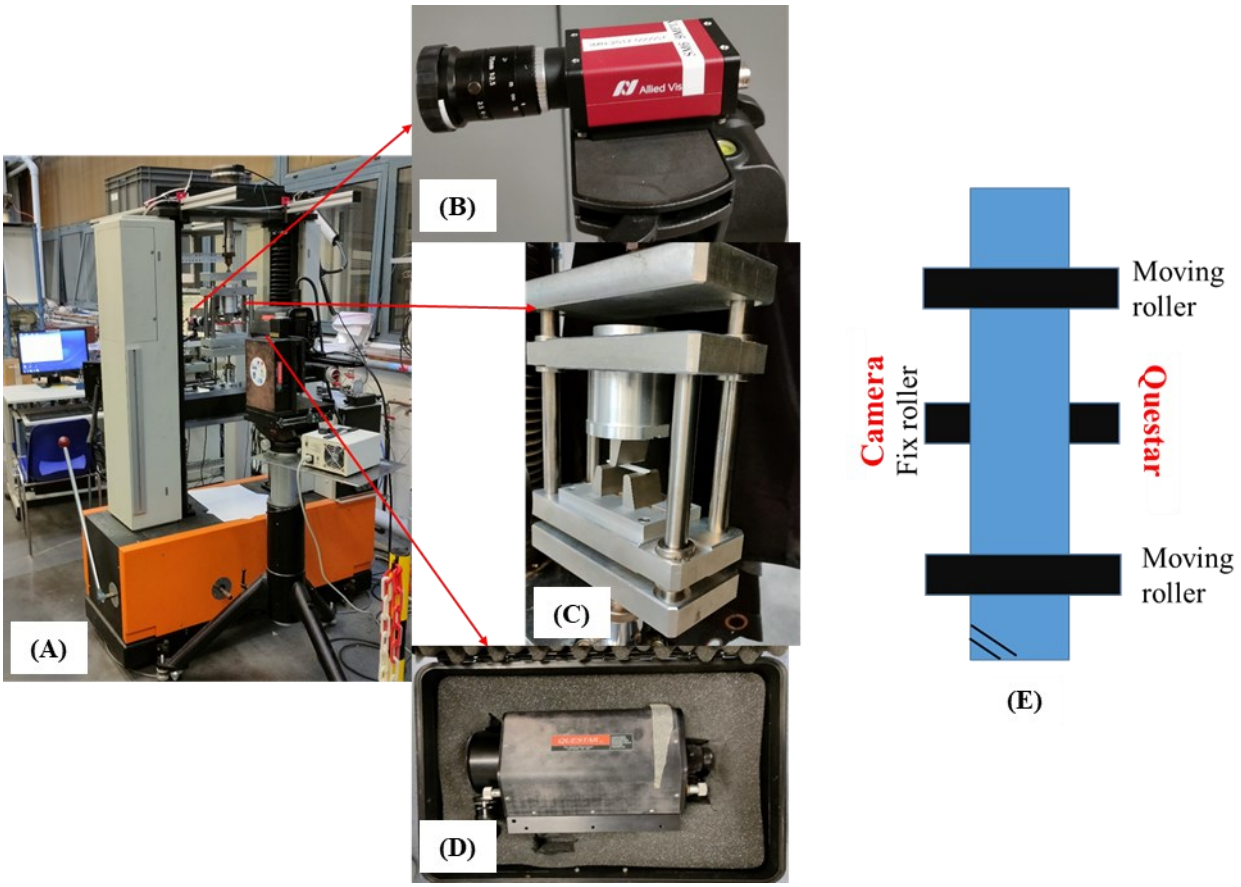

Figure 4-18 (A) Global experimental setup of 3PB test (B) Camera used to record mesoscopic properties during experiments (C) Mount used to perform 3PB test (D) QUESTAR (Long distance microscopic camera) use to record the mesoscopic properties (E) Schematic of 3PB test

4.4.3 Experimental procedure of compression test of PPC sandwich sample

Instron 1195 machine with a load cell of 5 kN is used to perform the tests for getting information about macro, meso, and global scale. The same setup as bending shown in Figures 4-18 is used for the compression test, except for the mount. Seven samples are tested at different displacement rates. Details about sample thickness and displacement rate can be found in Table 4-4. Numbers given to samples during tests are mentioned in Figure 4-15.

% of PPC in the sample	Number given to sample during the test	Thickness (mm)	Displacement rate ($mm.s^{-1}$)
80%	1	3.008	0.0025
	2	3.008	0.00025
	3	3.073	0.0125
	5	3.05	0.025
90%	4	3.1167	0.00025
	5	3.09	0.0025
	6	3.192	0.025

Table 4-4 Compression test details of PPC multilayer samples

Mount setup for a compression test is a little different than bending, the same has been shown in Figure 4-19. Other than this all-other setups for recording macroscopic, mesoscopic, and global properties are the same. The sample is in contact with a part painted in black in Figure 4-19. Before painting, the block had the same color as the test setup because of this reason when the LED light is turned on then there is a lot of reflection of light in images taken by the cameras. To avoid the problem of reflection of light, part is painted black except for the surface which is in contact with the sample.

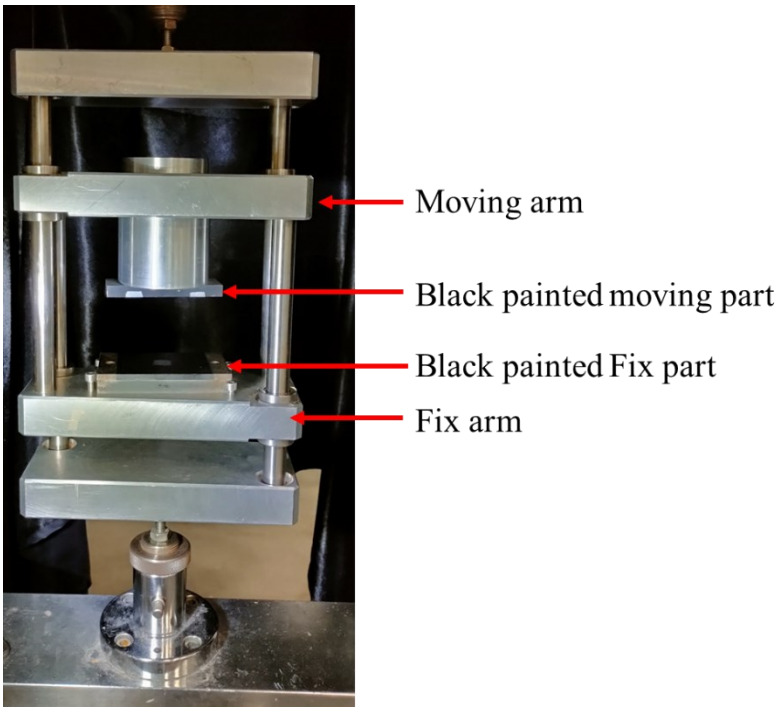

Figure 4-19 Mount setup for compression test

4.5 Experimental results of Multilayer

4.5.1 PE bending results

Figures 4-20 show the results of the samples 3PB and 4PB test results, whose detail is mentioned in Table 4-1 and Table 4-2. Colors curves shown in Figure 4-20 plotted between force per unit area of cross-section (area of cross-section is calculated at the center of the sample) vs. displacement imposed on moving roll, measured during experiments on all samples with different nominal thicknesses. For one nominal thickness, two or three samples are tested, depicted through colored lines in Figure 4-20, which permits quantifying the variability of experiments. Solid curves samples dimensions are used for the simulation, and the same has been mentioned in Table 4-1 and Table 4-2. For 3PB test results, the maximum force per unit area reduces as the thickness of the foam increases. A similar trend can be seen in the 4PB test results. One explanation for this is that the ratio of displacement rate to thickness is the same for all the samples, 8.33 10^{-4} s^{-1}, and the ratio of thickness to the distance between fixed roller is also the same, which is 15.

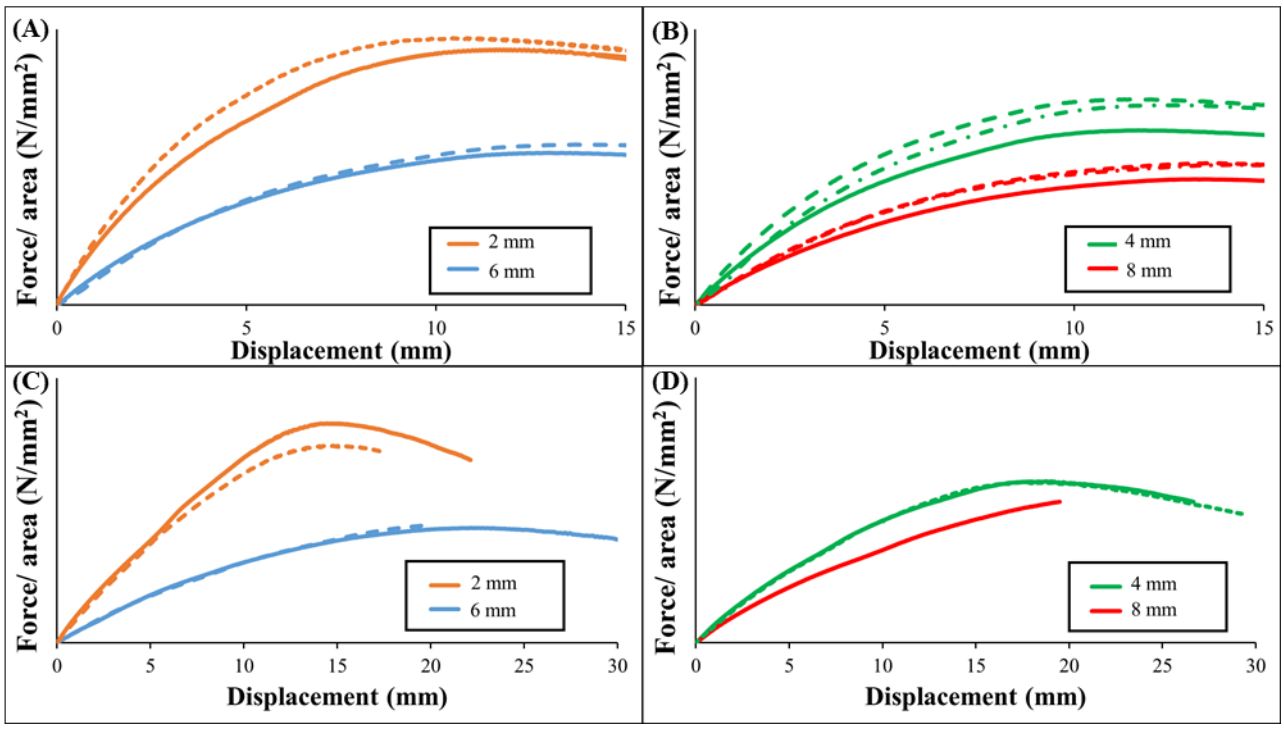

Figure 4-20 3PB test results of the sample whose foam nominal thickness is (A) 2 and 6 mm (B) 4 and 8 mm , 4PB test results of the sample whose foam nominal thickness is (C) 2 and 6 mm (D) 4 and 8 mm

4.5.2 PPC multilayer sample bending results

4.5.2.1 Global response

Figure 4-21 shows global results of samples extracted from 95% and 85% PPC plates subjected to the 3PB tests. The graph is plotted between global force per unit area (area of cross-section is calculated at the center of the sample) vs. global displacement imposed. The calculation of area is complex as the section is not uniform but not as variable as PE samples. Here the area is calculated with width and thickness at the center of the sample. Detail about samples dimension and displacement rate imposed during the 3PB tests is detailed in Table 4-3. For example, samples (samples extracted from a plate of 95% PPC) numbered 6 and 7 are subject to the same displacement rate, 1.25 10^{-2} s^{-1}, whereas sample 5 is subjected to 5 10^{-2} s^{-1}. Still, red curves (95%_6 and 95%_7) are well separated, which can be explained by local porosity, which is different, 8.96% and 10.63%, respectively. This gives evidence that the gradient of the porosity field influences the global results, so it is essential to consider this parameter in a predictive model. Sample numbered five is imposed with different displacement rates, and local porosity is different, which explains why the response curve is well separated. The porosity shown in Figure 4-21 seems lower in corresponding to samples numbered as 6 and 7 and justifies the stiffer response.

A similar trend has been observed with sky blue color curves (sample extracted from a plate with 85% PPC). Even though bending is performed at the same displacement rate, that is 2.5 10^{-2} s^{-1}, the mechanical response for the sample numbers 6 and 7 for 85% PPC is different due to the difference in local porosity (12.74% and 13.35% respectively). This also shows that a low difference in porosity influences the results.

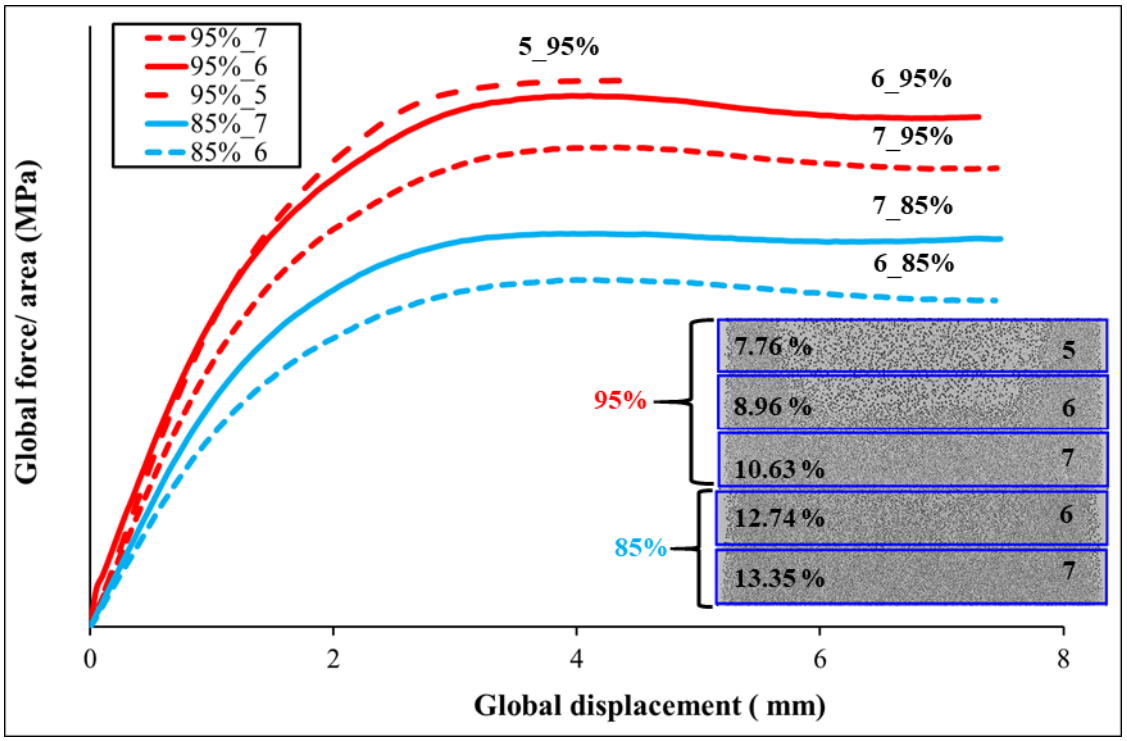

Figure 4-21 3PB test results of PPC multilayer samples extracted from global porosity of 95 and 85% plates

Figure 4-22 shows global results of samples extracted from global porosity of 90% and 80% PPC plates, subjected to 3PB. The graph is plotted between global force per unit area (area of cross-section is calculated at the center of the sample) vs. global displacement imposed. Detail about samples dimension and displacement rate imposed during the 3PB tests is detailed in Table 4-3. Green curves show the results of samples extracted from 90% of global porosity plates. Black curves show the results of samples extracted from 80% of global porosity plates. Green curves of samples numbered as 1 and 2 (90%_1 and 90%_2) are well separated as local porosity is different (9 and 9.39%, respectively). As there is no significant difference in local porosity still, there is separation in curves that can be explained by the fact that the thickness of that sample is not uniform along the length and width. Black curves of samples numbered as 10 and 11 are also well separated because of the difference in local porosity.

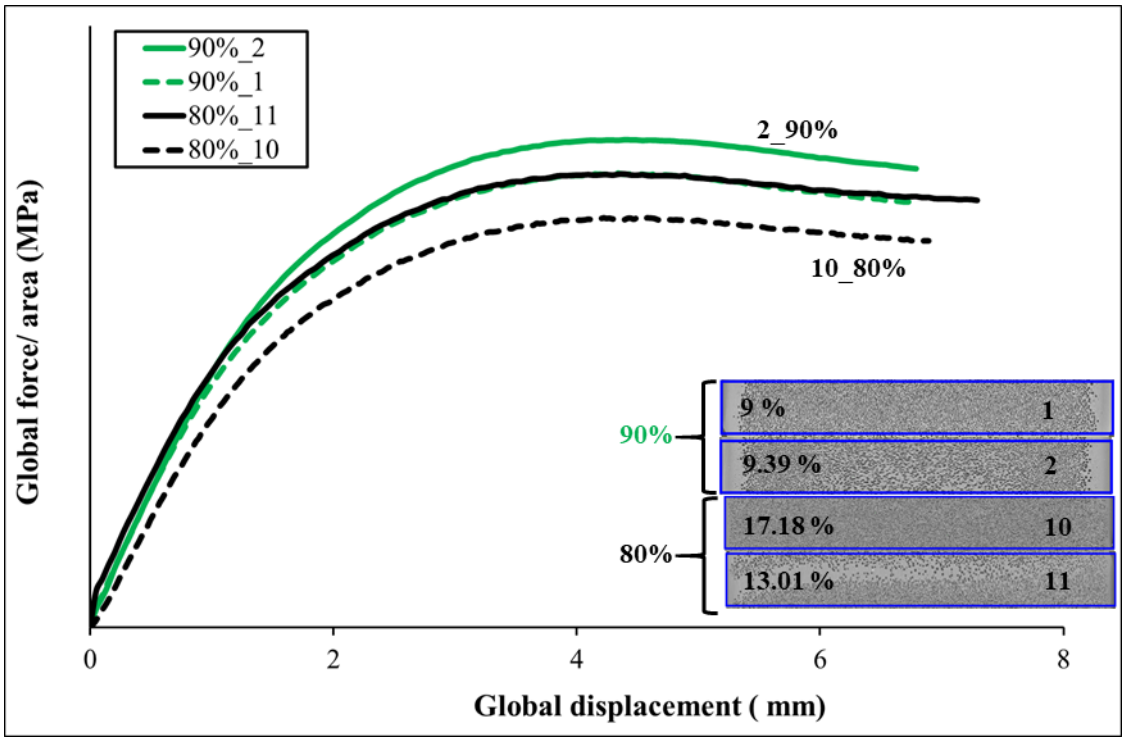

Figure 4-22 3PB test results of PPC multilayer samples extracted from global porosity of 90 and 80% PPC plates

It is also important to note that the shape of the response is very similar to that of the solid material tests. This implies that there should not be any significant difference in the mechanisms within the foam that would distort the response but this needs to be validated.

4.5.2.2 Mesoscopic analyze

As explained under heading 4.4.2, the camera and QUESTAR are used for the calculation of macroscopic and mesoscopic properties of the sample during the test. Figure 4-23 (A) and (B) show images taken by the camera at global displacement 0 mm and 6 mm respectively. Figure 4-23 (C) and Figure 4-23 (D) show images taken by the QUESTAR at global displacement 0 mm and 6 mm, respectively. Points indicated in Figure 4-23 (A) is used to calculate the local displacement. Various positions in an image from QUESTAR are used to calculate strain, which is the mesoscopic properties of the sample. As shown in Figure 4-18 (E) camera and QUESTAR are on the opposite side of the samples. Therefore, the red rectangle is shown in Figure 4-23 (A) and Figure 4-23 (B) on the opposite side of a sample where QUESTAR is taking images.

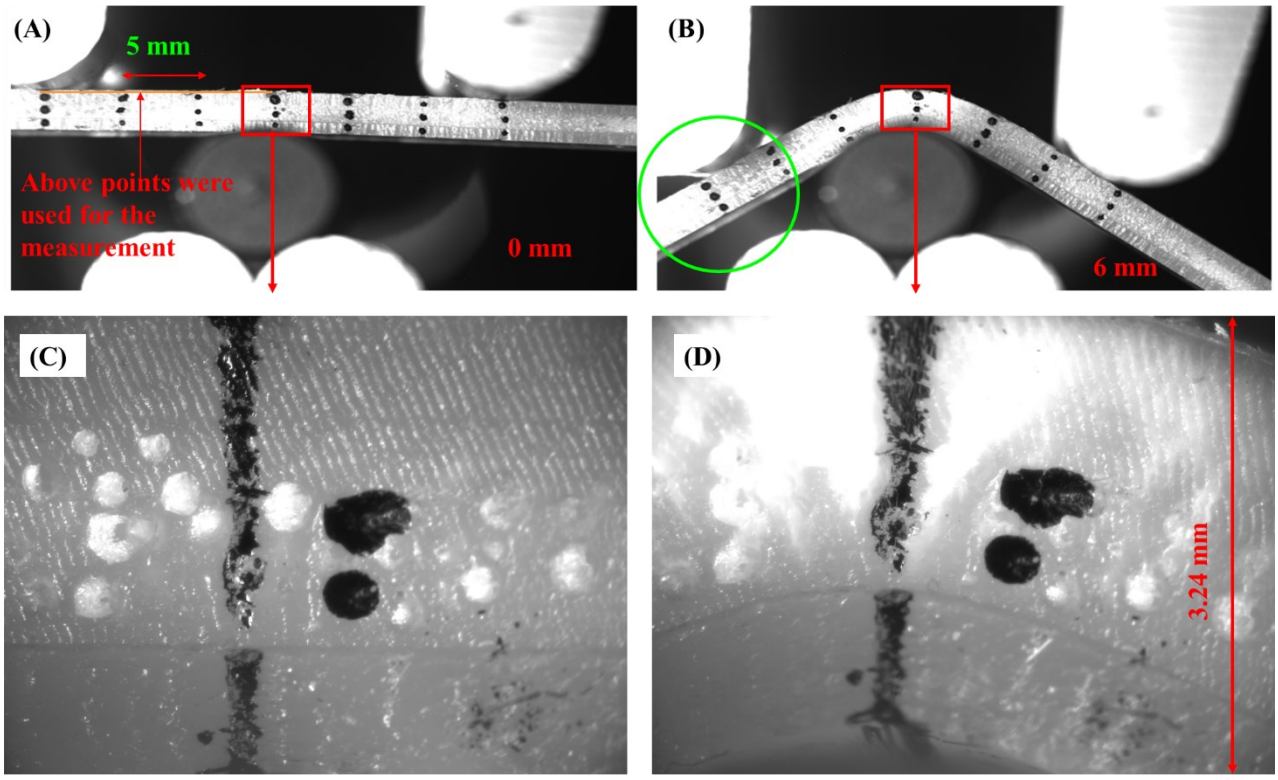

Figure 4-23 Image taken by the camera during bending test to calculate macroscopic properties at (A) Global displacement 0 mm (B) Global displacement 6 mm, Image taken by QUESTAR during bending test to calculate mesoscopic properties at (C) Global displacement 0 mm (D) Global displacement 6 mm

Results of macro and mesoscopic properties of sample 95% PPC numbered 5; are shown in Figure 4-24 (A) and Figure 4-24 (B), respectively. Figure 4-24 (C), Figure 4-24 (D), and (E) show the location where mesoscopic properties are calculated. Local displacements of the points, which are shown in Figure 4-23 (A) calculated at global displacements 2, 4, and 6 mm, are shown in Figure 4-24 (A). The images corresponding to respective global displacement are manually found, and displacements are calculated using ImageJ software. Similarly, corresponding images concerning global displacement from QUESTAR have been recovered, and manually strain is calculated at different locations as well as using different initial lengths are shown in Figure 4-24 (C), Figure 4-24 (D), and Figure 4-24 (E). Two black dots and one line (Figure 4-24 (C)) are made on sample thinking that can be used for the calculation, but at last, the strain is calculated at a different location using visible porosities as reference.

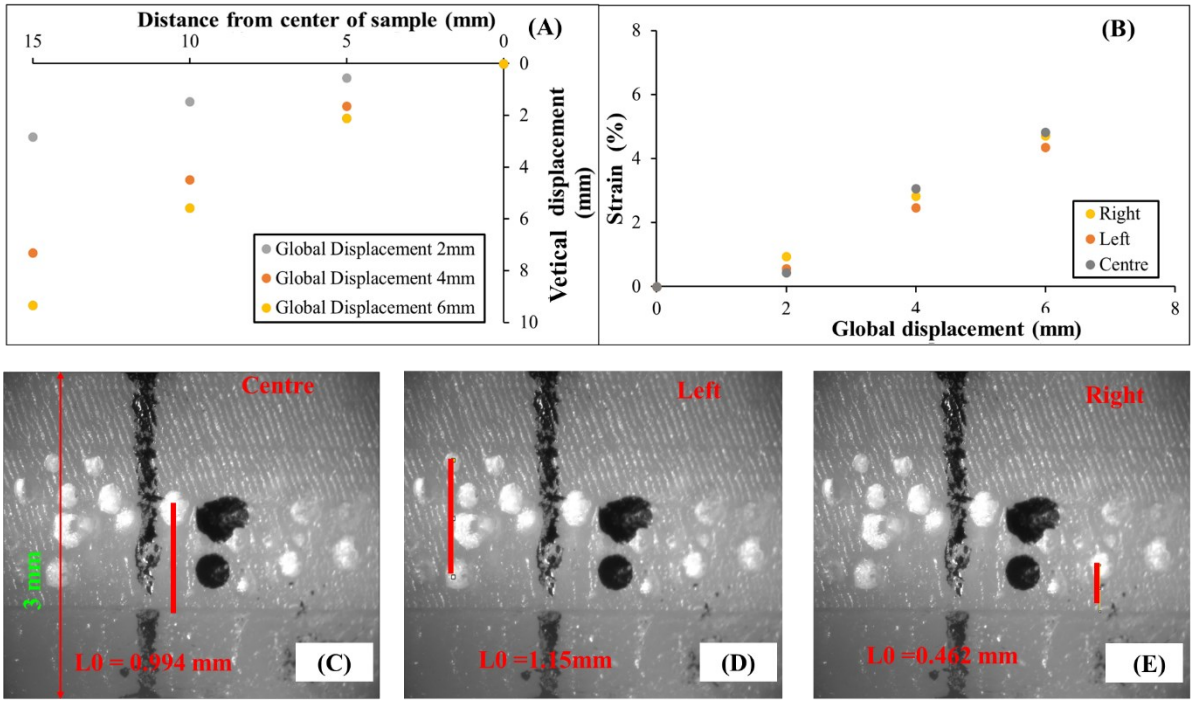

Figure 4-24 95% PPC sample-5 (A) Macroscopic (B) Mesoscopic properties results, location where mesoscopic properties are calculated (C) Centre (D) Left (E) Right

For all below figures (A) and (B) shows macro and mesoscopic results. Figures (C), (D), and (E) represent the position where strain is calculated.

Figure 4-25 - Show results sample 95% PPC numbered as 7.

Figure 4-26 - Show results sample 95% PPC numbered as 6.

Figure 4-27 - Show results sample 90% PPC numbered as 1.

Figure 4-28 - Show results sample 85% PPC numbered as 6.

Figure 4-29 - Show results sample 80% PPC numbered as 10.

Figure 4-30 - Show results sample 80% PPC numbered as 11.

General comments can be made from these results. As porosity increases, local strain is also increasing. When we talk about porosity, it means local porosity; even though the overall porosity of the plates may be high, the local porosity of the extracted sample may be lower than the macroscopic data. Moreover, the local porosity varies in the samples in a more or less critical way.

Generally, in the case of a constant field, the local strain in the center should be higher than that of the left and right sides. But this logic is not valid since the porosity is not uniform.

It is important to note that the strain calculation is strongly influenced by the initial length considered at a particular location. By examining the strain results below for different samples,

it can be seen that there is a gradient in the strain that mirrors the local porosity. Even though the overall displacement is 6 mm, the roller has a greater than 6 mm displacement at the lower point. The same can be seen in Figure 4-22 (A), which can be explained by the fact that the sample has moved from its initial position and slippage has occurred, as can be seen in Figure 4-23 (B) denoted by the green circle.

In this level of mechanical stress, the evolutions are quite linear, and the differences between the strain measurements on the side of the specimen in the foam fold are directly influenced by the porosity gradient.

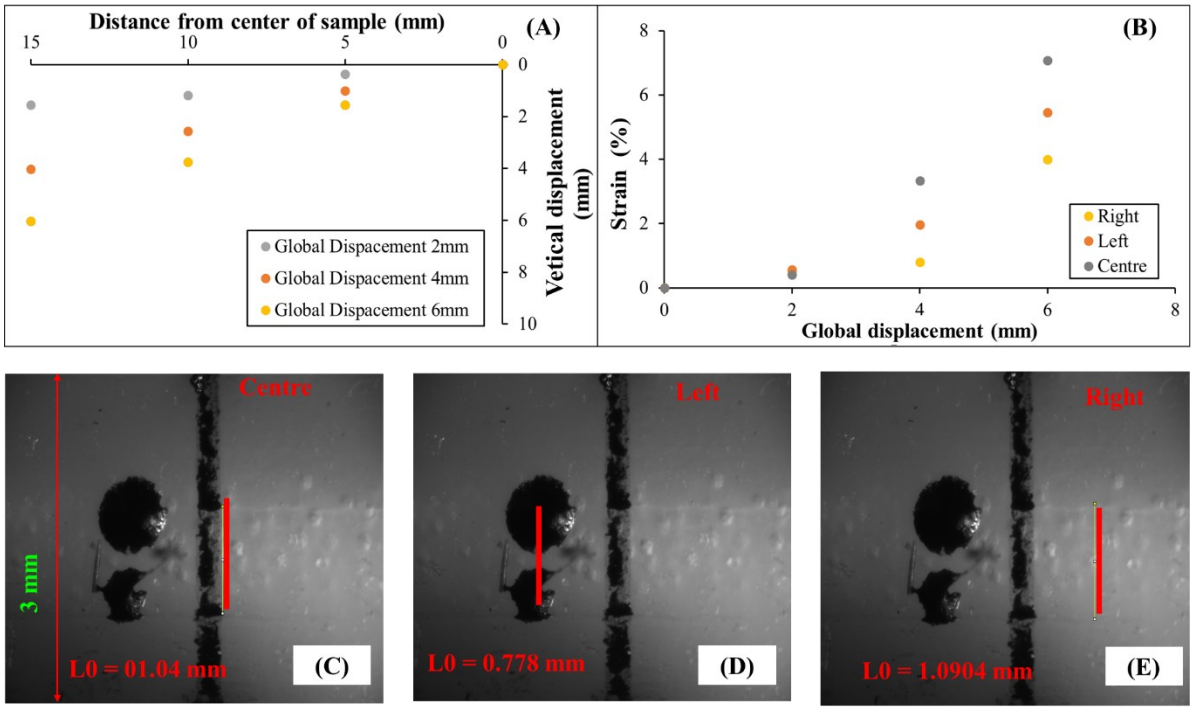

Figure 4-25 95% PPC sample-7 (A) Macroscopic (B) Mesoscopic properties results, location where mesoscopic properties are calculated (C) Centre (D) Left (E) Right

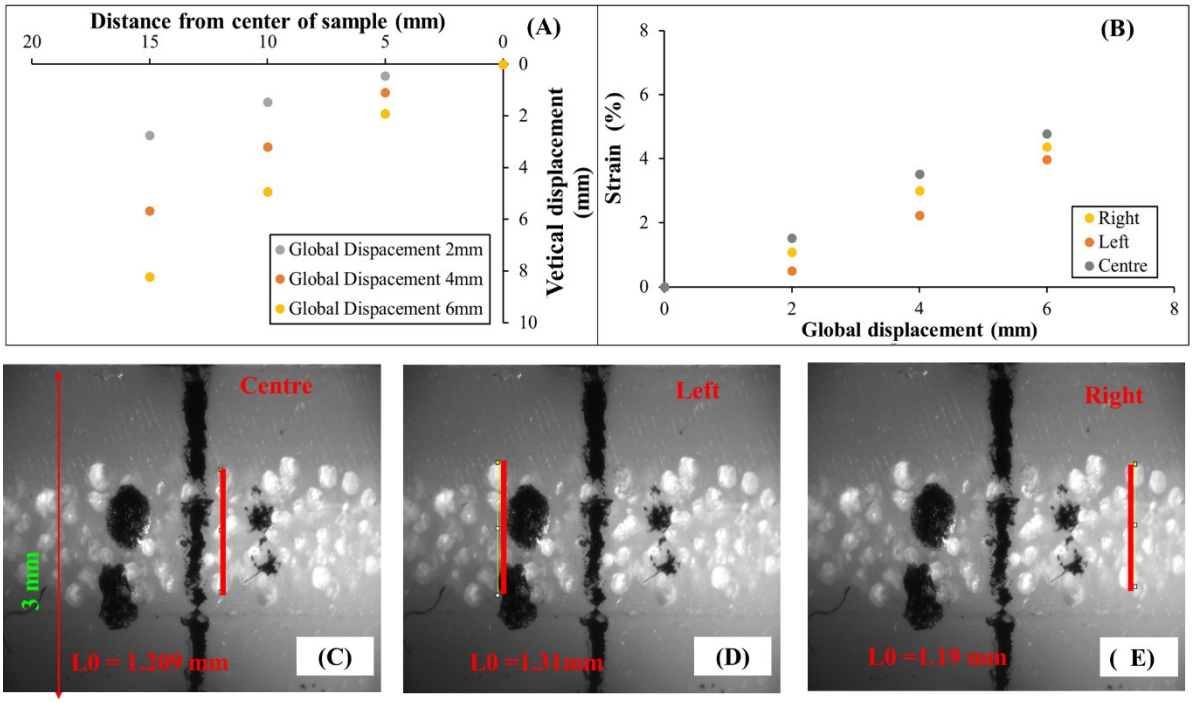

Figure 4-26 95% PPC sample-6 (A) Macroscopic (B) Mesoscopic properties results, location where mesoscopic properties are calculated (C) Centre (D) Left (E) Right

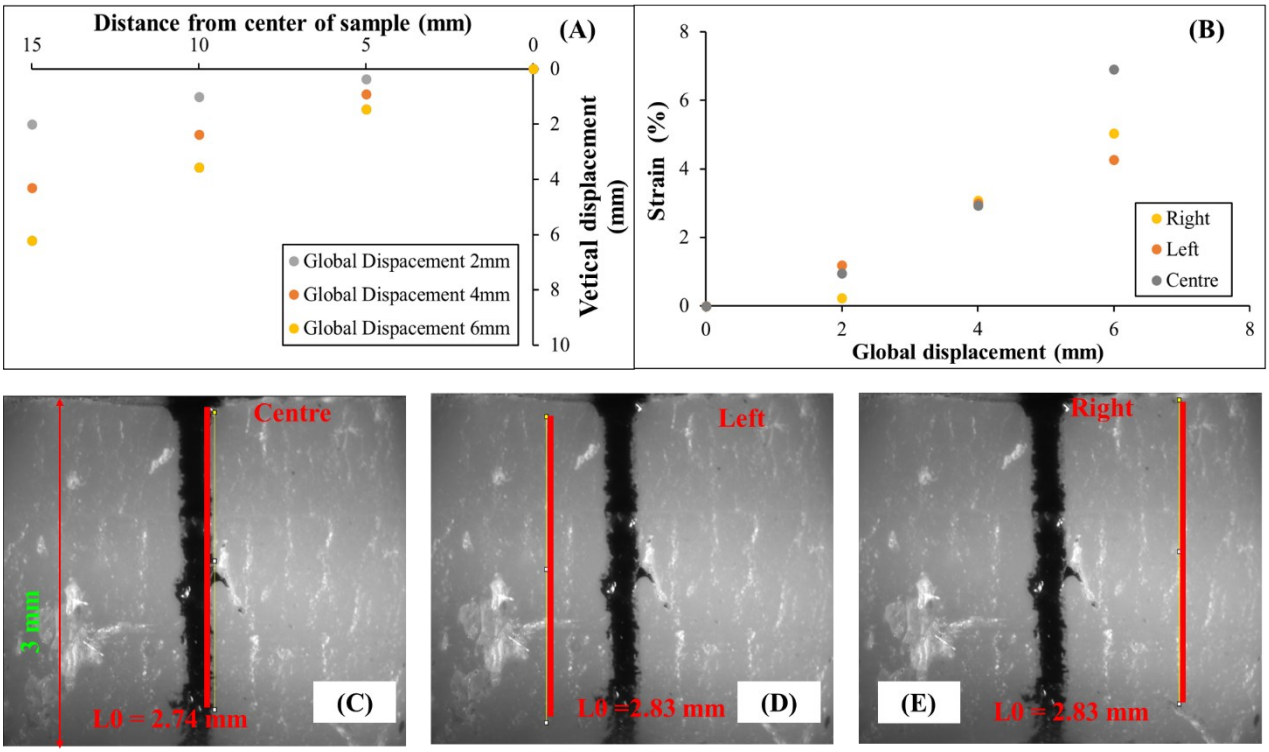

Figure 4-27 90% PPC sample-1 (A) Macroscopic (B) Mesoscopic properties results, location where mesoscopic properties are calculated (C) Centre (D) Left (E) Right

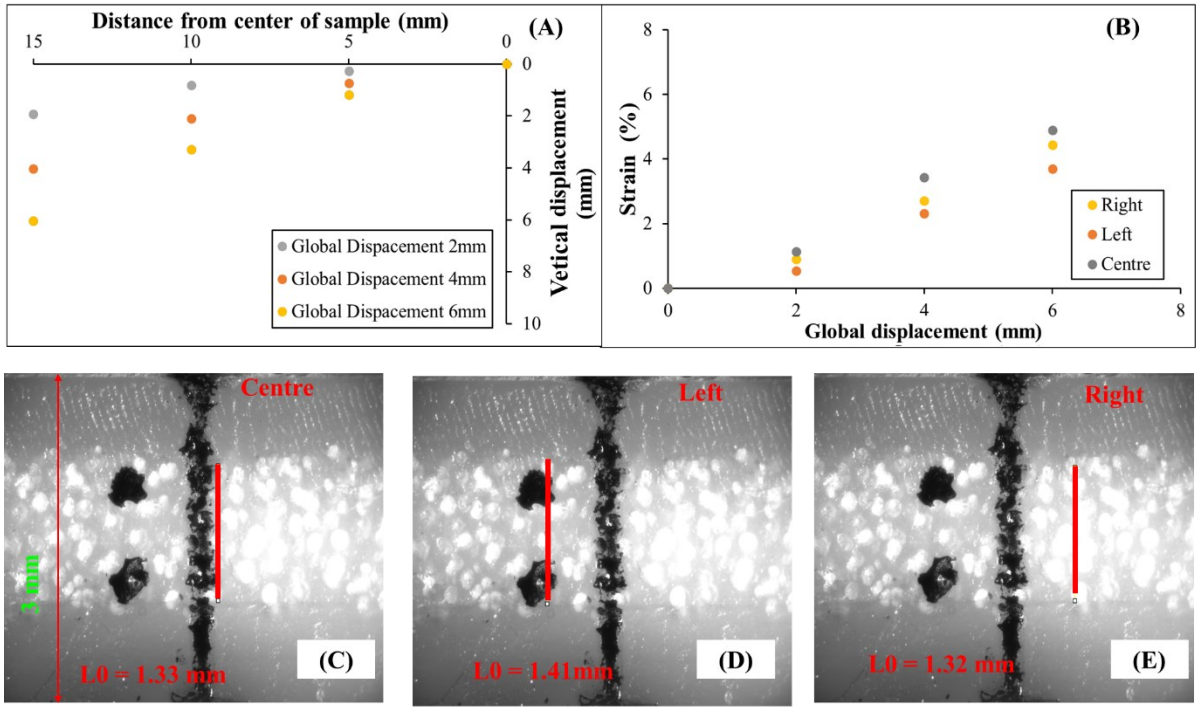

Figure 4-28 85% PPC sample-6 (A) Macroscopic (B) Mesoscopic properties results, location where mesoscopic properties are calculated (C) Centre (D) Left (E) Right

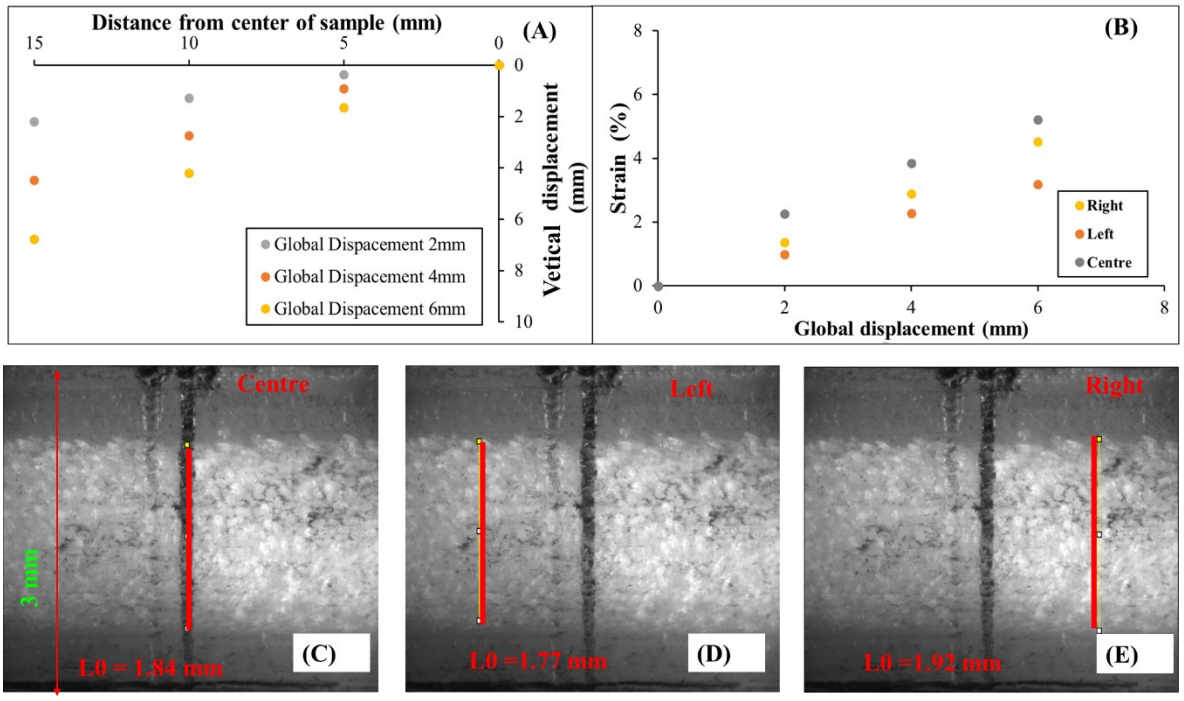

Figure 4-29 80% PPC sample-10 (A) Macroscopic (B) Mesoscopic properties results, location where mesoscopic properties are calculated (C) Centre (D) Left (E) Right

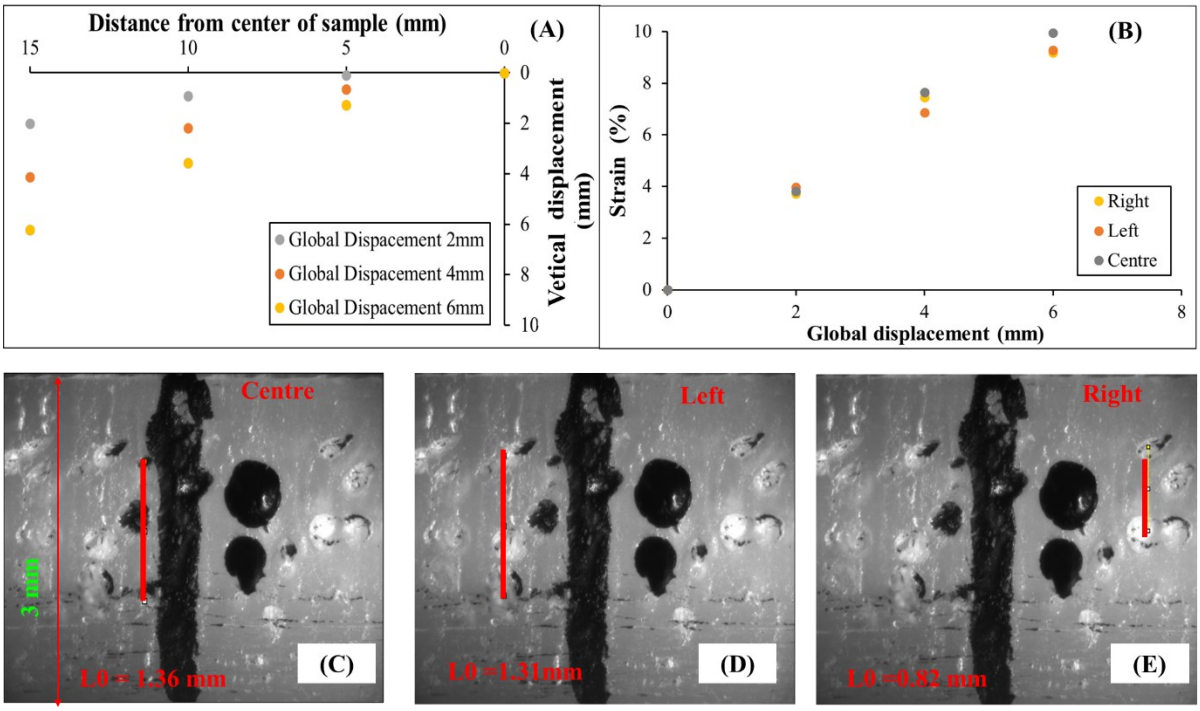

Figure 4-30 80% PPC sample-11 (A) Macroscopic (B) Mesoscopic properties results, location where mesoscopic properties are calculated (C) Centre (D) Left (E) Right

4.5.3 PPC bulk samples compression results

A compression test has been performed on bulk before performing on the sandwich sample in order to validate the protocol. Also, this test has been performed in order to verify if the displacement measured by the machine and at a local scale is the same or if there is some factor (stiffness of set-up). The sample with 7.95 x 7.5 x 3.05 mm (length x width x thickness) is subjected to the 0.0125 $mm.s^{-1}$ global displacement rate during the compression test. Displacement of two markers (Figure 4-31 (A)) has followed by the camera using software idpix 1.7 software (developed in-house by the Pprime lab) this gave use the local information of the displacement. Another test with the same dimension of a sample with the same displacement rate has been performed with the sample in focus. During the test, every second image is taken. The same has been shown in Figure 4-31 (B) and for global results, Instron machine data is taken after the test.

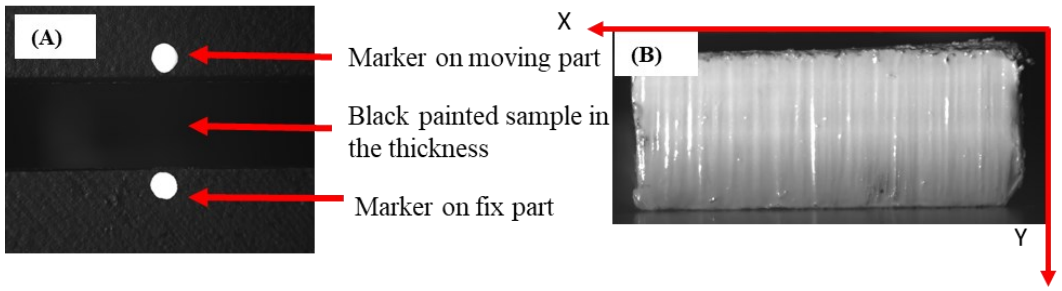

Figure 4-31 (A) Image taken by the camera by focusing on the markers on the moving and fix part (B) Image taken by the camera focusing on the sample during the compression test

Figure 4-32 (A) shows that global and local displacement are not the same. So it is interesting to take the ratio of them to find out the factor that can correspond to the stiffness of the sept-up. Figure 4-32 (B) shows how the ratio varies with force.

Thus, it is proposed to multiply the machine displacement by this ratio to compare the results with the simulation data to eliminate the rigidity of the setup.

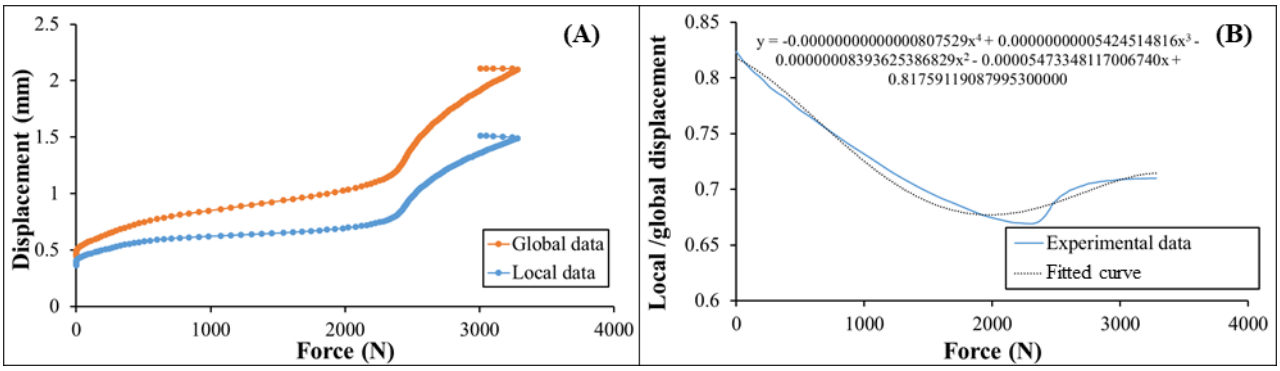

Figure 4-32 (A) Global and local displacements vs. force during compression test (B) Ratio of local/ global displacement vs. force

It is clear that global data should be corrected, it should be quantifying the influence on strain at the scale of the sample thickness. Figure 4-33 shows local and global, true stress vs. strain data. The compressive strain is calculated by the evolution of the length with logarithm definition, and the stress is estimated with the force of the initial section and the evolution of the section. For calculation of area of cross-section, isotropic, and iso-volume assumption is made, and using Equation (21) cross-section at a given instance is calculated

$$S = S_0 * (\exp(-0.5\,\varepsilon_l))^2 \quad (21)$$

Where S = current cross-section, S_0 = initial cross-section and ε_l is true longitudinal strain.

True stress is calculated by using this current section.

The yellow curve is when stress-strain is calculated without multiplying the corrected ratio, whereas the orange curve shows local data calculated using two markers on the moving and

the fixed plate. It is clear that there is a difference in these two curves is due to global displacement is not the same as local (Figure 4-32 (A)).

After multiplying global data with the ratio, corrected data is constructed. Figure 4-33 shows a comparison between corrected global data and not corrected global data. Yellows curve represents before multiplying with the ratio that is not corrected data whereas the blue curve shows corrected data. It can be observed that corrected global data (blue curve) and local data (orange curve) are very close. The correction is consistent.

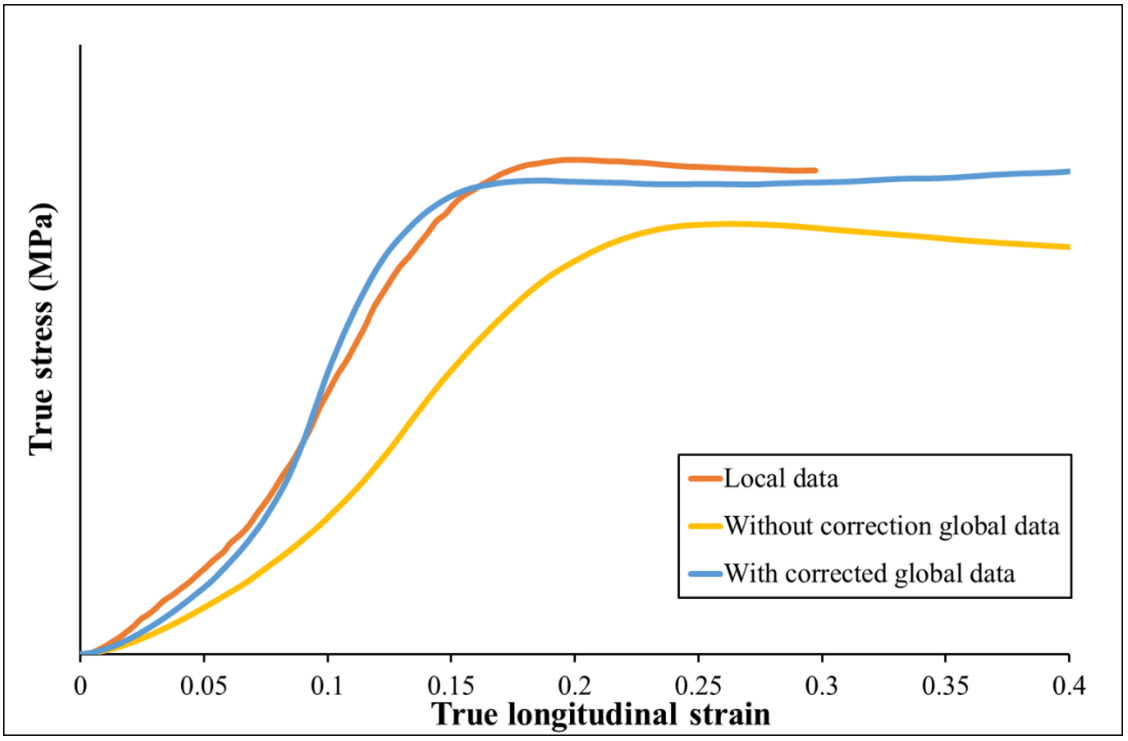

Figure 4-33 True stress vs. strain of local and global data before and after correction

Digital image correlation (named in the following, DIC) is performed using Ncorr V1.2 [143] in Matlab®. Ncorr is an open-source 2D digital image correlation Matlab® program. It has an accessible and intuitive GUI, uses many novel 2D DIC algorithms, is wholly contained within the Matlab® environment, and contains plotting tools for figure creation. The computationally intensive algorithms are optimized using C++/MEX, while the GUI is written mainly in m-code. The idea is to give the users an easy-to-use, efficient, and flexible DIC program [143]. This software is capable of calculating the field of displacement between two images. In software, first, we have to choose the radius of a circle. The pattern in this circle is found in the displaced image and then determines the displacement field. This circle is translated as defined by the subset spacing to build the field. If the radius of the circle decrease, it is essential to check that the variability of the image is pronounced enough. This size has a limit corresponding with the image, but in this case, it is necessary to estimate the fluctuation of a field in the foam layer and find the minimum radius value. If the radius value is kept the same and the

grid decreases the description in the field space, more points are obtained. At the same time, the calculation will increase, so parameters should be chosen to have a good compromise between accuracy and time of calculation.

Image from global data at 200 N and 0 N has been selected for the DIC. The software has given the results that have been presented in Figure 4-34. From Figure 4-34 (B), it can be seen that displacement in the Y-axis is not uniform, which clearly helps to conclude that the sample is not totally flat. There is heterogeneity in the thickness of the sample along the length (X-direction).

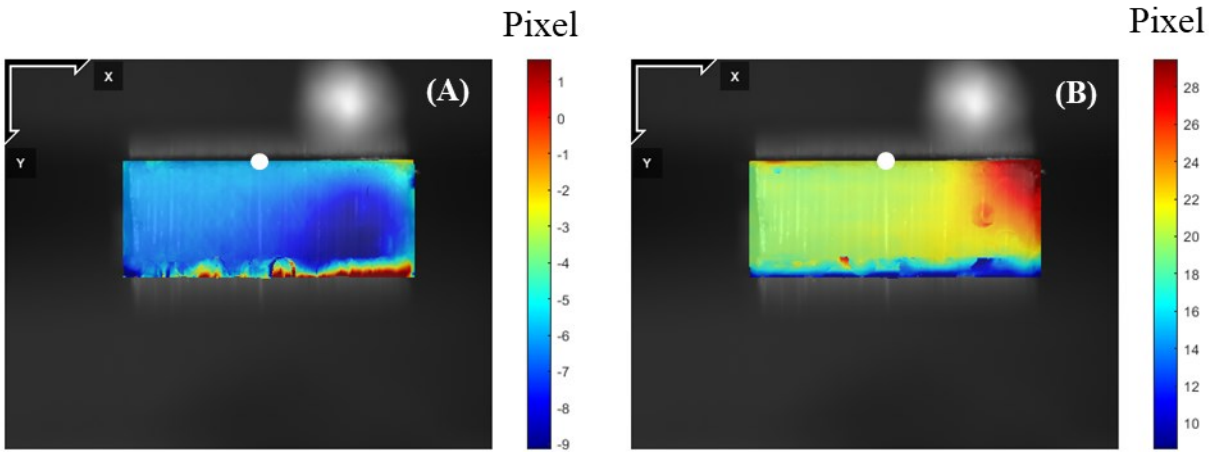

Figure 4-34 DIC images for the force 200 N (A) Displacement in X-direction (B) Displacement in Y-direction

A study about how parameters of DIC affect the same results has been presented in Figure 4-35. Different cases with respect to parameters of DIC are formed and presented below.

- For case-1 subset radius and subset spacing is 87 and 7 pixels (Figure 4-35 (A)).
- For case-2 subset radius and subset spacing is 40 and 7 pixels (Figure 4-35 (B).
- For case-3 subset radius and subset spacing is 87 and 7 pixels (Figure 4-35 (C).
- For case-4 subset radius and subset spacing is 100 and 15 pixels (Figure 4-35 (D).

After calculating displacement at the center (white point shown in Figure 4-34) for case-1, 2, 3, and 4 are 20.57, 20.22, 20.17, and 23.883, respectively. From this, it can be concluded that there is a maximum 4-pixel difference at center thickness, which is quite small, but still, that is variability in the results. For further calculation, case-1 parameters are used, which is a good optimization point between the time of calculation and accuracy.

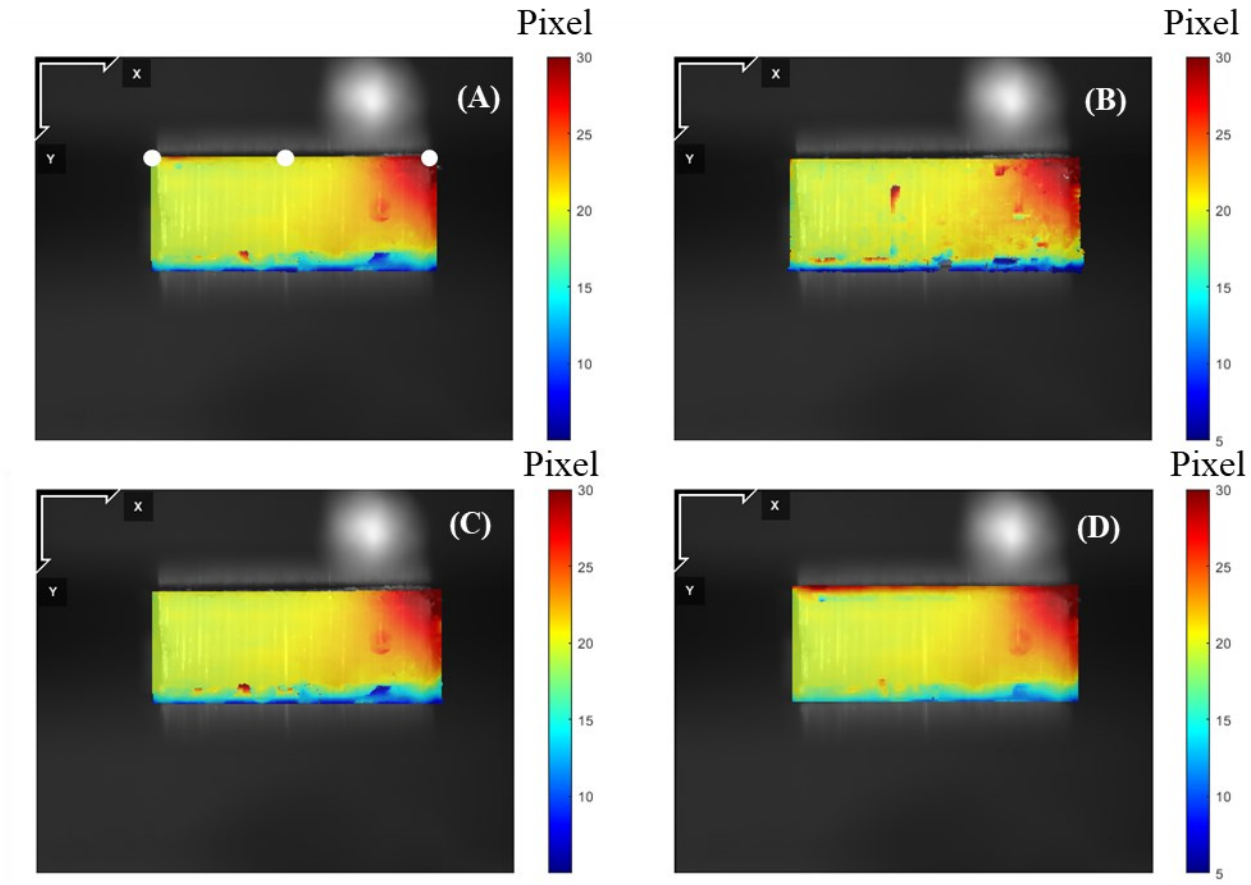

Figure 4-35 DIC images for the force 200 N for displacement in the Y-axis with different parameters of software (A) Case-1 (B) Case-2 (C) Case-3 (D) Case-4

Five images have been selected from global data experiments at 0, 200, 605.16, 1047.3, and 2001.7 N. Using DIC displacement in the thickness has been calculated at three different locations left, right, and center (as shown in Figure 4-35 (A) with white dots). After that true strain is calculated using displacement in the thickness. Using DIC data, true stress vs. strain is plotted in Figure 4-36 at a different location (black dots - left, blue dots - center, and red dots - right location). From the results, it can be concluded that strain in the sample is not uniform as well as the slopes of the curve resulting from the displacement measurements of the plates and DIC data are different.

In order to verify the data of DIC, manually by ImageJ displacement in the thickness at corresponding force is calculated at the center. Similar to DIC, data from ImageJ is treated to calculate the true stress and strain. The same has been plotted in Figure 4-36.

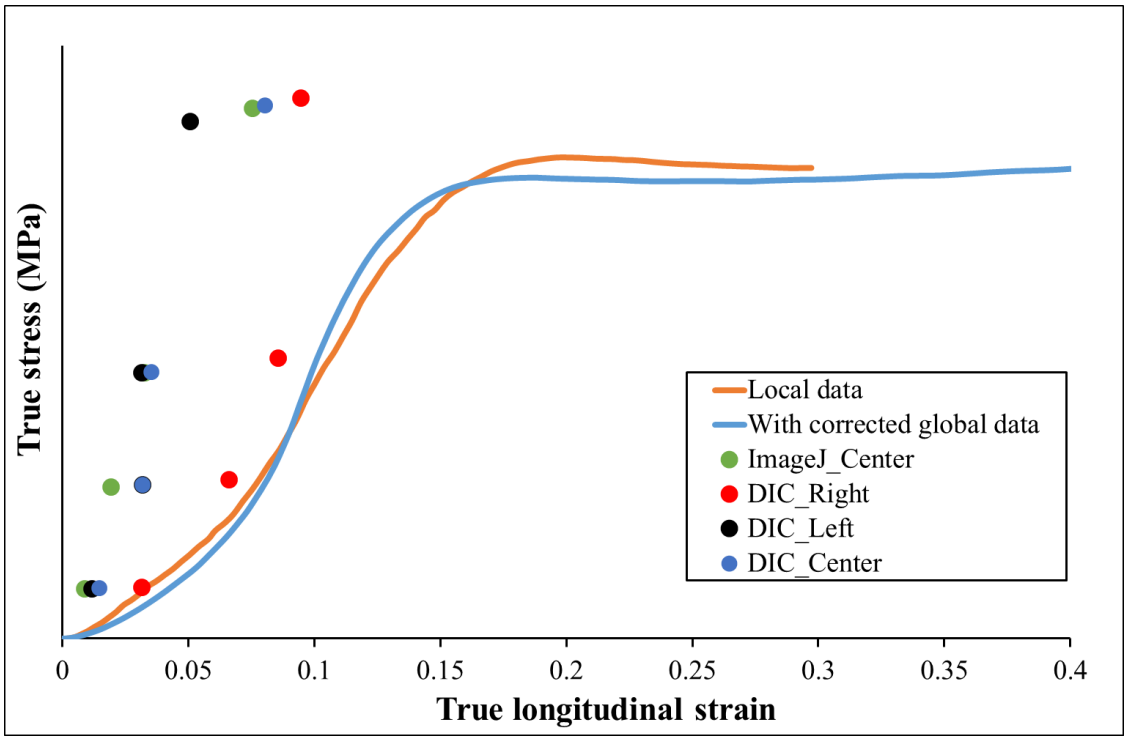

Figure 4-36 True stress vs. local and global strain along with DIC and ImageJ data

The effect of the geometrical defects of the specimen on the global response curve is clearly visible. It should be noted that the thicker side is very close to the global curve.

4.5.4 PPC multilayer samples compression results

4.5.4.1 Global response

80% PPC samples compression results, global displacement vs. global force have been shown in Figure 4-37. Sample dimensions and applied displacement rate (1 - 0.0025, 2 - 0.00025, 3 - 0.0125, and 5 - 0.025 $mm.s^{-1}$) during compression tests have been mentioned in Table 4-4. All different color curves are well separated, which can be explained by the two facts, different displacement rates applied as well as different local porosity. Different local porosities images are also shown in Figure 4-37 that are obtained after tomography to compare the variability in a better way.

The black, green, and red curve have three slopes; the first slope is indicative of the sample comes in complete contact with the upper support. In the case of sample-2 where the porosity seems homogeneous, the first slope does not appear, and the stiffness is close to that of the second slopes observed on samples numbered 1, 3, and 5. This result confirms the hypothesis that the beginning of the curves corresponds to the loading and not to a pore closure.

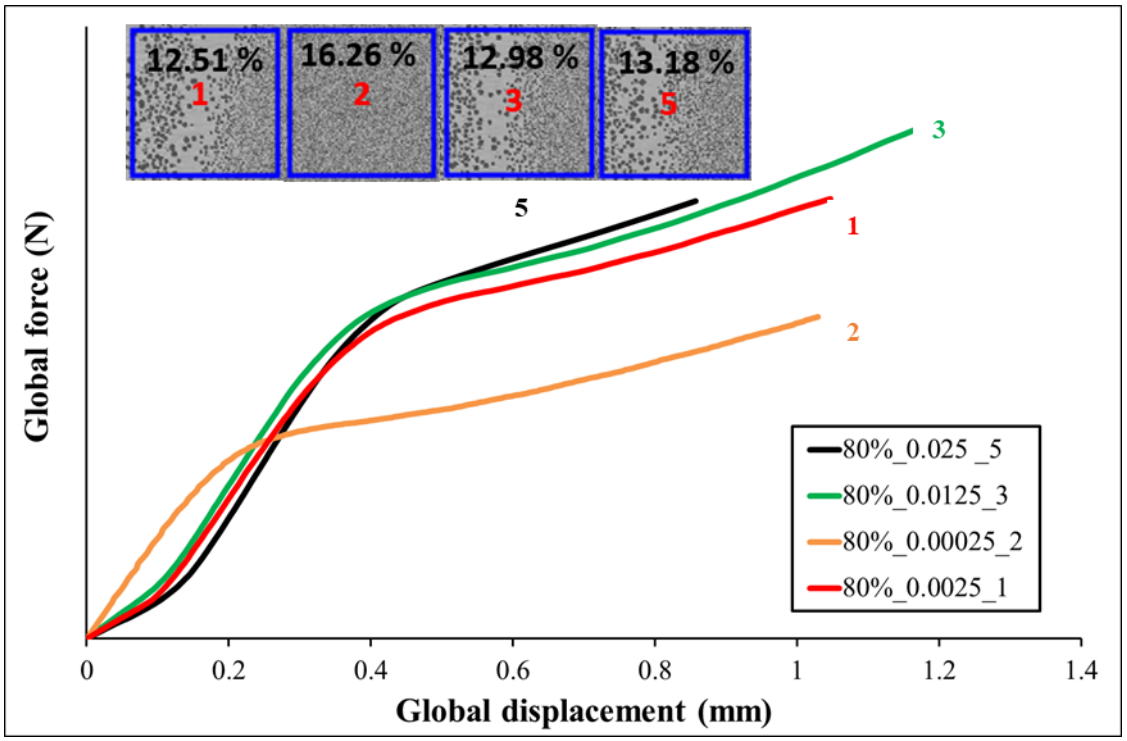

Figure 4-37 Compression results of 80% PPC multilayer samples

Consequently, as samples are not flat and there is heterogeneity in the thickness, it is essential to change the initial points of experimental data. The area is plotted on the Y-axis force per unit to remove the area effect on the results. New results with these changes are presented in Figure 4-38.

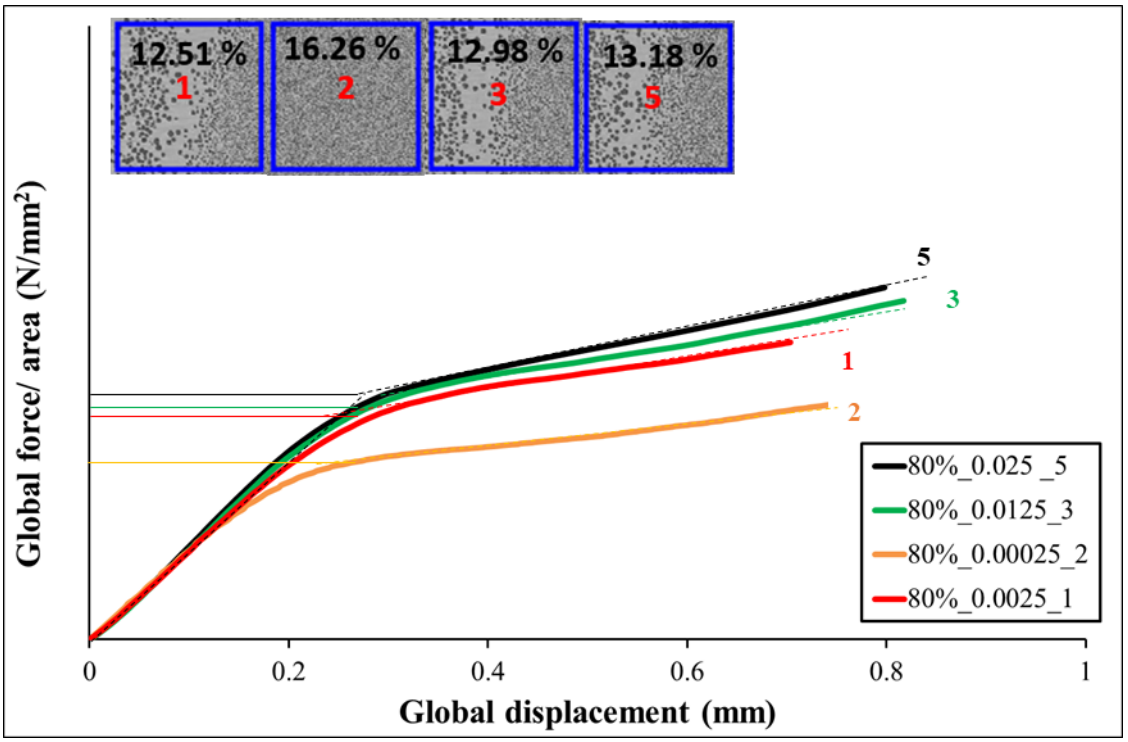

Figure 4-38 Compression results of 80% PPC multilayer samples with change of origin

As explained above (Figure 4-32) that there is a ratio between global and local displacement. Figure 4-39 shows results after the correction of global displacement.

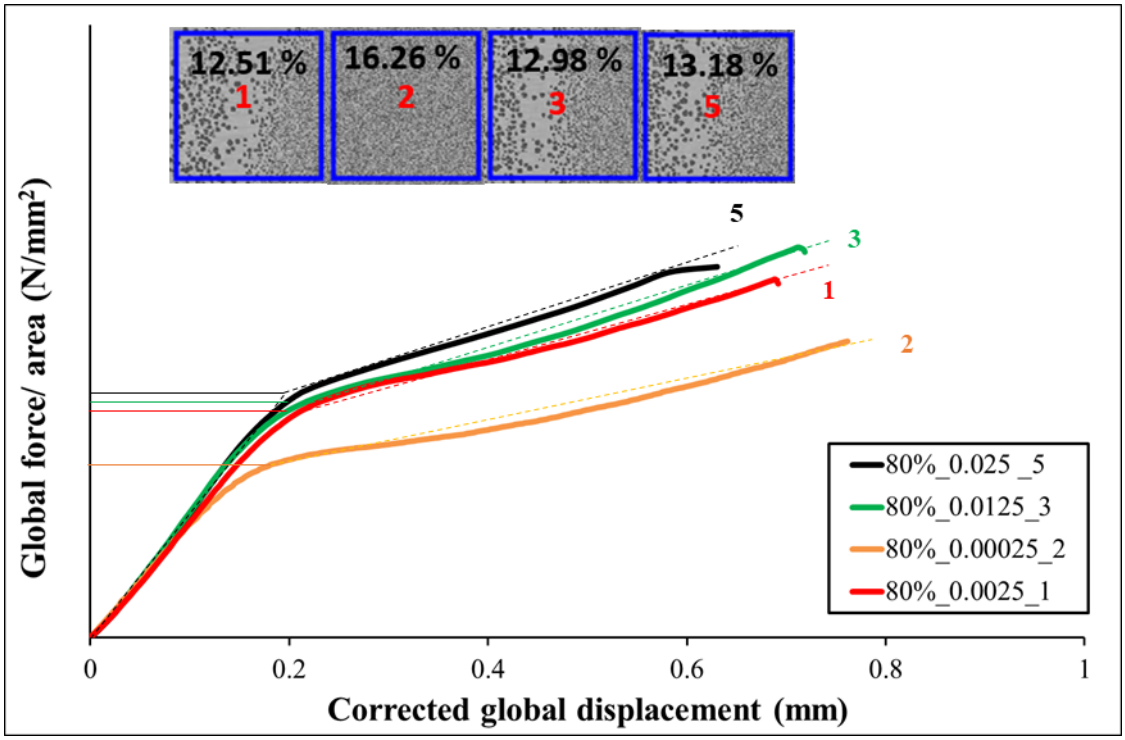

Figure 4-39 Compression results of 80% PPC multilayer samples with a change of origin and corrected global displacement

For the analysis of foam Young's modulus, a very simple study can be performed (see appendix to demonstration) Young's modulus of foam can be estimated by this relation in the interval of force 0 to 200 N:

$$E^{foam} = \frac{\left(F/S\right) l_{f1}}{\delta - \frac{F/S}{E^{bulk}}\left(l_{s1} + l_{s2}\right)} \tag{22}$$

where δ is a change in length of the sample, l_{s1} is the actual length of bottom skin, l_{s2} is the actual length of bottom skin, l_{f1} is the actual length of foam, F is force, S is an area of cross-section, E^{bulk} is Young's modulus of bulk (skin).

By using this simple equation, Young's modulus of foam has be calculated, and the results are mentioned in Table 4-5.

Sample number	Displacement rate (mm.s^{-1})	Color of curve	Slope_1	Slope_2	Local porosity (%)	Global porosity (%)	Young's modulus of foam (MPa)
1	0.0025	Red	65.70	14.06	12.51	80	79.16705
2	0.00025	orange	59.76	11.67	16.26	80	79.707
3	0.0125	Green	74.16	17.32	12.98	80	78.93
5	0.025	black	73.06	18.42	13.18	80	78.8711

Table 4-5 Detailed information of 80% PPC samples

In Figure 4-39, two straight lines are fitted to know the slope at the beginning of the curve and at the hardening part of the curve. The beginning line slope is represented in Table 4-5 as slope_1 and the hardening part line slope is as slope_2. As porosity in the sample is quite similar. The slope of two lines increases as the displacement rate imposed increases. For example, in Table 4-5 it is clearly visible using sample-5 and sample-2. The imposed displacement rate on sample-5 is 0.025 mm.s^{-1} slope of lines 1 and 2 is more as compared with sample-2 which imposes a displacement rate of 0.00025 mm.s^{-1}. As mentioned in Table 4-5 for all the samples, Young's modulus of foam is between 78.87 to 79.70 MPa. Therefore, it can be concluded that Young's modulus of foam is close in all the samples.

90% PPC samples compression results, global displacement vs. global force are shown in Figure 4-40. Sample dimensions and applied displacement rate (4 - 0.00025, 5 - 0.0025, and 6 - 0.025 mm.s^{-1}) during compression tests have been mentioned in Table 4-4. The same trend-like 80% of the sample, has also followed here. The separation of the curve is influenced by the two factors first is porosity and displacement rate applied during the compression. Here samples numbered 4 and 5 have the same porosity, still, curves are separated due to different displacement rates imposed that are 0.00025 and 0.0025 mm.s^{-1}, respectively.

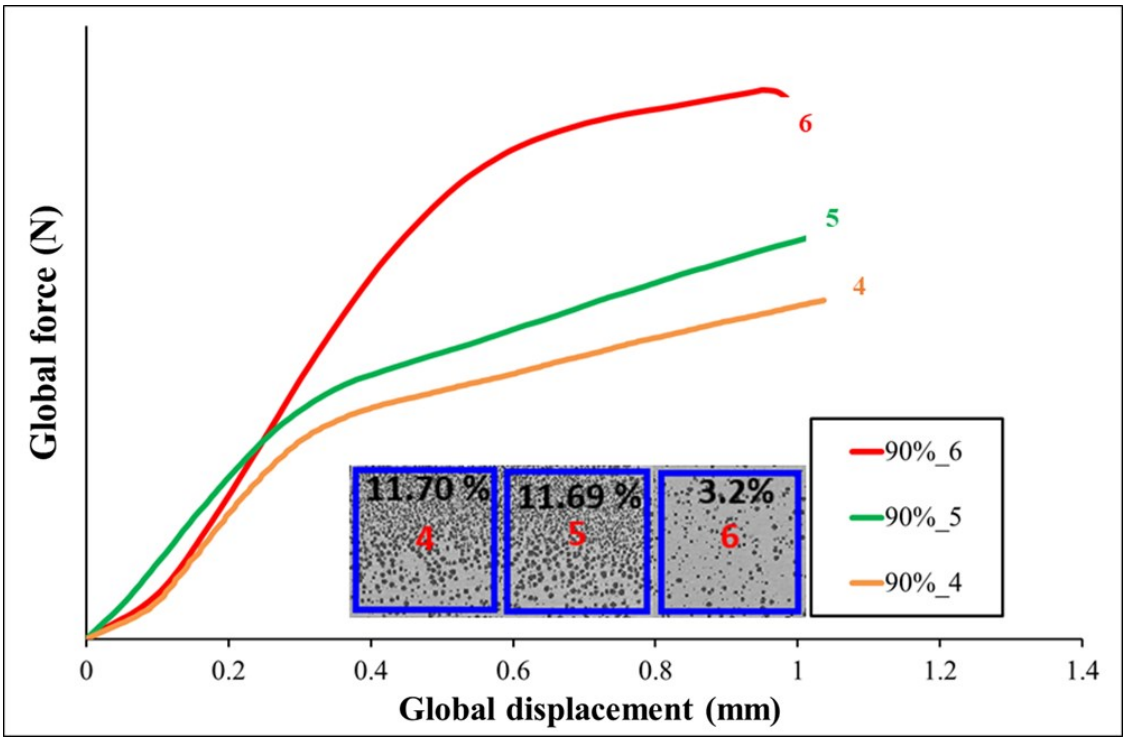

Figure 4-40 Compression results of 90% PPC multilayer samples

As samples are not flat, there is heterogeneity in the thickness. It is necessary to change the initial points of experimental data. The area is plotted on the Y-axis force per unit to remove the area effect on the results. New results with these changes are presented in Figure 4-41.

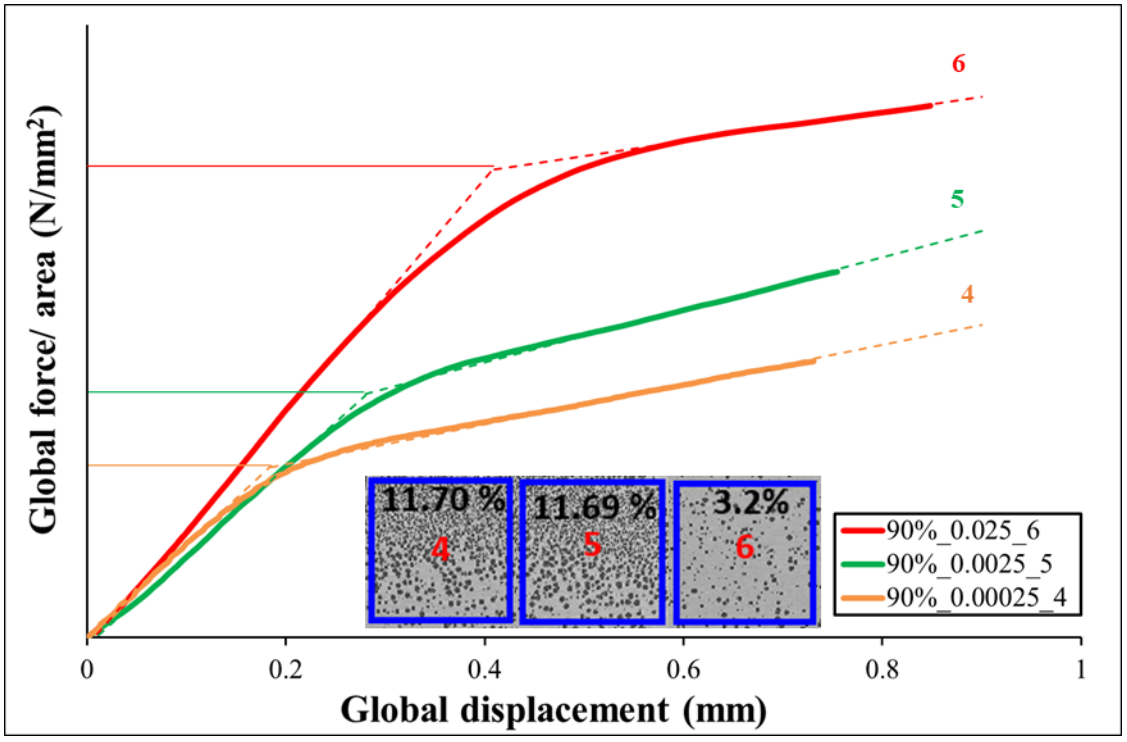

Figure 4-41 Compression results of 90% PPC multilayer samples with change of origin

As explained above (Figure 4-32), there is a global and local displacement ratio. Figure 4-42 shows results after the correction of global displacement.

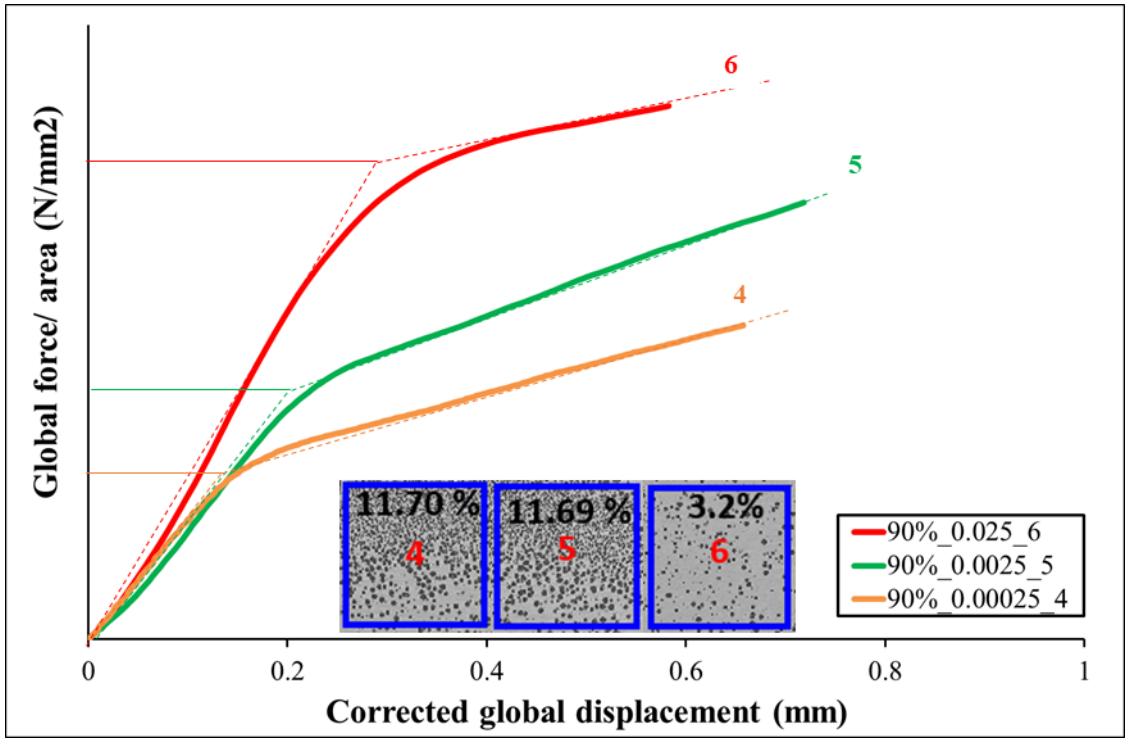

Figure 4-42 Compression results of 90% PPC multilayer samples with the change of origin and corrected global displacement

On this last graph (Figure 4-42), the effect of the porosity is perfectly quantifiable; the limit of strong loss of stiffness changes. We find a sensitivity of the strain rate, which is always expressed in the foam with a similar magnitude to that observed for the bulk material. At the beginning of the curve, variations are observed (Figure 4-40), which are indeed due to the placement of the sample on the friction mount or to the gaps in the fixture.

In Figure 4-40, two straight lines are fitted to know the slope at the beginning of the curve and at the hardening part of the curve. The beginning line slope is represented in Table 3-1 as slope_1 and the hardening part line slope is as slope_2. As porosity in the sample is not similar as compared to 80% PPC sample. Slope_1 is increasing with an increase in imposed displacement rate except for sample number 5. Slope_2 shows a trend as imposed displacement rate increases slope increase for similar porosity, the same can be observed with samples-4 and 5. It is interesting to note that as the porosity decreases, the slope_2 decreases, as observed with sample-6. As mentioned in Table 4-6 for all samples, Young's modulus of the foam is between 77.38 and 78.107 MPa. Therefore, it can be concluded that Young's modulus of the foam is also almost the same for all samples.

Sample number	Displacement rate ($mm.s^{-1}$)	Color of curve	Slope_1	Slope_2	Local porosity (%)	Global porosity (%)	Young's modulus of foam (MPa)
4	0.00025	Orange	53.037	11.364	11.7	90	78.107
5	0.0025	Green	66.16	20.73	11.69	90	77.64
6	0.025	Red	97.385	11.69	3.2	90	77.385

Table 4-6 Detailed information of 90% PPC samples

Compression experimental data and more specific relation force displacement will be used for validation of the constitutive model of the PPC and RVE of foam.

4.5.4.2 Local response correlates to the global response

Results of macro and mesoscopic properties evaluation of sample 80% PPC numbered 3 are shown in Figure 4-43 (A) and Figure 4-43 (B), respectively. Figure 4-43 (C), (D), and (E) show the location where macroscopic and mesoscopic properties are calculated. Local displacements of the points which are shown in Figure 4-43 (C) calculated at global forces 500, 1000, and 1500 mm are shown in Figure 4-43 (A). Manually images corresponding to respective global forces are found and displacements are calculated using ImageJ software. Similarly, corresponding images with respect to global force from QUESTAR have been recovered, and manually strain is calculated at the location and the initial length is shown in Figure 4-43 (D). Figure 4-43 (E) shows the final length and location where strain is calculated. It is important to note that we have taken global force as a reference, unlike previously global displacement. As imposed global displacement is a very small displacement that's why there is more error in the corresponding image finding manually to global displacement that's why it got changed to a global force.

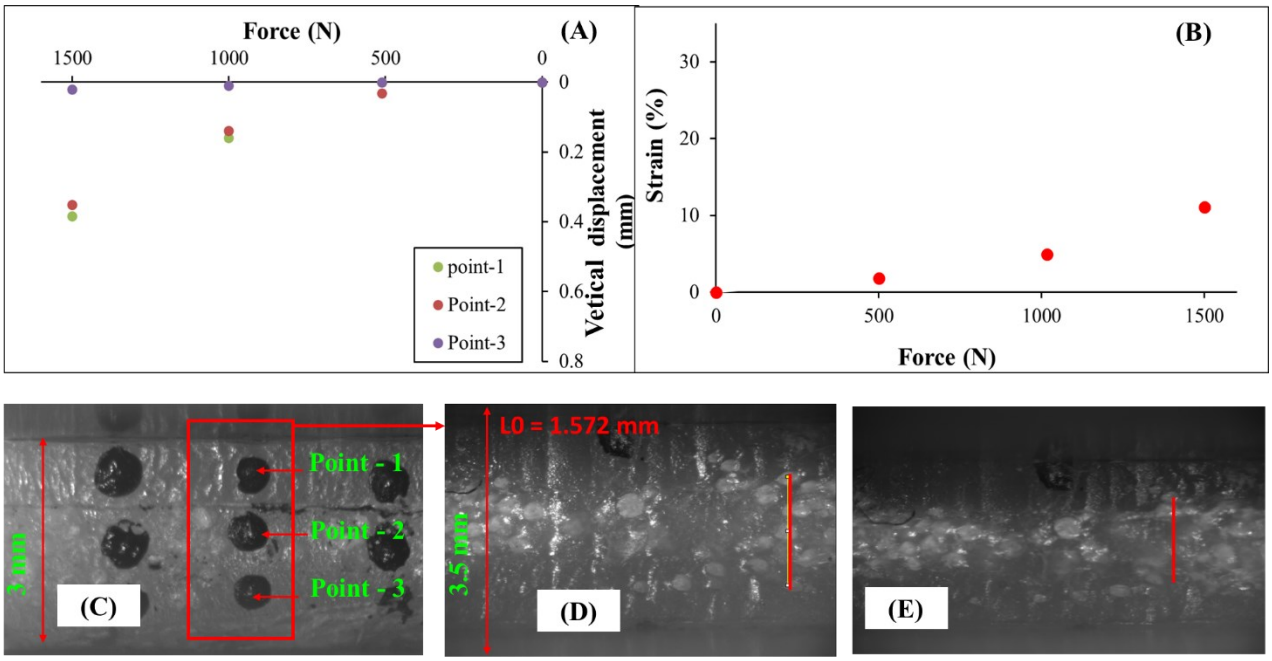

Figure 4-43 80% PPC sample-3 (A) Macroscopic (B) Mesoscopic properties results (C) Location where macroscopic properties are calculated, Location where mesoscopic properties are calculated (D) Initial (E) Final state

To verify the results obtain using ImageJ, DIC is performed on 80% PPC sample-2. The displacement of Point-1, 2, and 3 has been calculated and plotted in Figure 4-44. It can be seen that values are quite similar to values obtained by ImageJ software using manual calculation.

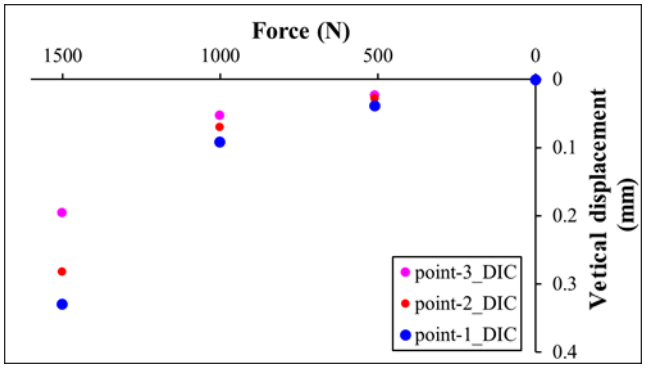

Figure 4-44 80% PPC sample-2 macroscopic properties are calculated

Figure 4-45 (A), Figure 4-45 (B), Figure 4-45 (C), Figure 4-45 (D), and Figure 4-45 (E) show strain in the X-direction, shear in-plane X-Y, strain in the Y-direction, displacement in the X-direction, and in the Y-direction, respectively. For calculation of these results using software Ncorr under Matlab® is used. During DIC subset radius is 39 pixels and subset spacing is 5 pixels. Two images at 0 N and 511 N are selected for the performance of image correlation. From Figure 4-45 (A) to Figure 4-45 (C) it can be observed that there is a gradient in strain along with the thickness of the sample. Strain in the X-direction is very complex locally (Figure 4-45 (A)), some areas are in transverse tension and another in compression. The shear strains

are low (Figure 4-45 (B)), but it fluctuates with the mesostructure, which is a good indicator of heterogeneity. In direction of compression, the strain does not present a constant value (Figure 4-45 (C)) and fluctuates between 0 and 2%. In Figure 4-43 (D), and Figure 4-43 (E) the mesoscopic strain, is calculated on the full thickness of the foam and it appears that on this measurement basis the strain fluctuates. The mesoscopic strain plotted in Figure 4-43 (B) is a coarse approximation.

Figure 4-45 (D) shows the displacement of a sample in the X-direction. Interestingly left part is fixed but the right part of the sample is moving in a positive X-direction. This shows the slip of sample in the X-direction, this might have taken place due to the misalignment of a machine during experiments.

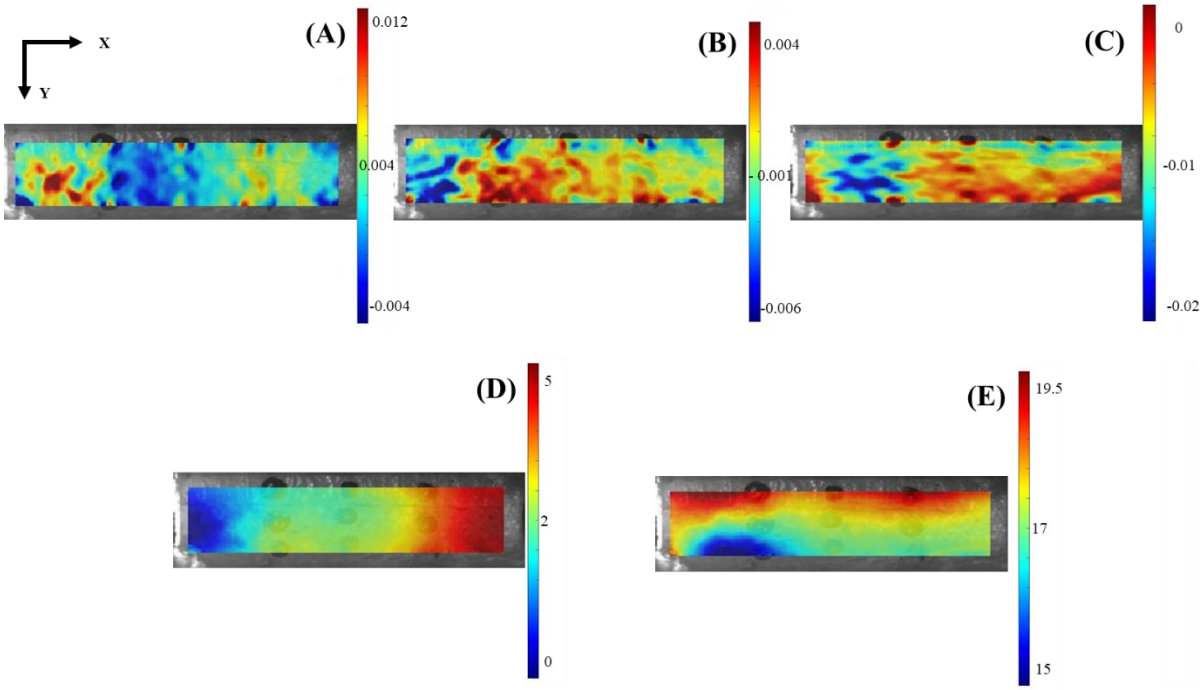

Figure 4-45 80% PPC sample-3 at 511 N (A) Strain in X-direction (B) Shear in plane X-Y (C) Strain in Y-direction (D) Displacement in X-direction (pixel) (E) Displacement in Y-direction (pixel)

In order to obtain the best representation of the strain field in the foam layer, DIC parameters have been changed. During this new DIC analysis, the subset radius is 26 pixels and the subset spacing is 3 pixels. Two same images at 0 N and 511 N are selected for the DSC. Figure 4-46 (A), (B), (C), (D), (E), and (F), show strain in X, XY, Y-direction, displacement in X, Y-direction, and zoom view of strain in Y-direction, respectively. It can be seen that the displacement field in Y-direction is quite the same as previous DIC parameters but the strain field is quite different and more fluctuating, this result is at the limit of the precision of the image and the field evolves at the scale of some pixels.

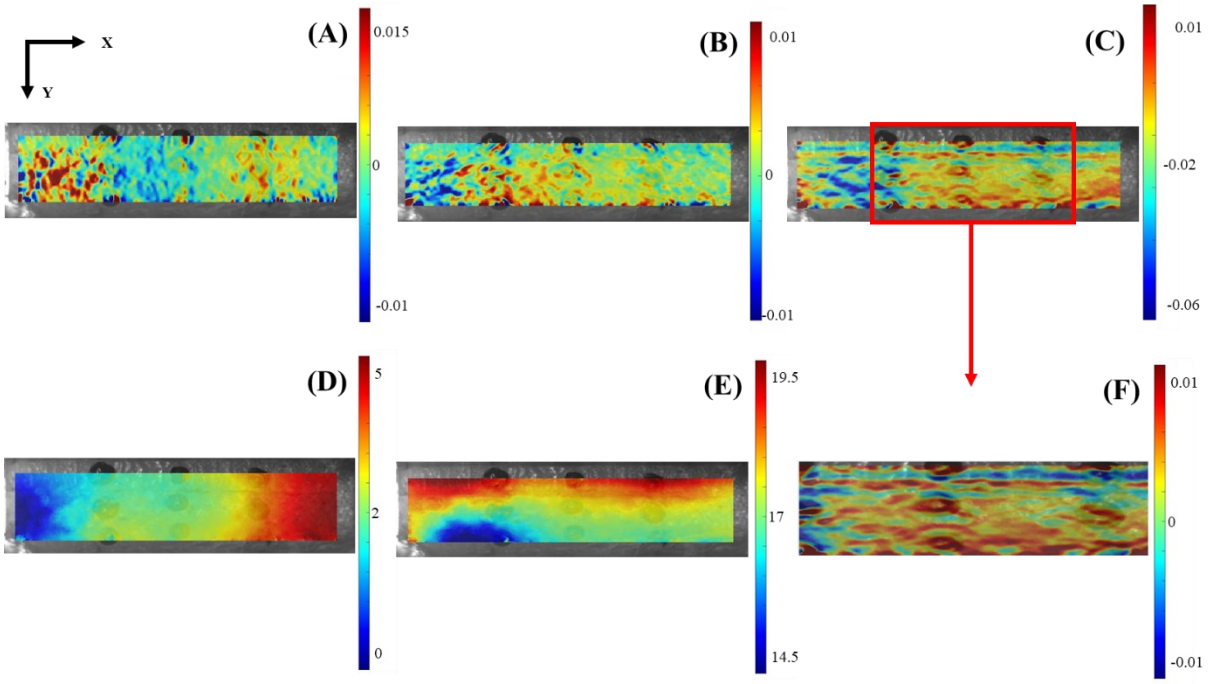

Figure 4-46 80% PPC sample-3 at 511 N (A) Strain in X-direction (B) Shear in plane X-Y (C) Strain in Y-direction (D) Displacement in X-direction (pixel) (E) Displacement in Y-direction (pixel) (F) Zoom view of strain in Y-direction

From the above comparison of the CID parameters, the results with a subset radius of 39 pixels and a subset spacing of 5 pixels (Figure 4-47) are relevant, it is not possible to increase the accuracy of the strain field evolution.

511 N	(A) 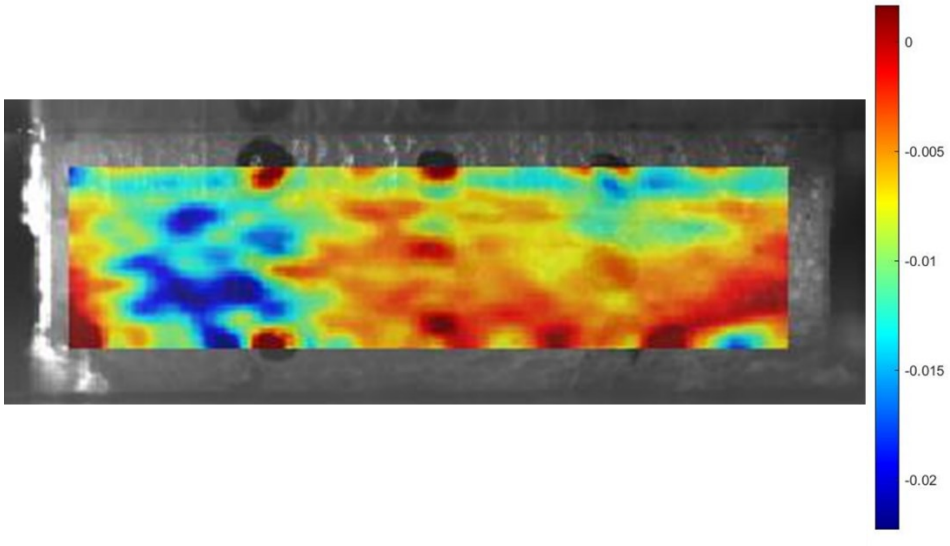 Scale 0.5% - 2%
1000 N	(B)

	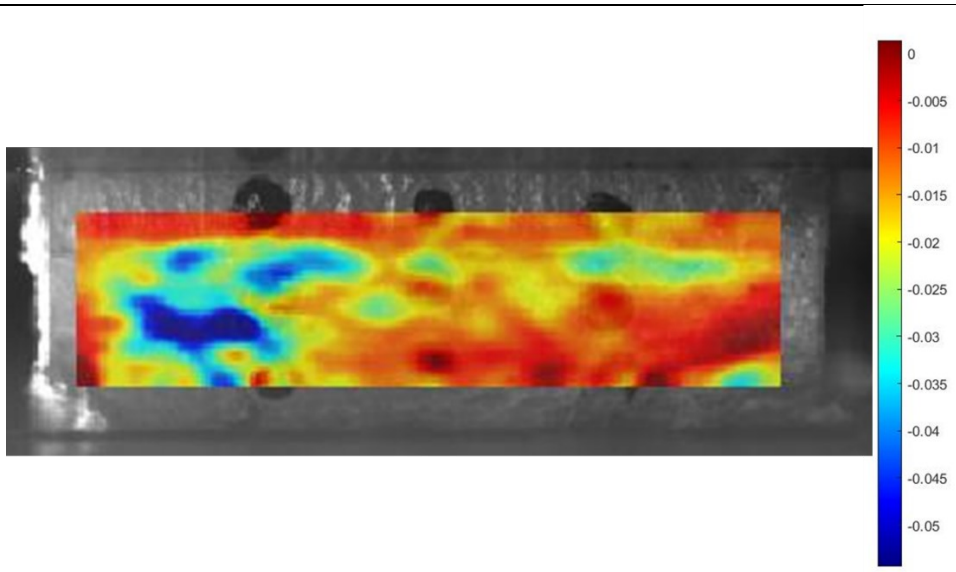 Scale 0.5% - 5%
1500 N	(C) 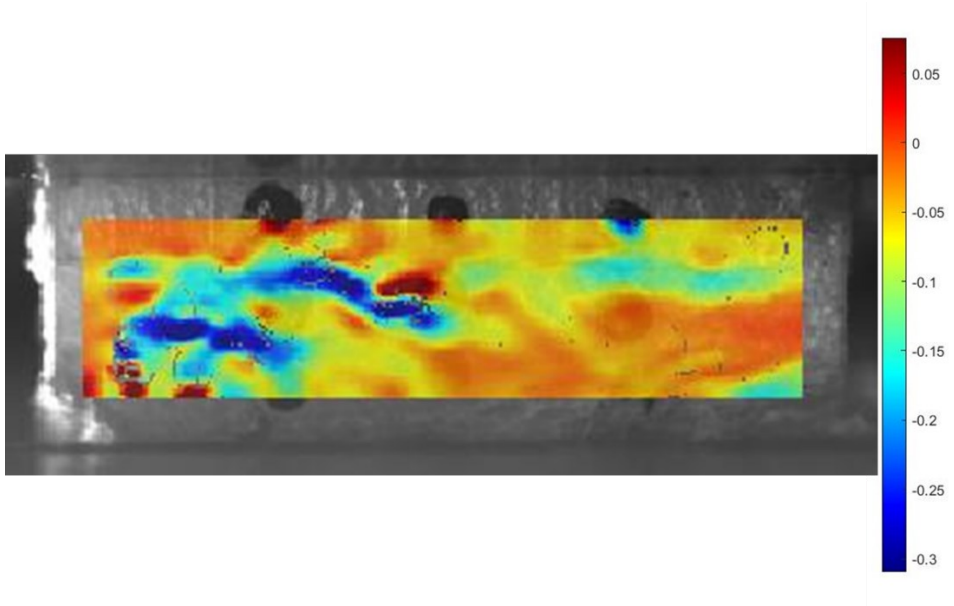 Scale 0.5% - 25%

Figure 4-47 Strain field at (A) 511 N (B) 1000 N (C) 1500 N

On these images (Figure 4-47) corresponding to different load levels, it is clear that the strain is localized. Compressive strain levels increase and localize low strain areas change little with loading. This evolution is not simple to explain.

The other samples have been analyzed, the results are presented below and systematically figures noted (A) and (B) show the macro and mesoscopic results whereas (C) and (D) and (E) show the location where macro and mesoscopic properties are measured respectively.

- Figure 4-48 - Shows results of 80% PPC sample numbered as 2
- Figure 4-49 - Shows results of 80% PPC sample numbered as 1
- Figure 4-50 - Shows results of 90% PPC sample numbered as 5
- Figure 4-51 - Shows results of 90% PPC sample numbered as 4

First, let us recall that point 3 is close to the fixed plate, and point 1 is close to the moving plate. The displacement of point 2 is the one that will bring the information about the local stiffness of the foam. It is why the Point-1 has always displaced more as compared to the other 2 points. Point-3 displacement is close to zero except in Figure 4-48 (A). That can be explained by the fact that the sample is not flat after a particular value force it became flat. Local strain is a function of local porosity as well as initial length.

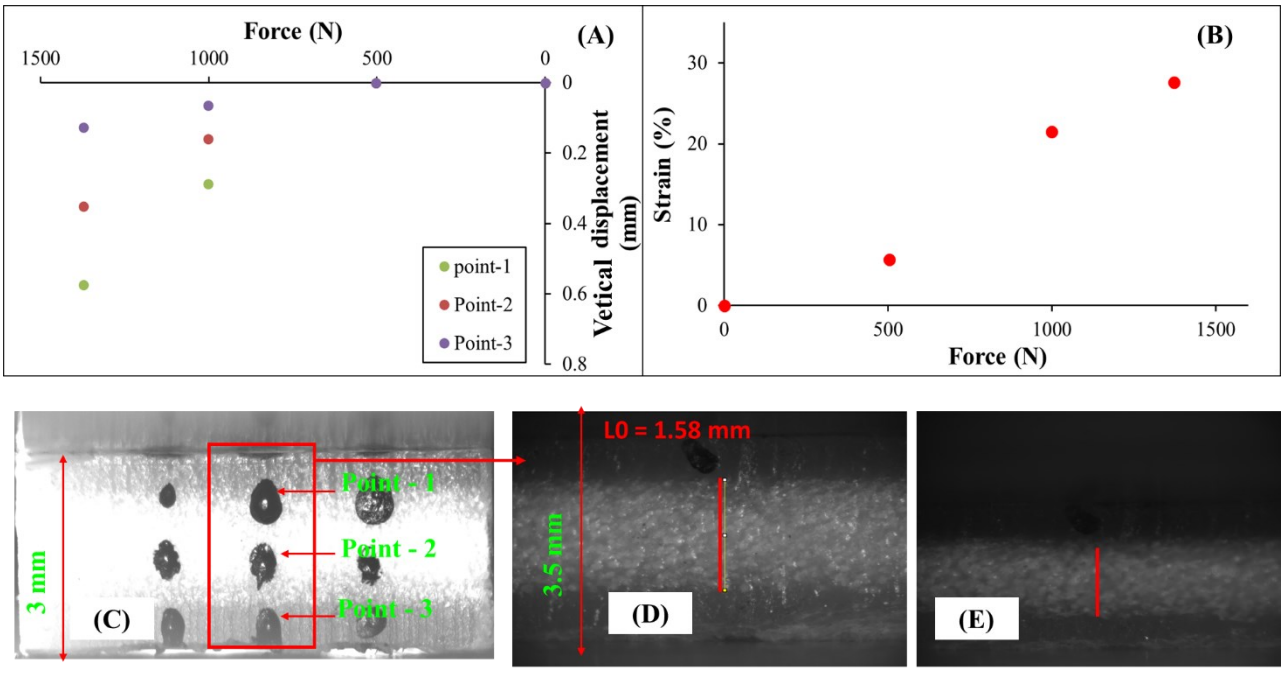

Figure 4-48 80% PPC sample-2 (A) Macroscopic (B) Mesoscopic properties results (C) Location where macroscopic properties are calculated, Location where mesoscopic properties are calculated (D) Initial (E) Final state

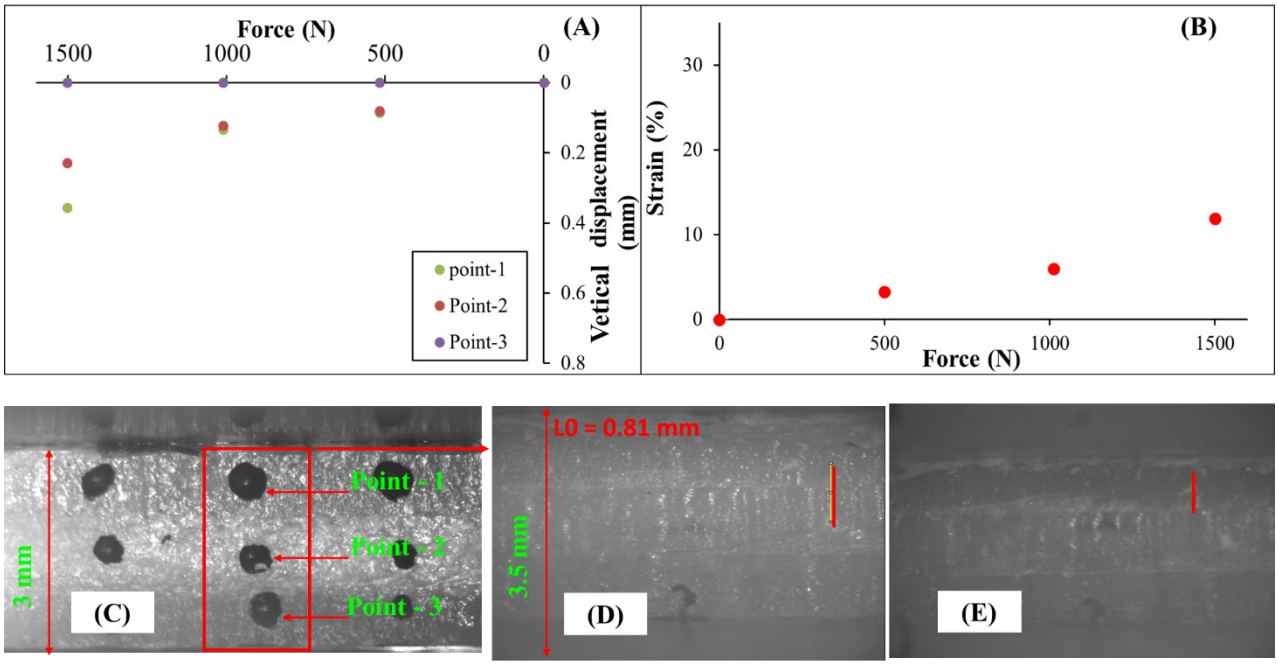

Figure 4-49 80% PPC sample-1 (A) Macroscopic (B) Mesoscopic properties results (C) Location where macroscopic properties are calculated, Location where mesoscopic properties are calculated (D) Initial (E) Final state

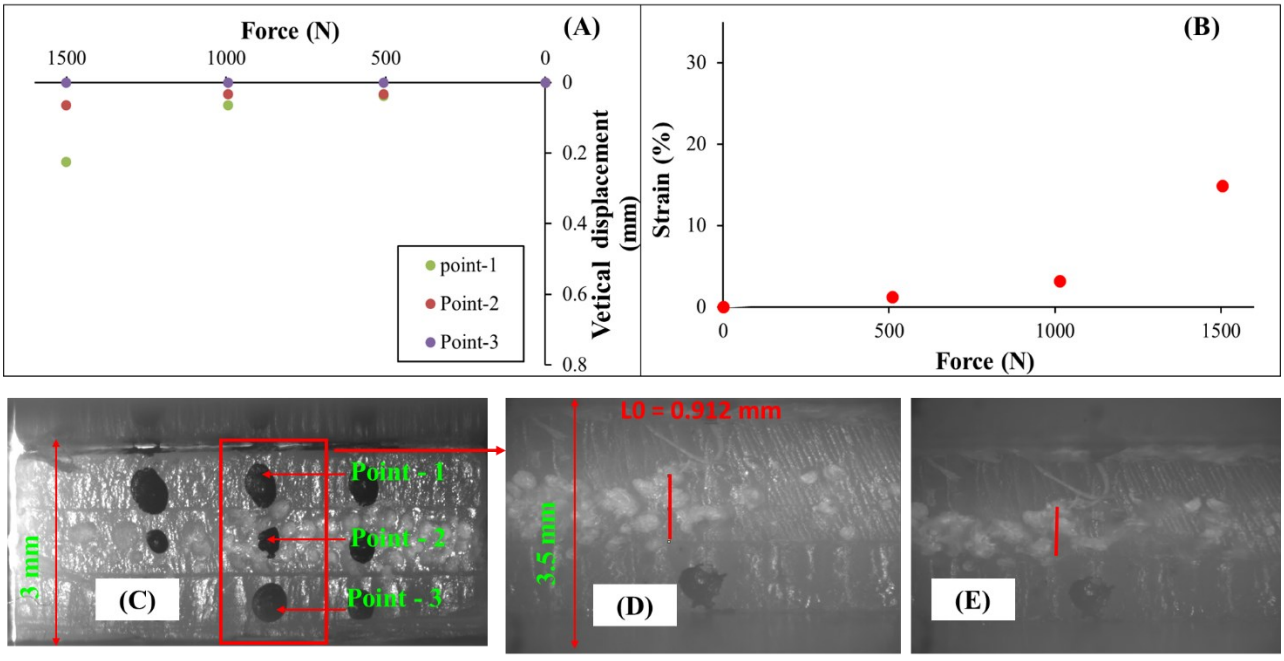

Figure 4-50 90% PPC sample-5 (A) Macroscopic (B) Mesoscopic properties results (C) Location where macroscopic properties are calculated, Location where mesoscopic properties are calculated (D) Initial (E) Final state

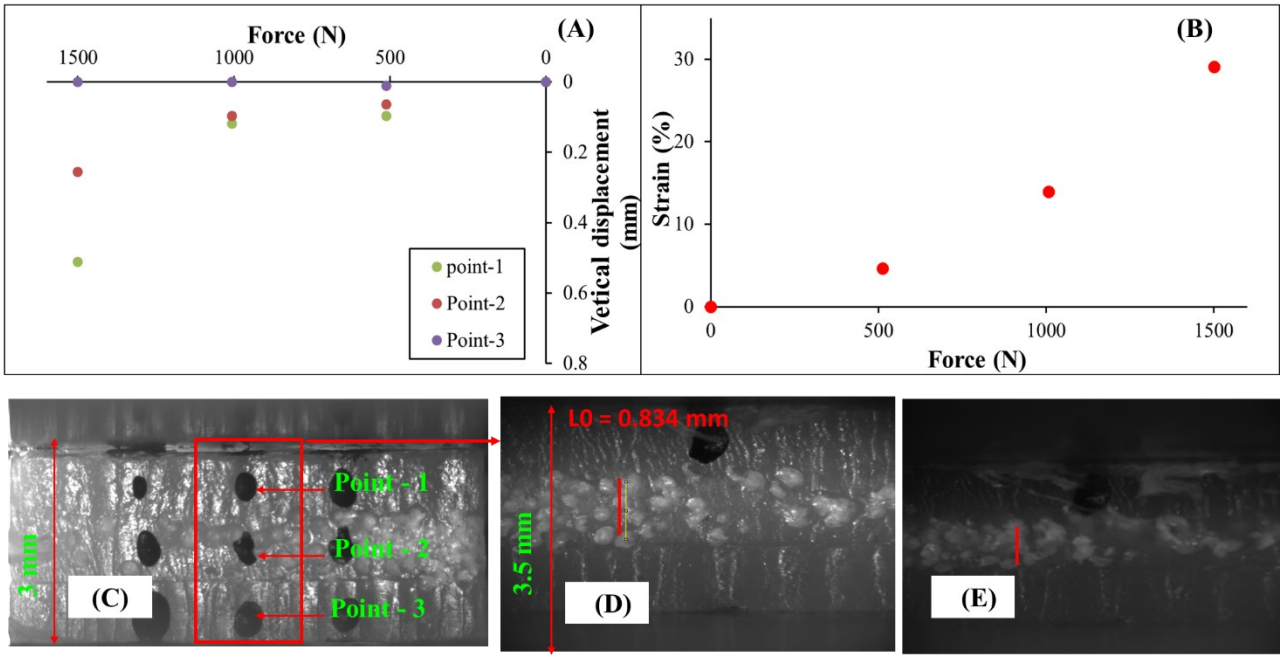

Figure 4-51 90% PPC sample-4 (A) Macroscopic (B) Mesoscopic properties results (C) Location where macroscopic properties are calculated, Location where mesoscopic properties are calculated (D) Initial (E) Final state

As explained above, in compression on the X-axis instead of global displacement-global force is represented as a value of displacement that is small, and there is more chance of error. It is interesting to note that the displacement rate highly influences global displacement corresponding to force. From Figure 4-48 (80% PPC sample-2 subjected to displacement rate of 0.00025 mm.s^{-1}) and Figure 4-49 (80% PPC sample-1 subjected to displacement rate of 0.0025 mm.s^{-1}) it is clear that as the displacement rate increases the global displacement to reach 1500 N force is reducing. Even though samples numbered 1, and 2 are taken from the same plate, the strain generated inside each sample is drastically different. This can be explained by the local porosity distribution inside the sample as well as the initial length considered for the calculation of strain. An exactly similar trend-like 80% PPC sample is seen in the sample of 90% PPC samples.

4.6 Conclusion

Tomography of the injection-molded sample has been performed using UltraTom can go up to 0.4 µm. The Matlab® tool to treat the tomography data has been constructed, which extracts the minimum distance between the pores, diameters of pores, and porosity. It is important to note that 2D (3D field of porosity) and 3D RVE (integrated into the thickness) are used while extracting this data. A histogram of all three quantities has also been plotted, which permits defining the foam's statistics. Basically, this histogram will help choose the diameter of pores and the minimum distance of pores of a foam. In the 3D RVE histogram, there are enormous

numbers of pores at 0 diameter and minimum distance pores; this represents nothing but noise during the segmentation. However, on the other hand, in the 2D RVE porosity histogram, there is a considerable number of pores at 0 porosity. This represents 2D RVE is in a skin (bulk).

In the second part of the chapter, the experimental procedure of a multilayer sample of PE and PPC has been explained. Global-scale results of the PE multilayer 3PB and 4PB results have been presented. To validate the model in different loading conditions, 3PB and 4PB test has been performed on samples of PE. As the sample's thickness increases, the response force reduces from 2 to 8 mm of foam sample thickness. As industrial partner wants us to work with PE, more focus shifted to PE.

However, with samples of PPC, just 3PB has been performed because of the smaller length of the sample. With PPC samples compression test has been performed. Macro, meso, and global scale results of PPC sample with different porosity has been presented. This experimental data will be used to validate the constitutive model of the multilayer. From bending results, it is evident that response force from a sample is the function of local porosity inside the sample as well as the displacement rate imposed during the test. The local strain generated inside the sample is a function of local porosity, displacement rate imposed during the test, initial length considered for calculation of strain, and location where it is calculated.

Compression tests on a solid specimen and sandwiches are carried out. Global and mesoscopic responses are studied for different specimens containing different porosity fields. Even if defects disturb the response, consistency between global and local measurements is obtained.

The effect of porosity is highlighted and the comparison shows that the effect of displacement rate is always present.

Chapter 5 **Constitutive model of foam and validation**

This chapter discusses the modeling of foam and sandwich behavior. The idea is to build the response of the foam, based on the image analysis of the previous chapter and the elasto-viscoplastic constitutive model. The proposed approach consists of creating RVEs of the mesostructure of the PPC, applying a simple loading to them, and proposing a model parameterized by geometrical characteristics.

The originality of the identification of the model comes from the use of the same tool as in chapter 3 by minimizing the response of an equivalent homogeneous medium with that of an RVE. Only tensile boundary conditions are applied to the RVEs with a treatment of the transverse strain to quantify the impact on the hydrostatic pressure coefficient.

The end objective of this study is to establish the relationship between the foam mesoscopic geometry and the constitutive model's material constants.

In the last part of this chapter, the constitutive model identified with respect to the porosity of foam is used for the simulation of structure (SFS). A comparison of compression and bending have been presented here, remembering that the numerical prediction is based only on tensile tests at different strain rate and simulations on RVE.

5.1 Protocol to identify the constitutive model of foam

This part corresponds to the last step of the explanation of the constitutive model of foam and eventually SFS. This protocol has been presented previously but is recalled here in Figure 5-1. It is based on the results of the two previous steps.

- First step - Find out the constitutive model of the polymeric skin.
- Second step - Validation of a constitutive model of monolayer (skin)

In Chapter 3, the numerical part of the identification of the constitutive model and its validation are presented:

- Third step - Find out the constitutive model of foam in connection with the geometrical mesoscopic properties of the foam.

Tomography of the samples has been performed, and the mesoscopic geometrical properties of the foam have been found, as explained in the chapter-4. By using mesoscopic description, several RVEs are proposed to identify the influence of foam mesostructure. It is assumed that the behavior for the monolayer and foam is the same. Consequently, the constitutive model with the same material constant as the monolayer has been used to do the simulations of RVE under tension. For simulation, RVE is subjected to displacement rate on one face by applying

symmetry conditions on other faces in Abaqus®. In this way, 'numerically experimental' data is constructed, and the same data is used to identify new material constants, which are representative of foam. All these steps are well explained in this chapter.

- Fourth step - Validate of multilayer (SFS) constitutive model

Simulations of the 3PB and compression tests are performed in Abaqus®, similar to the experiments in Chapter 4 for the multilayer. Experimental and simulation results have been compared for the validation of the model at the end of this chapter.

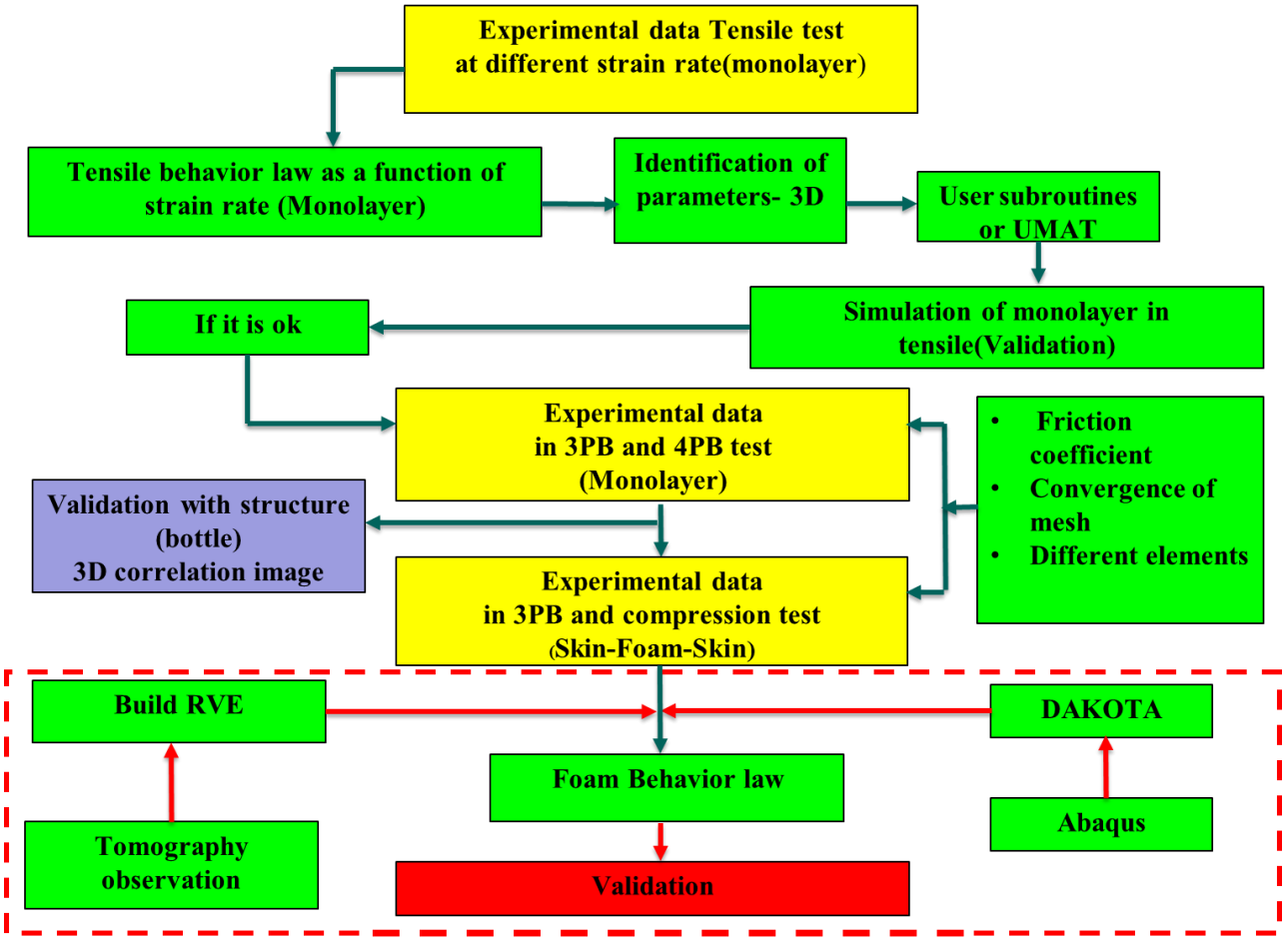

Figure 5-1 Protocol to find the constitutive model of foam

5.2 Assumption

The basic assumption in the construction of the constitutive model is that the polymer between the bubbles has very similar behavior to that of the bulk material. This implies that it is in the same physical state. Therefore, its crystallinity must at least be of the same level and the shape of the crystals should be very similar.

To validate the level of crystallinity, DSC tests have been performed and presented in detail in the following. However, this will not give any information about the shape of the crystals,

their size, and the distribution of the lamellae. In the laboratory, this kind of equipment is not present, and to get this kind of information is not simple; one needs to be a specialist.

The other point to check is that the tomography has provided a distribution of pores at the pixel scale of the image, which corresponds to one specific dimension of the pixel (26 µm). Under this resolution, cavities can exist and modify the behavior and the crystallinity. Therefore, more local observations are attempted and presented.

5.3 First validation of assumption

To validate the assumption of crystallinity, Differential Scanning Calorimetry (in other conversion abbreviation DSC will be used) is performed on polymer and foam. DSC measures the heat flow response of the material under temperature variations. Based on heat flow, the crystallinity of a polymer can be measured. Two chambers and a computer are two main constituents of the DSC machine. There are two chambers; one is empty, and the other contains a sample to be investigated. Both chambers are isolated from the exterior. The empty chamber is used as a reference. The system controls the temperature inside the chambers and energy (electrical), which permits equilibration of the temperature between each chamber. This energy corresponds to flow heat generated by the solid introduced inside one chamber. In this way, chemical and physical evolution can be quantified under constant temperature or a ramp, and a typical heating rate is around 10 °C.min^{-1}. As heat flow depends on the mass of the solid, this one should measure with higher accuracy.

For the studied polymer, in the temperature scale applied by DSC, the phase change is expected. Some secondary transitions can be observed, but here only the melting is analyzed.

The crystallinity of polymer can be characterized using two methods:

The first is based on the heat of fusion defined as follows:

$$\%\ of\ cristallinity\ = \frac{\Delta H_f}{\Delta H_f{}^0}\ x\ 100 \tag{23}$$

where, H_f - sample's heat of fusion (melting) (W.g^{-1}), $H_f{}^0$ - Heat of fusion (melting) (W.g^{-1}) of 100% crystalline form of the same polymer. Typically $H_f{}^0$ for polypropylene is 207 J.g^{-1} [144].

The second method is based on the heat of crystallization defined as follows:

$$\%\ of\ cristilinaty\ = \frac{\Delta H_c}{\Delta H_c{}^0}\ x\ 100 \tag{24}$$

where, H_c - sample's heat of crystallization (W.g^{-1}), $H_f{}^0$ - Heat of crystallization (W.g^{-1}) of 100% crystalline form of the same polymer. Typically $H_f{}^0$ for polypropylene is 163 J.g^{-1} [145].

For DSC samples from a plate of 80 and 90 % of PPC are extracted as there is top skin, foam, and bottom skin. Samples from each of these layers have been taken and DSC is performed from -40 to 180 ^{0}C at a ramp of 10 ^{0}C.min^{-1}. Figure 5-2 (A) shows heat flow during the DSC for bottom skin, foam, and top skin for an 80% PPC sample, whereas Figure 5-2 (B) shows heat flow during the DSC for bottom skin, foam, and top skin for 90% PPC sample. It can be seen that for both samples that are 80 and 90% PPC, all three curves are superposing. This indicates that the percent of crystallinity is very similar in the skin and the foam.

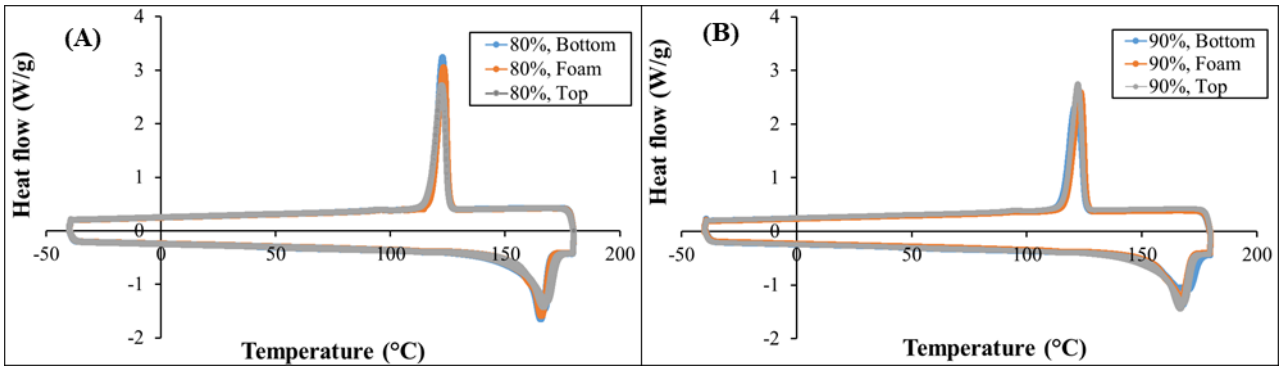

Figure 5-2 DSC results of (A) 80% (B) 90% PPC

When a second ramp is applied after a crystallization melting step, the curves are very close, which implies that the injection process has allowed the development of a crystallinity close to the one generated by the DSC temperature ramp applied to a small volume of material.

Regarding porosity at small scales, optical observations have been performed at the surface of a sample. Figure 5-3 shows an image taken by optical microscope MOZ2: Zeiss. The green pores are the big pores below the surface, whereas the red ones are small. On the left corner is the red box is shown with a dimension of 26 x 26 µm, which is the size of one pixel in the tomography. It appears that there are porosities below 26 µm. Red circles correspond to the small pores with diameters ranging from 1 to 3 µm. There are small pores between big pores. The percentage seems low but not zero. The effect of these porosities on the constitutive model as well as the response of RVE need to be investigated.

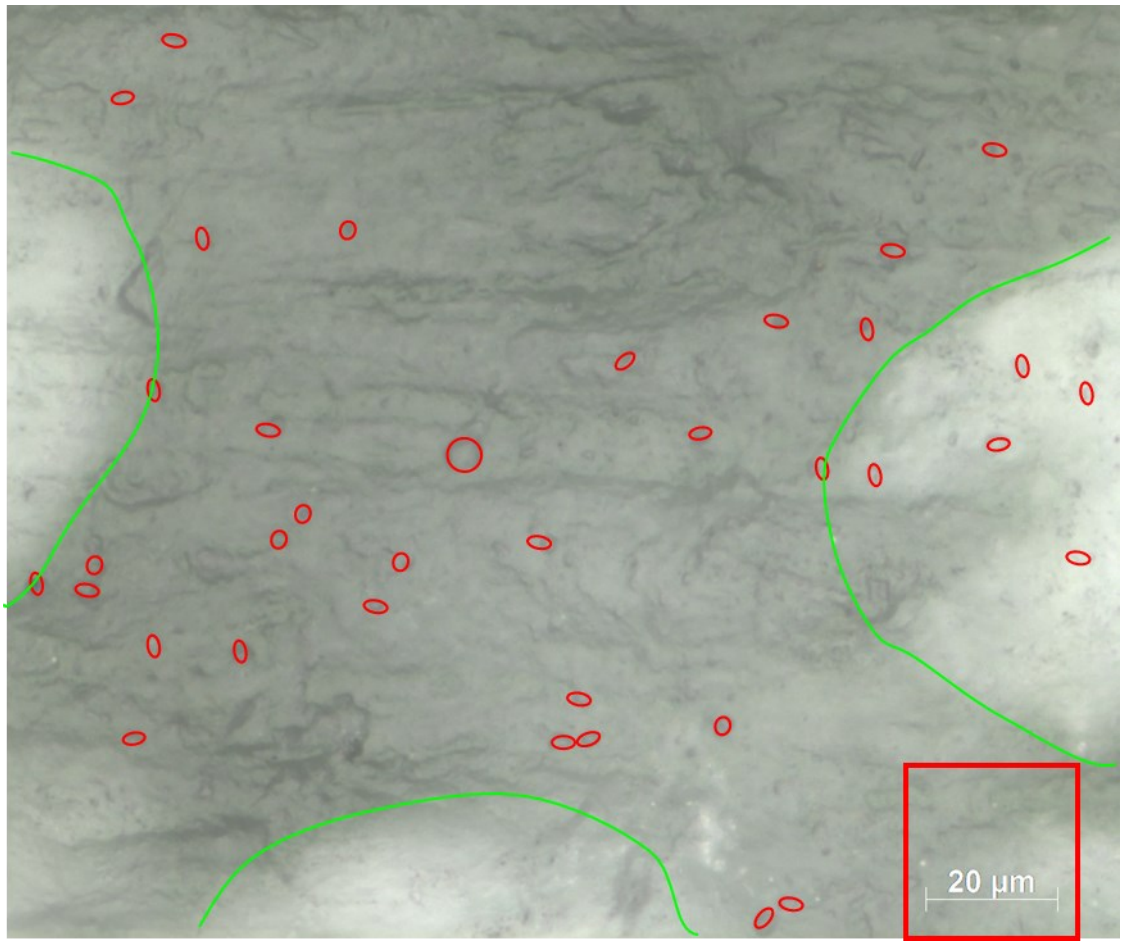

Figure 5-3 80% PPC sample image is taken by optical microscope MOZ2: Zeiss

5.4 Model of RVE

As explained in Chapter 4, heading 4.2.1 , the tomography set-up permits, the characterization of the distribution of bubbles inside the entire sample of PPC. Three selected parameters have been used to describe in more detail the foam. Matlab® has a tool that automatically generates a histogram of porosity, minimum distance between pores, and diameter of pores. Figure 5-4 (A) to Figure 5-4 (C) presented in Chapter 4 are reproduced below. Figure 5-4 (C) represents a histogram of porosity calculated using 2D RVE, which gives a 3D field.

The idea is to generate RVEs that are representative of this distribution. A collection is generated by varying the diameter of the bubbles and the distances between them. Internship student Mr. Benjamin LE SAVOUREUX, under our supervision, has developed a tool in Abaqus®. It can generate a cube with a pore inside it, based on the input provided by the diameter of pores (noted α) and the distance between two bubbles (noted β). For calculation of the length of the RVE cube following formula has been used;

$$length\ of\ cube = \alpha + 2\,\beta \tag{25}$$

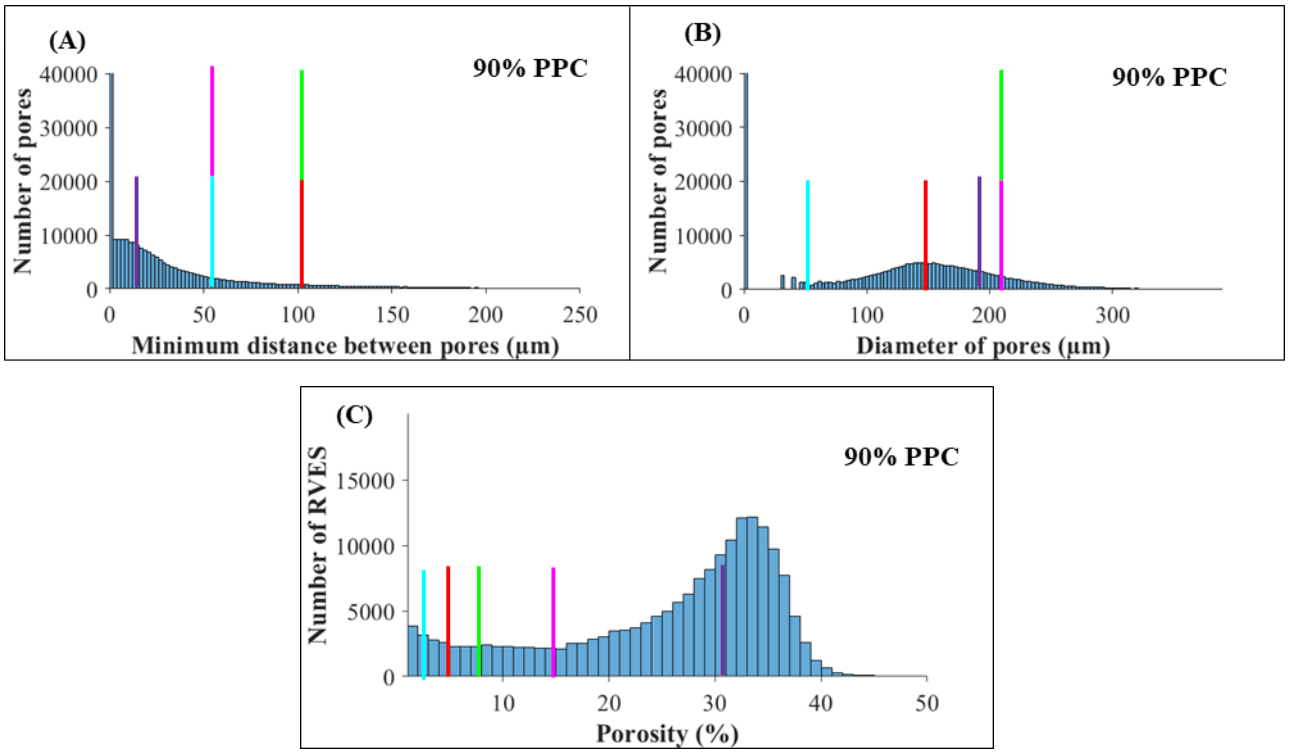

Figure 5-4 Histogram of (A) Minimum distance between the pores (B) Diameter of the pores (C) Porosity of 90% of PPC sample

Many RVES are generated based on different values of α and β, presented in Table 5-1. Five cases with different α and β are selected with corresponding porosity which has been colored in Table 5-1. All these cases have been plotted on the histogram (Figure 5-4) to show the spread of the RVE dimension section.

	Diameter (α) (µm)	Minimum distance between pores (β)(µm)	Porosity (%)
Case-1	52	52	1.935
Case-2	156	104	4.118
Case-3	208	156	3.343
Case-4	65	104	0.703
Case-5	52	156	0.156
Case-6	156	52	11.30
Case-7	156	156	1.935
Case-8	208	52	15.54
Case-9	208	104	6.547
Case-10	52	104	0.417
Case-11	200	20	30.28

Table 5-1 Information about RVEs

Figure 5-5 (A) to Figure 5-5 (G), show the protocol for the development of the complete RVE numerical model. Based on the α and β, how basic brick of RVE is created, and is represented in Figure 5-5 (A) with the python software. The basic brick of RVE which is indicated as a

red cube in Figure 5-5 (B) is duplicated in the three directions as illustrated in Figure 5-5 (C). Figure 5-5 (D) to Figure 5-5 (G) .show this progression in in X-direction in transparent form. The number of bubbles inside the RVE equals to 64 and if symmetry conditions are applied, the number reaches 512 bubbles.

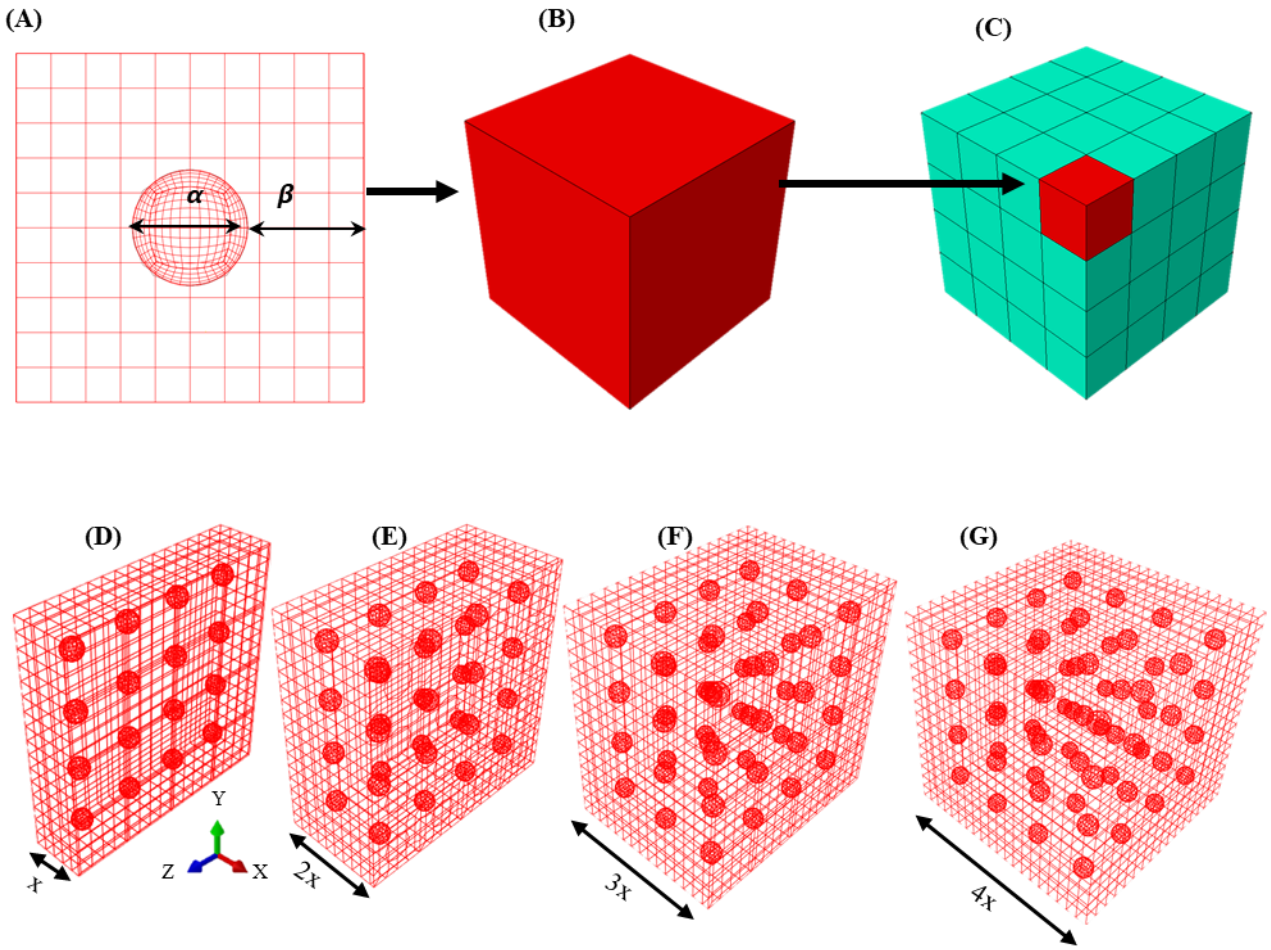

Figure 5-5 Protocol for the construction of RVE (A) to (G)

5.5 RVE response curves in the tensile test

Once RVEs are created, the next step is to apply loads and record their response to it. This will help to generate data numerically for finding out the relation between material constants of the model with porosity without doing real experiments.

Figure 5-6 shows the boundary conditions of RVE during the simulation. On three faces symmetry conditions are imposed (Figure 5-6 (A) to Figure 5-6 (C)) and on a face with a normal to Z-axis, a displacement in direction (- Z-direction) is applied on nodes (Figure 5-6 (D)). The displacement rate applied during the simulation depends on the length of the cube as well as the constant true strain rate which is applied. This kind of boundary condition will help us to

create tensile test responses of the RVEs, which are similar to the experimental curves obtained on bulk (skin).

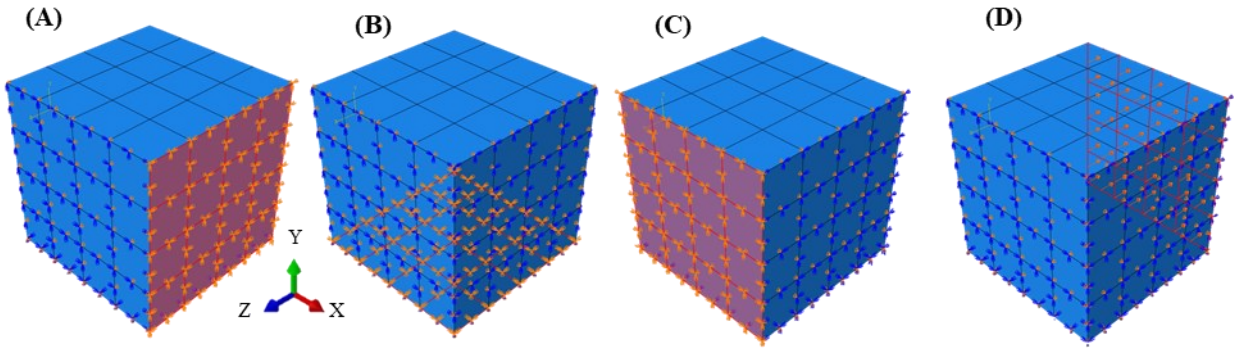

Figure 5-6 Boundary condition during simulation of RVE (A) X-symmetry (B) Y-symmetry (C) Z-symmetry (D) Face where displacement rate is applied with respect to the constant true strain rate

Figure 5-7 shows the force per unit area (area of the face where displacement rate applied is calculated at each step of simulation) vs. true longitudinal and transverse strain. Force per unit area is plotted to remove the cross-section area effect on the results as RVEs have a different area of a cross-section. Next, the area's evolution during the simulation is updated by considering the displacements at the nodes of the contour. Finally, the longitudinal strain and transverse strains are calculated with global displacements of the faces.

Case-1, case-2, case-8, case-9, and case-11 results are shown by light blue, red, green, pink, and purple curves, respectively. Each RVE is subjected to three different constant true strain rates, 10^{-2}, 1.10^{-3}, and 5.10^{-5} s^{-1}. Different types of same color curves represent the results of the same RVE with different strain rates. It can be observed from Figure 5-7 that as porosity increases response force by RVE also decreases. The porosity of case-1 is 1.93 % whereas case-11 is 30.28%. The difference in response between case-1 (light blue curve) and case-11 (purple curve) is visible. From the case-11 curve (purple curve) it can be noted that the hardening curve response is not decreasing only, to understand this more investigation is needed but due to time limitations here this study is limited.

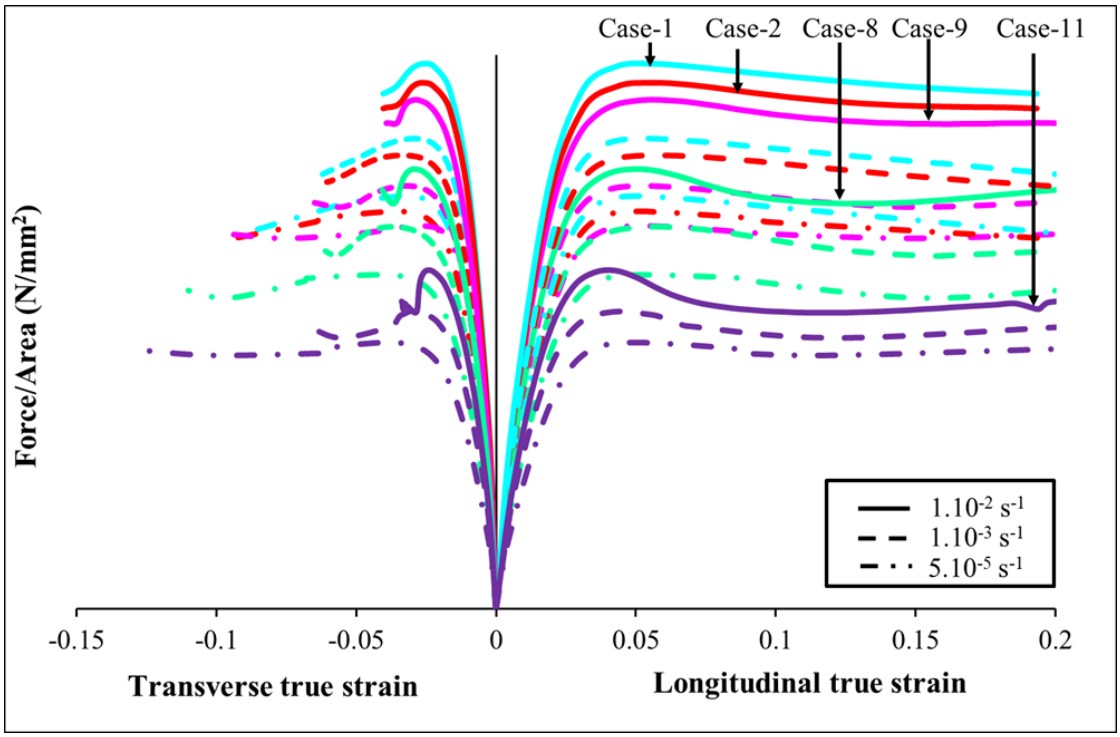

Figure 5-7 RVE's response at the different strain rates with different porosity

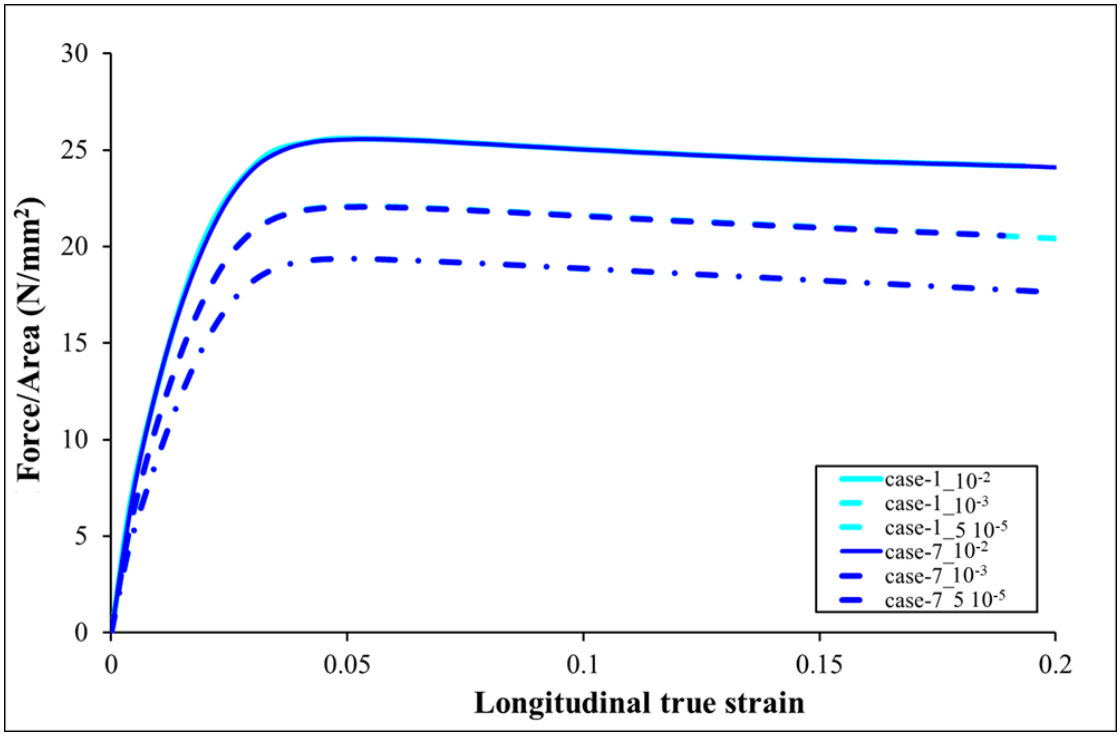

Figure 5-8 Same porosity but different α and β results for the case-1 and case-7

A significant result in all the simulations comes from comparing cases with the same porosity with different geometric parameters. As suggested in Figure 5-8, the responses are close, which implies that the major parameter is the porosity. It is not proof for all but in the scale of geometry parameters investigate, these results confirm this assumption.

5.6 Identification of constants of Young's modulus

Similar to bulk, after having experimental data first step is to find out Young's modulus concerning different strain rates is followed here also. As 'numerically experiment' data is generated then by taking yield stress as 1.5 MPa (as explained in Chapter 3, heading 3.5, Figure 3-14) Young's modulus is calculated for each RVE at 3 different strain rates. Figure 5-9 (A) shows Young's modulus vs. log (equivalent strain rate) for Case-1, case-2, case-8, case-9, and case-11. Results are shown by light blue, red, green, pink, and purple color curves. As porosity increases, Young's modulus decreases, and the same has been obtained in the literature by Drozdov and Christiansen [146]. For each RVE, as strain rate decreases Young's modulus is also degreasing in the same manner as bulk(skin). Consequently, Equation (26) explained in Chapter 3, Equation (8) can be used

$$E = E_1 + E_2 * \left(1 + \tanh\left(E_3 * \log\left(\dot{\varepsilon}_{eq}\right) + E_4\right)\right) \tag{26}$$

E_1, E_2, E_3, and E_4 constants are found using an Excel solver (optimization tool) for each value of porosity. The objective function used is an absolute difference between the tangent response of RVEs and Young's modulus of Equation (26).

Results of the identification of Young's modulus are plotted in Figure 5-9 (B). More precisely, in Figure 5-9 (B) color lines represent values of Young's modulus obtained with RVE and black dots represent identified values of a homogeneous Young's modulus. Each black dot constant of Equation (26) is determined concerning porosity, the values are analyzed below, to find out the relation between these constants and porosity.

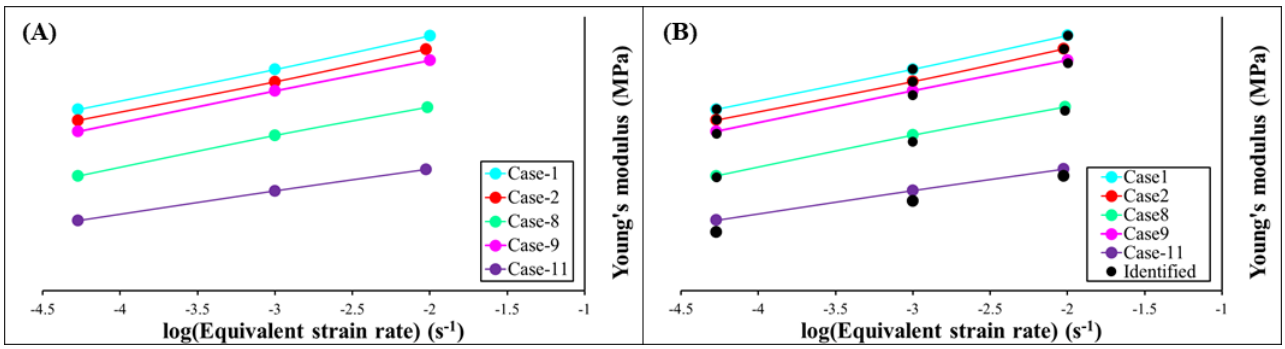

Figure 5-9 (A) Young's modulus of different cases of RVEs at different equivalent strain rates (B) With identified values of Young's modulus

5.7 Procedure for the identification of isotropic hardening constants using the 3D identification tool DAKOTA

Constants of Young's modulus are identified for each RVE, next step is to find out the constants of the isotropic hardening curve and hydrostatic pressure coefficient. Q_1,B_1, Q_2, B_2 from

Chapter 3, Equation (17) and K, N from Chapter 3, Equation (12) are to be identified along with constants of hydrostatic pressure coefficient from Chapter 3, Equation (15). As reminder equations are presented here.

Flow rule is as follows:

$$\dot{P} = \left(\frac{(1-a)\,J_2(\bar{\bar{\sigma}} - \bar{\bar{X}}) - R + a\,tr(\bar{\bar{\sigma}})}{K}\right)^N \tag{27}$$

Isotropic hardening is as follows:

$$R_F = R + Q_1(1 - e^{-B_1 P}) + Q_2\,(1 - e^{-B_2 P}) \tag{28}$$

The hydrostatic pressure coefficient is as follows:

$$\begin{aligned} a = \Big(A_1 + A_2 * \big(1 + \tanh\left(A_3 * \log(\dot{\varepsilon}_{eq}) + A_4\right)\big)\Big) * (1 \\ - \exp\Big(-\Big(A_5 + A_6 * \big(1 + \tanh\left(A_7 * \log(\dot{\varepsilon}_{eq}) + A_8\right)\big)\Big) * 3P\Big) \\ + \Big(A_9 + A_{10} * \big(1 + \tanh\left(A_{11} * \log(\dot{\varepsilon}_{eq}) + A_{12}\right)\big)\Big) * 3P \\ + \Big(A_{13} + A_{14} * \big(1 + \tanh\left(A_{15} * \log(\dot{\varepsilon}_{eq})\right)\big)\Big) \end{aligned} \tag{29}$$

1D model of this hardening curve along with flow rule is generated and checked which constants affect translation of hardening curves. It is evident in Figure 5-7, that as porosity increases, maximum force decreases, and the shape of hardening is very similar. After a 1D parametric study, it is found that Q_1 and N are the two constants that more influence the translation of the hardening curve. Consequently, only these two parameters Q_1 and N are to be identified using the 3D identification tool (heading 3.9) for each RVE and other values of the hardening curve will be the same as bulk (skin).

The identification protocol is based on the comparison between the response of RVEs with bubbles and a homogeneous RVE with equivalent homogeneous properties to be determined. The values of the constants of the equivalent homogeneous Young's modulus correspond to the porosity level of the RVE with bubbles are used.

During the first try, it is decided that all the constants of the hydrostatic pressure coefficient would be used as bulk (skin). Therefore, by using DAKOTA, Q_1 and N constants of the constitutive model have been identified, minimizing the difference between the RVEs with bubbles and homogeneous RVE. The other constants here are the same as PPC identification in Chapter 3 heading 3.9.4.

Figure 5-10 (A) and Figure 5-10 (B) show homogenization results of RVE of case-1, 2, 7, 8, and 11. Same color curves with solid lines, dash lines, and dash-dot curves represent experimental data (numerically generated) of RVE with a constant true strain rate of 10^{-2}, 1.10^{-3},

and 5.10^{-5} s^{-1}, respectively. Black dash lines are results after the identification of respective RVEs.

It can be observed from curves that identification for strain and force per unit area is good for RVE, which has less porosity like case-1 and case-2 RVEs. However, as porosity increases, strain vs. force per unit area identification is not as good as low porosity RVEs. The same can be observed from the identification of RVE with case-11. This result is due to the hypothesis formulated at the end of the parametric study, stating that only Q1 and N vary with porosity. To improve the mode, another parameter should be introduced in the identification, but the times to obtain a solution come very large, and the time on the cluster is limited, it is necessary to make a choice.

As porosity increases, the transverse strain identification degrades, which implies that constants of hydrostatic pressure coefficient should be identified to increase the quality of homogenization. However, the quality obtained is surprising. By not integrating any dependence of the porosity on this coefficient, the prediction is not too far off.

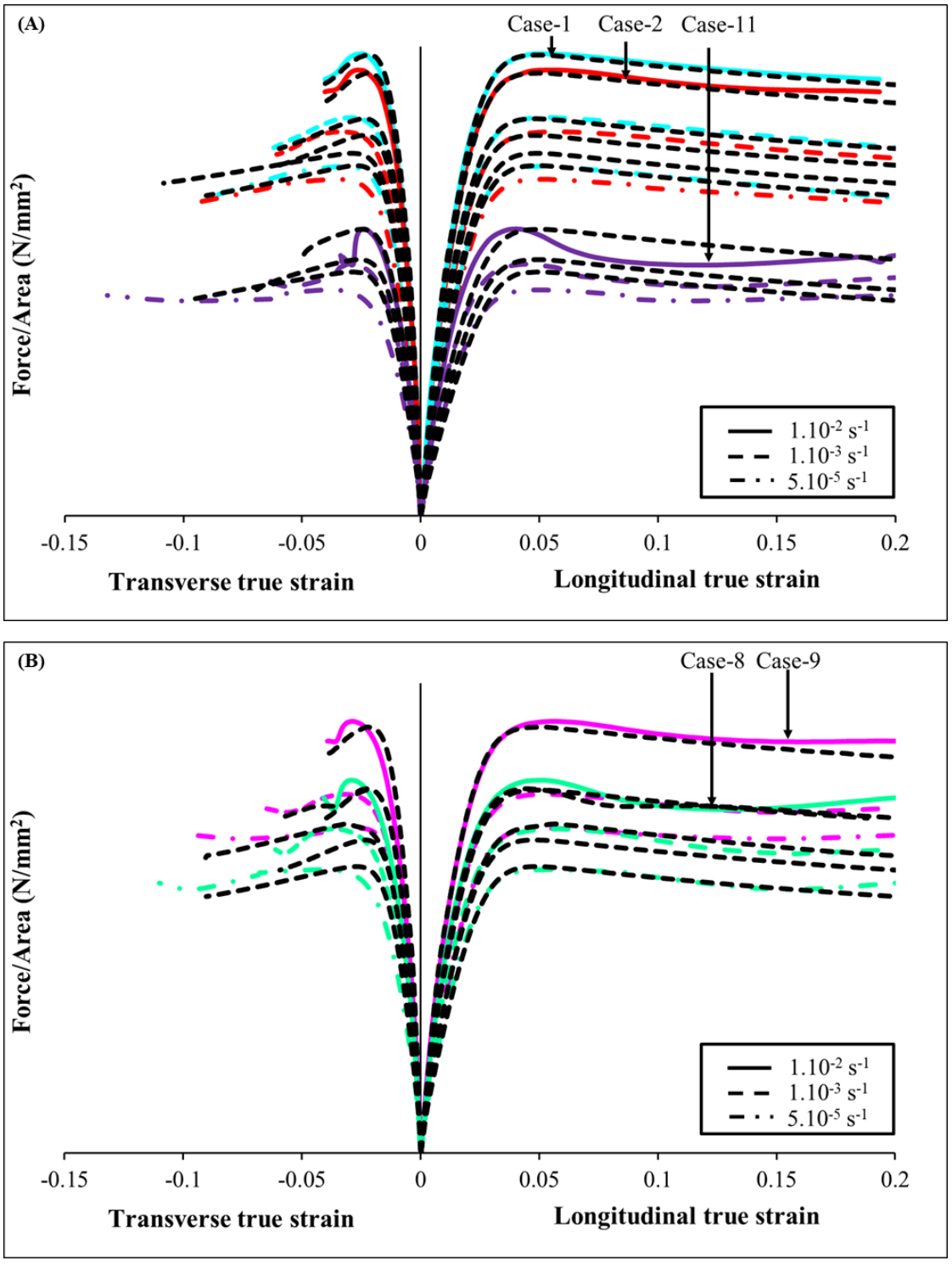

Figure 5-10 Comparison of experimental (numerically generated) and homogenized RVE simulated tensile test results after homogenization for constant true strain rate, (A) Case-1, 2, and 11 (B) Case-8 and 9

5.8 Constitutive model dependencies with porosity (alpha and beta)

After homogenization constants of the constitutive model have been identified for each RVE. The next step is to connect these constants with the porosity of RVE. Figure 5-11 shows

constants of young's modulus variation concerning the porosity of RVE. Figure 5-11 (A) shows values identified for E_1 as a function of porosity. Blue dots are identified values of RVEs, whereas a dotted line is constructed to fit these points. The equations of these lines are also shown in the graph. The red dot is the value of Young's modulus constant for bulk. It can be seen that the value of E_1 varies linearly concerning the porosity of RVE. Figure 5-11 (B) represents the values identified for E_2 as a function of the porosity. It can be seen that the value of E_2 is also varying linearly concerning the porosity of RVE as E_1. The green dots are identified values, whereas the dotted line is constructed to fit these points. The equation of this line is also shown in the graph. Figure 5-11 (C) demonstrates values identified for E_3 as a function of the porosity. It can be seen that values are constants and the level is close to the bulk value. Figure 5-11 (D) shows, E_4 vs. porosity of RVE. Similar to E_3 constant value equal to bulk value is observed even if there is a variation in the porosity of RVEs.

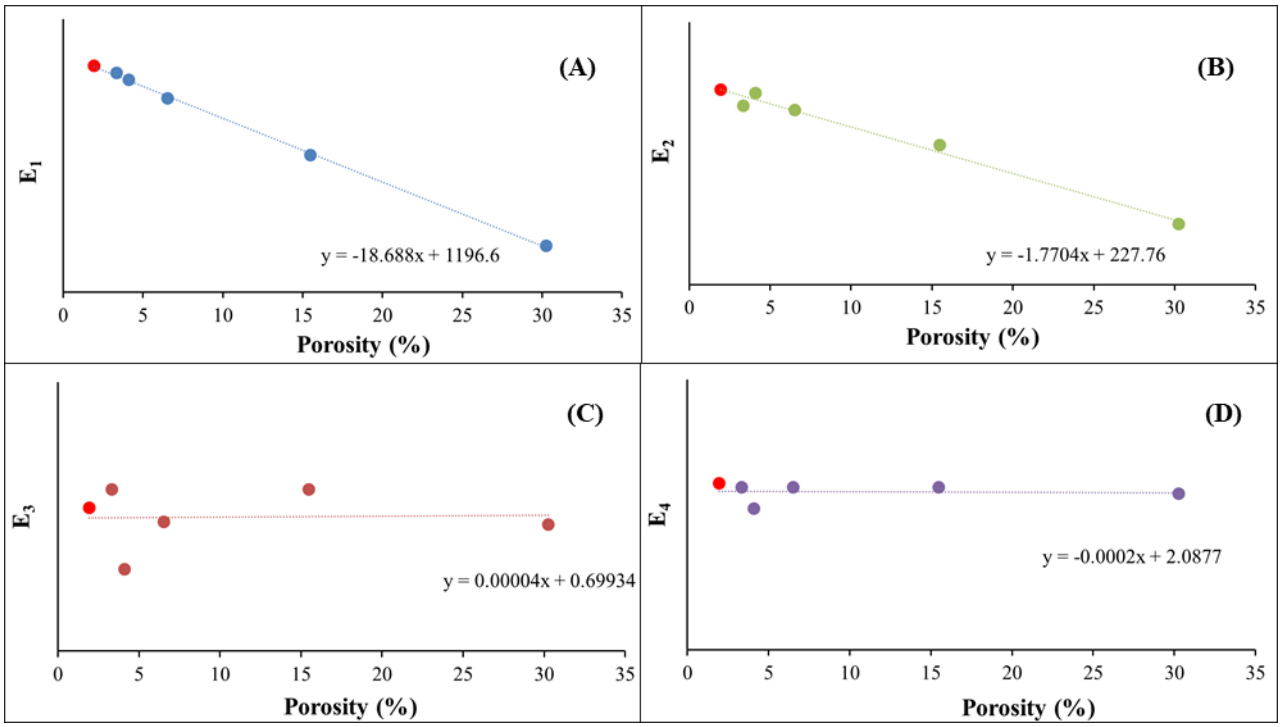

Figure 5-11 Connection of constants (A) E_1 (B) E_2 (C) E_3 (D) E_4 of Young's modulus with porosity of RVE

As discussed above Q_1 and N coefficients are identified using the 3D identification tool. Similar to constants of Young's modulus values of Q_1 and N plotted in a graph with respect to porosity in Figure 5-12. From Figure 5-12 (A) it can be noticed that, unlike all other constants which have been identified, the variation of N is not linear with respect to the porosity of RVE. So to fit the identified values of N, Equation (30) has been generated. Again constants of this equation are identified using an Excel solver with an objective function as the absolute difference between identified values and equation generated values of N.

$$N = N_1 + N_2 * (exp(-N_3 * porosity\ (\%)) - 1) \tag{30}$$

Figure 5-12 (A) shows blue and brown dots, which represent identified values of N and equation generated values respectively. It can be seen that both are in good agreement with each other. Using this one can conclude that Equation (30) represents a variation of N with porosity effectively. Figure 5-12 (B) shows a variation of the identified value of Q_1 with respect to porosity. It can be seen that Q_1 is varying linearly with the porosity of RVE.

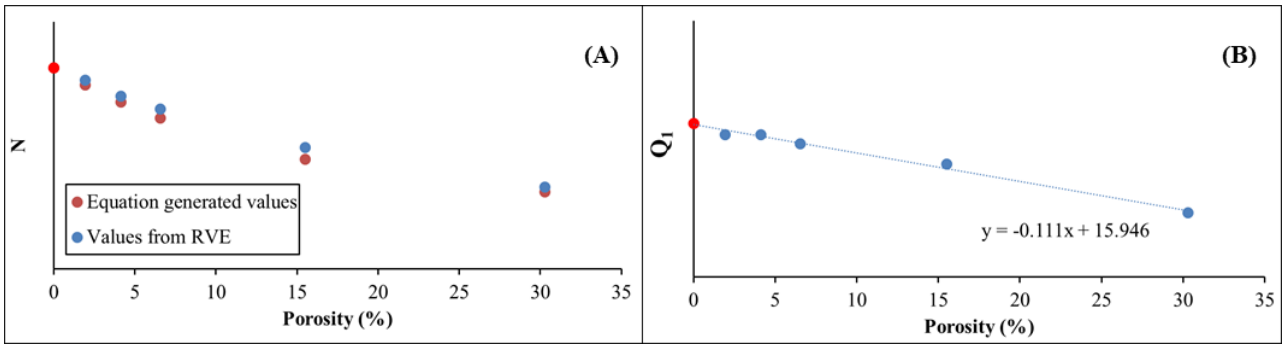

Figure 5-12 Connection of constants (A) N (B) Q_1 of hardening curve with porosity of RVE

5.9 Discussion

From Figure 5-3, it is evident that some pores below 26 µm are present in the foam. This image suggests that two families exist. This small porosity can explain the difference between the global porosity calculated by the mass measurement and estimated with the total volume of pores identified with tomography. For the 80% PPC sample, the difference in this porosity permits us to estimate the small porosity at the level of 1%. To evaluate the influence and maximize the effect of these small porosities, the RVE without bobbles of case-11 has been generated with the constitutive model constants corresponding to the porosity of 2% and 6% (as the relation between porosity and constants is known). Simulation on the RVE has been performed with a constant true strain rate of 10^{-2} s^{-1}. Figure 5-13 shows the response of RVE without small porosity in the polymer (solid purple curve), with 2% (dash purple curve), and with 6% of small porosity constants (dash-dot purple curve). There is an effect on the plastic response of RVE when constitutive model constants are changed in the polymer between big bubbles. The stiffness is slightly modified with the stress threshold. With these RVEs, it is quite possible to develop cascade constitutive models by conducting simulations with micrometer sub-porosities and evaluating the effect on the equivalent homogeneous behavior while integrating the strain rate dependencies.

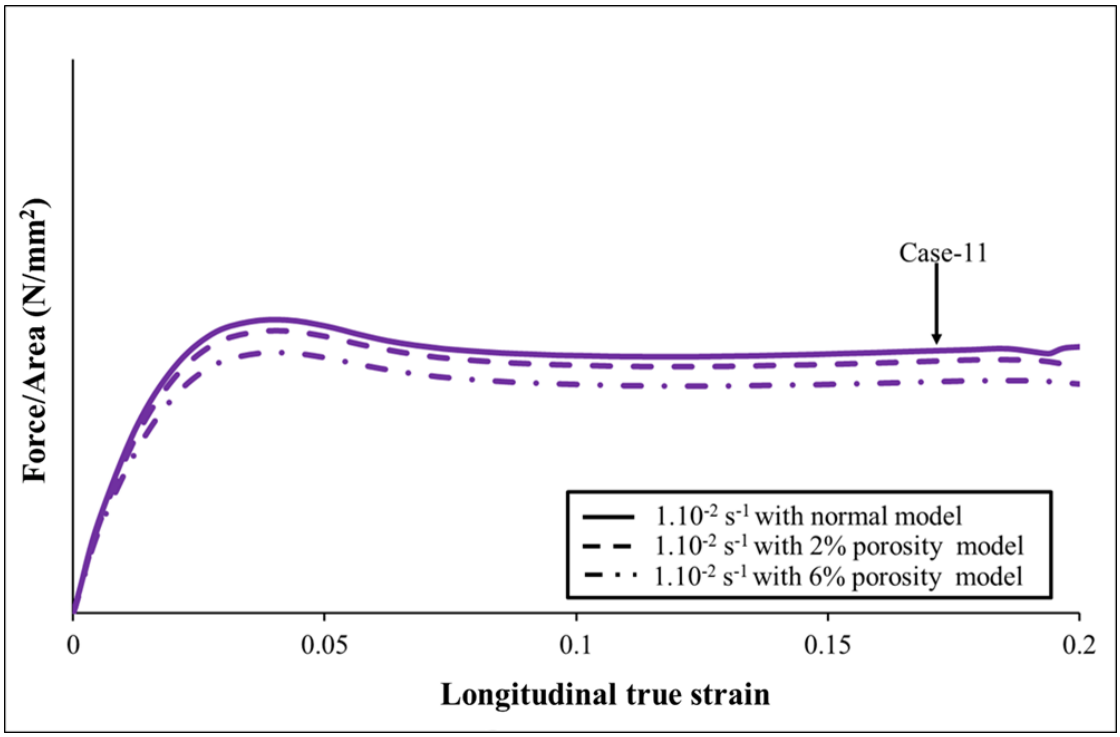

Figure 5-13 Case-11 results with 0%, 2% and 6% of porosity's material constants.

5.10 Validation of model

The study has been performed on RVE in tension to build the constitutive model; the effect of hydrostatic pressure is taken into account by the transverse strain. It is obvious that this is a daring gamble that must be evaluated. In order to verify the behavior of RVE in compression, one simulation has been performed. For performing compression RVE case-11 is chosen. From Figure 5-14 is clear that behaviors in compression and tension are different. Maximum force per unit area is in order of 20 MPa and 50 MPa in tension and compression respectively. This is due to the term $tr(\bar{\sigma})$; this one has a sign and influences the hardening and the flow of plastic strain. Figure 5-14 shows that the force is very high in compression, and the tangent stiffness under compression during plastic flow is very important.

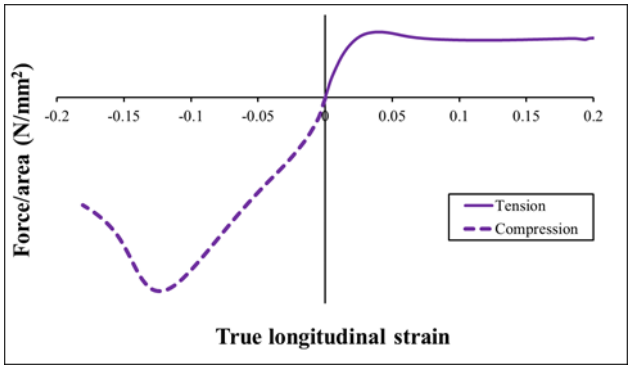

Figure 5-14 RVE case-11 simulation in tension and in compression

Before any comparison between experiments and simulations, this stiffness is expected to be a problematic area. In order to propose other way, the subroutine can be modified by considering an identical response in traction and compression. It is assumed that the effect of hydrostatic pressure is always nonlinear and depends on strain rate, but it is symmetric in traction and compression. Consequently, the term $tr(\bar{\bar{\sigma}})$ is just the term is replaced by $|tr(\bar{\bar{\sigma}})|$ as detailed in the following paragraph.

5.10.1 Modification of constitutive model

As a reminder viscoplastic strain (Equation (11)), normal to the load surface (Equation (13)) from Chapter 3 has been presented here.

Viscoplastic strain rate is defined by Drucker's postulated associated flow

$$\dot{\bar{\bar{\varepsilon}}}^{pl} = \dot{P}\,\bar{\bar{n}} \tag{31}$$

The expression of the tensor of the external normal to the load surface

$$\bar{\bar{n}} = (1-a)\frac{3}{2}\left(\frac{\bar{\bar{\sigma}}' - \bar{\bar{X}}'}{J_2\left(\bar{\bar{\sigma}} - \bar{\bar{X}}\right)}\right) + a\bar{\bar{I}} \tag{32}$$

Modified expression of the tensor of the external normal to the load surface. Basically, in order to separate compression and tension, the sign is needed. The purpose of this sign has been served by this term $\frac{tr(\bar{\bar{\sigma}})}{|tr(\bar{\bar{\sigma}})|}$.

$$\bar{\bar{n}} = (1-a)\frac{\bar{\bar{\sigma}}'}{J_2} + a\,\frac{tr(\bar{\bar{\sigma}})}{|tr(\bar{\bar{\sigma}})|}I \tag{33}$$

The expression of the viscoplastic strain rate becomes

$$\dot{\bar{\bar{\varepsilon}}}^{pl} = \dot{P}\left((1-a)\frac{\bar{\bar{\sigma}}'}{J_2} + a\,\frac{tr(\bar{\bar{\sigma}})}{|tr(\bar{\bar{\sigma}})|}I\right) \tag{34}$$

Demonstration of Equation (34) in tension (Equation (35)) and in compression (Equation (36)) has been shown below.

Demonstration:

- In tension

$$\sigma > 0$$

$$J_2 = \sigma\,;\; tr(\bar{\bar{\sigma}}) = \sigma\,;\; |tr(\bar{\bar{\sigma}})| = \sigma$$

$$\begin{bmatrix} \dot{\varepsilon}_{11}^{pl} & \dot{\varepsilon}_{12}^{pl} & \dot{\varepsilon}_{13}^{pl} \\ \dot{\varepsilon}_{21}^{pl} & \dot{\varepsilon}_{22}^{pl} & \dot{\varepsilon}_{23}^{pl} \\ \dot{\varepsilon}_{31}^{pl} & \dot{\varepsilon}_{32}^{pl} & \dot{\varepsilon}_{33}^{pl} \end{bmatrix} = \dot{p} \left((1-a) \begin{bmatrix} \frac{2}{3} & 0 & 0 \\ 0 & \frac{-1}{3} & 0 \\ 0 & 0 & \frac{-1}{3} \end{bmatrix} + a \begin{bmatrix} 1 & 0 & 0 \\ 0 & 1 & 0 \\ 0 & 0 & 1 \end{bmatrix} \right) \quad (35)$$

- In compression

$$\sigma < 0$$

$$J_2 = -\sigma \; ; \; tr(\bar{\bar{\sigma}}) = \sigma \; ; \; |tr(\bar{\bar{\sigma}})| = -\sigma$$

$$\begin{bmatrix} \dot{\varepsilon}_{11}^{pl} & \dot{\varepsilon}_{12}^{pl} & \dot{\varepsilon}_{13}^{pl} \\ \dot{\varepsilon}_{21}^{pl} & \dot{\varepsilon}_{22}^{pl} & \dot{\varepsilon}_{23}^{pl} \\ \dot{\varepsilon}_{31}^{pl} & \dot{\varepsilon}_{32}^{pl} & \dot{\varepsilon}_{33}^{pl} \end{bmatrix} = \dot{p} \left((1-a) \begin{bmatrix} \frac{-2}{3} & 0 & 0 \\ 0 & \frac{1}{3} & 0 \\ 0 & 0 & \frac{1}{3} \end{bmatrix} + a \begin{bmatrix} -1 & 0 & 0 \\ 0 & -1 & 0 \\ 0 & 0 & -1 \end{bmatrix} \right) \quad (36)$$

Case-11 RVE without pores has been considered for testing the new subroutine with modified normal to the surface. Compression and tension have been performed with a true strain rate of 10^{-2} s^{-1}. Figure 5-15 (A) represents true longitudinal vs. volumetric strain in compression and tension. From Figure 5-15 (A), is clear that even if the formulation of normal to the load surface is modified in tension, there is no change in volumetric strain and true longitudinal strain. Figure 5-15 (B) indicates orange and blue curve that shows the results with the previous subroutine and new subroutine, respectively. Figure 5-15 (B) shows that volumetric strain is changed due to modification in a subroutine. It can be observed that results of compression and tension with new subroutines are similar except for the sign of volumetric strain.

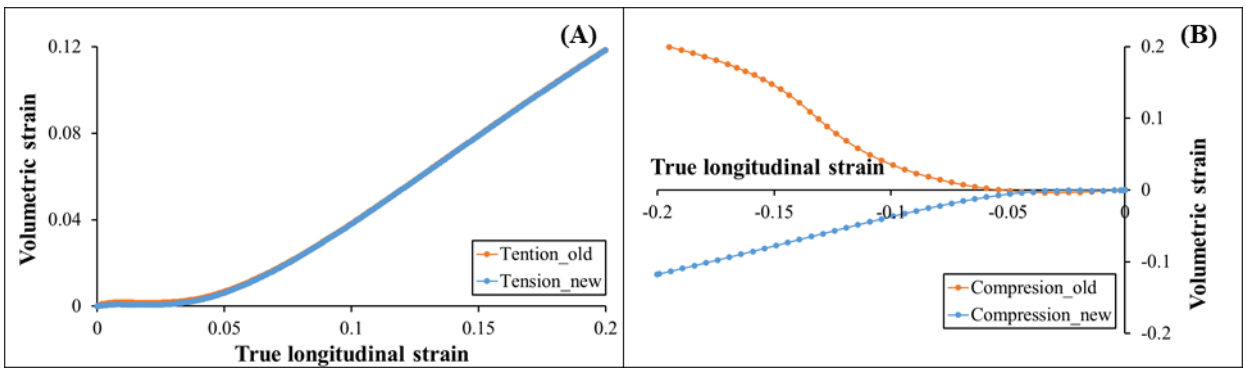

Figure 5-15 Comparison of the volumetric strain vs. true longitudinal strain using old and new subroutine in (A) Tension (B) Compression

5.10.2 Presentation of models for the correlation with 3PB test of SFS

The models are built to reproduce exactly the 3PB experiments. More precisely, it has been shown in Figure 5-16. The dimension of the samples can be found in the Chapter 4 Table 4-3. Mirror to experiments, the red two rollers are moving whereas the green roller is fixed. C3D8 elements are used for the meshing. (14172 elements and 17720 nodes). For meshing of rollers, R3D4 elements are used. Two samples (samples 10 and 11) are compared to simulations predictions. The displacement rate during the test for both the samples is 2.5 10^{-3} mm.s^{-1} as the experiments. The results of this simulation are presented in the next part.

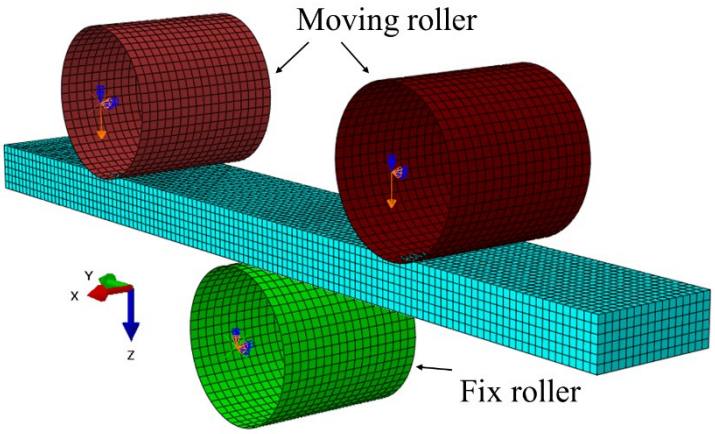

Figure 5-16 3PB model created in ABAQUS

To take into account the gradient in the mesostructure, two points are integrated:

1) A function in UMAT is written in which, the porosity associated with the position (X, Y, and Z-axis data) similar to the one identified by the tomography is recorded in variables.
2) Another function is written to integrate this data at each gauss point in the Abaqus® and use the corresponding constitutive model.

In this way, real data from tomography is integrated with the Abaqus®. Figure 5-17 (A) and Figure 5-17 (B) show this real porosity distribution identified from tomography integrated into the Abaqus® for samples 10 and 11, respectively. The black color in Figure 5-17 represents zero porosities, but when Abaqus® creates graphics with color levels, it shows below zero. When that area is checked with probe values, there are porosities equal to zero.

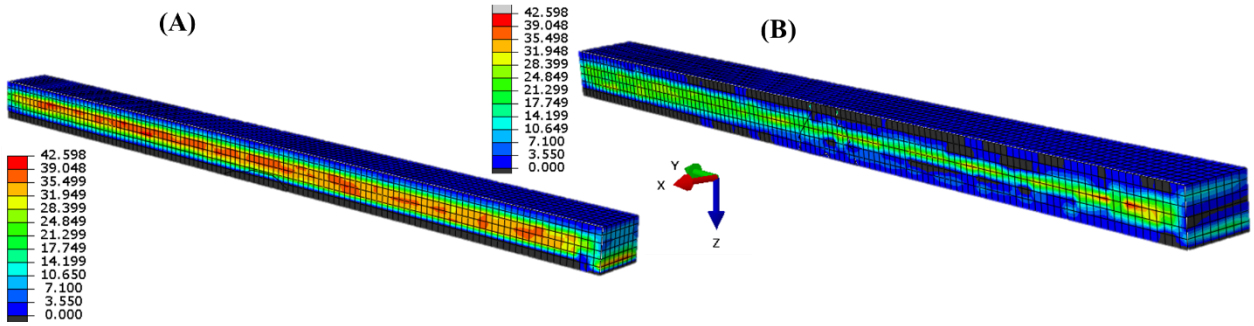

Figure 5-17 Integration of tomography porosity data into the Abaqus® for (A) Sample-10 (B) Sample-11

Figure 5-18 shows the porosity and how porosity distribution is impacted by variation in mesh density. Figure 5-18 (A) corresponds to a coarse mesh, on the other hand, Figure 5-18 (B) shows the results with a fine mesh. Basically real porosity data from tomography is linked with each gauss point by the UMAT function, but when mesh density is changed. It results in a variation of gauss points in number and in position. As porosity data is linked with gauss points which eventually affects the porosity distribution. This porosity distribution will be improved as long as the mesh is refined till we reach tomography pixel size. Figure 5-18 shows that the distribution of porosity is more detailed but the overall distribution is similar when a mesh is refined.

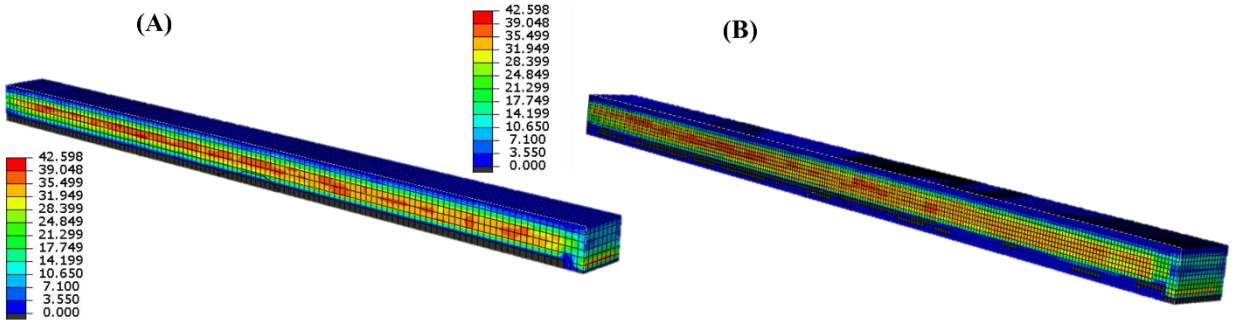

Figure 5-18 Porosity distribution with (A) Coarse mesh (B) Fine mesh

5.10.3 Comparison of experimental and simulation results in bending of SFS

Once the constitutive model is modified, the validation is the next and last step. Displacement vs. force per unit area (cross-section area is calculated at the center of the sample) is plotted in Figure 5-19 for both simulation and experiment results in bending. Figure 5-19 (A) and Figure 5-19 (B) show results for the 80% PPC sample-10 and 11, respectively. The black curve shows experimental results, whereas the green curve shows the simulation results. The result represented by the green curve is with a modified subroutine, and porosity calculated by the tomography is integrated into it. The orange curve represents the results with finer mesh.

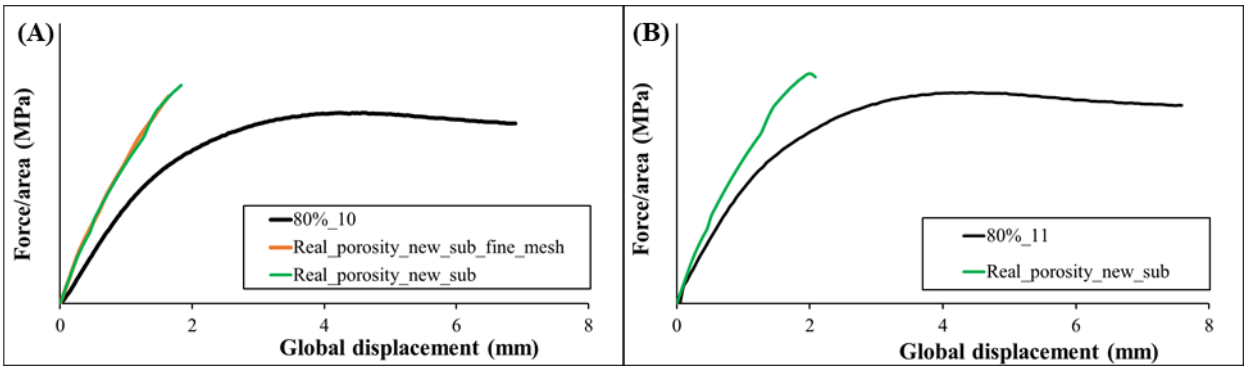

Figure 5-19 Comparison of the global displacement vs. global force per unit area 80% PPC (A) Sample-10 (B) Sample-11

It can be observed for both samples that the initial part of the curve is not superposing with the experimental results. Even if mesh density is changed, there is little influence on the simulation results since both orange and green curves are superposed in Figure 5-19 (A).

The numerical stiffness is higher in experimental results, but this difference is lower for sample 11, which has a lower mean porosity.

When comparing the two meshes, the numerical result seems to converge; the explanation should be found in the constitutive model. In the following paragraph, an attempt to explain this phenomenon is proposed.

5.10.4 Discussion based on a simplified model in 3PB of SFS with average porosity inside the foam

Figure 5-20 (A) shows a simplified model of 3PB with properties of average porosity inside the foam. The boundary condition and dimension of samples are precisely the same as 3PB presented in Figure 5-16. The major difference is a sample which subjected to bending has three layers SFS. The thickness of the layers is determined by the tomography data. In Abaqus® two different sections with foam and skin material are created, same as Figure 5-20 (B). The relation between constitutive model parameters and porosity is known by the study of RVE. Using those relations parameters corresponding to zero porosity is assigned to the skin in Abaqus® section skin. For Abaqus® section foam properties corresponding to a constant porosity in the foam are given. The results of these simulations are presented in the next part.

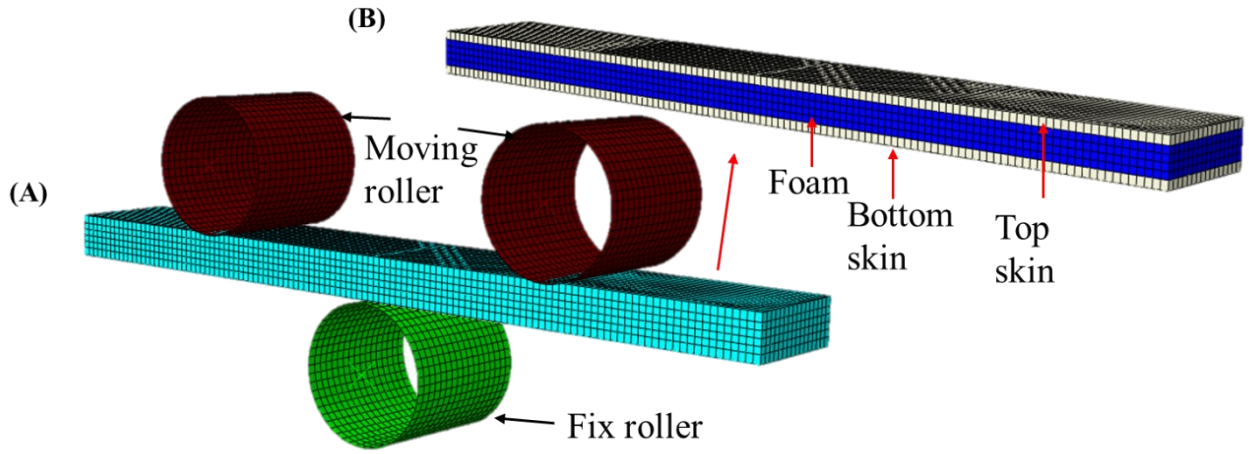

Figure 5-20 3PB simplified model created in ABAQUS

As shown in Figure 5-19 (A) and Figure 5-19 (B), an important difference between experimental results and simulation results of 3PB exists. Therefore, some simulations have been performed with a simplified model (Figure 5-20) to understand, and the results are plotted in Figure 5-21.

The first question is, results with real distribution of porosity is relevant or not? A simulation with a foam layer with the 30% porosity (please see Figure 5-11, Figure 5-12, and Figure 5-20) is done to answer this question. Figure 3-21 (A) shows bending results of sample-10. The green curve represents the simulation results with the real distribution of porosity (respective constants) inside the foam whereas the pink and red curve represents the simulation results with constants corresponding to 30 and 60% average porosity in the foam. The 30% value is close to the mean of porosity inside the foam layer in sample-10. Figure 5-21(B) shows the results for the sample-11. Color coding for the curve is the same as sample-10. Figure 5-21 (A), it can be seen that the green and pink curves are almost superimposed. This gives a reason to conclude that simulation results with real porosity distribution give relevant results.

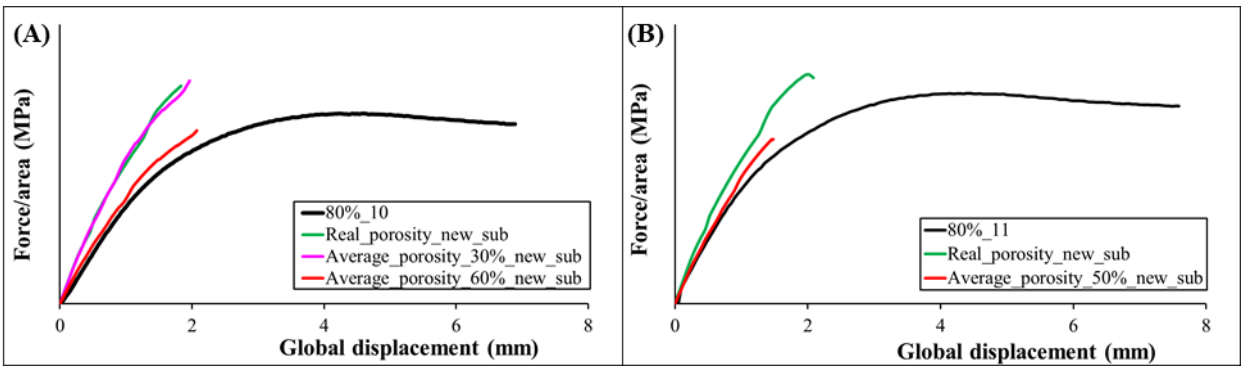

Figure 5-21 Comparison of global displacement vs. global force per unit area of bending simulation and experimental results (A) Sample-10 (B) Sample-11 of 80% PPC.

This result suggests that the measurement of global quantities (force-displacement) during this 3PB test is not sufficient to characterize the response of the foam. These measurements do not seem to be discriminating but further analysis is needed to better evaluate this experiment.

Some simulations with foam parameters corresponding to the 30%, 50%, and 60% of porosity are done. It can be seen from Figure 5-22 how a constant porosity inside the center layer affects the final response of the simulation in 3PB. Black, red, purple, and green color curves show results corresponding to simulation with constant respect to the average porosity 0, 30, 40, and 60%, respectively. As average porosity increases the slope of the curve decreases, and this test is fully capable of capturing the differences in responses for the different foams.

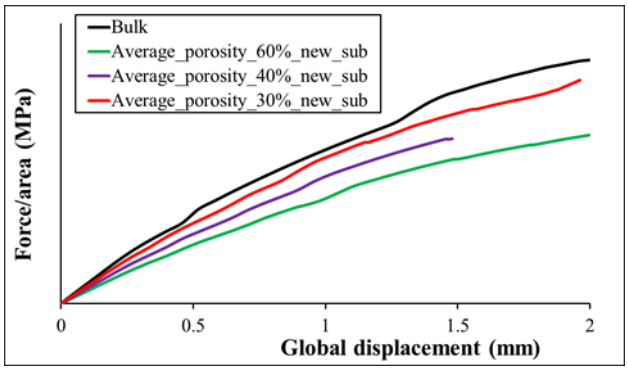

Figure 5-22 3PB simulation results of global displacement vs. global force per unit area with different average porosity (0, 30, 40, and 60%)

The next question arises about the mean porosity inside the sample-10 and 11, which will give similar results to experiments? Two simulations with foam parameters corresponding to the 50% and 60% of porosity are done.

The red curve in Figure 5-21 (A) shows the numerical results for sample 60%, it is very close to experiments.

The same comparison has been performed on a sample-11 of 80% PPC. The red curve in Figure 5-21 (B) shows that the foam parameters correspond to the 50% porosity and this porosity gives good results with respect to experiments.

A comparison of the numerical models with the experimental curves suggests that the porosity would be much higher than that observed. This seems to confirm the role played by the small porosities observed optically in Figure 5-3.

To support or eliminate this hypothesis, two simple calculations have been made:

1) The first is the level of small porosities in the polymer of the foam, which surrounds the bubbles identified by tomography. Approximately it would be 42% to reach 60% porosity in total. However, the images of a section show only a few percent of small porosities, which discredits this hypothesis.

2) The mass ratio of the complete plate with a 60% porosity in the foam layer would be 63.2% PPC, but the ratio measured for sample-10 (measurement of the mass with a precision balance and measurement of the volume with a tomography) is 87.5%, the difference is too large, which also discredits this hypothesis.

5.10.5 Discussion, comparison of experimental and simulation results in compression of SFS

The comparison study will be conducted on the compression tests to confirm the previous results. Figure 5-23 (A) represents the Abaqus® model of compression test for sample-3 with 80% PPC. Real dimensions are taken into account which is 8 x 8 x 3.1 (L x W x T) mm. The top face (Orange arrows can be seen on it in Figure 5-23 (A)) is applied with the same local displacement rate (computed with ratio calculation. For more details please see Chapter 4 4.5.3) as the experiments along Z-axis. Bottom face displacement is zero along Z-axis. There are two points on the bottom face, one point which is at the center whose displacement along the X and Y-axis is zero, and the second point which is at the edge on the bottom face where displacement along Z-axis is zero. Figure 5-23 (B) shows porosity distribution inside the compression sample taken into account in the same way as bending simulations.

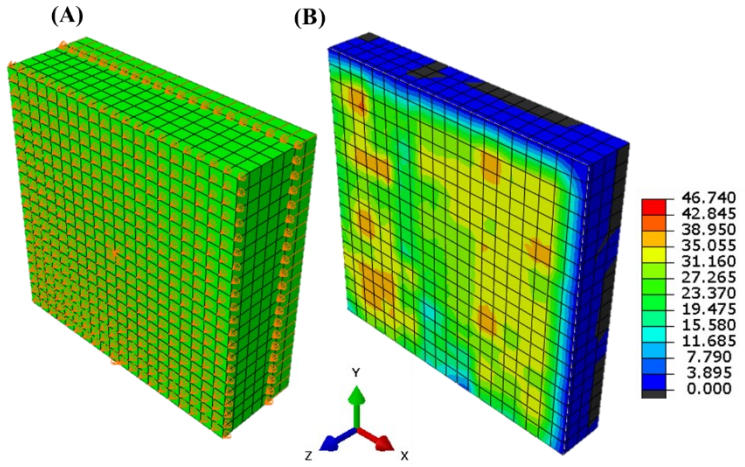

Figure 5-23 (A) Compression test model created in Abaqus® (B) Integration of tomography porosity data into the Abaqus®

Figure 5-24 shows the results of compression for the sample-3 80% PPC. The green color curve is experimental data whereas the blue and orange curves are simulation data. It can be observed that simulation and experimental results have different initial slop. That is explained by the fact that the sample is not flat as explained in Chapter 4 heading 4.5.3, but the local displacement has been added in Figure 5-24 in order to eliminate the artifact of the set-up. Basically, Red, blue, and back dots represent local information calculated from DIC at the

right, center and left location of sample whereas green dot represents data calculated using ImageJ software at center of sample.

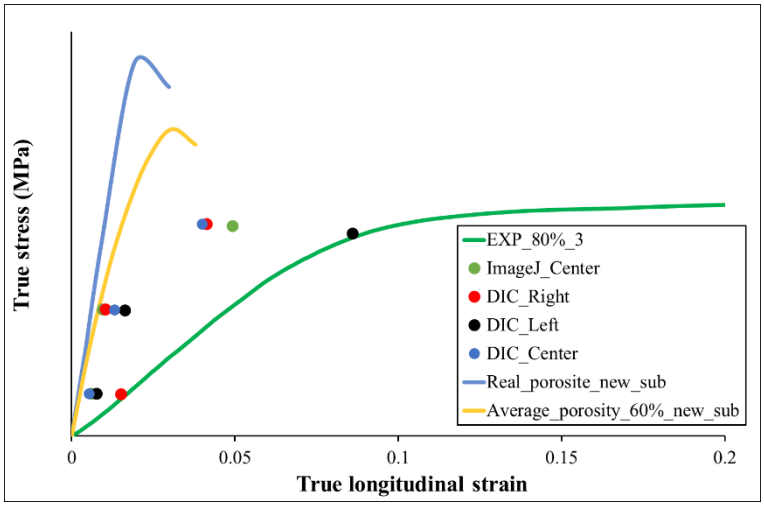

Figure 5-24 Comparison of the corrected global displacement vs. global force per unit area 80% PPC sample-3 in compression

As in the case of the bending test, the compressive numerical stiffness is higher than the experimental data, but the difference with local measurement seems lower.

The same simulation with a layer with a 60% constant porosity is plotted to confirm the bending results. Although the compression tests are difficult to use, the trend is found concerning stiffness.

However, it seems that the calculated threshold in compression is much higher than the experimental one, which suggests that the plastic response in the foam layer of the specimen is fundamentally different from the one obtained from the modeling.

On the basis of all these results, the confrontation of numerical simulations with experiments leads us to think that the polymer in the foam is in a different physical state from that of the skins. However, its crystallinity is the same level as what is measured in DSC. So, could the crystal structure be different? It is an open question.

The basic assumption in the construction of the constitutive model is that the polymer between the bubbles has a very similar behavior to that of the bulk material; this one is certainly not relevant.

This is a debatable result, but everything seems to converge towards this proposal that should be studied further in future work.

5.11 Conclusion

RVEs are created based on the tomography data to build the constitutive model and a specific protocol has been followed to identify the model's parameters in the function of the porosity. Detailed about RVE creation is explained. Different values of pore radius, and distance between pores have been chosen to create the RVE numerical models. When these parameters are changed that leads to the variation of porosities. It has been identified that porosity is the major factor.

Responses of these numerical tension simulations on different RVEs are used as the experimental data. After that, cubes of the same size without porosities are created in Abaqus® and subjected to the same boundary condition as RVEs to identify the homogenized parameter. By using a 3D optimization tool consisting of DAKOTA which homogenize properties of new material corresponding to each RVE. This simple homogenization led us to a table with RVEs and their corresponding material constants. Basically E_1, E_2, E_3, E_4, Q_1 and N constants are identified concerning each RVE and eventually with respect to porosity. After this relation between porosity and material constant is established. Modification in the constitutive model has been performed in order to have similar behavior in compression and tension.

To validate some experiments that have been performed, compression and bending are investigated. The sample contains a gradient of porosity in the foam layer. Global and local measurements are applied to obtain much information about the foam behavior. Compression testing does not give reliable results, but trends can be shown. The bending tests are much better controlled, and the influence of the porosity distribution has been highlighted. Numerical model is then proposed to simulate these experiments, and the distribution of porosity is deployed in the numerical model at each Gauss point. The numerical responses show a higher stiffness than the experimental measurements in both bending and compression.

Taking maximum advantage of the numerical tool, it is shown that porosity of 50% for sample-11 and 60% for samples-10 gives similar results to experiments. However, these values are not consistent with local observations and mass measurements. This led us to conclude that in the foam, the physical state of the polymer must be investigated.

Chapter 6 **Conclusion and perspective**

A new modeling solution to the new type of materials is proposed to the engineers; this work contributes to the identification of a particular sandwich composed of a single material and generated by injection or rotational molding processes. Part of a car where low-speed impacts must be controlled for the safety of pedestrians, in this industrial context, describing the behavior of a new material requires numerous characterization tests (tensile, bending, shear, etc.). However, the industry needs efficient constitutive models, which can predict the behavior of materials and the structures under different types of loading as well as with a minimum number of material constants (or a minimum number of experiments). The more material constants are introduced to describe the tri-axial behavior, the more tests are necessary, which require a substantial investment of time and resources. So, it is crucial from the industrial point of view to require a lesser number of material constants determined from a smaller set of (number and type) experiments. The challenge has been to build a constitutive model of the sandwich with the minimum of experiments data.

There are many challenges with these kinds of materials. The process parameters highly influence the microstructure of the skin. Here the distance between the edges of the pores is such that the material can more or less retain its spherulitic mesostructure. The morphology in these areas of the material is an interesting open question. There is a gradient of pores inside the foam. The size of the pores and the distance between the pores vary inside the sample, and this is not perfectly known, for the development of a constitutive model for sandwich composite (SFS) concerning the description of microstructure which contains gradient.

To characterize the behavior of bulk, only tensile tests have been performed to reduce the time and effort needed to find the material constants as highlighted before. The optical measurements (longitudinal and transverse strains) during these tests allow the hydrostatic pressure coefficient to be evaluated. It is one key of the protocol to obtain predictive results. Two materials have been studied: polyethylene (PE), and polypropylene (PPC). The elasto-visco-plastic constitutive model has been identified for each material. The Abaqus® extension, which is UMAT, has been used to write this specific constitutive model in Fortran. To optimize the material parameters of the constitutive model, Abaqus® with UMAT is integrated with the open-source optimization toolkit DAKOTA. The validation of the PE model has been performed by comparing 3PB, and 4PB simulation results with experimental results, and the analysis of the global responses allowed us to conclude:

- the excellent consideration of the behavior in different stress modes (tension-compression, under 4PB, and shear under 3PB),
- the capability to numerically identify a friction coefficient from the correlation in the bending tests (only unknown parameter). But for an even more accurate representation

of the coefficient of friction as a function of sliding speed and contact pressure, additional experimental data is required.

The good correlation observed on the different sample thicknesses permits us to confirm at the global scale that there is no influence of the process (rotational molding). If microstructure variations exist, the effects are within the variability of validations tests.

Therefore, the constitutive model is adapted to predict the behavior of the structure with different thicknesses. To prove this one, the predictability of the numerical calculation has been evaluated by comparing the results with those of the tests on the bottle subjected to internal pressure. It seems the model can predict the onset of damage with localization of hydrostatic pressure and equivalent strain rate and fields of strain and displacement are in the range of measurement accuracy.

Once the constitutive model for the skin is developed, the next step is to find a model for the foam. X-ray tomography has been used to understand the foam's mesostructure inside the sandwich deeply. The Matlab® tool to treat the data of tomography has been constructed, which extracts the minimum distance between the pores, diameters of pores, as well as porosity at different scales. It is important to note that 2D (3D field of porosity) and 3D RVE (integrated into the thickness) are used while extracting this data. A histogram of all three quantities has served as a database to define the foam's statistics and create RVEs of foam. Different diameters of pores and distances between the pores corresponding with statistical parameters have been chosen to study numerically their influence on behavior.

Then a specific numerical protocol has been proposed to identify the constitutive model of SFS sensitive to the speed and hydrostatic pressure. Unlike the more classical approach here numerical tensile tests have been performed on REV which contains a large number of pores. As for the bulk, Abaqus® and DAKOTA are linked to find the homogenized properties and dependencies of elasto-viscoplastic parameters with respect to the porosity inside RVE. The principal assumption is that the polymer inside the foam between bubbles is in the same state as skin. DSC tests have supported this hypothesis, but it is not sufficient. In this framework, rotational molded specimens have been avoided since the porosity level is too high, and it is not reasonable to apply this numerical protocol. To validate the constitutive model of the PPC, some compression and bending experiments have been performed on injected SFS specimens. The macroscopic field and mesoscopic field are quantified. Compressive tests are difficult to analyze due to the uneven thickness of samples and slight misalignment of specimen and set-up. The bending tests give probing results. When simulation of bending and compression tests of SFS sample have been performed, it appears that the foam stiffness is overevaluated. A very simple modification in the model permits a reduction of the difference but it can be concluded that the assumption of the polymer state inside the foam or the evaluation

of porosity is not validated. Following optical observations show that there are minor porosities. Second scales of bubbles are present inside the matter between the bubbles.

It is important to underline this protocol permits to evaluate of the behavior with macroscopic experiments and suggests two propositions that should be confirmed in the future work:

- the porosity has a second level (smaller bobbles seen during optical observations) which influences the behavior in the foam
- the crystallinity has the same level but the shapes of spherulite generate a specific behavior. Some local experiments should be done as ultra-micro indentations tests to characterize this at last.

With respect to the application, it is possible to integrate into a model this variability of porosity at the scale of the structure, which allows in the more or less long term to establish a bridge between the process and the properties by implementing a completely numerical chain.

A characterization campaign must be resumed to improve the understanding of the mechanisms related to the state of the material. If it is possible to carry out tests under tomography, the difficulty here is that the porosity or the state of the material seems to play the central role, and that is not achievable in the state unless to go on the X-ray beams of gas pedals which allow finer resolutions.

Concerning the foam generated by rotational molding, a specific study must be carried out using more classical homogenization techniques. Because the degree of porosity is much higher, but the difficulty will be to define an RVE that is truly representative of the microstructure. The distribution of porosity is very random with small bubbles next to bigger ones. A work of micromechanics is to be carried out in the future.

APPENDIX

For the analysis of foam Young's modulus following very simple study can be performed.

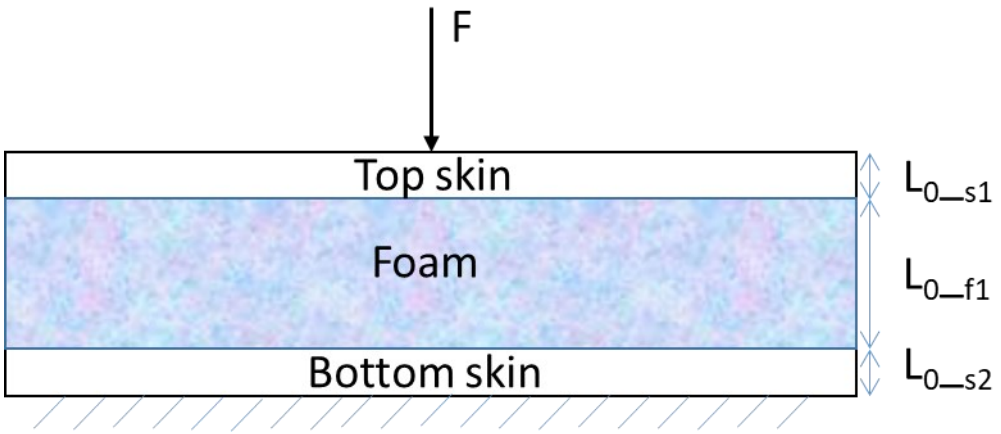

Figure 6-1 Schematic of sample under compression

$$\delta = l^{actual} - l^{initial} \tag{37}$$

Where δ is change in length of the sample, l^{actual} - actual length during compression, $l^{initial}$ = initial length of sample.

$$l_{s1} = \varepsilon^{s1} L_{0\_s1} + L_{0\_s1} \tag{38}$$

Where l_{s1} is actual length of top skin during the test, L_{0_s1} is initial length of top skin, ε^{s1} is true strain in top skin.

$$l_{s2} = \varepsilon^{s2} L_{0\_s2} + L_{0\_s2} \tag{39}$$

Where l_{s2} is actual length of bottom skin during the test, L_{0_s2} is initial length of bottom skin, ε^{s2} is true strain in bottom skin.

$$l_{f1} = \varepsilon^{f1} L_{0\_f1} + L_{0\_f1} \tag{40}$$

Where l_{f1} is actual length of foam during the test, L_{0_f1} is initial length of foam, ε^{f1} is true strain in foam.

$$l^{actual} = l_{s1} + l_{f1} + l_{s2} \tag{41}$$

By putting in Equation(41) in Equation (37)

$$\delta = \left(\varepsilon^{s1} L_{0_{s1}} + L_{0_{s1}}\right) + \left(\varepsilon^{s2} L_{0_{s2}} + L_{0_{s2}}\right) + \left(\varepsilon^{f1} L_{0\_f1} + L_{0\_f1}\right) - l^{initial} \tag{42}$$

For more simplification, following equation of strain has been used.

$$\varepsilon^{s1} = \frac{F/S}{E^{bulk}} \tag{43}$$

Where F is force, S is area of cross section, E^{bulk} is Young's modulus of bulk (skin)

$$\varepsilon^{f1} = \frac{F/S}{E^{foam}} \tag{44}$$

Where E^{foam} is Young's modulus of foam.

Now by putting Equation (43) and Equation (44) in Equation (42)

$$\delta = \frac{F/S}{E^{bulk}} l_{s1} + \frac{F/S}{E^{foam}} l_{f1} + \frac{F/S}{E^{bulk}} l_{s2} \tag{45}$$

By doing simplification we get Young's modulus of foam

$$E^{foam} = \frac{(F/S)\, l_{f1}}{\delta - \frac{F/S}{E^{bulk}}(l_{s1} + l_{s2})} \tag{46}$$

REFERENCE LIST

[1] A. Aremu, I. Ashcroft, R. Hague, R. Wildman, and C. Tuck, "Suitability of SIMP and BESO topology optimization algorithms for additive manufacture," *21st Annual International Solid Freeform Fabrication Symposium - An Additive Manufacturing Conference, SFF 2010*, pp. 679–692, 2010.

[2] D. M. Nieto and D. M. Sánchez, "Design for additive manufacturing: Tool review and a case study," *Applied Sciences (Switzerland)*, vol. 11, no. 4, pp. 1–13, 2021.

[3] C. Roiron *et al.*, "Caractérisation et modélisation d ' un composite PolyÉthylène Auto-Renforcé To cite this version : HAL Id : hal-02420773 Caractérisation du comportement d ' un composite PolyÉthylène Auto -Renforcé Characterization of the behaviour of a Self-Reinforced Po," 2019.

[4] C. Roiron, E. Lainé, J. C. Grandidier, D. Olivier, N. Garois, and C. Vix, "Study of the thermomechanical behavior of UHMWPE yarns under different loading paths," *Polymer Testing*, vol. 89, no. July, 2020.

[5] Eric MAZIERS, "Rotomoulded articles," 9862169, 2014.

[6] S. Emami, "Development of Probabilistic Models for Long Term Reliability of Sandwich Composites in Saline Freeze / Thaw Environment for Civil Engineering Applications," Georgia Southern University, 2018.

[7] M. O. Kaman, M. Y. Solmaz, and K. Turan, "Experimental and numerical analysis of critical buckling load of honeycomb sandwich panels," *Journal of Composite Materials*, vol. 44, no. 24, pp. 2819–2831, 2010.

[8] A. B. Morgan and E. Toubia, "Cone calorimeter and room corner fire testing of balsa wood core/phenolic composite skin sandwich panels," *Journal of Fire Sciences*, vol. 32, no. 4, pp. 328–345, 2014.

[9] T. Khan, V. Acar, M. R. Aydin, B. Hülagü, H. Akbulut, and M. Ö. Seydibeyoğlu, "A review on recent advances in sandwich structures based on polyurethane foam cores," *Polymer Composites*, vol. 41, no. 6, pp. 2355–2400, 2020.

[10] M. M. Ratwani, "Composite Materials and Sandwich Structures – A Primer," *Rto-En-Avt*, vol. 156, pp. 1–16, 2010.

[11] B. Vijaya Ramnath, K. Alagarraja, and C. Elanchezhian, "Review on sandwich composite and their applications," *Materials Today: Proceedings*, vol. 16, pp. 859–864, 2019.

[12] J. M. Davies, *Lightweight sandwich construction*. John Wiley & Sons, 2008.

[13] W. Nsengiyumva, S. Zhong, J. Lin, Q. Zhang, J. Zhong, and Y. Huang, "Advances, limitations and prospects of nondestructive testing and evaluation of thick composites

and sandwich structures: A state-of-the-art review," *Composite Structures*, vol. 256, p. 112951, 2021.

[14] E. B. Ndiaye and H. Duflo, "Non Destructive Testing of sandwich composites: adhesion defects evaluation; Experimental and Finite Element Method simulation comparison," *Acoustics 2012 Nantes*, no. April, pp. 2659–2664, 2012.

[15] M. Vikström, J. Bäcklund, and K. A. Olsson, "Non-destructive testing of sandwich constructions using thermography," *Composite Structures*, vol. 13, no. 1, pp. 49–65, 1989.

[16] M. Street and G. Davies, "Metallic foams: their production, properties and applications," *Journal of Materials Science*, vol. 18, no. 7, pp. 1899–1911, 1983.

[17] V. Shapovalov, "Porous Metals," *MRS Bulletin*, vol. 19, no. 4, pp. 24–28, 1994.

[18] N. J. Mills, "Chapter 18 - Sandwich panel case study," in *Polymer Foams Handbook*, N. J. Mills, Ed. Oxford: Butterworth-Heinemann, 2007, pp. 425–447.

[19] J. Banhart, "Manufacture, characterisation and application of cellular metals and metal foams," *Progress in Materials Science*, vol. 46, no. 6, pp. 559–632, 2001.

[20] P. Veale, "Investigation of the Behavior of Open Cell Aluminum Foam," University of Massachusetts Amherst, 2010.

[21] J. W. Brockmeyer and L. S. Aubrey, "Application of Ceramic Foam Filters in Molten Metal Filtration," in *Application of Refractories: Ceramic Engineering and Science Proceedings*, John Wiley & Sons, Ltd, 2008, pp. 63–74.

[22] H. X. Peng, Z. Fan, J. R. G. Evans, and J. J. C. Busfield, "Microstructure of ceramic foams," *Journal of the European Ceramic Society*, vol. 20, no. 7, pp. 807–813, 2000.

[23] Y. I. Vaisman, A. A. Ketov, and P. A. Ketov, "The scientific and technological aspects of foam glass production," *Glass Physics and Chemistry*, vol. 41, no. 2, pp. 157–162, 2015.

[24] B. Wang, K. Matsumaru, and J. Yang, "High Strength Borosilicate Foams by Expansion of Ar-Filled Pores and Release of Dissolved Ar Gas," *AZoM*, pp. 1–10, 2011.

[25] Milhail Ionescu, *Chemistry and Technology of Polyols for Polyurethanes*. Shrewsbury, UK: Rapra Technology, 2007.

[26] Rapra, "High-Performance Polymer Foams to 2021—Market Reports," Shawbury, UK, 2018.

[27] S. Das, P. Heasman, T. Ben, and S. Qiu, "Porous Organic Materials: Strategic Design and Structure-Function Correlation," *Chemical Reviews*, vol. 117, no. 3, pp. 1515–1563, 2017.

[28] M. Howe-Grant and A. Pfennig, "Kirk Othmers Encyclopedia of Chemical Technology, 4th Ed., Vol. 8. M. Howe-Grant (Ed.), John Wiley & Sons, New Yourk 1993. 1093 S., zahlr. Abb. und Tab., geb., £ 185,00.," *Chemie Ingenieur Technik*, vol. 66, no. 9, p. 1274, 1994.

[29] C. Okolieocha, D. Raps, K. Subramaniam, and V. Altstädt, "Microcellular to nanocellular polymer foams: Progress (2004-2015) and future directions - A review," *European Polymer Journal*, vol. 73, pp. 500–519, 2015.

[30] M. M. Hirschler, "Polyurethane foam and fire safety," *Polymers for Advanced Technologies*, no. November 2007, pp. 229–236, 2008.

[31] N. V. Gama, A. Ferreira, and A. Barros-Timmons, "Polyurethane foams: Past, present, and future," *Materials*, vol. 11, no. 10, 2018.

[32] S. Mali, "Biodegradable foams in the development of food packaging," *Polymers for Food Applications*, pp. 329–345, 2018.

[33] K. H. Lo, A. Miyase, and S. S. Wang, "Failure strength predictions for closed-cell polyvinyl chloride foams," *Journal of Composite Materials*, vol. 52, no. 30, pp. 4185–4201, 2018.

[34] F. Saint-michel *et al.*, "Mechanical properties of high density polyurethane foams: I. Effect of the density," 2019.

[35] Z. Zakaria, Z. M. Ariff, and C. S. Sipaut, "Effects of parameter changes on the structure and properties of low-density polyethylene foam," *Journal of Vinyl and Additive Technology*, vol. 15, no. 2, pp. 120–128, 2009.

[36] R. Bouix, P. Viot, and J. L. Lataillade, "Polypropylene foam behaviour under dynamic loadings: Strain rate, density and microstructure effects," *International Journal of Impact Engineering*, vol. 36, no. 2, pp. 329–342, 2009.

[37] E. Y. R. Gautam, A. Bassi, "A Review of Biodegradation of Synthetic Plastic and Foams," *ACM SIGCPR Computer Personnel*, vol. 7, no. 4, pp. 12–12, 1978.

[38] K. Sivertsen, "Polymer Foams 3.063 Polymer Physics Spring 2007," 2007.

[39] Z. Zakaria, Z. Mohamad Ariff, and A. Abu Bakar, "Monitoring deformation mechanism of foam cells in polyethylene foams via optical microscopy: Effect of density and microstructure," *Journal of Cellular Plastics*, vol. 54, no. 6, pp. 957–976, 2018.

[40] A. International, "ASTM D575-91 Rubber Compression Test Standard," *ASTM International*, vol. 91, no. Reapproved, pp. 13–16, 1996.

[41] L.J. Gibson and M.F. Ashby, *Cellular solids: Structure & properties*. Oxford: Pergamon Press, 1989.

[42] M. E. Kabir, M. C. Saha, and S. Jeelani, "Tensile and fracture behavior of polymer foams," *Materials Science and Engineering A*, vol. 429, no. 1–2, pp. 225–235, 2006.

[43] D. Zenkert and M. Burman, "Tension, compression and shear fatigue of a closed cell polymer foam," *Composites Science and Technology*, vol. 69, no. 6, pp. 785–792, 2009.

[44] Standard, "C273 (2000) Standard test method for shear properties of sandwich core materials," *ASTM, West Conshohocken*, vol. 15, pp. 1–4, 2000.

[45] D. F. Adams and D. R. Doner, "Transverse Normal Loading of a Unidirectional Composite," *Journal of Composite Materials*, vol. 1, no. 2, pp. 152–164, 1967.

[46] P. Suquet, "Elements of Homogenization Theory for Inelastic Solid Mechanics, in Homogenization Techniques for Composite Media," 1987.

[47] S. Kruch and S. Forest, "Computation of coarse grain structures using a homogeneous equivalent medium," *Journal De Physique. IV : JP*, vol. 8, no. 8, 1998.

[48] F. Fritzen, S. Forest, T. Böhlke, D. Kondo, and T. Kanit, "Computational homogenization of elasto-plastic porous metals," *International Journal of Plasticity*, vol. 29, no. 1, pp. 102–119, 2012.

[49] F. Feyel and J. L. Chaboche, "FE 2 multiscale approach for modelling the elastoviscoplastic behaviour of long fibre SiC/Ti composite materials," *Computer Methods in Applied Mechanics and Engineering*, vol. 183, no. 3–4, pp. 309–330, 2000.

[50] V. G. Kouznetsova, M. G. D. Geers, and W. A. M. Brekelmans, "Multi-scale second-order computational homogenization of multi-phase materials: A nested finite element solution strategy," *Computer Methods in Applied Mechanics and Engineering*, vol. 193, no. 48–51, pp. 5525–5550, 2004.

[51] R. J. M. Smit, W. A. M. Brekelmans, and H. E. H. Meijer, "Prediction of the large-strain mechanical response of heterogeneous polymer systems: Local and global deformation behaviour of a representative volume element of voided polycarbonate," *Journal of the Mechanics and Physics of Solids*, vol. 47, no. 2, pp. 201–221, 1999.

[52] H. Moulinec and P. Suquet, "A FFT-Based Numerical Method for Computing the Mechanical Properties of Composites from Images of their Microstructures," pp. 235–246, 1995.

[53] S. Forest and K. Sab, "Cosserat overall modeling of heterogeneous materials," *Mechanics Research Communications*, vol. 25, no. 4, pp. 449–454, 1998.

[54] F. Feyel, "A multilevel finite element method (FE2) to describe the response of highly non-linear structures using generalized continua," *Computer Methods in Applied Mechanics and Engineering*, vol. 192, no. 28–30, pp. 3233–3244, 2003.

[55] V. Kouznetsova, M. G. D. Geers, and W. A. M. Brekelmans, "Multi-scale constitutive

modelling of heterogeneous materials with a gradient-enhanced computational homogenization scheme," *International Journal for Numerical Methods in Engineering*, vol. 54, no. 8, pp. 1235–1260, 2002.

[56] M. G. D. Geers, V. G. Kouznetsova, and W. A. M. Brekelmans, "Multi-scale computational homogenization: Trends and challenges," *Journal of Computational and Applied Mathematics*, vol. 234, no. 7, pp. 2175–2182, 2010.

[57] A. C. Eringen and D. G. B. Edelen, "On nonlocal elasticity," *International Journal of Engineering Science*, vol. 10, no. 3, pp. 233–248, 1972.

[58] H. Gao, Y. Huang, and W. D. Nix, "Modeling plasticity at the micrometer scale," *Naturwissenschaften*, vol. 86, no. 11, pp. 507–515, 1999.

[59] K. Kitazono, E. Sato, and K. Kuribayashi, "Application of mean-field approximation to elastic-plastic behavior for closed-cell metal foams," *Acta Materialia*, vol. 51, no. 16, pp. 4823–4836, 2003.

[60] V. S. Deshpande and N. A. Fleck, "Isotropic constitutive models for metallic foams," *Journal of the Mechanics and Physics of Solids*, vol. 48, no. 6, pp. 1253–1283, 2000.

[61] C. Chen and N. A. Fleck, "Size effects in the constrained deformation of metallic foams," *Journal of the Mechanics and Physics of Solids*, vol. 50, no. 5, pp. 955–977, 2002.

[62] L. J. Gibson, M. F. Ashby, J. Zhang, and T. C. Triantafillou, "Failure surfaces for cellular materials under multiaxial loads-I.Modelling," *International Journal of Mechanical Sciences*, vol. 31, no. 9, pp. 635–663, 1989.

[63] P. R. Onck, E. W. Andrews, and L. J. Gibson, "Size effects in ductile cellular solids. Part I: Modeling," *International Journal of Mechanical Sciences*, vol. 43, no. 3, pp. 681–699, 2001.

[64] A. Jung and S. Diebels, "Modelling of metal foams by a modified elastic law," *Mechanics of Materials*, vol. 101, pp. 61–70, 2016.

[65] H. X. Zhu, J. F. Knott, and N. J. Mills, "Analysıs Of The Elastıc Propertıes Of Open-Cell Foams Wıth Tetrakaıdecahedral Cells," *Journal of the Mechanics and Physics of Solids*, vol. 45, no. 3, pp. 319–343, 1997.

[66] S. K. Nammi, P. Myler, and G. Edwards, "Finite element analysis of closed-cell aluminium foam under quasi-static loading," *Materials and Design*, vol. 31, no. 2, pp. 712–722, 2010.

[67] A. Czekanski, M. S. Attia, S. A. Meguid, and M. A. Elbestawi, "On the use of a new cell to model geometric asymmetry of metallic foams," *Finite Elements in Analysis and Design*, vol. 41, no. 13, pp. 1327–1340, 2005.

[68] A. Ghazi, P. Berke, K. Ehab Moustafa Kamel, B. Sonon, C. Tiago, and T. J. Massart,

"Multiscale computational modelling of closed cell metallic foams with detailed microstructural morphological control," *International Journal of Engineering Science*, vol. 143, pp. 92–114, 2019.

[69] J. Mcconn, E. Ku, C. Odell, G. Czerlinski, and G. P. Hess, "Section of Biochemistry and Space-Filling Polyhedron : Its Relation to Aggregates of Soap Bubbles , Plant Cells , and Metal Crystallites," vol. 161, no. 9, 1964.

[70] S. Santosa and T. Wierzbicki, "On the modeling of crush behavior of a closed-cell aluminum foam structure," *Journal of the Mechanics and Physics of Solids*, vol. 46, no. 4, pp. 645–669, 1998.

[71] H. X. Zhu *et al.*, "The effects of regularity on the geometrical properties of Voronoi tessellations," *Physica A: Statistical Mechanics and its Applications*, vol. 406, pp. 42–58, 2014.

[72] A. P. Roberts and E. J. Garboczi, "Elastic moduli of model random three-dimensional closed-cell cellular solids," *Acta Materialia*, vol. 49, no. 2, pp. 189–197, 2001.

[73] C. Tekoğlu, L. J. Gibson, T. Pardoen, and P. R. Onck, "Size effects in foams: Experiments and modeling," *Progress in Materials Science*, vol. 56, no. 2, pp. 109–138, 2011.

[74] Y. Song, Z. Wang, L. Zhao, and J. Luo, "Dynamic crushing behavior of 3D closed-cell foams based on Voronoi random model," *Materials and Design*, vol. 31, no. 9, pp. 4281–4289, 2010.

[75] S. Kanaun and S. B. Kochekseraii, "Conductive properties of foam materials with open or closed cells," *International Journal of Engineering Science*, vol. 50, no. 1, pp. 124–131, 2012.

[76] Y. Chen, R. Das, and M. Battley, "Effects of cell size and cell wall thickness variations on the stiffness of closed-cell foams," *International Journal of Solids and Structures*, vol. 52, pp. 150–164, 2015.

[77] C. Redenbach, I. Shklyar, and H. Andrä, "Laguerre tessellations for elastic stiffness simulations of closed foams with strongly varying cell sizes," *International Journal of Engineering Science*, vol. 50, no. 1, pp. 70–78, 2012.

[78] C. Redenbach, "Microstructure models for cellular materials," *Computational Materials Science*, vol. 44, no. 4, pp. 1397–1407, 2009.

[79] I. Jeon, T. Asahina, K. J. Kang, S. Im, and T. J. Lu, "Finite element simulation of the plastic collapse of closed-cell aluminum foams with X-ray computed tomography," *Mechanics of Materials*, vol. 42, no. 3, pp. 227–236, 2010.

[80] O. Caty, E. Maire, S. Youssef, and R. Bouchet, "Modeling the properties of closed-cell

cellular materials from tomography images using finite shell elements," *Acta Materialia*, vol. 56, no. 19, pp. 5524–5534, 2008.

[81] M. A. Kader *et al.*, "Macro and micro collapse mechanisms of closed-cell aluminium foams during quasi-static compression," *Materials and Design*, vol. 118, pp. 11–21, 2017.

[82] T. Kanit, "Notion of representative volume element for heterogeneous materials : statistical and numerical approach Toufik Kanit To cite this version : HAL Id : tel-00005751 Notion de Volume Elémentaire Représentatif pour les Matériaux Hétérogènes : Approche Statist," 2004.

[83] C. Pelissou, J. Baccou, Y. Monerie, and F. Perales, "Determination of the size of the representative volume element for random quasi-brittle composites," *International Journal of Solids and Structures*, vol. 46, no. 14–15, pp. 2842–2855, 2009.

[84] I. M. Gitman, H. Askes, and L. J. Sluys, "Representative volume: Existence and size determination," *Engineering Fracture Mechanics*, vol. 74, no. 16, pp. 2518–2534, 2007.

[85] Hashin, "Analysis of Composite Materials," *Experimental Characterization of Advanced Composite Materials*, vol. 50, no. September 1983, pp. 25–48, 2014.

[86] W. J. Drugan and J. R. Willis, "A micromechanics-based nonlocal constitutive equation and estimates of representative volume element size for elastic composites," *Journal of the Mechanics and Physics of Solids*, vol. 44, no. 4, pp. 497–524, 1996.

[87] R. Hill, "Elastic properties of reinforced solids: Some theoretical principles," *Journal of the Mechanics and Physics of Solids*, vol. 11, no. 5, pp. 357–372, 1963.

[88] A. Mouritz, "Introduction to Aerospace Materials 1st Edition," Woodhead Publishing, 2012, pp. 268–302.

[89] S. Ahzi, A. Makradi, R. V Gregory, and D. D. Edie, "Modeling of deformation behavior and strain-induced crystallization in poly(ethylene terephthalate) above the glass transition temperature," *Mechanics of Materials*, vol. 35, no. 12, pp. 1139–1148, 2003.

[90] M. C. Boyce, D. M. Parks, and A. S. Argon, "Large inelastic deformation of glassy polymers. part I: rate dependent constitutive model," *Mechanics of Materials*, vol. 7, no. 1, pp. 15–33, 1988.

[91] E. M. Arruda, M. C. Boyce, and R. Jayachandran, "Effects of strain rate, temperature and thermomechanical coupling on the finite strain deformation of glassy polymers," *Mechanics of Materials*, vol. 19, no. 2–3, pp. 193–212, 1995.

[92] G. Ayoub, F. Zaïri, M. Naït-Abdelaziz, and J. M. Gloaguen, "Modelling large deformation behaviour under loading-unloading of semicrystalline polymers: Application to a high density polyethylene," *International Journal of Plasticity*, vol. 26, no. 3, pp. 329–347, 2010.

[93] R. N. Haward and G. Thackray, "The use of a mathematical model to describe isothermal stress-strain curves in glassy thermoplastics," *Proceedings of the Royal Society of London. Series A. Mathematical and Physical Sciences*, vol. 302, no. 1471, pp. 453–472, 1968.

[94] E. M. and B. Arruda, "A three-dimensional constitutive model for the large stretch behavior of rubber elastic materials.," *Journal of theMechanics and Physics of Solids*, vol. 41, pp. 389–412, 1993.

[95] P. D. Wu and E. van der Giessen, "On neck propagation in amorphous glassy polymers under plane strain tension," *International Journal of Plasticity*, vol. 11, no. 3, pp. 211–235, 1995.

[96] S. R. Bodner and Y. Partom, "Constitutive equations for elastic-viscoplastic strain-hardening materials," *Journal of Applied Mechanics, Transactions ASME*, vol. 42, no. 2, pp. 385–389, 1975.

[97] A. Khan and H. Zhang, "Finite deformation of a polymer: Experiments and modeling," *International Journal of Plasticity*, vol. 17, no. 9, pp. 1167–1188, 2001.

[98] C. F. Popelar, C. H. Popelar, and V. H. Kenner, "Viscoelastic material characterization and modeling for polyethylene," *Polymer Engineering & Science*, vol. 30, no. 10, pp. 577–586, 1990.

[99] E. Ghorbel, "A viscoplastic constitutive model for polymeric materials," *International Journal of Plasticity*, vol. 24, no. 11, pp. 2032–2058, 2008.

[100] O. U. Colak and N. Dusunceli, "Modeling viscoelastic and viscoplastic behavior of high density polyethylene (HDPE)," *Journal of Engineering Materials and Technology, Transactions of the ASME*, vol. 128, no. 4, pp. 572–578, 2006.

[101] C. Zhang and I. Moore, "Nonlinear mechanical response of high density polyethylene. Part II: Uniaxial constitutive modeling," *Polymer Engineering and Science*, vol. 37, no. 2, pp. 414–420, 1997.

[102] S. RA, "Correspondence principles and a generalized J- integral for large deformation and fracture analysis of viscoelastic media," *International Journal of Fracture*, vol. 25, pp. 195–223, 1984.

[103] C. G'Sell and J. J. Jonas, "Yield and transient effects during the plastic deformation of solid polymers," *Journal of Materials Science*, vol. 16, no. 7, pp. 1956–1974, 1981.

[104] L. Anand and M. E. Gurtin, "A theory of amorphous solids undergoing large deformations, with application to polymeric glasses," *International Journal of Solids and Structures*, vol. 40, no. 6, pp. 1465–1487, 2003.

[105] L. Anand and N. M. Ames, "On modeling the micro-indentation response of an

amorphous polymer," *International Journal of Plasticity*, vol. 22, no. 6, pp. 1123–1170, 2006.

[106] N. M. Ames, V. Srivastava, S. A. Chester, and L. Anand, "A thermo-mechanically coupled theory for large deformations of amorphous polymers. Part II: Applications," *International Journal of Plasticity*, vol. 25, no. 8, pp. 1495–1539, 2009.

[107] S. Nikolov and I. Doghri, "A micro/macro constitutive model for the small-deformation behavior of polyethylene," *Polymer*, vol. 41, no. 5, pp. 1883–1891, 2000.

[108] B. J. Lee, D. M. Parks, and S. Ahzi, "Micromechanical modeling of large plastic deformation and texture evolution in semi-crystalline polymers," *Journal of the Mechanics and Physics of Solids*, vol. 41, no. 10, pp. 1651–1687, 1993.

[109] A. D. Drozdov and R. K. Gupta, "Non-linear viscoelasticity and viscoplasticity of isotactic polypropylene," *International Journal of Engineering Science*, vol. 41, no. 20, pp. 2335–2361, 2003.

[110] C. Regrain, L. Laiarinandrasana, S. Toillon, and K. Saï, "Multi-mechanism models for semi-crystalline polymer: Constitutive relations and finite element implementation," *International Journal of Plasticity*, vol. 25, no. 7, pp. 1253–1279, 2009.

[111] D. M. Parks and S. Ahzi, "Polycrystalline plastic deformation and texture evolution for crystals lacking five independent slip systems," *Journal of the Mechanics and Physics of Solids*, vol. 38, no. 5, pp. 701–724, 1990.

[112] A. D. Drozdov and J. de, "Viscoelasticity and viscoplasticity of semicrystalline polymers: Structure-property relations for high-density polyethylene," *Computational Materials Science*, vol. 39, no. 4, pp. 729–751, 2007.

[113] J. L. Chaboche, "Thermodynamic formulation of constitutive equations and application to the viscoplasticity and viscoelasticity of metals and polymers," *International Journal of Solids and Structures*, vol. 34, no. 18, pp. 2239–2254, 1997.

[114] F. Khan and C. Yeakle, "Experimental investigation and modeling of non-monotonic creep behavior in polymers," *International Journal of Plasticity*, vol. 27, no. 4, pp. 512–521, 2011.

[115] A. S. Khan and B. Farrokh, "Thermo-mechanical response of nylon 101 under uniaxial and multi-axial loadings: Part I, Experimental results over wide ranges of temperatures and strain rates," *International Journal of Plasticity*, vol. 22, no. 8, pp. 1506–1529, 2006.

[116] D. A. Wang and J. Pan, "A non-quadratic yield function for polymeric foams," *International Journal of Plasticity*, vol. 22, no. 3, pp. 434–458, 2006.

[117] J. C. Grandidier and É. Lainé, "Identification by genetic algorithm of a constitutive law taking into account the effects of hydrostatic pressure and speeds," *Oil and Gas Science*

and Technology, vol. 61, no. 6, pp. 781–787, 2006.

[118] C. G'sell and J. J. Jonas, "Determination of the plastic behaviour of solid polymers at constant true strain rate," *Journal of Materials Science*, vol. 14, no. 3, pp. 583–591, 1979.

[119] BAYSTAR, "Technical Data Sheet mPE M4041UV," 2019. [Online]. Available: https://cdn2.hubspot.net/hubfs/5262664/files/Data Sheets/PE Lumicene mPE M4041 UV.pdf.

[120] TotalEnergies, "Technical data sheet PPC 6742," 2021. [Online]. Available: https://polymers-products.totalenergies.com/site_collection_documents/Technical Datasheets/PPC_6742.pdf.

[121] A. Cross and R. N. Haward, "Thermal fracture of plastics," *Journal of Polymer Science Part A-2: Polymer Physics*, vol. 11, no. 12, pp. 2423–2439, 1973.

[122] H. Oberst and W. Retting, "Influence of molecular relaxation processes on mechanical properties of polyvinyl chloride in tensile experiments," *Journal of Macromolecular Science, Part B*, vol. 5, no. 3, pp. 559–590, 1971.

[123] J. M. Andrews and I. M. Ward, "The cold-drawing of high density polyethylene," *Journal of Materials Science*, vol. 5, no. 5, pp. 411–417, 1970.

[124] G. Pezzin, G. Ajroldi, T. Casiraghi, C. Garbuglio, and G. Vittadini, "Dynamic-mechanical and tensile properties of poly(vinyl chloride). Influence of thermal history and crystallinity," *Journal of Applied Polymer Science*, vol. 16, no. 7, pp. 1839–1849, 1972.

[125] G. Meinel and A. Peterlin, "Plastic deformation of polyethylene II. Change of mechanical properties during drawing," *Journal of Polymer Science Part A-2: Polymer Physics*, vol. 9, no. 1, pp. 67–83, 1971.

[126] E. Lainé, C. Bouvy, J. C. Grandidier, and G. Vaes, "Methodology of Accelerated Characterization for long-term creep prediction of polymer structures to ensure their service life," *Polymer Testing*, vol. 79, no. January, p. 106050, 2019.

[127] P. Chitchumnong, S. C. Brooks, and G. D. Stafford, "Comparison of three- and four-point flexural strength testing of denture-base polymers," *Dental Materials*, vol. 5, no. 1, pp. 2–5, 1989.

[128] F. Mujika, "On the difference between flexural moduli obtained by three-point and four-point bending tests," *Polymer Testing*, vol. 25, no. 2, pp. 214–220, 2006.

[129] N. european N. E. I. 178, "Plastiques — Détermination des propriétés en flexion." 1997.

[130] ASTM INTERNATIONAL, "Standard Test Methods for Flexural Properties of Unreinforced and Reinforced Plastics and Electrical Insulating Materials. D790," *Annual*

Book of ASTM Standards, pp. 1–12, 2002.

[131] E. Lainé, J. C. Dupré, J. C. Grandidier, and M. Cruz, "Instrumented tests on composite pressure vessels (type IV) under internal water pressure," *International Journal of Hydrogen Energy*, vol. 46, no. 1, pp. 1334–1346, 2021.

[132] N. Bretagne, V. Valle, and J. C. Dupré, "Development of the marks tracking technique for strain field and volume variation measurements," *NDT and E International*, vol. 38, no. 4, pp. 290–298, 2005.

[133] M. Cottron, P. De, G. Bouchoux, and V. Valle, "Spectrométrie de masse - Principe Mesures en mécanique par méthodes optiques et appareillage Par : ´ canique Mesures en me ´ thodes optiques par me," vol. 33, no. 0, 2014.

[134] J. L. Chaboche, "Constitutive equations for cyclic plasticity and cyclic viscoplasticity," *International Journal of Plasticity*, vol. 5, no. 3, pp. 247–302, 1989.

[135] S. Chambaudet, "Étude et modélisation du comportementmécanique de la matrice polymère dans un composite à fibres decarbone sous compression transverse," Université INPL,École des Mines de Nancy, 2001.

[136] D. C. Drucker, "A more fundamental approach to plastic stress–strain relations.," *Proceedings of the First U. S. National Congress of Applied Mechanics, Chicago, The American Society of Mechanical Engineers*, pp. 487–491, 1951.

[137] M. Andersen, O. S. Hopperstad, and A. H. Clausen, "Volumetric strain measurement of polymeric materials subjected to uniaxial tension," *Strain*, vol. 55, no. 4, pp. 1–13, 2019.

[138] L. Eriksson, "Modeling and Control of TC SI and DI enignes," *Oil & Gas Science and Technology*, vol. 63, no. 1, pp. 9–19, 2008.

[139] M. Smith, *ABAQUS/Standard User's Manual, Version 6.17*. United States: Dassault Systèmes Simulia Corp, 2017.

[140] J. G. Adams, B.M., Bohnhoff, W.J., Dalbey, K.R., Ebeida, M.S., Eddy, J.P., Eldred, M.S., Hooper, R.W., Hough, P.D., Hu, K.T., Jakeman, J.D., Khalil, M., Maupin, K.A., Monschke, J.A., Ridgway, E.M., Rushdi, A.A., Seidl, D.T., Stephens, J.A., Swiler, L.P., and Wi, "'Dakota, A Multilevel Parallel Object-Oriented Framework for Design Optimization, Parameter Estimation, Uncertainty Quantification, and Sensitivity Analysis: Version 6.12 User's Manual,' Sandia Technical Report SAND2020-12495, November 2020." .

[141] T. Munch, "Presses à injecter - Fonctions et solutions constructives," *Techniques de l'ingénieurnieur*, vol. 33, no. 0, p. 19, 2009.

[142] RX solutions, "UltraTom." [Online]. Available: https://www.rx-solutions.com/en/ultratom-rx-solutions-1197.

[143] Justin Blaber, "Ncorr," *GitHub*, 2022. [Online]. Available: https://github.com/justinblaber/ncorr_2D_matlab.

[144] A. K. Ahmed, M. Atiqullah, D. R. Pradhan, and M. A. Al-Harthi, "Crystallization and melting behavior of i-PP: A perspective from Flory's thermodynamic equilibrium theory and DSC experiment," *RSC Advances*, vol. 7, no. 67, pp. 42491–42504, 2017.

[145] J. P. Luongo, "Chemical structure by absorption spectroscopy," *Analytical Chemistry*, vol. 33 (13), no. 28, pp. 1816–1823, 1961.

[146] A. D. Drozdov and J. de Claville Christiansen, "The effect of porosity on elastic moduli of polymer foams," *Journal of Applied Polymer Science*, vol. 137, no. 10, pp. 1–10, 2020.